APPLICATIONS OF MAGNETOTELLURIC AND TRANSIENT ELECTROMAGNETIC METHODS IN GROUNDWATER AND ENGINEERING STUDIES

By

Adel K. Mohamed, Msc (Mansoura Univ., Egypt)

Thesis submitted for the degree of

Doctor of philosophy

At the University of Leicester

Department of Geology

University of Leicester

2002

Abstract

Applications of Magnetotelluric and transient electromagnetic methods for groundwater and engineering studies

Adel K. Mohamed

The main aim of this study is to use the transient electromagnetic (TEM) and magnetotelluric (MT) methods to determine the electrical resistivity distribution of the subsurface and locate possible structural features controlling groundwater distribution in the northern and south-eastern margins of Parnaiba basin, Brazil. MT data from 24 stations along two profiles across the margins of the basin have been processed using standard tensorial techniques to obtain the interpretable response functions. The TEM data recorded at the same sites facilitated the removal of static shift and the recovery of the near-surface structure. One-dimensional (1-D) joint inversion of TEM and MT data yielded an approximate geoelectric structure for each profile. Subsequent two-dimensional (2-D) modelling revealed a more realistic resistivity distribution for each profile.

The result of 2-D regularized inversion of MT data delineated the main sedimentary sequences and deep basement features. A resistive crystalline basement ($\geq$ 200 $\Omega.m$) is overlain by relatively conductive sedimentary sequences of varying resistivities and thicknesses. The existence of a major basement trough at the expected position of a concealed fault in the north-eastern margin of the basin was proved by the MT model. This anomalous zone is interpreted to have a thick development of granular sediments and may be a good site for groundwater development. The 2-D model for the south-eastern profile defined the position of a major fault, which is interpreted as Picos fault and may have implication for groundwater development. A graben-like structure is also suggested ~10 km further east from Picos fault and considered to be a good target for groundwater development. Overall, the 2-D MT inversion results are consistent with the available geological information and offer new insights into the deep structure of the basin margins of Parnaiba basin.

As a shallow-depth complement to the Parnaiba study, a new azimuthal TEM surveying technique has been evaluated as a possible engineering tool for rapid mapping of a fractured granodioritic rock-mass in Quorn, Leicestershire (UK). The azimuthal TEM field data recorded in this area have been presented in the form of apparent resistivity and voltage responses at selected channels and also inverted using a 1-D inverse modelling scheme. The azimuthal TEM data were found to be successful in locating most of the fractured/faulted zones identified using the conventional 2-D DC resistivity inversion and VLF profiling methods. It is suggested that a more sophisticated azimuthal TEM field surveying technique will be a useful tool for engineering studies.

Acknowledgements

I thank Almighty God for enabling me to undertake this research work. I would like to thank Dr. Maxwell A. Meju for his supervision, guidance, valuable support during the course of this work, and for providing me the opportunity to work with him in various field trips in the UK and Brazil.

I seize this opportunity to thank the Egyptian Government, which has funded my studies at Leicester University. Many thanks to Mansora University, which granted me this scholarship.

I would like to thank Dr. Segio Fontes of the National Observatory, Rio de Jeneiro in Brazil for allowing me to get involved in the joint project with Leicester University, which enabled the acquisition of magnetotelluric and transient electromagnetic data in Brazil. I would like also to thank Dr. Emin Ulugergerli, Emanuele La Terra, and Carlos Germano for their advice and technical support during the field work campaign in Parnaiba basin.

My thanks are also extended to my colleagues R. Brown, L. Gallardo, A. El-Gezeeri, T. Grossey, J. Tomlinson, and all research students in Geology Department; Dr. A. Myers for his help on the SUN system.

My special thanks go to my wife for her patience during my study and my daughter Alaa for making our lives interesting. Despite not being able to see me during the duration of this study, my great Mother and wonderful family in Egypt have been supportive.

Contents

List of Figures

List of tables

1. Introduction and research objectives

1.1 Introduction

Geophysical methods measure the physical properties of the Earth using invasive or non-invasive techniques. Electrical conductivity is one such physical parameter that can be observed to great depths via measurements on or near the surface of the Earth. The electrical conductivity of rocks and minerals has a very wide range of values. This variation is caused by a large number of physical properties such as rock porosity, temperature, lithology, fluid and electrolyte content.

The geoelectrical methods comprise one of the three principal topics in applied geophysics; the other two are seismic and potential field methods. These methods have been successfully used in groundwater exploration (Sharma, 1997). Seismic refraction technique is often used when bedrock is overlain by alluvium because the bedrock surface is usually a strong refractor but the seismic reflection method provides more detailed images of the subsurface and can detect the presence of thin layers (Birkelo et al., 1987). Gravity and magnetic methods are commonly used for locating faulted and other structural boundaries affecting the groundwater distribution, and mapping alluvium-filled valleys (e.g. Sternberg et al., 1990; Street and Engel, 1990). On the other hand, electrical methods described below are the most common techniques for these targets. Geoelectrical methods mainly respond to the presence of highly conductive minerals or water in rocks. They also have a broad range of useful applications, including mineral exploration, engineering and environmental investigations, and archaeological studies. Geo-electrical methods have become well established over several decades for groundwater exploration in sedimentary and crystalline rocks (e.g. Patra, 1967; Palacky et al., 1981; Goldestein et al., 1990; Barker et al., 1992; Wright, 1992; Nobes, 1994, 1996; Barker and Moore, 1998). This is due to the fact that the electrical resistivity varies, not only from formation to formation but even within a particular formation. Generally speaking, hard rocks are bad conductors of electric current, but many geological processes such as dissolution, faulting, weathering, columnar jointing, can alter a rock and significantly lower its resistivity. In contrast to the above processes, precipitation of calcium carbonate or silica reduces porosity and hence increases resistivity (Sharma, 1997). Therefore, there is no general correlation of lithology with resistivity. Nevertheless, approximate resistivity ranges (Palacky, 1987) of the common Earth materials are shown in Figure 1.1. Note that saltwater is highly conductive. Unaltered igneous and metamorphic rocks are resistive. The resistivity of sedimentary formations is highly variable depending on the degree of saturation and the nature of the pore electrolytes. In sedimentary environments and because of the commonly small difference in resistivity contrasts of the formations, it is sometimes difficult to delineate layers carrying water in more detail and so the interpretation is in large scale and not in fine scale as that deduced from well logging data.

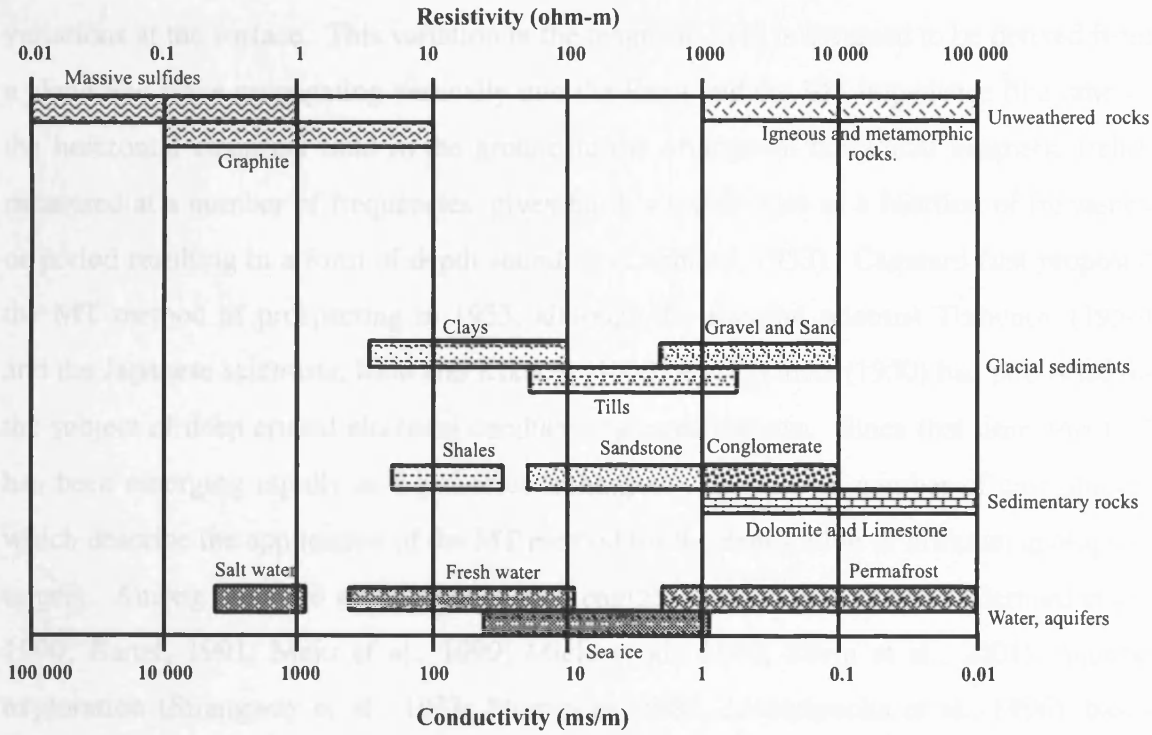

Figure 1.1: The approximate resistivity ranges of Earth materials (after Palacky, 1987)

The geoelectrical methods can be divided into two categories:

a) Electrical techniques: namely DC resistivity, induced polarisation (IP) and self-potential (SP).

b) Inductive or electromagnetic techniques: which consist of frequency domain electromagnetic (FDEM) techniques, such as magnetotelluric (MT), and time domain or transient electromagnetic methods.

In this chapter, a brief historical background of the magnetotelluric, and transient electromagnetic method of exploration are given since these are the methods used in this research study. Also, the research objectives and thesis outline are presented here.

1.2 Magnetotelluric and transient electromagnetic as exploration tools

Magnetotellurics is an electromagnetic method employing simultaneous measurements of natural electric and magnetic fields to infer the electrical conductivity distribution within the Earth beneath the site of the surface fields. This technique depends on the time-varying, naturally occurring Earth's magnetic field which induces eddy currents (called telluric currents) in the conductive crust of the Earth that are detectable as electric field variations at the surface. This variation in the magnetic field is assumed to be derived from a plane EM wave propagating vertically into the Earth and the EM impedance (the ratio of the horizontal electrical field in the ground to the orthogonal horizontal magnetic field), measured at a number of frequencies, gives Earth's resistivities as a function of frequency or period resulting in a form of depth sounding (Cagniard, 1953). Cagniard first proposed the MT method of prospecting in 1953, although the Russian scientist Tikhonov (1950) and the Japanese scientists, Kato and Kikuchi (1950) and Rikitake (1950) had published on the subject of deep crustal electrical conductivity investigations. Since that time, this tool has been emerging rapidly as a powerful technique. There are a number of case studies which describe the application of the MT method for the exploration of different geological targets. Among them are application to civil engineering and groundwater (Bernard et al., 1990; Bartel, 1991; Meju et al., 1999; Miele et al., 2000; Savin et al., 2001), mineral exploration (Strangway et al., 1973; Strangway, 1983; Livelybrooks et al., 1996), basin evaluation for petroleum exploration (Tikhonov and Berdichevsky, 1966; Vozoff, 1972; Stanley et al., 1985; Hastie et al., 1989; Christopherson, 1991; Lu, 1995; Ceron et al., 2001), geothermal exploration (Hermance and Grillot, 1974; Hutton et al., 1984; Devlin, 1984; Galanopoulos, 1989; Wannamaker, 1997; Lagios et al.,1998; Kagiyama et al., 1999; Risk et al., 1999, Matsushima et al., 2001), and for acquiring information about Earth's deep interior, lower crust and mantle (Egbert and Booker, 1992; Bahr et al., 1993). This technique has been successfully applied for imaging subduction–related features like conductive zones associated with the top of conducted plate and the movement of volatiles within the subduction system (e.g. Kurtz et al., 1986,1990; Wannamaker et al., 1989; Fujita et al., 1997; Ingham et al., 2001). It is also applied in offshore conditions and for earthquake prediction (e.g. Morat, 1974; Honkura et al., 1977; Constable et al., 1998). MT method represents an important exploration tool, particularly for reconnaissance surveys and in areas where the seismic reflection method performs poorly, the latter includes buried salt, carbonate, and volcanic horizons that efficiently reflect and scatter acoustic energy

(Constable et al., 1998). Also, because electrical conductivity is a strong function of porosity, it can be used alone or in conjunction with seismic velocities to interpret porosity and permeability (Constable et al. 1998). It has shown its effectiveness for tectonic studies (Arora et al., 1997, 1999). Also, it is emerging as a powerful technique for near-surface environmental groundwater contamination studies (Tezkan et al., 1996; Unsworth et al., 2000; Pedersen et al., 2001). These ranges of applications suggest the suitability of this technique for shallow and deep structural investigations (see Fig. 1.2).

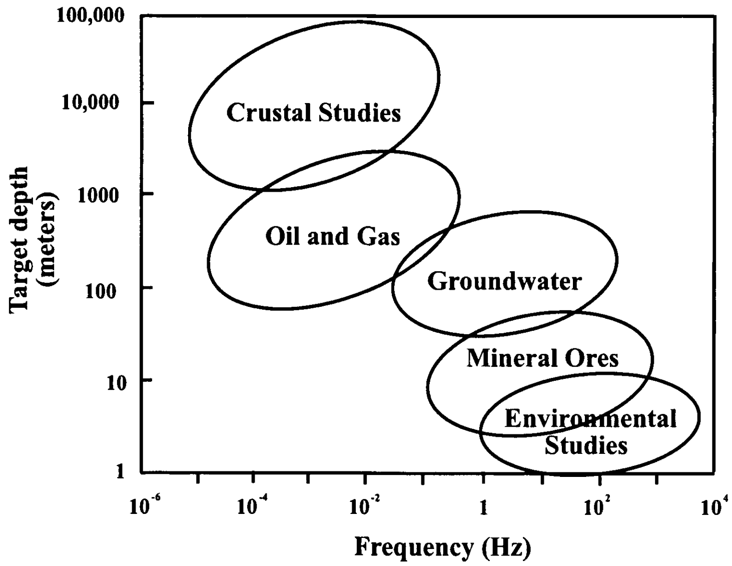

Figure 1.2: Ranges of frequencies that are appropriate in using electromagnetic fields for exploring for various objectives (after Zhadanov and Keller, 1994).

TEM is another EM technique. In this method, a strong direct current (DC) is usually passed through a rectangular loop laid out on the ground. This current is abruptly terminated. The secondary fields due to the induced current are measured in a receiver. The voltage response of secondary field can delineate zones of high conductivity within the ground. The TEM technique has been around for almost 40 years but has been used widely in the last 20 years. The first ground TEM system was developed in 1962 by Newmont Exploration Ltd as a part of a joint Newmont Cyprus Mines developed program (Dolan, 1970). The first airborne INPUT system was introduced at the same period (Barringer, 1962). After that time, the MPPO1 single loop TEM system was developed in the Soviet Union (Velikin and Buggakov, 1967). Since that time and due to advances in electronics, new TEM systems have been developed. In 1972, the PEM (pulse electromagnetic) system was developed by Crone Geophysics and Newmont Exploration as a semiportable horizontal-loop unit (Crone, 1977). The UTEM system was then developed in Canada at the University of Toronto between 1971 and 1979 (West et al., 1984; Lamontaque, 1975). SIROTEM was developed by the Commonwealth Scientific Industrial Research Organization (CSIRO) in Australia between 1972 and 1977 (Buselli and O'Neill, 1977). Geonics Ltd introduced the first version of EM37 in 1980 (McNeill, 1980a). The Colorado School of Mines then developed a megasource TEM system that can provide depths of investigation of up to 10 km (Keller et al., 1984). The use of TEM system for downhole electromagnetic work has become very widespread; several systems were modified to carry out DHEM including the Newmont and Crone systems, SIROTEM and EM37 (Eadie and Staltari, 1987 and Dyck, 1991). The interest now is concentrated in faster and denser coverage of an area with the TEM technique; this has led to the development of the Pulled Array Transient Electromagnetic Method (PA-TEM, Sorensen et al., 1995). Recently, multipurpose systems such as the Zong GDP-32 and the phoenix V-5 system, originally designed for controlled source audiofrequency magnetotelluric surveying, have been reprogrammed for TEM data acquisition.

TEM method is widely used in mining, geothermal, geological, hydrogeological, environmental, and geotechnical investigations. Nevertheless, most case histories on TEM reported in the literature concentrate on its use in mining exploration programmes and groundwater studies especially for mapping saline water intrusion in coastal aquifers (e.g. Stewart and Gay, 1986; Mills et al., 1988; Kruse et al., 1998; Yang et al., 1999; Shtivelman and Goldman, 2000). TEM is a very effective method in detecting subtle changes in resistivity, especially in highly conductive environments. This attribute has enabled it to be applied to some new problems in the fields of engineering and environmental geophysics such as the detection of likely areas of ground subsidence, mapping the extent of groundwater contamination and monitoring the spread of contamination plumes. Goldman et al. (1989, 1994a) have showed its effectiveness for seawater intrusion studies and locating freshwater-seawater interface. This is attributed to the fact that seawater has lower resistivity than freshwater; the resistivity of freshwater ranges between 20-100 ohm-m (Kelly and Mares, 1993). The resistivity of the aquifers saturated with seawater and freshwater therefore differs widely and TEM method can be used to locate their contact; its combination with DC method proved to be the fastest and most comprehensive methods of detecting and mapping freshwater-bearing aquifer and also saltwater-affected aquifers in some regions (e.g. Yang et al, 1999; Meju et al., 2000). However, the differentiation of permeable clay sediments from sandy layers saturated with seawater is difficult due to the equivocal or the similarities in resistivity values. The TEM has been effective for mapping brine pockets in the bedded salt and anhydrite formations at waste repository sites (Buselli et al., 1990) and for delineating the boundary of other waste dumps (Mauldin-Mayerle et al., 1998). The time-domain electromagnetic (TEM/TDEM) method provides a surface geophysical technique suitable for interpreting deep permafrost conditions (e.g. Todd and Dallimore, 1998).

Meju et al. (2001) successfully adapted a joint single loop TEM and horizontal loop electromagnetic (HLEM) profiling methods for detecting fracture zone in granitic terrain. It also was found to be a useful tool for geological mapping in sedimentary basins as an aid to oil exploration (Strack et al., 1989). Lithological mapping using TEM sounding method has been shown to be applicable for coal exploration (Asten, 1987). The ability to resolve layering at a wide range of depths has been used for structural mapping in more complex environments (Keller et al., 1984). Recent advance in instrumentation have produced equipment capable of measuring the response from very shallow depths, less than 10 m in some cases. Despite all this work there remain many unanswered questions, especially about the performance of the TEM sounding method in complex geological environments. The presence of this type of complicated terrain (2D/3D) will distort the eddy currents induced in the Earth and 1-D inversions from such data will not reflect the true Earth structure (e.g. Goldman et al., 1994b). More sophisticated programs to model the mostly 3-D Earth structure would be needed to obtain a true geoelectrical model for the ground. Nevertheless, TEM has shown itself in many circumstances to be more advantageous over DC resistivity and seismic methods in some areas; the equipment is portable, and acquisition is faster giving greater production per day. The ability to derive a geoelectric section for several tens of metres depth from a single, relatively small loop is an obvious improvement over DC soundings where huge electrode separations would be needed for the same depth of penetration. With large separations the chance of distortions to the DC sounding curve brought by lateral resistivity variations become much greater (see Barker, 1981). Another advantage over DC methods is that the source and receiver require no ground connections thereby circumventing the problem of contact resistance (Swift, 1990). In some areas the inductive source allows the method to be used where other geophysical techniques such as seismics are not viable such as over loosely consolidated sediments or swamp. TEM has the best lateral and vertical resolution with regard to highly conductive targets (Kaufman and Keller, 1983) and is less influenced by near surface inhomogeneities which is the main problem for MT interpretation. Therefore, TEM has been used for static shift correction of MT data (e.g. Sternberg et al., 1988; Pellerin and Hohmann, 1990; Meju, 1996; Meju et al., 1999). A combination of the two EM methods (TEM-MT) should therefore yield resistivity, structural and lithological information at shallow and great depths.

1.3 Research objectives

The EM techniques used most widely for geophysical soundings are the magnetotelluric (MT) and time-domain or transient electromagnetic (TEM) methods which together comprise approximately 76 percent of EM surveys (by dollar percent) in the western world (Montgomery, 1987). Magnetotelluric method is used mainly for structural mapping of basins, whereas TEM is used for shallower soundings and stratigraphic applications.

The first part of this research is part of a major collaborative project by the National Observatory in Rio de Janerio (Brazil) and Leicester University (UK) to locate the deep graben-like structures which may be aquiferous or faults that possibly affect groundwater distribution in Panaiba basin in Brazil. Joint TEM and MT methods were used in these studies. The TEM method served to facilitate the removal of static shift effects from the MT data (Sternberg et al., 1988; Meju, 1996) and to recover the near-surface structure. It is also applied to see if there is any seawater intrusion on land in the coastal region because saltwater represents a significant threat to water quality in coastal aquifers. MT method was applied to yield valuable information at greater depths reaching to the base of the sedimentary basin. Resolution of structures within the basement requiring low frequency soundings is outside the scope of this study. A combination of the two EM methods should therefore yield resistivity information at shallow and great depths. This information is necessary for understanding any structures controlling the groundwater distribution. Assessment of the changes in the thickness of the basin sediments, mainly the determination of any significant variations in the bedrock topography can also contribute to the general knowledge of tectonic structure of a sedimentary basin. The thickness of these sediments is also still unknown and requires detailed studies.

The second part of this research deals with the utility of TEM method for shallow investigation (i.e. engineering application). In this study a novel small-loop, short-offset TEM configuration is employed for rapid 3D mapping of a fractured granodiorite rock mass in Quorn Park, Leicestershire (UK). This is comparable to the single loop TEM method that has been applied successfully for detecting fracture zones in deeply weathered granitic terrain (Meju et al., 2001). In this particular study DC resisitivity and VLF methods were also employed for comparison with the TEM results and for mapping the geoelectric sequences.

In summary, the main objectives of this project are the following:

1- Determination of the deep structures of the north-eastern and south-eastern margins of Parnaiba basin, with emphasis on locating deep faults and fracture-zones.

2- Mapping of potential aquifers and locating the best positions for groundwater development.

3- Evaluation of possible seawater intrusion on land on the coastal part of Parnaiba basin.

4- Evaluating a rapid 3-D TEM surveying technique for locating fracture zones at shallow-depth in the Mountsorrel granodiorite of Quorn Park, Leicestershire (UK).

1.4 Thesis outline

This introduction has given an overview of the electromagnetic methods and their application in geophysical exploration. It also has presented the objectives that need to be achieved with this project. The rest of this thesis is as follow;

Chapter two describes the basic theory of magnetotelluric method; it includes the source of EM field variations and the fundamental relationships from basic EM wave theory. It is followed by presenting the Earth's response functions used in MT. The current distortion technique is also briefly discussed. This chapter also gives a short review of MT modelling.

Chapter three reviews the basic theory of TEM method. The most common TEM loop configurations are outlined. The various effects and source of noise on the TEM data are also discussed. The remaining part is concerned with the processing and interpretation of field data.

Chapter four contains a hydrogeological background including aquifer properties, and groundwater geology. This chapter also outlines the concept of predicting hydrogeological parameters from bulk resistivity.

Chapter five comprises the EM field survey in Parnaiba basin, Brazil. It starts with describing the geology of the area of study and a review of previous geophysical studies of the basin. Then, the field methods, the equipment used, and the strategy employed for the acquisition of MT and TEM data are given. It is followed by the processing of data; the impedance tensor decomposition, strike determination, and the correction of the static shift effects from MT apparent resistivity using the TEM data are discussed. A qualitative interpretation of the resulting data in the form of pseudosection is also given.

Chapter six deals with the numerical modelling of MT and TEM data. First invariant resistivity is presented for each profile. Then, 1-D joint inversion of TEM-MT data is discussed. The remainder of this chapter is concerned with the 2-D inverse modelling of MT data for each profile.

Chapter seven deals with the Quorn Park study. Processing and interpretation of TEM, DC, and VLF data are given. 2-D modelling of pre-existing DC resistivity data is given. Comparisons between TEM and the other methods are provided.

Chapter eight summarizes the most important conclusions and results of this study. It is followed by some recommendations for further research work.

2. Basic theory of magnetotelluric method

2.1 Sources of magnetotelluric fields

The magnetotelluric field can be defined as the time-varying portion of the Earth's magnetic field which induces current flow in the Earth. The source of the MT fields is natural electromagnetic energy from sources in the ionosphere and magnetosphere. This energy is utilised to probe the resistivity structure of the Earth's interior from depths of tens of metres to many hundreds of kilometres. The external magnetic fields penetrate the ground to induce electric fields and secondary magnetic fields. Then the components of the electric and magnetic fields are measured on the surface. The study of natural EM fields has shown that the amplitude of the electric field component (E) is strongly dependent on local geology and can vary by a factor of 20 over a distance of about 1 km (Yungul, 1996). On the other hand, the magnetic field component (H) is very much less dependent on local geology and seldom varies by more than a factor of 1.5 within the distance of a few kilometres (Yungul, 1996). A typical average amplitude spectrum of the magnetic variations shows a minimum at about 1 Hz (Fig. 2.1) and allows the source field to be classified into two types of activities, one above and the other below 1 Hz. This frequency (1 Hz) distinguishes two kinds of activities with relative sources above and below 1 Hz.

2.1.1 Sources above 1 Hz

The electrical storms or meteorological activities in the lower atmosphere are the main source of fields of frequencies above 1Hz. It includes fields from lightning associated with thunderstorms. The lightning signals are referred to as "sferics" and attain their peaks in the early afternoon, local time, their frequency ranges being between 5 Hz and 30 MHz (Yungul, 1982). They propagate around the world trapped in the waveguide formed between the ionosphere and the Earth's surface. In the daytime the wave-guide width is 60 km increasing to 90 km during the nighttimes. This wave-guide at large distance from the source is converted into a plane wave of variable frequency. There are three storm centres in the equatorial regions (Brazil, central Africa, and Malaysia). These centres have an average of 100 storm days per year; their geographic distribution is such that during any hour of the day there is probably a storm in progress in one of the centres. This is in addition to small areas within these centres which average more than 200 stormy days per year. These MT fields penetrate the Earth's surface to produce the telluric currents. The amplitude of the induced current has peaks at distinct frequencies (e.g. the Schumann resonance; 8, 14, 20, 26, 32 Hz) since the wave-guide absorbs energy at these frequencies to become enhanced (Jiracek et al., 1995). Man-made power distribution systems are other minor sources of signals which are generally localised and restricted, to 50 or 60 Hz and subsequent harmonics. However, the total energy available from these frequencies is very small.

2.1.2 Sources below 1 Hz

The complex interaction between the solar wind (charged particles emanating from the sun) with the Earth's magnetic field and atmosphere is the main cause of the natural EM field below 1 Hz. When ionised particles moving outward from the sun encounter the Earth's magnetosphere, the ionised particles produce protons and electrons. When the protons and electrons encounter the terrestrial magnetic field, they are deflected in opposite directions and thus current systems are produced with their own secondary magnetic field to oppose the Earth's field which appears to change at a level of a few gammas at a boundary called the "magnetopause" which is the outer boundary of the Earth's magnetosphere. This complex interaction results in what is called micropulsations which are the main source of fields in the range of frequency of 0.00167 to 5 Hz (Yungul, 1996). Their amplitudes depend on solar activity, latitude, frequency, season, local and universal times, and local geology. Depending on their continuity and periods, the micropulsations are classified as continuous pulsation (regular) and irregular pulsation (Parkinson, 1983). Continuous pulsations occur mostly during the daytime forming wave trains that last for tens of minutes. Their amplitudes tend to peak in the early afternoon (local mean time) and diminish during the night. Irregular pulsations occur mostly during night time with wave trains that are of limited duration and a period range of about 40 to 120 seconds (frequency range 0.025 to 0.00833 Hz). In areas where industrial electromagnetic noise is too high for any meaningful exploration during day time, irregular pulsations are very useful.

2.2 Basic EM theory

Electromagnetic theory was first comprehended by Maxwell who recognized that Ohm's law, Faraday's law, and Amperes's law were all part of a great whole, that now being called Maxwell's equations. These equations are the quintessence of the development of electromagnetic theory. Further development was only a matter of performing the appropriate mathematical manipulations. Maxwell's field equations for

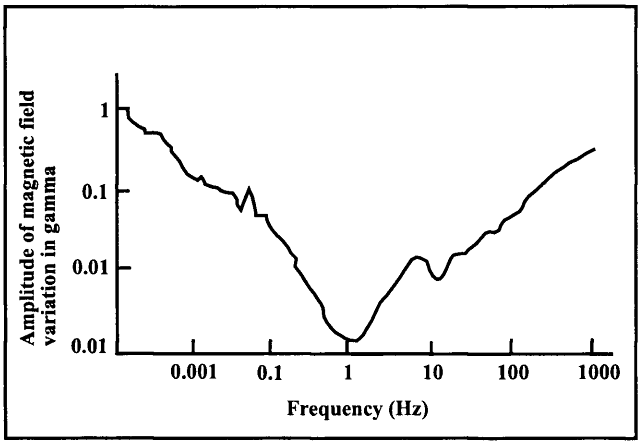

Figure 2.1: Typical spectrum of amplitudes of electromagnetic noise in the extremely low frequency (ELF) range (after Keller and Frichknect, 1966).

an isotropic medium are;

$$\nabla \times E = -\partial B / \partial t \tag{2.1}$$

$$\nabla \times H = J + \partial D / \partial t \tag{2.2}$$

$$\nabla . B = 0 \tag{2.3}$$

$$\nabla . D = \rho^*, \tag{2.4}$$

where E is the electric field intensity (V/m), H is the magnetic field intensity (A/m), B is the magnetic induction (W/m^2), D is the displacement current (C/m^2), J is the current density (A/m^2), and ρ^* is the volume charge density in coulombs.

To relate Maxwell's equations to properties of the subsurface, the constitutive equations (Keller, 1988) must be used

$$D = \varepsilon E \tag{2.5}$$

$$B = \mu H \tag{2.6}$$

$$J = \sigma E, \tag{2.7}$$

where ε (F/m) is the dielectric constant or electrical permittivity, μ is the magnetic permeability($\mu_0 = 4\pi \times 10^{-7} H/m$ in free space), $\sigma(S/m)$ is the electrical conductivity. In most materials, μ and ε do not differ appreciably from the values of μ_0 and ε_0 in free space. A combination of Maxwell's and constitutive equations form a single characteristic of the medium referred to as the wave number which then determines the behaviour of the EM field.

One way of solving the induction equations is to consider models comprising distinct regions in each of which the conductivity is uniform. At the interface between the regions, the following boundary conditions apply: tangential *E*, tangential *H* and normal *B* must be continuous.

Reformulation of Maxwell equations (2.1 and 2.2) in terms of the magnetic and electrical field strengths, gives the following;

$$\nabla \times H = \sigma E + \frac{\partial}{\partial t}(\varepsilon E) \tag{2.8}$$

$$\nabla \times E = -\frac{\partial}{\partial t}(\mu H). \tag{2.9}$$

Taking the curl of both sides of the above equations, taking into consideration equations (2.3 and 2.4), and using the vector identity,

$$\nabla \times \nabla \times F = \nabla(\nabla . F) - \nabla^2 F, \tag{2.10}$$

where *F* is either the *E* or *H* field, for a region where ε, μ and σ are constant, we can get the wave equations for time domain in the form

$$\nabla^2 E = \mu\varepsilon \frac{\partial^2 E}{\partial t^2} + \mu\sigma \frac{\partial E}{\partial t} \tag{2.11}$$

$$\nabla^2 H = \mu\varepsilon \frac{\partial^2 H}{\partial t^2} + \mu\sigma \frac{\partial H}{\partial t}, \tag{2.12}$$

provided also that the volume charge distribution is zero. This is so for all practical purposes although care must be taken at the interface where surface charges may accumulate.

Assuming time dependence of the form e^{iwt} then replacing $\frac{\partial}{\partial t}$ with iw ($w = 2\pi f$) equations 2.8 and 2.9 can be written as

$$\nabla \times H = (\sigma + iw\varepsilon)E \tag{2.13}$$

$$\nabla \times E = -i\mu wH. \tag{2.14}$$

Applying the same steps as above, gives the wave equations in frequency domain

$$\nabla^2 H - (\mu\varepsilon w^2 + i\mu\sigma w)H = 0 \tag{2.15}$$

$$\nabla^2 E - (\mu\varepsilon w^2 + i\mu\sigma w)E = 0. \tag{2.16}$$

2.2.1 Magnetotelluric diffusion equations

Equations 2.15 and 2.16 can be rewritten as

$$\nabla^2 H - K^2 H = 0 \tag{2.17}$$

$$\nabla^2 E - K^2 E = 0, \tag{2.18}$$

where $K^2 = (\mu\varepsilon w^2 + i\mu\sigma w)$. K is the wave propagation constant referred to as the radian wave length or wave number.

At low frequencies used by the magnetotelluric method (less than $10^5\,Hz$), $\mu\varepsilon w^2 \ll \mu\sigma w$ for real earth materials; displacement currents are much smaller than conduction currents and the second term in K^2 is dominant. Under this condition the dependence of K on ε disappears and the behaviour of the EM field is described as diffusion and the equations can be written as

$$\nabla^2 H - i\mu\sigma w H = 0 \tag{2.19}$$

$$\nabla^2 E - i\mu\sigma w E = 0. \tag{2.20}$$

In this case, the propagation constant is given by $K = (iw\mu\sigma)^{1/2}$.

This complex number can be written in terms of its real and imaginary components as

$$K = (\frac{\mu\sigma w}{2})^{1/2} + i(\frac{\mu\sigma w}{2})^{1/2}. \tag{2.21}$$

2.3 Induction in a homogeneous structure

In a homogeneous medium and for an externally uniform and harmonically time varying field, equations 2.19 and 2.20 in Cartesian coordinates are simplified to

$$\frac{\partial^2 Hy}{\partial z^2} - i\mu\sigma w H_y = 0 \tag{2.22}$$

$$\frac{\partial^2 E_x}{\partial z^2} - i\mu\sigma w E_x = 0, \tag{2.23}$$

where the direction of propagation of the plane wave coincides with z (positive vertically down) and the electrical field with x direction.

The general solution for equation (2.23) is

$$E_x = A_0 e^{Kz} + B_0 e^{-Kz}. \tag{2.24}$$

Substituting E_x in equation (2.14), H_y can be obtained as

$$H_y = -\frac{K}{iw\mu}\left[A_0 e^{Kz} - B_0 e^{-Kz}\right]. \tag{2.25}$$

Particular boundary conditions:

a) At $z \to \infty$; in a homogeneous medium and according to the boundary condition, the electric field should be zero at the infinity; then A_0 in equation 2.24 should be zero and this gives equations 2.24 and 2.25 to be in the final form;

$$E_x = B_0 e^{-Kz} \tag{2.26}$$

$$H_y = \frac{K}{iw\mu} B_0 e^{-Kz}. \tag{2.27}$$

b) At $z = 0$; equations 2.26 and 2.27 are;

$$E_x(z=0) = E_{x0} = B_0, \tag{2.28}$$

$$H_y(z=0) = H_{y0} = \frac{K}{iw\mu} B_0. \tag{2.29}$$

Then it is possible to define a ratio between the electrical and magnetic fields, called the EM impedances

$$Z = \frac{Ex}{Hy} = \frac{iw\mu}{K}. \tag{2.30}$$

This expression was originally proposed by Cagniard (1953); the above equation is used to compute the resistivity in a homogeneous medium (Vozoff, 1991);

$$\rho = \frac{1}{w\mu}\left|\frac{Ex}{Hy}\right|^2. \tag{2.31}$$

Equation 2.31 can be applied to an inhomogeneous medium but in this case ρ is called the apparent resistivity.

The depth z at which the amplitude of an EM field has been attenuated by *1/e* or 0.37 of its value at the surface of the medium is called skin depth and is given by

$$\delta = \frac{1}{real(K)} = \sqrt{\frac{2}{w\mu\sigma}}. \tag{2.32}$$

In MKS units, $\delta \cong 503(\rho T)^{1/2}$ metres (2.33)

The effect of conductivity on penetration depth (Fig. 2.2) can be explained physically as follows (Zhdanov and Keller, 1994): as an electromagnetic field penetrates a conductor, its energy is expended on the vibration of free electrical charge carriers present in the conductor. The vibration excited by the electromagnetic field represents conversion of the energy of electromagnetic field to heat. As a result, the field in a conductor loses energy rapidly as it travels, and is attenuated. When an electromagnetic field travels into an extensive conductor, its energy is almost entirely lost in a zone near the entry surface; this zone is like a skin protecting the interior of the conductor from penetration by electromagnetic field, and hence the name skin effect. In an insulator, there are no free charge carriers to vibrate and extract energy from the electromagnetic field, and so, the field can propagate to greater distance.

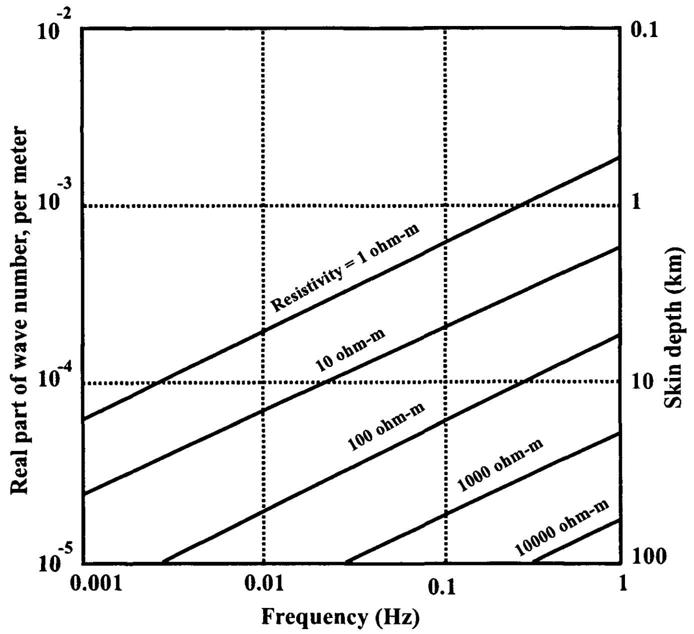

Figure 2.2: Wave number as a function of frequency and resistivity. A scale for converting wave numbers to radian wave lengths or skin depths is shown on the right hand side (Keller and Frischknecht, 1966).

2.3.1 Induction in an N-layered structure

In an n layered earth, the conductivity is a function of depth only where the subsurface consists of n-1 horizontal homogeneous and isotropic layers underlain by a half space (the nth layer) of resistivity ρ_n (Fig. 2.3). Although in reality the earth is never one-dimensional, the representation of the earth by n horizontal layers is an important approximation in MT, and with appropriate care can be used as a reasonable approximation to depth under a measurement site in many cases. In a layered earth, continuity conditions which must hold at each boundary permit us to express the wave impedance observed at the surface in terms of the wave impedances in each of the lower layers. Both the electric field and the magnetic field must be continuous across the boundaries between layers. The wave impedance at the bottom of the first layer must equal the wave impedance at the top of the second layer, and so on. If we consider a model in which the earth is represented by n horizontal layers where the conductivities of the layers are $\sigma_1, \sigma_2, ..., \sigma_n$ respectively and the thickness of the top n-1 layers are $h_1, h_2, ..., h_{n-1}$ the MT impedance at the surface, can be evaluated by first computing the impedance for each individual layer and imposing continuity conditions for

Ex and Hy across boundaries. The following relation can be obtained for the impedance at the surface (Ward et al., 1973; Kaufman and Keller, 1981)

$$Z_0(w) = \frac{i\mu w}{K_1} \coth\left[K_1 h_1 + \coth^{-1}\left[\frac{K_1}{K_2}\right] \coth\left[K_2 h_2 + \coth^{-1}\left[\ldots\ldots \coth^{-1}\left[\frac{K_{n-2}}{K_{n-1}} \coth\left[K_{n-1} h_{n-1} + \coth^{-1}\left[\frac{K_{n-1}}{K_n}\right]\right]\right]\right]\right]\right] \quad (2.34)$$

where K_i is the propagating constant for the i-th layer. Equation 2.34 is used in the 1-D MT forward problem to calculate the apparent resistivity and phase of a layered earth structure at any given frequency.

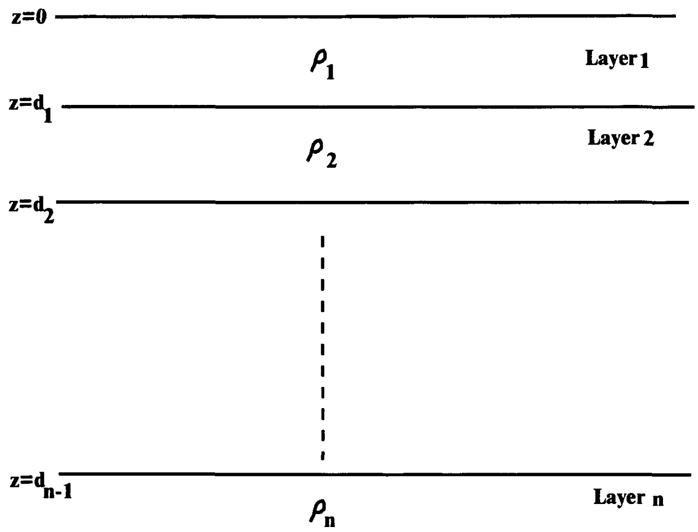

Figure 2.3: One-dimensional model

2.4 Induction in 2-Dimensional Earth

In a two-dimensional case, conductivity $[\sigma = \sigma(y, z)]$ varies along one horizontal coordinate direction and with depth (Fig. 2.4). The other horizontal direction is called the strike. In two-dimensional structures, z and hence ρ_a vary with measurement direction i.e. $\left|\frac{Ex}{Hy}\right| \neq \left|\frac{Ey}{Hx}\right|$.

Cantwell (1960) and Swift (1967) extended the method for laterally inhomogeneous structures by expressing the relationship between field components through a pair of linear equations

$$Ex = ZxxHx + ZxyHy \quad (2.35)$$

$$Ey = ZyyHy + ZyxHx. \quad (2.36)$$

These two equations can be written in the form

$$E = Z.H, \quad (2.37)$$

where the tensor impedance Z has been written in the matrix form

$$Z = \begin{bmatrix} Zxx & Zxy \\ Zyx & Zyy \end{bmatrix} \tag{2.38}$$

Zxy and Zyx are the principal impedances, while Zxx and Zyy are the subsidiary impedances which are produced due to contribution from parallel components of the magnetic fields.

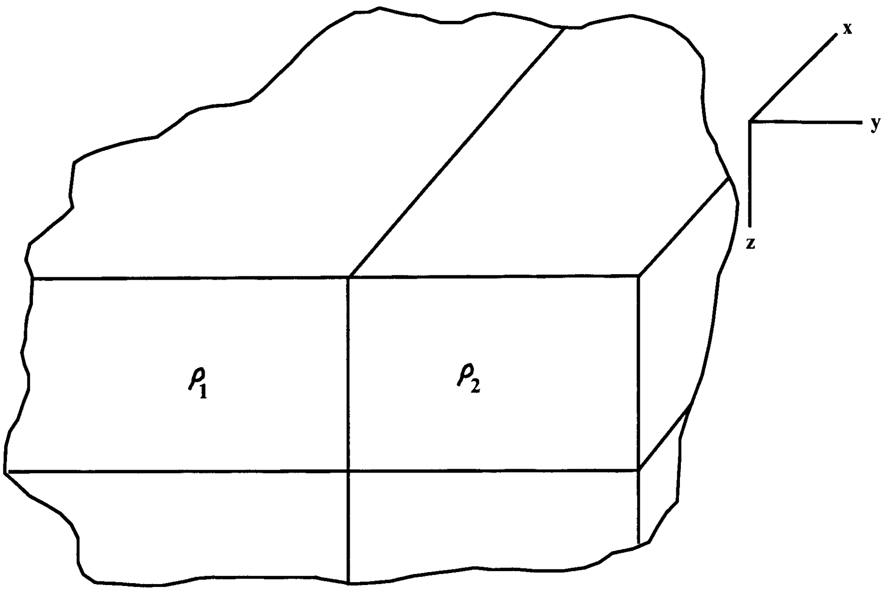

Figure 2.4: A simple 2-Dimensional model

In a uniform or 1-D horizontally layered earth,

$$Zxx = Zyy = 0 \text{ and } Zyx = -Zxy \tag{2.39}$$

In a 2-D case, if x or y is along strike, then

$$Zxx = Zyy = 0 \quad \text{but} \quad Zxy \neq -Zyx \tag{2.40}$$

In the field, the measurement axes may not be aligned with the strike such that equation (2.40) is not valid (i.e. $Zxx, Zyy \neq 0$ and $Zxy \neq -Zyx$).

The elements of Z vary as the coordinate axes are rotated (Swift, 1967). When the structure is truly 2-D, the EM fields decouple into two distinct polarizations. The first of these is called the TE mode or E polarization (transverse electric). This mode describes the field components (E*x*, H*y*, H*z*). In this case the currents are flowing parallel to the structure. The other mode is called TM mode or B polarization and belongs the field components (*Ey*, *Hx*, Ez); the currents are perpendicular to the structure. In such case Maxwell's equations will be modified as given below

$$\frac{\partial H_z}{\partial y} - \frac{\partial H_y}{\partial z} = \sigma E_x, \; \frac{\partial E_x}{\partial z} = iw\mu H_y, \; \frac{\partial E_x}{\partial y} = -iw\mu H_z \tag{2.41}$$

$$\frac{\partial E_z}{\partial y} - \frac{\partial E_y}{\partial z} = iw\mu H_x, \; \frac{\partial H_x}{\partial z} = \sigma E_y, \; \frac{\partial E_x}{\partial y} = -\sigma E_z. \tag{2.42}$$

2.5 Induction in 3-Dimensional structure

If conductivity varies in all the three directions (x, y, z), we are dealing with the general case of 3-dimensional models. In reality, the conductivity distribution in MT problems is 3-D since the conductivity is mostly a function of all three coordinate axes such that $\sigma = \sigma(x, y, z)$. In this condition, the four elements of the impedance tensor (equation 2.38) should be accounted for. This leads to getting four apparent resistivity and four phase curves. Finding a model to fit all these data for each frequency at every station in order to interpret the subsurface is an extremely complicated problem (Yungul, 1996). In addition, the analytical solutions to Maxwell's equations are difficult. Therefore, a better understanding of three-dimensionality can be performed by a numerical three-dimensional modelling technique.

2.6 Earth response functions

The objective of the MT method is to extract valuable information about the conductivity structure of the subsurface. Any function that can provide valuable information about the earth is an earth response function (Rokityanski, 1982). The parameters such as the impedance tensor, the apparent resistivity or the phase of the impedance are considered the principal functions for characterising the conductivity structure. The conductivity strike, and the other dimensionality indicators are auxiliary functional parameters for describing the pattern and nature of the conductivity structures of the earth.

2.6.1 The impedance tensor

All the parameters obtained from the MT field data are mainly based on determination of the impedance tensor. The impedance is contained in the relationships among the field components at a single site. It is the quantity from which the conductivity structure is interpreted. In general, *Hx* has an associated *Ey* and some *Ex* (Vozoff, 1991). Likewise, *Hy* causes an *Ex* and *Ey,* so that at each frequency we would expect a linear system to behave as shown in equations 2.35 and 2.36.

In an ideal 1-D environment, Cagniard (1953) has defined the apparent resistivity and phase by

$$\rho_{axy} = 0.2T|Zxy|^2 , \quad \rho_{ayx} = 0.2T|Zyx|^2 \tag{2.43}$$

$$\varphi_{xy} = \arg\left|\frac{Ex}{Hy}\right| = \arctan\left(\frac{\mathrm{Im}(Zxy)}{R(Zxy)}\right), \ \varphi_{yx} = \arg\left|\frac{Ey}{Hx}\right| = \arctan\left(\frac{\mathrm{Im}(Zyx)}{R(Zyx)}\right), \tag{2.44}$$

where E is measured in *mv/km*, H in gamma or nanotesla, apparent resistivity is in ohm-m(Ωm), and $(T=1/f)$ *is* the period in seconds, φ is the phase differences between the E and H fields, and Z is the magnetotelluric impedance. Satisfying the condition of 1-D ($Zxy=Zyx$), the apparent resistivities and phases for both directions at each frequency should be equal. A similar relationship between Hz and the horizontal magnetic field components at any frequency can be written

$$Hz = TxHx + TyHy, \tag{2.45}$$

where Tx and Ty are known as the Tipper elements (Vozoff, 1972). The tipper values are complex since they may include phase shifts. T values are zero in one-dimensional cases, but nonzero in two-dimensional cases.

2.6.2 Rotation of the impedance tensor

Suppose our measurement axes (x, y) form an angle θ with the true strike and the field components in the principal anisotropy axes are x^-, y^- as shown in Figure 2.5.

The transformed field components are

$$E^- = R.E \quad \text{and} \quad H^- = R.H \tag{2.46}$$

$$R = \begin{bmatrix} \cos\theta & \sin\theta \\ -\sin\theta & \cos\theta \end{bmatrix} \tag{2.47}$$

and $$E^- = Z^-.H^-. \tag{2.48}$$

Due to the rotation of the tensor elements from (x,y) to (x^-,y^-) by an angle about θ, the rotated impedance tensor becomes

$$Z^-(\theta) = R(\theta)ZR^T(\theta). \tag{2.49}$$

So that the impedance tensor relationship in the rotated frame is

$$E^- = R(\theta)ZR^T(\theta)H^- \tag{2.50}$$

In the general case and from equation 2.49 the elements of Z^- in terms of the elements of Z, is given by (Vozoff, 1972)

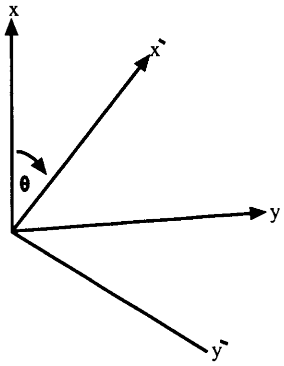

Figure 2.5: Axis rotation.

$$Z^{-}xx(\theta) = (Zxx + Zyy)/2 - Z_0\left(\theta + \frac{\pi}{4}\right) \quad (2.51)$$

$$Z^{-}yy(\theta) = (Zyy + Zxx)/2 + Z_0\left(\theta + \frac{\pi}{4}\right) \quad (2.52)$$

$$Z^{-}xy(\theta) = (Zxy - Zyx)/2 + Z_0(\theta) \quad (2.53)$$

$$Z^{-}yx(\theta) = (Zyx - Zxy)/2 + Z_0(\theta), \quad (2.54)$$

where $$Z_0 = \frac{(Zxy + Zyx)}{2}\cos 2\theta - \frac{(Zxx - Zyy)}{2}\sin 2\theta. \quad (2.55)$$

As the diagonal elements of the rotated impedance tensor rarely reach zero, several different ways have been used to find the rotation angle θ between the measured direction and strike. One of them is to rotate the Z_{ij} in steps, plot them on a polar diagram, and pick an optimum angle from the plots (Vozoff, 1991). During a rotation through pi radians, elements of Z trace out ellipses in the complex planes; the ellipses for all elements have the same shape and size. From these rotation ellipses, the principal axes can be determined. Alternatively it is possible to use one of Swift's (1967) solutions, in which the expressions for Zxy(θ) and Zyx(θ) are differentiated with respect to θ to give an angle θ_0 which maximises:

$$\left|Z^{-}xy(\theta_0)\right|^2 + \left|Z^{-}yx(\theta_0)\right|^2, \quad (2.56)$$

where

$$\tan 4\theta_0 = \left(\frac{(Zxx - Zyy)\cdot(Zxy + Zyx)^* + (Zxx + Zyy)^*(Zxy + Zyx)}{|Zxx - Zyy|^2 - |Zxy + Zyx|^2}\right) \quad (2.57)$$

where * denotes complex conjugate.

This solution also minimises:

$$|Zxx|^2 + |Zyy|^2. \quad (2.58)$$

In an ideal 2-D structure, Zxx and Zyy should be zero at this angle θ_0, but in practice they seldom reduce to zero and the angle θ_0 is estimated with $\pm 90^0$ ambiguity and can be resolved if additional geologic information is taken into account.

On rotation through 180 degrees, two minima for the diagonal elements are obtained and the corresponding axes are termed the principal conductivity axes. The apparent resistivities and phase in these directions are called the major and minor apparent resistivities and phases. These are expressed as

$$\rho_{maj} = 0.2T\left|Z^{-}xy\right|^2 \ \ \& \ \ \varphi_{maj} = \arg\left(Z^{-}xy\right) \tag{2.59}$$

$$\rho_{\min} = 0.2T\left|Z^{-}yx\right|^2 \ \ \& \ \ \varphi_{\min} = \arg\left(Z^{-}yx\right). \tag{2.60}$$

It is now relatively common to define an effective response function for a medium which is rotationally invariant (Tikhonov and Berdichevsky, 1966; Ranganayaki, 1984). The effective impedance which is the square root of the determinant of the impedance tensor is given by

$$Z_{eff} = \left(ZxxZyy - ZxyZyx\right)^{1/2}. \tag{2.61}$$

It has the physical sense of mean impedance for the medium. The corresponding apparent resistivity and phase are given by

$$\rho_{eff} = \frac{1}{\mu w}\left|ZxxZyy - ZxyZyx\right| \tag{2.62}$$

$$\varphi_{eff} = \arg\left(ZxxZyy - ZxyZyx\right). \tag{2.63}$$

In a strictly 2-D environment, $\rho_{eff} = \left(\rho_{xy}\rho_{yx}\right)^{1/2}$ and $\varphi_{eff} = \varphi_{xy} + \varphi_{yx}$. These two quantities $(\rho_{eff}, \varphi_{eff})$ are the geometric mean of parallel and perpendicular resistivities and phases (Ranganayaki, 1984).

2.6.3 Impedance skew

Skew is an indicator of anisotropy and is given by Swift (1967) as:

$$S = \left|\frac{Zxx + Zyy}{Zxy - Zyx}\right|. \tag{2.64}$$

For ideal 1-D and 2-D conductivity distributions, skew reduces to zero. However, for real data this is seldom the case and it will approximate to zero for a 1-D or 2-D earth measured in strike direction. For the general 3-D structure skew is non-zero. Reddy et al. (1973), Ting and Hohman (1981), and Park et al. (1983), suggested limits of 0.4, 0.12 and 0.5, respectively for the onset of 3-D behaviour. Generally, an upper limit of 0.4 is accepted for a 2-D interpretation to be valid.

2.6.4 Coherency

The coherency is a frequently used MT data quality measure calculated for two components (Swift, 1967). When the auto power and cross-power spectra are determined, then it is possible to estimate the correlation between two time series by using their coherence function. Suppose A and B are the two components of the Fourier transformed EM fields. Then

$$\text{Coherency}(A,B)=\frac{\left[A^{*}B\right]}{\left(\left[A^{*}A\right]\left[B^{*}B\right]\right)^{1/2}}\ , \tag{2.65}$$

where $\left[A^{*}B\right]$ is the cross power averaged over a range of frequencies and $\left[A^{*}A\right]$ $\left[B^{*}B\right]$ are the auto power averaged over the same range of frequencies.

Coherency lies between 0 and 1. When the two time series are well correlated, then coherency equals unity. This means that the two signals are perfectly linearly related. For uncorrelated time series coherency is equal to zero.

2.7 Distortion of MT impedance tensors

In magnetotellurics, the response of regional structures can be masked by the distortion produced by local, near-surface inhomogeneities (Berdichevsky & Dimitriev 1976; Jones 1988; Jiracek, 1990; Bahr 1991). These effects cause three different types of distortion (Groom and Bahr, 1992): (1) The well-known static shifts of the sounding curves; (2) when the underlying regional setting is two-dimensional then the two regional impedances are mixed in an arbitrary coordinate system; and (3) at sufficiently high frequencies these effects generate anomalous magnetic fields which alter the background phases. To explain the reason of this near surface inhomogenity effect, when a plane EM wave interacts with a laterally inhomogeneous 3-D earth it induces anomalous excess currents and charge concentrations (Berdichevsky and Dmitriev, 1976; Jones, 1983a; Berdichevsky et al., 1989). These produce respectively, inductive and galvanic distortion of the electrical field measurements and consequently the impedance estimates. The inductive effect follows Faraday's law, whereby the time derivative of the primary magnetic field induces excessive currents. These currents following in closed loops produce secondary magnetic fields which add vectorially to the primary magnetic fields (Jiracek, 1990). On the other side, the galvanic effect is caused by electric charges produced by primary electric field and are built up on the boundaries of inhomogeneities. These charges result in secondary electric fields which add vectorially to the primary electric field. The magnetic field for small size inhomogeneties remains almost unaffected by the build up of boundary charges (Wannamaker et al., 1984a); however, the galvanic magnetic field distortion could be significant in situations of large galvanic distortion (Groom and Bailey, 1989). This electric distortion can also affect the sounding curves to cause what is called static shift. Since static shift correction and distortion tensor techniques applied in this study, brief outline is presented below.

2.7.1 Static shift correction

For a layered earth, if two measured apparent resistivity sounding curves XY (electric field parallel to the north) and YX (electric field parallel to the east) have the same shape but exhibit a vertical, parallel displacement but with impedance phase being unaffected, they are probably affected by a surficial body. Hence static shift must be removed before accurate interpretation of deep structures can be made. If YX and XY apparent resistivity sounding are not parallel and the phase are not identical, this indicates an inductive response from 2-D or 3-D structures (Wannamaker et al., 1984b).

Several methods have attempted to remove static shift. Jones (1988) suggested a solution based on shifting the curve into agreement with the model resistivity values of a known layer. Sternberg et al., (1988) have shown the effectiveness of using borehole logged TEM data. Beamish and Travassos (1992) have considered the use of well logging data. It seems that one of the most common techniques to deal with this problem is TEM or transient electromagnetic method which depends upon measuring secondary magnetic field and hence is less affected by near surface inhomogenities (Sharma, 1997). Case histories (Andrieux and Wightman, 1984; Sternberg et al., 1988; Pellerin and Hohmann, 1990; Meju and Fontes, 1993; Meju, 1996; Meju et al., 1999) have shown TEM sounding to be quite effective in this respect. Central-loop TEM sounding is commonly used to correct MT static shift because it is less sensitive to lateral resistivity variations than other TEM configurations (Spies, 1980) and the strength of the induced signal is highest at the centre of the Tx loop. Meju et al. (1999) suggested the use of both central and single loop TEM data for static shift correction for TE and TM modes respectively.

2.7.2 Distortion tensor technique

In one or two-dimensional modelling, the interpretation of the experimental MT result is easy. However, experimentally determined magnetotelluric impedance tensor rarely conforms to the ideal 2-D impedance tensor (Groom and Bailey, 1989). That is, there is no rotation of the coordinate axes such that these diagonal elements of the tensors are both exactly zero. The reason for that may be because of 1) data error in the case of 1-D or 2-D induction, 2) 3-D induction, or 3) the effect of galvanic distortion coupled with 1-D or 2-D induction. Improvements in data quality in recent years make the examination of the third possibility feasible. Two tensors decomposition methods that are more general than that of Swift (1967) have been developed. They are eigen analysis and explicit tensor decomposition methods. The second method is described by Bahr (1988) and Groom and Bailey (1989,1991) and is based on physical models. This second method is used in this study which is called physically-based decomposition and is briefly presented here.

2.7.2.1 Physically based decomposition

The purpose of this approach is to yield more obviously physical parameters like regional strike and regional impedances. This technique was first described by Larsen (1977), and generalised by Bahr (1988) and Groom and Bailey (1989,1991) and Groom and Bahr (1992). Bahr (1988) has indicated that galvanic current distortion does not destroy most of the information present about an underlying 2-D inductive process. Groom and Bailey (1989) make specific assumption that the measured impedance tensor is produced by local galvanic distortion, by arbitrary 3-D structures, of the electric currents induced on a large scale in a regionally 1-D or 2-D structure. So the purpose of Groom and Bailey (1989) decomposition is to separate local and regional parameters as much as possible under the assumption that the regional structure is at most 2-D and the local structure causes only galvanic scattering of the electric field, and to do so in the form of a product factorisation. This technique is restricted to certain structure, which is the serious defect. According to Bahr (1991), the conductivity structure might be less or more complex than assumed in the general model and therefore irrelevant model parameters are derived to give erroneous results.

Based on Groom-Bailey (1989), the measured electric field must be related to the regional field by distortion tensor C which in the absence of galvanic distortion reduces to the identity tensor, i.e. $$e = ce_r = \begin{bmatrix} c_1 & c_2 \\ c_3 & c_4 \end{bmatrix} e_r . \quad (2.66)$$

If Z_m is the measured impedance tensor and Z_2 is the regional impedance, then Z_m can be decomposed as

$$Z_m = RCZ_2R^T , \quad (2.67)$$

where R is the rotation matrix which rotates vectors through an angle θ to the measurement axis system.

Groom and Bailey (1989) suggested that a useful factorisation of C is as the product

$$C = gTSA , \quad (2.68)$$

where g is a scalar "site gain" necessary for normalization, and the respective tensors $T, S,$ and A are responsible for" Twist", "Shear", and "Anisotropy" effects and are defined by

$$T = N_1 \begin{bmatrix} 1 & -t \\ t & 1 \end{bmatrix} \quad (2.69)$$

$$S = N_2 \begin{bmatrix} 1 & e \\ e & 1 \end{bmatrix} \quad (2.70)$$

$$A = N_3 \begin{bmatrix} 1+s & 0 \\ 0 & 1-s \end{bmatrix} , \quad (2.71)$$

where $N_1 = 1/\sqrt{1+t^2}$, $N_2 = 1/\sqrt{1+e^2}$ and $N_3 = 1/\sqrt{1+s^2}$. The factors N_i are normalisation vectors, whereas *t, e and s* are real numbers. Figure 2.6 shows the effect of tensors *A*, *S*, and *T* on a family of unit vectors. As shown in this figure, the effect of the "Twist" tensor is to rotate the electric field vector through a clockwise angle defined as twist angle $\phi_t = \tan^{-1} t$. The "shear" tensor develops anisotropy along axes dissecting the principal directions of the regional impedance. The shear angle e is defined as an angle given by $\phi_e = \tan^{-1} e$ through which the X-axis is deflected clockwise and the Y-axis anticlockwise by the same angle. The anisotropy tensor multiplied by the regional impedance tensor, simply adds to the anisotropy already existing in the regional impedance tensor Z_2 . Neither g nor A can be determined separately from $\bar{Z}_2$, so the term gAZ_2 is lumped together to be $\bar{Z}_2$. Therefore, equation 2.67 will be modified to

$$Z_m = RTS\bar{Z}R^T . \quad (2.72)$$

If the product decomposition in equation 2.72 is multiplied out, it yields after some algebra a non-linear system of equations:

$$Z_{xx} + Z_{yy} = t\sigma + e\delta \tag{2.73}$$

$$Z_{xy} + Z_{yx} = (\delta - et\sigma)\cos 2\theta - (t\delta + e\sigma)\sin 2\theta \tag{2.74}$$

$$Z_{yx} + Z_{xy} = -\sigma + et\delta \tag{2.75}$$

$$Z_{xx} - Z_{yy} = -(t\delta + e\sigma)\cos 2\theta - (\delta - et\sigma)\sin 2\theta\,, \tag{2.76}$$

where $\sigma = a + b$ and $\delta = a - b$ for the sum and difference of the principal impedances a and b.

Equation (2.72) has seven real parameters, which are the following:

-Two that represent the real and imaginary parts of the major principal impedance

-Two that represent the real and imaginary parts of the minor principal impedances

-Three angles (azimuth, shear angle, and twist angle).

In practice, experimental data with noise deviations from the physical model will never exactly fit the proposed decomposition. In this case, a solution of least squares or other fitting procedure to the data can be calculated, giving a misfit ε that can be used as the eight parameter, and can detect the deviation from the ideal distortion model (Groom and Bailey, 1989).

2.7.3 Bahr classes

To evaluate the necessity of Groom-Bailey decomposition and to evaluate the measured impedance tensors, Bahr (1991) described seven classes to categorize the data and which depend mainly upon twist and shear, Bahr phase sensitive skew, and Swift (1967) skew.

Using the notations of Bahr (1991), the required parameters are defined as follow:

$$S_1 = Z_{xx} + Z_{yy} \qquad S_2 = Z_{xy} + Z_{yx} \tag{2.77}$$

$$D_1 = Z_{xx} - Z_{yy} \qquad D_2 = Z_{xy} - Z_{yx}\,. \tag{2.78}$$

From the above definitions, the parameters can be defined as follow:

$$K = |S_1| / |D_2|\,, \tag{2.79}$$

where K is Swift skew

$$\Sigma = \frac{\left(D_1^2 + S_2^2\right)}{D_2^2}\,, \tag{2.80}$$

where Σ is a rotationally invariant measure of two-dimensionality

$$\mu = \left(|[D_1, S_2]| + |[S_1, D_2]|\right)^{1/2} / |D_2|\,, \tag{2.81}$$

where μ is a rotationally invariant measure of the phase differences in the impedance tensor.

$$\eta = \left(\left| [D_1, S_2] - [S_1, D_2] \right| \right)^{1/2} / |D_2|, \tag{2.82}$$

where η is a rotationally invariant dimensionality parameter or Bahr skew.

$$\beta_1 = \phi_e - \phi_t \tag{2.83}$$

$$\beta_2 = \phi_t + \phi_e, \tag{2.84}$$

where ϕ_t and ϕ_e are defined as twist and shear, respectively.

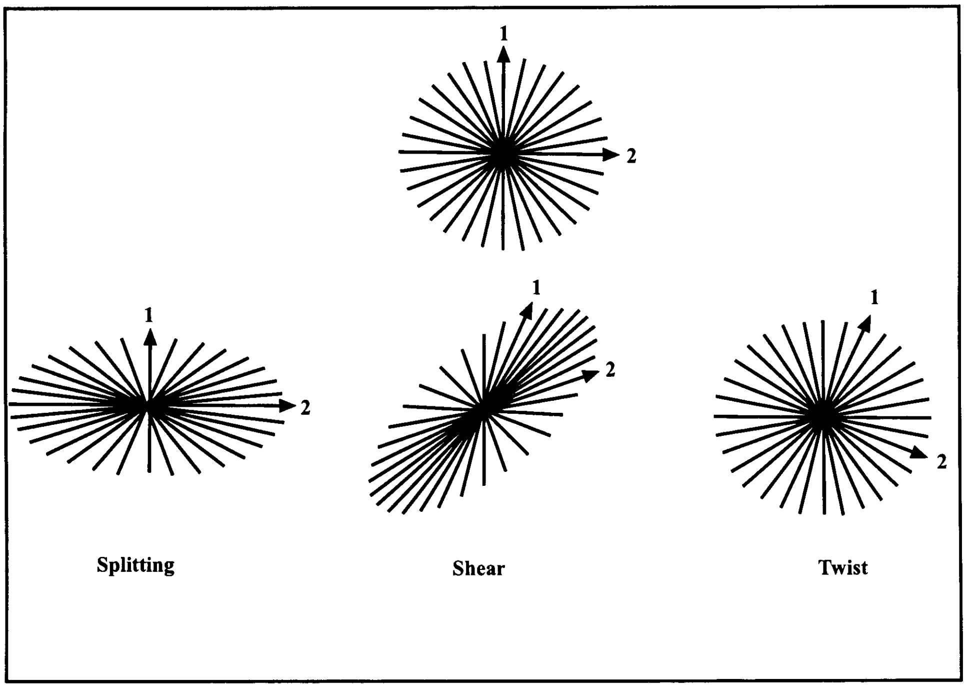

Figure 2.6: Distortion parameters from Groom-Bailey decomposition (1989).

Based on the above parameters, the seven classes of Bahr are categorised as follows

Class 1: The simple 2-D anomaly characterized by Σ>0.1 and k<0.1. the conductivity distribution should be considered to be 2-D. Also Swift's method of determining strike may be applied.

Class 2: The purely local 3-D anomaly superimposed on a layered earth, is characterized by η<0.05.

Class 3: A regional 2-D anomaly with weak local distortion. This class includes all cases for which $\beta_1 < 5^0$ and $\beta_2 < 20^0$ or $\beta_2 < 5^0$ and $\beta_1 < 20^0$.

Class 4: A regional 2-D anomaly in rotated coordinates, is characterised by

$\beta_1 = \beta_2$.

Class 5: A regional 2-D anomaly with strong local distortion. In this class decomposition is necessary and it is described by $\eta < 0.3$ and a large angles of twist and shear.

Class 6: A regional 2-D anomaly with strong local channelling. This class includes the cases where $-\beta_1 + \beta_2 \approx 90^0$.

Class 7: A regional 3-D anomaly. This class includes those cases where $\eta > 0.3$.

It is vital to apply Bahr classes on data first since Groom-Bailey decomposition needs certain constraints and any condition outside these can lead to erroneous results.

2.8 Numerical modelling on computers

The main objective of modelling techniques is to improve the understanding of the relationship between the MT response functions and the various subsurface resistivity discontinuities that have generated them (Meju, 1988). The MT response functions such as the apparent resistivity and phase over a range of frequencies can be used to deduce the conductivity structure compatible with the observed data using modelling techniques.

2.8.1 1-D modelling

A great variety of 1-D modelling and inversion schemes exist (e.g. Niblett and Sayn-Wittgenstein, 1960; Jupp and Vozoff, 1975; Fischer et al., 1981; Meju and Hutton, 1992; and Hobbs and Dumitrescu, 1997). A simple resistivity-depth transformation can also be used to generate the approximate model as shown below. An algorithm based on the asymptotic response of impedance in half space is widely used (e.g. Niblett and Seyn-Wittgenstein, 1960, Bostick, 1977, Jones, 1983b). In the Niblett-Bostick transformation used in this study, penetration depth h is given by (Niblett and Sayn-Wittgenstein, 1960; Bostick, 1977),

$$h = \left[\frac{\rho_a(w)}{\mu_0 w}\right]^{1/2}. \tag{2.85}$$

The Bostick resistivity, $\rho_B(h)$, at depth h is given by

$$\rho_B(h) = \rho_a(T)\frac{1+m(T)}{1-m(T)}, \tag{2.86}$$

where m (T) is the gradient of apparent resistivity curve on a log-log scale,

$$\text{i.e.}\quad m(t) = \frac{\partial \log(\rho_a(T)}{\partial \log(T)} = \frac{T}{\rho_a(T)}\frac{\partial \rho_a(T)}{\partial T}. \tag{2.87}$$

In other word, The Niblett resistivity (Niblett and Sayn-Wittgenstein, 1960, Jones, 1983b) is given by

$$\rho_B(h) = \rho_a(T)\frac{(1+\frac{T}{\rho_a}\frac{\partial\rho_a}{\partial T})}{(1-\frac{T}{\rho_a}\frac{\partial\rho_a}{\partial T})} = \rho_a(T)\frac{1+m(T)}{1-m(T)}, \tag{2.88}$$

An alternative expression for the Bostick resistivity has been used by various authors (e.g. Goldberg and Rostein, 1982). This form is given by

$$\rho_B(h) = \rho_a(w)\left[\frac{\pi}{2\varphi(w)} - 1\right], \tag{2.89}$$

where ρ_a = the observed apparent resistivity

w = angular frequency

φ = phase.

The 1-D MT inversion programme employed in this study (Meju, 1992, 1994) uses the ridge-regression or Marquardt method (Marquardt, 1970). In ridge regression we minimize the linearised function

$$\Phi = q_1 + \beta q_2 = e^T e + \beta(x^T A - L_0^2), \tag{2.90}$$

where q_1 and q_2 are the quantities required to be minimized. L_0 is the bound on the energy of the parameter increments, A is called the Jacobian matrix, x is the solution length, $e = |y - Ax|$, and β is the damping factor, an undetermined Lagrange multiplier which determines the relative importance that is given to q_1 and q_2, $q_1 = e^T e = (y - Ax)^T (y - Ax)$, where y is a vector containing the difference between the initial model response and the observed data (see Meju, 1994).

For minimisation, the following solution for the parameter perturbations is derived

$$x = (A^T A + \beta I)^{-1} A^T y. \tag{2.91}$$

Adding the damping factor leads to stable inversion of the matrix A and overcomes the ill conditioning of $A^T A$ in Gauss-Newton method. To get optimum value for β, there are many different ways (see Vozoff and Jupp, 1975; Johansen, 1977; Meju, 1992).

If the observational errors are available, they may be incorporated directly in the problem formulation to obtain more acceptable weighted solution. So the ridge regression estimate becomes (Meju, 1992):

$$x = \left[(WA)^T WA + \beta I\right]^{-1} (WA)^{-1} Wy \tag{2.92}$$

where the diagnonal weighting matrix W contains the reciprocal of data errors,

i.e. $$W = diag\left(\frac{1}{\sigma_1}, \frac{1}{\sigma_2} ..... \frac{1}{\sigma_n}\right).$$

2.8.2 2-D modelling

The earth structure is complex and at least 2-D modelling is required. There are four basic methods for the solution of 2-D forward model response: The finite difference (e.g. Patrick and Bostick, 1969; Jones and Price, 1970; Brewitt-Taylor and Weaver, 1976), the finite element (e.g. Reddy and Rankin, 1973; Wannamaker et al., 1986, 1987), the integral equation (e.g. Patra and Mallick, 1980; Hohman, 1983), and the transmission line analogy (e.g. Madden and Thompson, 1965). In all these methods the region to be modelled is divided into a mesh of elements at which field values are evaluated subject to boundary conditions. The finite element methods are usually the most accurate, and the finite difference methods are the quickest and simplest (Madden and Mackie, 1989; and Mackie et al., 1993). Some of these forward modelling methods have been incorporated into linearized 2-D inversion schemes (e.g. Jupp and Vozoff, 1975; Mackie, 1996). In this study a computer program based on the finite difference equations has been used. The 2-D scheme used in this program uses Tikhonov (1963) regularization. The forward model simulations are computed using different equations generated by network analogs to Maxwell's equations. The 2-D inversion solution is based on the maximum likelihood procedure described by Mackie et al. (1988). The approach used in this study to solve the maximum likelihood equations was the conjugate gradient relaxation technique (Madden and Mackie, 1989; Mackie et al., 1993; Mackie and Madden, 1993). This specific program was written by Mackie (1996). A more detail description of this program is given with the practical work in chapter 6.

3. Transient electromagnetic (TEM) method

3.1 Basic principles

The transient electromagnetic (TEM) method is an inductive method that utilises strong current which is passed through a rectangular loop commonly laid on the surface of the ground. The flow of this current in the surface loop will create a magnetic field that spreads out into the ground in the form of a primary magnetic field and induces eddy currents in the subsurface. When the current is abruptly terminated, this primary magnetic field is time varying and in accordance with Faraday's law, there will be an electromagnetic induction during this time. This electromagnetic induction in turn results in eddy current flow in the subsurface. The intensity of these currents at a certain time and depth depends on ground resistivity (Kaufman and Keller, 1983), in other words, the conductivity, size, and shape of subsurface conductor. The voltage response, which is proportional to the time rate of change of the secondary magnetic field created by the eddy currents, is measured. For poor conductors, these initial voltages are large but the fields decay rapidly. For good conductors, the initial voltages are smaller but the field decays slowly. Nabighian (1979) has shown that at any given time after switch off, this system of induced currents can be represented by a simple current filament of the same shape as the transmitter loop, and moves outward and downward with decreasing velocity and diminishing amplitude with time (Fig. 3.1). This is known as the smoke ring.

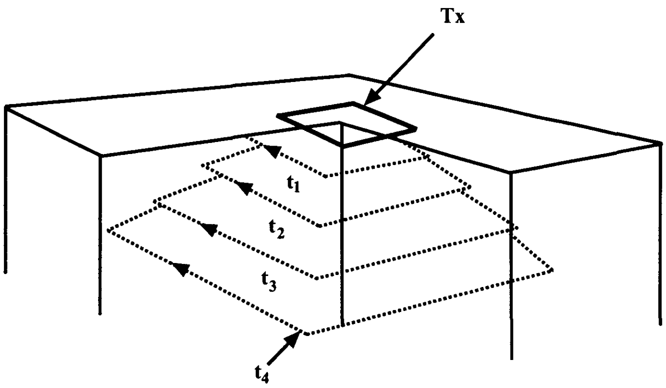

Figure 3.1: System of equivalent current filaments at various times after current interruption in the transmitter loop, showing their downward and outward movement (after McNeill, 1990).

The velocity V_z with which the ring expands away from the transmitter, at a time t is given by the equation (Nabighian, 1979)

$$V_Z = \frac{2}{\sqrt{\pi\sigma\mu t}}, \tag{3.1}$$

and the diffusion depth, *d*, of the wave is given by

$$d = 2\pi\sqrt{\frac{2t}{\mu\sigma}}. \tag{3.2}$$

The depth of investigation is determined by the time interval after the transmitter current is turned off and the subsurface conductivity (equation 3.2). As the time increases, the current intensity migrates to greater depths.

The current driven through the transmitter loop consists of equal periods of on-time and off-time (Fig. 3.2). The TDEM signal is measured during the transmitter off time period only, i.e. in the absence of a primary field. When the TEM response is plotted logarithmically against the logarithm of time in a homogeneous medium, the response can be divided into three stages, early stage (where the response is constant with time), an intermediate stage (response shape is continually varying with time), and late stage (response is a straight line). In the early time stage of the transient process, the induced currents (Grant and West, 1965) will be independent of the conductivity and firstly (i.e. at time t=0) be confined to the surface of the conductor in such a way as to preserve the

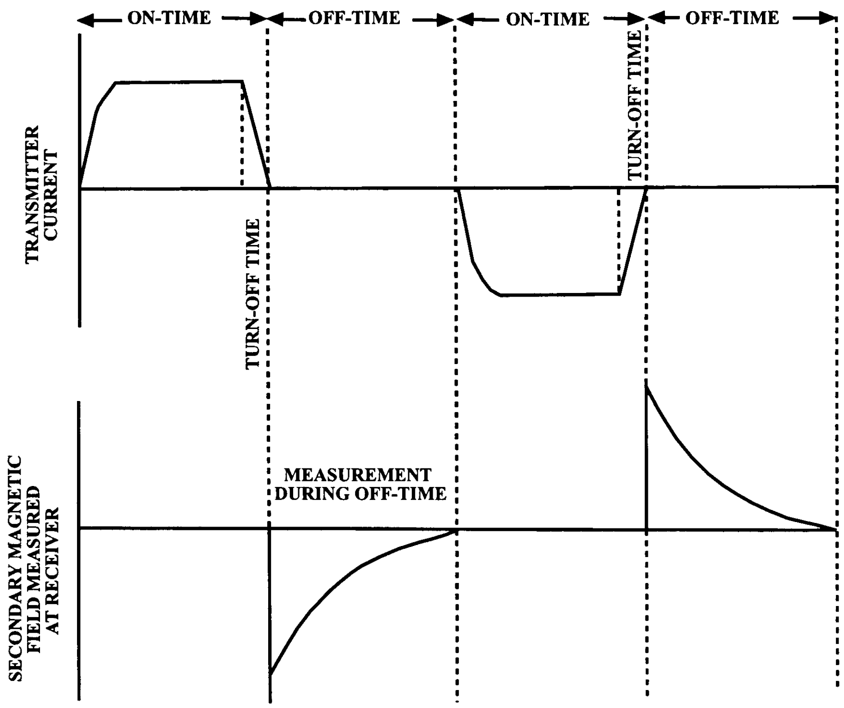

Figure 3.2: Schematic diagram showing on and transmitter current linear ramp turn-off time and receiver signal (after Swift, 1990).

normal component of the pre-existing primary magnetic field at the surface of the conductor (Weaver, 1970). At this stage, the initial current distribution is only a function of the size and shape of the conductor (Grant and West, 1965). In the subsurface, an inward diffusion of the current pattern later occurs as a result of ohmic losses which leads to the region immediately inside the conductor seeing a decreasing magnetic field and an induced emf that causes new current to flow. This is the intermediate stage. This continues until a stage is reached at which current distribution becomes more or less invariant with time. The inductance and resistance of each current ring have reached stabilised values and both the currents and their associated external magnetic fields begin to decay with a time constant given by

$$\tau = \frac{\sigma\mu a^2}{\pi^2}, \tag{3.3}$$

where a is the radius of an equivalent circular loop.
This is the late–time stage of the transient process.

3.1.1 TEM in homogeneous medium

The derivative of the vertical magnetic field, B_Z as a function of time is given by (McNeill, 1980)

$$\frac{\partial B}{\partial t} = \left(\mu M / 4\pi t^{3/2}\right)\frac{\left(\mu\sigma\right)^{3/2}}{t^{5/2}}. \tag{3.4}$$

Re-arranging this equation by inversion, we have

$$\rho_a(t) = \left(\frac{\mu}{4\pi t}\right)\left(\frac{2\mu M}{5tB_z^{\bullet}}\right)^{2/3}, \tag{3.5}$$

where M is the transmitter dipole moment,

$B_z^{\bullet} = \frac{\partial B}{\partial t}$ and ρ_a is the apparent resistivity of the ground.

3.1.2 TEM in layered earth model

In a two-layer situation and at early times, the diffusing current will be concentrated entirely in the upper layer and the measurement of field component will be characteristic of that layer. At much later times the current will be predominantly in the second layer and the measurement of the magnetic field will be diagnostic of that layer.

McNeill (1980b), Yungul (1961), and Hoversten and Morrison (1982) have published computational results for the induced electric field inside some two and three-layered geoelectric sections. The solution for the TEM forward problem for a layered earth with a step source is given in Knight and Raiche (1982) and Raiche (1984). This gives the mutual impedance, Z, between the transmitter and receiver loops, located on the ground surface, as a function of measurement time. This equations is

$$Z(t) = -\pi\mu ab \int_0^\infty L_p^{-1}\{I(P)PA_0(m,P,\lambda)\}J_1(\lambda a)J_1(\lambda b)d\lambda\,, \tag{3.6}$$

where a and b are respectively the radius of the transmitter and receiver loops, $A_0(m,P,\lambda)$ is the layered earth impedance function, m represents the layer thickness and conductivities, P is the Laplace transform variable rather than the Fourier transform variable i.e. replacing $-iw$ with P, λ is the integration variable for the inverse Hankel transform and is equal to $-p^{-1}$ for a step function turn-off, J_1 is the Bessel function of order one, and L_p^{-1} is the inverse Laplace transform operator with respect to P.

For a structure with n layers above a uniform half-space of conductivity σ_{n+1}, the reflection coefficient at the interface between layer j, of conductivity σ_j, and layer $j+1$ of conductivity σ_{j+1}, is:

$$R_j = \frac{S_j - S_{j+1}}{S_j + S_{j+1}}. \tag{3.7}$$

The exponential factor E_j is defined

$$E_j = \exp\left(-2S_j h_j\right),$$

where h_j is the thickness of layer j and

$$S_j = \left(\lambda^2 - iw\mu\sigma_j\right)^{1/2}.$$

Working from the bottom to the top for the sequence of the layers, we define (Knight and Raiche, 1982)

$$F_{n+1} = 0 \tag{3.8}$$

for the basal half-space,

$$F_N = E_N R_N \tag{3.9}$$

for the overlying layer n, and

$$F_j = E_j \frac{\left(R_j + F_{j+1}\right)}{(1 + R_j F_{j+1})}, \tag{3.10}$$

for any layer j $(0 < j < n)$ on top of layer n.

Using the recursive relation, the function A_0 in equation (3.5) is simply

$$A_0 = \frac{R_0 + F_1}{1 + R_0 F_1}. \tag{3.11}$$

3.2 TEM field measurements

In the TEM survey, the transmitter is connected to a loop of wire laid on the ground. With the exception of the on time measuring system (UTEM and INPUT), all TEM transmitters generate a bipolar waveform with a ramp turn-off time as shown in Figure 3.2. The decaying voltage in the receiver is measured when the transmitter is turned off which allows the very small voltage to be measured without interference from the large primary field. The receiver samples the amplitude of the transient decay using a number of gates. The width of gates increases with time so the early time gates are narrow in order to accurately measure the voltage while the later gates, situated where the transient varies more slowly, are much broader. This wider gate enhances the signal to noise ratio which decreases with time as the amplitude of the signal decays.

The design of TEM survey depends on the depth of investigation required. The practical limitation on the depth of investigation for TEM system is determined by the maximum recording time, the time t at which the signal decays to the noise level, the source moment and earth resistivity. These independent parameters render the depth of investigation difficult to quantify. Spies (1989) has studied the depth of investigation of TEM survey; he has shown that in case of transmitter-receiver separation or loop size less than the depth of investigation (near-zone) and induced voltage measured with an induction coil, the depth of investigation is proportional to the 1/5 power of the source moment and ground resistivity $(IA\rho)^{1/5}$. On the other hand, if the receiver is a magnetometer the depth of investigation is proportional to the 1/3 power of the source moment and is no longer a function of resistivity. In case of loop size greater than the depth of investigation (far-zone), the depth of investigation for an induced voltage receiver is proportional to the ¼ power of the source moment and resistivity and is inversely proportional to the source-receiver separation (Spies, 1989). This analysis gives the maximum depth of investigation based on detection of a buried layer. The minimum depth, at which individual conductivity variations can be resolved, is determined by the earliest sample time.

3.2.1 TEM loop configurations

The most common factor for designing all time domain techniques is the fact that they all utilise either square shaped or rectangular as the transmitter. Also a large transmitter loop offers a better capability for depth penetration. These methods use either fixed- or moving-loop configurations and measure the rate of decay of the secondary field when the primary field is switched off. They are mostly used to investigate the variation of conductivity with depth (resistivity sounding). A number of different loop configurations are possible for TEM measurements, some being better than others for specific geologic situations. They include the common zero-offset (in-loop and single-loop), short offset (separated-loop or soTEM) and the long-offset (loTEM) techniques. Figure 3.3 illustrates the most common loop configurations. Brief descriptions of the most commonly used TEM loop configurations are given below.

3.2.1.1 Central loop (or in-loop) configuration:

In this method, a dipole multi turn receiver is located at the centre of the transmitter loop. The size of transmitter loop varies between 50 x 50 and 500 x 500 m depending upon the exploration depth required. The rule of thumb is that the transmitter size is approximately one half the depth of penetration. The receiver coil is much smaller (usually a multi turn coil of 1 m diameter). Several different receivers can be used consecutively to record the transient over a large dynamic range with better resolution. Shallow anomalies near the centre of the loop are expected to have a large effect on the central receiver. The advantage of in-loop technique is that it gives high resolution of conductor position, provided inhomogeneities are minimal, and provides horizontal as well as vertical components of the magnetic field.

3.2.1.2 Coincident (transmitter-receiver) loop or single loop:

This configuration utilises a single loop both as a transmitter and a receiver. The loop acts as transmitter when the current is in the loop and as a receiver once the current is switched off. Coincident transmitter-receiver loop has the same geometry and response as the single loop configuration except that the transmitter and receiver are separate loops laid out spatially coincident. This loop is widely used in the search for large stratiform targets at depth since the propagation distances to and from the target are minimised, resulting in less signal attenuation of both primary and secondary fields. Further, the secondary field effects are purely additives. This simplifies interpretation and facilitates the detection of weak secondary signals. Common sizes are 50, 100 or 200 m per side. Loops smaller than 50 m per side may require more than one turn to give effective dipole moments but such loops can be time consuming to lay out. Depth of penetration increases with increasing loop size and is 2-3 times the loop side length or more. The advantage of this loop is its highest signal level because the receiver loop is in place of strongest transmission especially when the transmission field is attenuated by conductive overburden. This also ensures a degree of coupling with targets at any orientation especially if they lie at a near horizontal attitude.

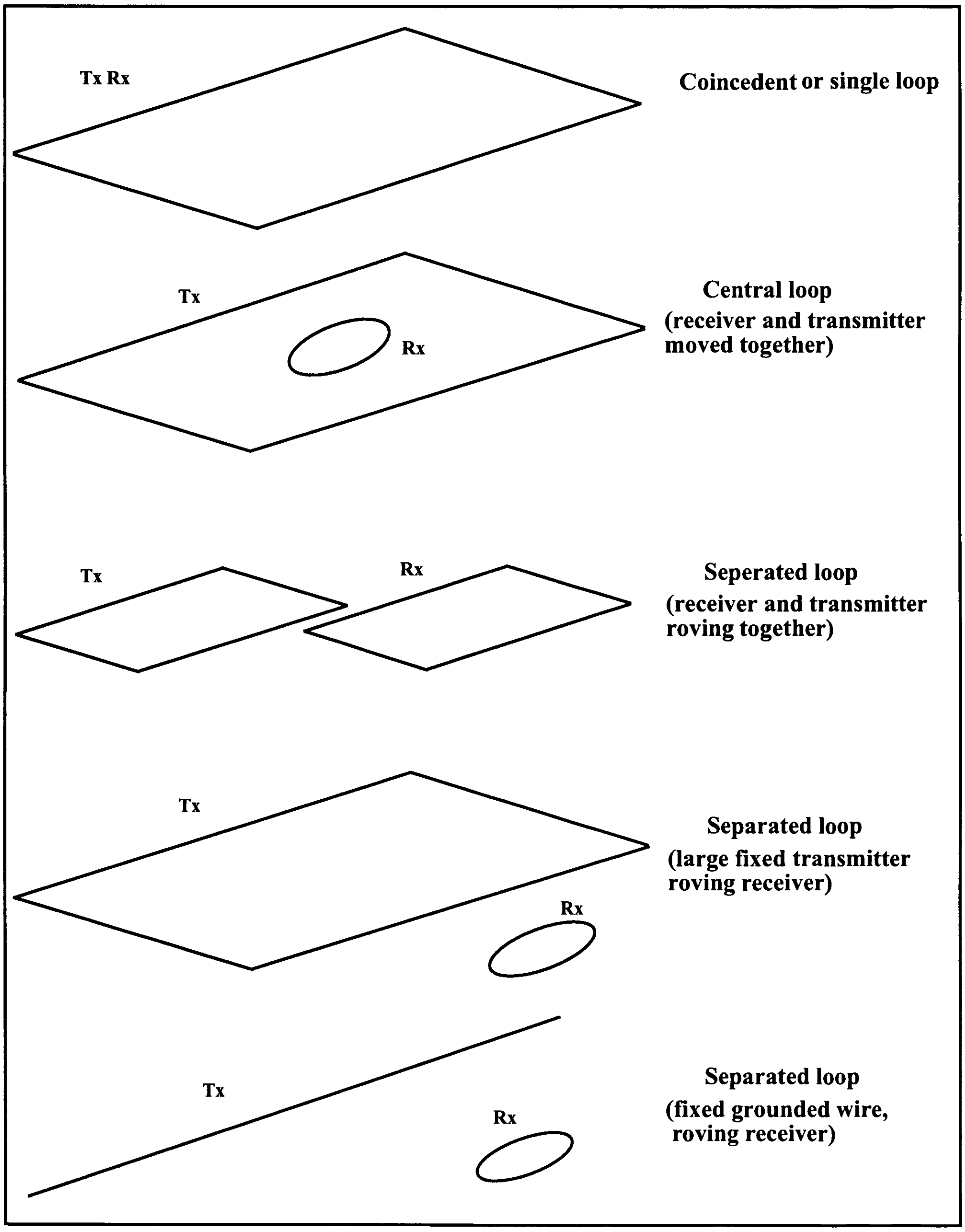

Figure 3.3: TEM loop configurations (after Swift, 1990).

3.2.1.3 Offset loop:

It consists of a large transmitter loop that can have sides up to 1km long. A small roving receiver is moved both inside and outside the Tx loop along lines that are perpendicular to the side of the loop. The main advantage of this is its greater depth of penetration and high productivity but some consideration must be taken into account from erroneous interpretation due to current gathering and channelling phenomena that occur, especially in conductive terrain (Spies and Parker, 1984).

3.3 Various effects on TEM

3.3.1 IP effects

The data from TEM can normally be assumed to be independent of frequency or delay time. In most cases this assumption is excellent for the bandwidth (approximately 10 to 10,000 Hz) of typical TEM system. When variation in conductivity with frequency exists, the conductivity tends to increase with increasing frequency. In that case such material are termed polarizable. IP effect is attributed to electrical polarisation induced by current flow in polarizable materials and might be measurable by an inductive sensor (Nabighian and Macnae, 1991). The inductive EM response of a ground with a realistic small polarizability is generally indistinguishable from the response of another ground without polarization. The polarisation current is usually in the opposite direction acting to depress the fundamental inductive current which is positive. This effect is very severe and may cause the transient response to become negative over some range of the measurement time. IP negative response has been reported before in the literature. Smith and West (1988) reported negative transients for only coincident loop soundings while Smith and West (1989), Walker and Kawasaki (1988), and Meju et al. (1999) reported negative transients for central loop soundings too. The current associated with the positive response polarises the body, the larger the positive response, and the greater the polarisation. However, the positive response must also decay rapidly, so that the smaller response associated with the polarisation will be observed as a negative transient at late time (Smith et al., 1988).

3.3.2 Superparamagnetic effect

This effect is caused by near-surface or super paramagnetic materials in the lateritic soil cover that have frequency dependent magnetic permeability and leads to incorrect apparent resistivity determination with time. These effects are restricted to within 3 m of the transmitter loop. It could be detectable with loop configurations where the receiver loop is in close proximity of the transmitter loop. The theoretical work by Lee (1984) also attributes the observed 1/t anomalous response to the presence of near-surface material with a frequency dependent magnetic permeability and suggests that under certain conditions superparamagnetic effects could also prove bothersome for large transmitter loop-roving receiver TEM system. Therefore, if a superparamagnetic effect is present, it may be necessary to displace the transmitting and receiving wires by 2 to 3 m. More information can be found in Buselli (1981) and Lee (1984).

3.3.3 Magnetic permeability variations

Local variations in magnetic permeability can cause detectable TEM effect. However, except for some iron-rich minerals, the magnetic permeability varies by at most a few percent from that of free space (Nabighian and Macnae, 1991). These permeability variations are commonly mapped using static field magnetometers such as proton precession devices. Where near-surface permeability variations cause for example 600 nT or 1 percent positive anomaly in a background of 60000 nT due to earth's magnetic field, any time varying magnetic field such as the total TEM response would be slightly enhanced by about 1 percent. Such enhancement is usually only detected in measurements made during the transmitter on time (Lamontagne, 1975) or correspondingly in the in-phase component of FEM surveys (Fraser, 1973) where a reference primary field amplitude is measured.

3.3.4 Conductive overburden

The weathered surface rocks or overburden are mostly conductive and can significantly hamper EM measurements even in the presence of relatively poorly conducting host rocks (Nabighian and Macnae, 1991). Many authors described this phenomenon and modelled it (e.g. Lamontagne, 1975; Lowrie and West, 1965; and Irvine and Staltari, 1984). The conductive overburden can delay and smooth the target responses within a resistive host rock. This delay is proportional to conductivity-thickness product of the overburden and the overall dimension of the measuring system. Also inhomogeneities within the overburden may give rise to current channel whose effects can easily be confused with those of conductors beneath the overburden.

3.4 Sources of error in TEM measurements

The TEM method is affected by source of errors. It can be categorized into four main types of noise sources: a) instrumental noise, b) cultural or man-made noise, c) natural EM noise, d) geologic noise.

3.4.1 Instrumental noise

Instrumental noise arises from electronic components on circuit boards. It can be caused by thermal motion of charged carriers, shot noise caused by the discreteness noise of electronic charges analogous to the noise produced by the rain falling on a tin roof, modulation noise, and other causes. This type of noise is significantly reduced by stacking whereby a series of readings is taken and the results averaged to give the final figure. This can result in S/N ratio improved by a factor of $\sqrt{N}$ where N is the number of stacks.

3.4.2 Cultural or man made noise

Currents induced from man-made noise produce anomalous TEM responses. Junge (1996) subdivided the man made noise into active and passive. Power lines (50 or 60 Hz) are the main source of active noise, while telephone lines, metallic pipelines, fences, and others are examples of passive noise. VLF radio stations (10-25 kHz) also cause high frequency noise. However, most of the TEM instruments have internal filters (notches) which are set to the local main frequency to reject the effect of such noise. Pruning can significantly improve the S/N ratio by rejecting power line transients.

3.4.3 Natural EM noise

The natural noise spectrum which is in the range of 5-25 Hz, is essentially due to atmospheric discharges, especially those associated with lightening. This sferics noise can be of such high strength to become the main limitation in obtaining sufficient signal to noise (S/N) ratio. Below about 6 Hz, the natural EM noise field is primarily of geomagnetic and ionospheric origin with relatively little noise present within the frequency range 1 to 6 Hz (McCracken et al., 1984). Motion induced noise or microphonics, due to the movement of the magnetic field sensors in the earth's magnetic field, can be very significant because the earth's field is more than 100 000 times larger than the fields used in TEM measurements. This is often called wind noise and is most significant in open areas and airborne EM systems (Nabighian and Macnae, 1991). TEM systems use a form of synchronous detection and stacking and also have sferics rejection filters to enhance signal to noise ratio.

3.4.4 Geologic noise

Geological noise can be considered as all geological phenomena which result in incorrect layered-earth interpretations using quasi-static 1-D models. The complex geology can lead to current channelling and gathering (Spies and Parker, 1984). Current channelling is a restriction on current migration due to an insulating barrier or a constricting or narrowing of a conductor, while current gathering occurs when eddy currents migrating through a conductive host or overburden are concentrated in a locally more conductive zone. 1-D modelling can lead to erroneous results with this type of distortion. According to Spies and Parker (1984) and Swift (1990), the source of geologic noise can be divided into the following:

- 3-D bodies within the survey area which lead to current channelling and gathering.
- Lateral and vertical variations within layers caused by differences in pore fluid content, alteration, weathering and sediment deposition.
- Discontinuities such as faults and dikes which interrupt the current flows.
- Depth variations in the interfaces between layers.

Lowrie and West, (1965), Lamontagne (1975), McCracken et al. (1986), and Newman et al. (1987) have discussed these effects in more details.

3.5 Data Processing

The TEM data are recorded in the form of transient voltage at a number of sample times. The first step of processing is editing, checking the data for accuracy, normalising with respect to the transmitter current and receiver area and gain. Sirotem Mk3, which was used in the first part of this study, its raw data are in nV/A and have been normalized for the Tx currents and Rx gain and also the receiver area. Geonics (TEM47), which are used in the second part of this research, its raw data are in nV/Am^2 and is normalized for the receiver gain and area using the formula

$$\frac{19.2 * 2^{-g} * V}{A_R}, \tag{3.12}$$

where V is the reading of the receiver in mV, g is the amplifier gain and A_R is the area of the receiver coil in m^2. The turn-off time effect has to be taken into account; several ways of dealing with turn-off effect have been reported in the literature (Raiche, 1984; Asten and

Price, 1985; Fitterman and Anderson, 1987). The approach applied in this study is based on Raiche (1984). Then the data are plotted in the form of graphs to aid interpretation. Some of the most popular presentations are as follow:

- Transient decay plots, on either log-log or semi-log paper, of voltage (in microvolts) versus time (in milliseconds).
- Response profiles, i.e., graphs of measured voltage at a selected time along points of profile.
- Response contours, i.e., contour of measured voltage at a selected time at all stations in the survey area.
- Apparent resistivity plots, profiles or contours.
- Vector plots, either in a horizontal plane or in a given vertical section (XZ or YZ planes).

3.6 Interpretation

The main objectives of interpretation are to get the location and possible shape of the target and its conducting quality and also the subsurface resistivity distribution. The location and possible shape of the conducting target is determined from profiles and contours of the field measurements at various times. These data can be converted into apparent resistivities which are favoured by a number of geophysicists particularly when a sounding type of interpretation is desirable. The conductor "quality" is estimated from its time constant determined from decay plots of the field intensity at one or more key stations. 1-D modelling or more sophisticated models can be used as a quantitative technique using forward and automatic inversion approaches. Novel schemes exist for direct or approximate 1-D analysis of TEM data (e.g. Nekut, 1987, Eaton and Hohman, 1989, Fullagar, 1989, Fullagar and Reid, 1992, Smith et al., 1994), but they require a considerable numerical skill to implement. Therefore, simple approximate schemes for TEM data analysis have been proposed (Meju, 1995,1998) referred to here as the Meju transformation.

3.6.1 Resistivity pseudosection

A qualitative interpretation of the data by pseudosection before modelling can provide prior information about the geological structure of the study area and lead to more realistic view of the subsurface structure. It is also valuable in showing how well the available data constrain the resistivity distribution, both in terms of the spatial density of the sites and the frequency range of the observations (Banks et al., 1996). A drawback in this technique is that features shown at common transient times may be generated by structures at different depth. However this method is carried out as "a first pass" interpretation.

3.6.2 Meju transformation

The TEM apparent resistivity data are converted into effective subsurface resistivity at depth yielding a continuous picture of the resistivity-depth distribution of the subsurface (Meju, 1998). According to this transformation, the effective resistivity at a given transient time is approximated by (Meju, 1998, equation 1):

$$\rho_{eff} = \rho_a\left[(90 / \varphi) - 1\right], \tag{3.13}$$

while the effective depth is taken as

$$\delta_{eff} = (3.9\rho_a t / 2\pi\mu_0)^{1/2}, \tag{3.14}$$

where ρ_a is the observed apparent resistivity at time t

t is the transient decay time in seconds

μ_0 is the magnetic permeability of free space

φ is the approximate equivalent phase.

The value of φ can be determined from the derivative of the apparent resistivity curve in logarithmic scale.

Using the definition of the equivalent MT period, T (in second) to the transient decay time (Meju, 1995)

$$T = 3.9t, \tag{3.15}$$

Meju (1998) showed that

$$\rho_{eff} \equiv \rho_a\left[\left(1 + \partial\log\rho_a / \partial\log T\right) / (1 - \partial\log\rho_a / \partial\log T)\right] \tag{3.16}$$

and

$$\delta_{eff} = \left(\rho_a T / 2\pi\mu_0\right)^{1/2}. \tag{3.17}$$

This scheme closely resembles to the Niblett- Bostic transformation (see chapter 2) but requires an iterative solution for apparent resistivity and adjusting the TEM data for transmitter turn-off effects (Raiche, 1984).

It was found that the above transformation yields the preferential enhancements of the resistive and conductive parts of the computed effective resistivity distribution better than the observed apparent resistivity data using the concept of diffusion depth (Meju, 1995) given below

$$\delta_{eff} = \frac{\delta t}{2.3}, \tag{3.18}$$

where δt is the analogous quantity to the skin-depth and referred to as 'diffusion depth' given by:

$$\delta t = \left[\frac{2t\rho_a}{\mu_0}\right]^{1/2} \tag{3.19}$$

and

$$\rho eff = \mathrm{K}\rho_a e^{-(1-\alpha)}, \tag{3.20}$$

where the variable parameter α in the exponent takes a value between 0.15 and 0.2 for field data and is zero for synthetic data, and the constant K may be needed to improve the fit between the field and computed model response.

4. Hydro-geological background

4.1 Introduction

Groundwater plays an important role in the development of the world's water-resource potential. It is important as an indispensable feature of the natural environment; it can lead to environmental problems such as landslides and in some cases offers a medium for environmental solutions like transport of industrial and domestic wastes (Hatzichristodulu, 1998). Also it is vitally important to be able to detect its occurrence and protect it from the increasing threat of contamination. The term groundwater is usually reserved for the subsurface water that occurs beneath the water table in soils and geological formations that are saturated. Some soils are seldom saturated because their voids are only partially filled with water, the remainder of the pore space being taken up by air. The water table is the surface on which the fluid pressure in the pores of a porous medium is exactly equal to atmospheric pressure. An aquifer is defined as a geological formation comprising of layers of rocks or unconsolidated deposits that contain sufficient saturated material to yield significant quantities of water; while other formations that are much less permeable and can only transmit water at much lower rates than the adjacent aquifers are commonly known as aquitards (Freeze and Cherry, 1979; Price, 1985). An aquiclude is defined as a saturated geological unit that is incapable of transmitting significant quantities of water under ordinary hydraulic gradients. The most common aquifers are unconsolidated sands and gravels, permeable consolidated sedimentary rocks such as sandstones and limestones, and heavily fractured volcanic and crystalline rocks. The most common aquitards and aquicludes are clay, shales, and dense permeable rocks.

Aquifers can be classified into three types; confined, perched, and unconfined (Fig. 4.1). A confined aquifer is usually confined between two aquitards and occurs at depth while an unconfined aquifer occurs near the ground surface and the water table forms its upper boundary. A saturated lens that is bounded by a perched water table is sometimes called a perched aquifer (Fig. 4.1).

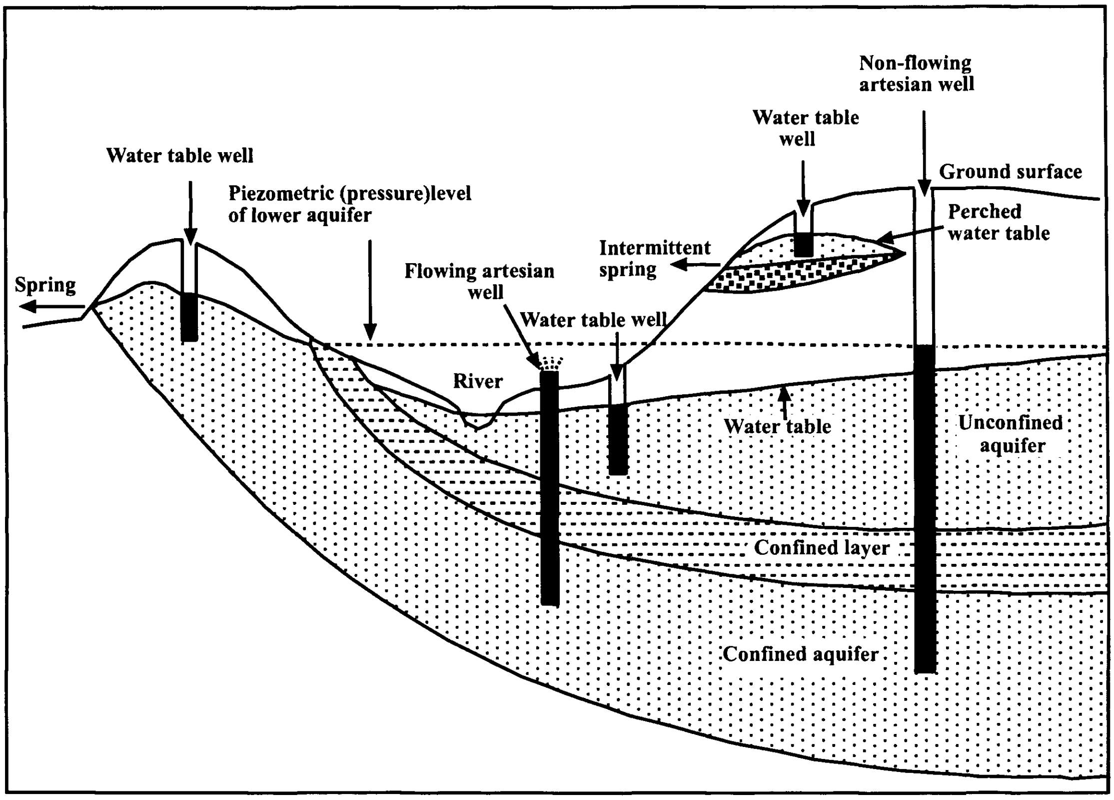

Figure 4.1: Schematic showing the different types of aquifers (after Brassington, 1988).

4.2 Aquifer properties

There are some basic hydrogeologic properties that govern the motion of groundwater in aquifers. These are porosity, permeability, transmisssivity, specific yield, storativity, and specific capacity. This section will give descriptions of these properties. More details can be found in standard textbooks (e.g. Freeze and Cherry, 1979; Domenico and Schwartz, 1990).

4.2.1 Porosity and Permeability

An adopted definition of total porosity (Φ), described by Domenico & Schwartz (1990) is the percentage of volume of rock that is void space,

i.e. $$\Phi = {}^{V_V}\!/_{V_T}\,. \qquad (4.1)$$

Where V_V is the volume of the void, V_T is the total volume.

There are two kinds of porosity: a) primary porosity or the porosity that formed during deposition, sedimentation and compaction without any subsequent chemical changes by water flowing through the sediments, and b) secondary porosity developed by subsequent chemical changes which can lead to fissures and fractures. Permeability is the rate of flow or the capacity of a rock to transmit fluid. It is expressed in m/day or m/sec. Most fine-grained detrital rocks have relatively high porosities but very low permeabilities (Price, 1985). For instance, clay-rich soils usually have higher porosity than sandy or gravely soils but lower permeability. This is because clay particles are platy with large surface areas causing high molecular forces between the clay and water particles; these forces adsorb water onto the clay minerals and therefore are not free to flow under natural conditions (Hatzichristodulu, 1998). On the other hand, sediments of large and small grains have low porosities because small grains tend to occupy larger grain voids which are usually interconnected to create higher permeability. Table 4.1 lists porosity and permeability for some of the major consolidated and unconsolidated sedimentary and basement rocks (Brassington, 1988). As shown in this table, the physical properties of rock change during consolidation because of compaction due to burial depth.

4.2.2 Transmissivity

The term transmissivity was first introduced by Theis (1935) to define the rate of flow of water through a vertical strip of aquifer of unit width and extend the full-saturated height under a hydraulic gradient equal to unity. It is denoted by T and expressed in m^2/day. The concept of transmissivity is valid only in two-dimensional, or aquifer-type flow.

4.2.3 Storativity and specific yield

Both terms are defined as the volume of water released or stored per unit surface area of the aquifer per unit change in the component of head normal to the surface. Storativity refers only to the confined parts of an aquifer. It can be determined by means of pumping tests in which boreholes are pumped and the change in water levels measured in one or more nearby observation wells situated at known distances from the pumping well. Specific yield, on the other hand, refers to the unconfined parts of an aquifer and it is also determined on the basis of pumping tests.

4.2.4 Specific capacity

The term specific capacity is defined as the rate of discharge of a well per unit length of drawdown. The effectiveness of wells can be balanced according to this concept. However, although the specific capacity gives some indication of water-bearing properties of aquifer, a great variety of testing procedures makes this parameter subject to differences that cannot be related to aquifer.

Geological Material	Grain size (mm)	Porosity (%)	Permeability (meters per day)
Unconsolidated sediments			
Clay	0.0005-0.002	45-60	$<10^{-2}$
Sillt	0.002-0.06	40-50	10^{-2}-1
Alluvial sand	0.06-2	30-40	1-500
Alluvial gravel	2-64	25-35	500-10000
Consolidated sedimentary rocks			
Shale	Small	5-15	$5x\ 10^{-8}$-$5x10^{-6}$
Sandstone	Medium	5-30	10^{-4}-10
Limestone	Variable	0.1-30	10^{-5}-10
Basement rocks			
Basalt	Small	0.001-1(up to 50 if vesicular)	0.0003-3 (secondary permeability)
Granite	Large	0.001-1 (up to 10 if fractured)	0/003-0.03 (secondary permeability)
Schist	Medium	0.001-1	10^{-7}-10^{-4}

Table 4.1: Variations of porosity and permeability for some unconsolidated, consolidated sedimentary and basement rocks (after Brassington, 1988).

4.3 Groundwater geology

There are three main parameters which can control the nature and distribution of aquifers in a geologic context. These are the lithology, stratigraphy and structure of the geological deposits. The hydrogeological definitions of these parameters are adopted from Freeze and Cherry (1979). The lithology is the physical makeup, including the mineral composition, grain size, and grain packing, of the sediments or rocks that make up the geological systems. The stratigraphy describes the geometrical and age relations between the various lenses and formations in geologic systems of sedimentary origin. Structural features, such as cleavages, fractures, folds, and faults, are the geometrical properties of the geologic systems produced by deformation after deposition or crystallization. Figure 4.2 shows the effect of these parameters on the occurrence of aquifers and aquitards in sedimentary rocks. As shown in this figure, the permeable sandstones that are gently dipping are potential regional artesian aquifers (Fig. 4.2a); an aquifer of permeable sand and gravel in alluvial fans interfingers with layers of clay and silt (Fig. 4.2 b); occurrence of surface water is controlled by faults or folds or where the desert floor is eroded close to the top of the aquifer (Fig. 4.2c). Unconformities that are considered as stratigraphic features also play an important role in hydrogeology. Aquifers are commonly associated with unconformities, either in the weathered or in the fracture zone immediately below the surface of a buried landscape (Linsley et al., 1988).

A basement aquifer occurs within the weathered residual overburden (the regolith) and the fractured bedrock. According to Wright (1992), the weathered layer can be classified into collapsed and saprolitic zones while the bedrock can be divided into saprock and fresh bedrock (Fig. 4.3). The collapsed zone has developed from originally saprolitic material by further dissolution and leaching, combined with other formative processes (chemical, physical and biological). It includes the surface soils and other layered features such as laterites, calcretes, and illuviated clay layers and stone lines. The surface material is typically sandy on watershed areas where these overlie quartz-rich rocks but changes to sandy clays and clay (montmorillonite) in the valley bottom. The surface sands have high infiltration capacities which decrease markedly in any underlying illuviated clay horizons. Saprolite is derived from in situ weathering and is disaggregated. An upper saprolite may be distinguished by its higher proportions of the more advanced secondary clay mineral (kaolinite); the lower saprolite has a greater abundance of primary minerals combined with the earlier forms of secondary clay minerals (smectites). The boundary with the underlying saprock may be sharp (against coarser-grained, massive rock) or transitional (against banded or finer-grained rocks). Regolith thickness and lithology, along with corresponding aquifer hydraulic parameters, depend on a complex combination of controls, including 1) bedrock characteristics (chemistry, mineralogy, petrology and structure); 2) climate (past and present); 3) relief and other site factors. The saprock is generally transitional or even fluctuating in banded sequences. The fracture systems within this zone and fresh bedrock are related either to decompression or to tectonic forces. The former tends to be subhorizontal with a decreasing frequency with depth. The latter tends to be subvertical

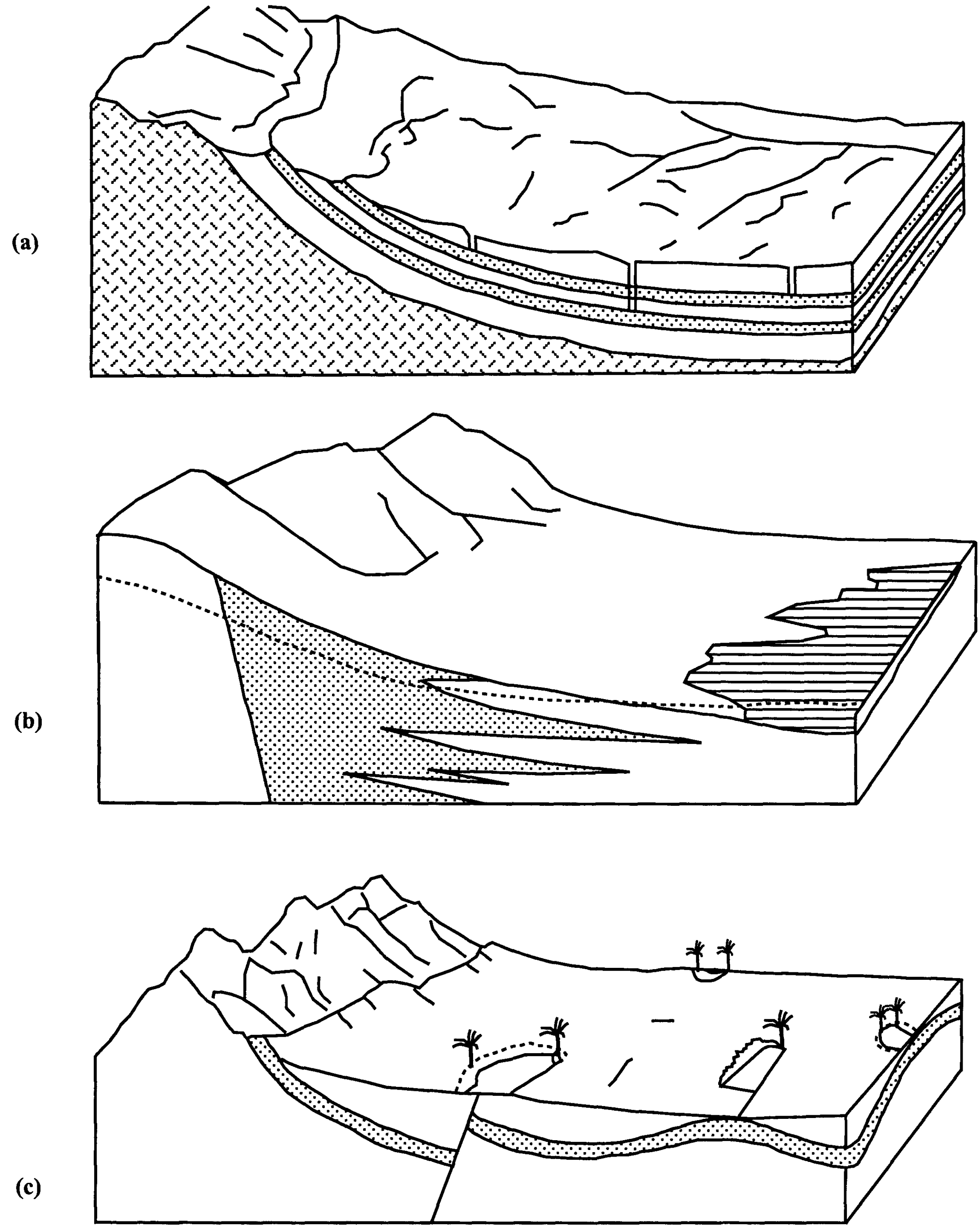

Figure 4.2: Influence of stratigraphy and structure on regional aquifer occurrence. (a) Gently dipping sandstone aquifers; (b) interfingering sand and gravel aquifers; (c) faulted and folded aquifers (after Freeze and Cherry, 1979).

and is often in zonal concentrations. According to this division and based on electrical conductivity properties, a typical fracture zone target may consist of weathered surficial zones (consisting of relatively resistive leached or molted upper zone and underlying highly conductive saprolite zone) and moderately resistive transition zone of partial weathering above fresh bedrock of high resistivity (Palacky, 1987; Meju et al., 2001).

In unfractured metamorphic and plutonic igneous rocks, porosities are rarely greater than 2%; the primary permeabilities of these rocks are also small (10^{-11}-10^{-13} m/s, see Table 4.1). Permeabilities of this magnitude indicate that these rocks are impermeable within the context of most groundwater problems. However, in fractured and crystalline rocks, appreciable fracture permeability generally occurs within tens of meters and in

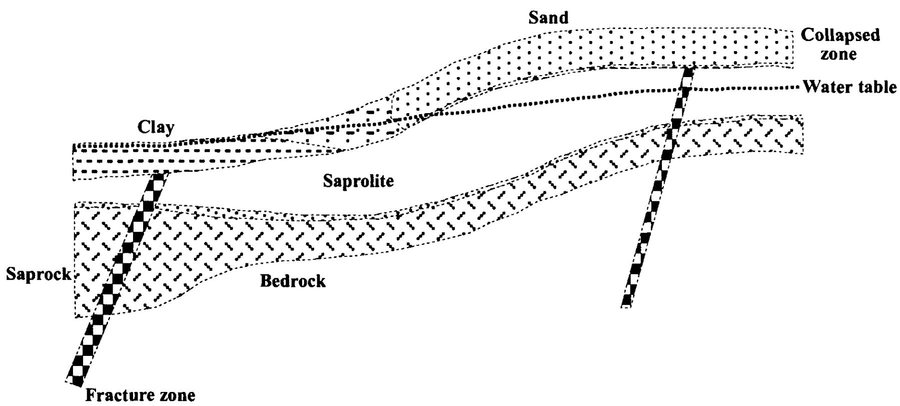

Figure 4.3: Schematic section of basement aquifer (after Wright, 1992).

some cases within a few hundred meters of ground surface. These fractures are caused by changes in the stress conditions that have occurred during various episodes in the geologic history of the rocks (Freeze and Cherry, 1979). The width of the fracture can control the amount of groundwater in aquifer since the discharge of groundwater is proportional to the fracture widths raised to a power of about 3 and consequently, the difference in permeability between rock masses with fracture widths of tenths of a millimetre and those with fracture widths on the order of millimetres or more is enormous (Freeze and Cherry, 1979). This permeability generally decreases with depth as described by Davis and De Wiest (1966). This is because stress variations that cause fracturing is larger and, over geologic time, occur more frequently near the ground surface. Moreover, fractures tend to close at depth because of vertical and lateral stresses imposed by overburden loads and "locked-in" horizontal stresses of tectonic origin. In granite, the occurrence of near-horizontal fracture parallel to the ground surface has been attributed by Legrand (1949) to the removal of overburden load caused by erosion. With depth, fracture of this type decreases rapidly in frequency and aperture width. They are probably unimportant contributors to permeability at depths greater than about 100 m (Davis and De Wiest, 1966). Tolman (1937) and Davis (1969) draw attention to the fact that in some cases dissolution of siliceous rocks may cause significant increases in the width of fracture openings along the surface. However as groundwater passes through overburden prior to entering the fractured rock, it normally acquires appreciable dissolved silica. It is therefore relatively aggressive with respect to silicate minerals along the fracture faces. Topography is also important factor since water well yields in the crystalline rocks are highest in valleys and broad ravines which mostly develop along fault zones, and lowest at or near the crests of hills (Legrand, 1954; Davis De Wiest, 1966). Yields in flat uplands and beneath slopes are between these extremes.

4.4 Seawater intrusion

When groundwater is pumped from aquifers that are in hydraulic connection with the sea, the gradients that are set up may induce a flow of salt water from the sea towards the well. This migration of saltwater into freshwater aquifers under the influence of groundwater development is known as seawater intrusion. Seawater intrusion is a significant problem in many coastal areas. In normal unconfined groundwater conditions with water table sloping towards sea level, the groundwater body takes the form of a lens of fresh water 'floating' on saline water from land to sea (Ward and Robinson, 1990, Mahesha & Nagaraja, 1995).

The physical controls on the position of the saltwater-freshwater interface were independently established by Badon Ghyben and Herzberg (Todd, 1959). This relationship is referred to as the Ghyben-Herzberg Principle (Lefleur, 1984). According to this relationship and under static condition each metre of freshwater head above sea level depresses the interface 40 m below sea level (Fig. 4.4) as shown in the following equation

$$\rho_s g Z_s = \rho_f g (Z_s + Z_w) \tag{4.2}$$

$$Z_s = \frac{\rho_f}{\rho_s - \rho_f} Z_w . \tag{4.3}$$

Where g is gravity constant; Z_w is freshwater head above sea level,

Z_s is the distance of interface, ρ_f is freshwater density (=1000),

ρ_s is saline water density (1025).

When the known values are applied to the equation, we can get

$$Z_s = 40Z_w \tag{4.4}$$

Todd (1959) suggested five solutions to protect coastal aquifers from contamination and to control spreading of seawater to freshwater, viz;

1. Reduction and/or rearrangement of pattern of pumping draft.
2. Direct recharge.
3. Increase pumping from the area of saline-water through paralleling the coast.
4. Maintenance of freshwater ridges above sea level along the coast.
5. Construction of subsurface barriers.

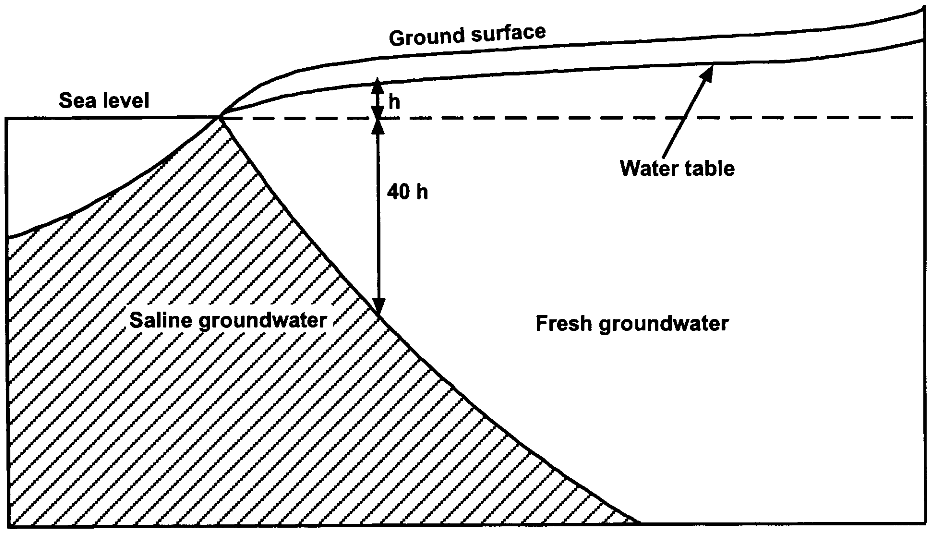

Figure 4.4: Standard model for seawater intrusion (after Ward and Robinson, 1990).

4.5 Predicting hydrogeologic parameters from resistivity information

Aquifer properties are usually obtained either from pumping tests or laboratory experiments when core samples exist. However, an alternative approach can be applied using non-invasive geophysical information. The electrical resistivity of sediments is mostly related to porosity by Archie's (Archie, 1942) equation. This equation can be written as:

$$\rho_b = k\rho_f \Phi^{-m} S^{-n}, \tag{4.5}$$

where ρ_b is the rock resistivity, ρ_f is the resistivity of the pore fluid, Φ is the porosity, m is the cementation exponent, S is the pore saturation and n is the saturation exponent, k is constant and usually has the value of one. In case of a full pore saturation (i.e. S = 1) and clean matrix (i.e. a clay-free medium), Archie equation can be reduced to

$$\rho_b = \rho_f \Phi^{-m}. \tag{4.6}$$

The value of m for most rocks lies between 1.3 and 2.5 (Schopper, 1982). Deriving values of porosity from bulk resistivity obtained from the inversion model is not easy task especially if there is no borehole data or laboratory measurements through which we can obtain accurate value of m, ρ_f, and also n when the pores are not fully saturated by fluid.

For mainly clean sand, it is possible to obtain approximate values of ρ_f and the total dissolved solids (TDS). In case of highly saline, relatively homogeneous, sandstone aquifers, Meju (2000) suggested the following relationship:

$$\log \sigma_b = -0.3215 + 0.7093(\log TDS) \tag{4.7}$$

where σ_b is the bulk conductivity of the formation in *mS/m*, and TDS in mg/l.

Also Meju (2000) suggested a relationship:

$$\log TDS = 0.8 + 1.015 \log \sigma_w, \tag{4.8}$$

where σ_w is the fluid conductivity in ms/m.

For an acid mine drainage problem, Ebraheem et al., (1990) obtained the relation

$$\log \sigma_b = -0.333 + 0.6453(\log TDS), \tag{4.9}$$

and

$$\log(TDS) = 1.216 \log(\sigma_w) - 0.584, \tag{4.10}$$

where σ_w is in μ mho/cm.

Then the porosity can be calculated using Archie (1942) equation. Although the above equations are empirical and often site specific, they are useful for obtaining approximate prediction of the sought parameters.

5. Combined TEM\MT field studies in Parnaiba basin, Brazil

The northern and south-eastern margins of the Parnaiba basin are the sites of the first part of this research for assessing the regional structures affecting the groundwater distribution and locating the best place for groundwater resource development using TEM-MT methods. This section describes the stratigraphy, structures and tectonics of the Parnaiba basin (NE brazil) and gives an overview of the published geophysical studies in the basin. It is followed by a description of the field studies undertaken. Details of data acquisition and processing as well as a preliminary interpretation are given in this chapter.

5.1 The area of study

The Parnaiba basin (previously referred to as the Maranhao basin) is located in NE Brazil and extends for about 1000 km northeast-southwest and 800 km northwest-southeast, giving it an elliptical shape with an area of approximately 600,000 km^2 (Fig. 5.1). It is one of the three major intracratonic basins in Brazil (the Amazon and Parana basins are the others); it is named after the Parnaiba river which runs approximately parallel to the major axis of the basin. Most of the geological and geophysical studies in the Parnaiba basin are found in unpublished commercial reports (Cunha and Goes, 1989; Goes, 1991). Some relevant publications are also available (Meju et al., 1999; Arora et al., 1997, 1999) as well as dissertations (De Sousa, 1996; Vidotti, 1997; and Ulugergerli, 1998). The geological information given below was taken from the above references.

The Parnaiba basin is mainly Paleozoic in age and infilled with siliciclastics of mostly continental origin deposited in five depositional cycles from Upper Ordivician to the Cretaceous. Regional unconformities occur due to slow epeirogenic crustal movements. This sedimentary infill was intruded by volcanic rocks during the Lower Jurassic and Middle Cretaceous (Goes et al., 1993). The oldest dated sediments are Upper Ordovician-Lower Silurian (Petri and Fulfaro 1983). The margins of the basin are defined by large marginal arches (Ferrer, Urbano Santos, Tocantins and Sao Francisco arches). These structural arches are usually associated with fold belts active during the Brasiliano cycle (Fig. 5.1). The Tocantins arch has been interpreted as the result of uplifting and intensive erosion from the upper Jurassic to middle Cretaceous. The Ferrer and Urbano Santos arches formed in the Lower Cretaceous as a result of the rupturing of Gondwana and the opening of the Equatorial Atlantic Ocean (De Sousa, 1996).

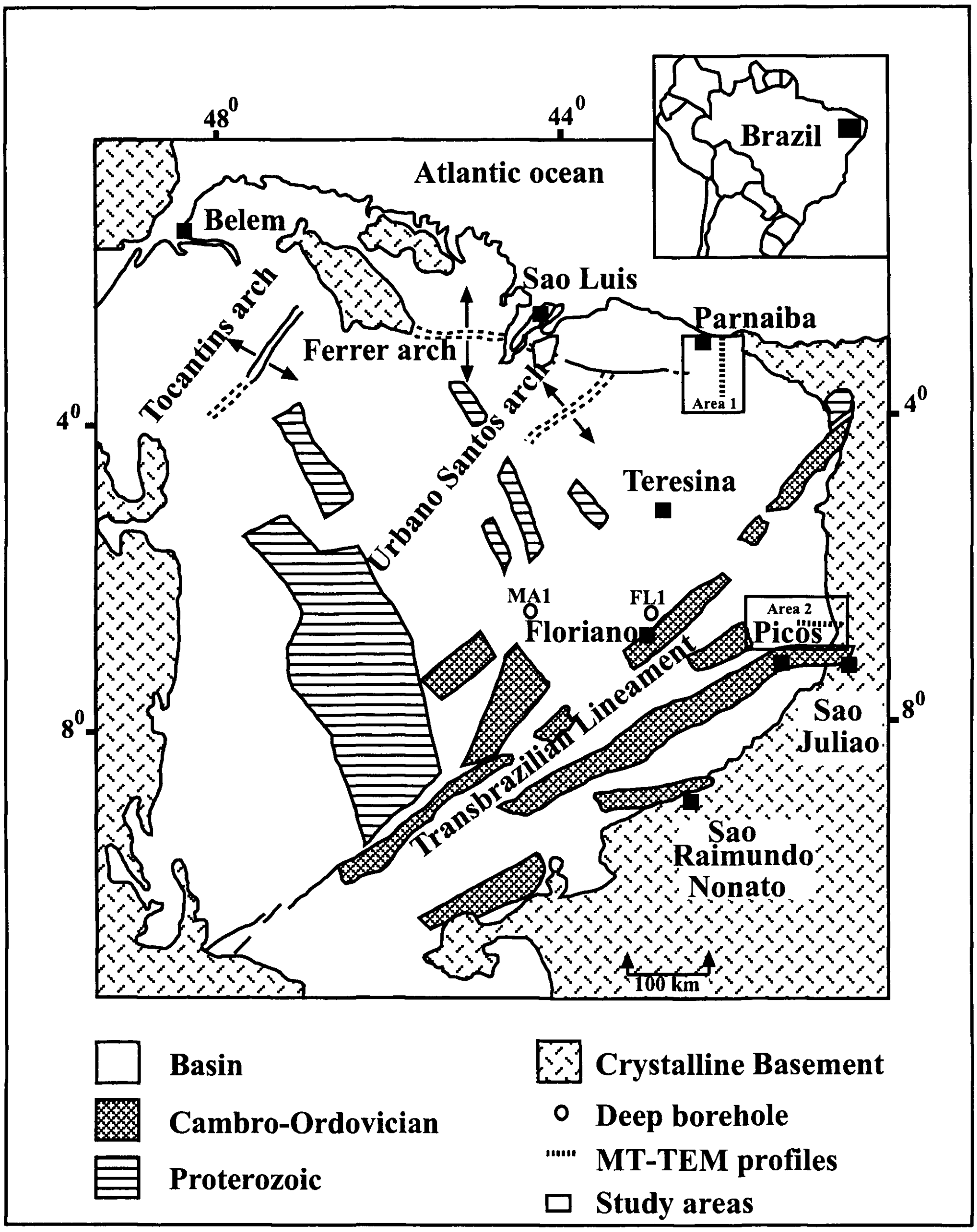

Figure 5.1: Simplified structural framework of the basement of Parnaiba basin deduced from qualitative aeromagnetic interpretation (Goes et al., 1993). The location of the present TEM-MT profiles in two areas of study is also shown.

5.1.1 Structural features and tectonics

The most important structural trends in the basin are NE and NNW (Fig. 5.1) and the most frequent structural features are basinal fractures, especially in the eastern part of the basin. Normal faults are more common than reverse faults which have been recognised mostly southwest of the basin (Vidotti, 1997). The Parnaiba basin shows some asymmetry with dip angles in the southern and southeastern borders being steeper than those in the northwest (Cunha, 1986). Folding is not a frequent structural feature but is associated with sedimentary layers that have been intruded by igneous bodies. Dips in the basin are usually quite low, typically 3-4^0 (Vidotti, 1997). One of the major tectonic controls on the development of the basin is the NE-SW Tansbrasiliano lineament. This is a complexly faulted shear zone including structural highs and grabens that were possibly initiated in the Middle-Upper Proterozoic (Marini, 1984) and have since been intermittently reactivated. Several graben structures were mapped along structural trends especially in the eastern portion of the basin (Cunha, 1986; Goes et al., 1993).

De Sousa (1996) suggested that the initial subsidence of the Parnaiba basin was caused by extension, following the break-up of super-continents in the Upper Precambrian-Lower Paleozoic. During this time a rift zone trending NE-SW started to develop. This was followed by a thermal phase which led to the deposition of 3.5 km of post rift strata (Fig. 5.2) in the Parnaiba basin (Goes et al., 1993; De Sousa, 1996).

The Precambrian basement in the basin comprises of fold belts, crustal blocks and median massifs which were metamorphosed in the Brasiliano cycle. They consist of varying metamorphic grades and originated in tectonomagmatic processes not older than Middle Proterozoic (De Sousa, 1996). Subordinate sedimentary rocks (Mirador and Riachao Formations), showing varying degrees of metamorphism, are preserved in graben-like structures of Upper Proterozoic and Cambrian-Ordovician age. The Mirador Formation does not outcrop and seems to be restricted to the central-southeast part of the basin. Lithologically, it consists of light grey-greenish to grey-whitish sandstones, with some intercalations of extremely micaceous siltstones and greenish shales at the top (De Sousa, 1996). Goes et al. (1993) interpreted the few available seismic sections as showing evidence of carbonatic and peltitic facies in deeper parts of the Riachao Formation and tentatively assigned them as Upper Precambrian. Wells reaching the Riachao Formation yielded the largest heat flow estimates in Parnaiba, ranging from 60-90 MW M^{-2} (Pereira and Hamza, 1991). The deposition of the Mirador and Riachao Formations preceded the regional sedimentation of Parnaiba which supports the interpretation that this crustal block in the northeast of Brazil has been the site of intermittent extensional tectonics since the Upper Proterozoic (De Sousa, 1996).

The Parnaiba basin was partially flooded by basalts and intruded by dykes and sills during two main phases of magmatic activity (Bellieni et al., 1990). The first phase in the Permo-Triassic was related to the opening of the North Atlantic Ocean and the second phase, in the Upper Jurassic-Lower Cretaceous, was related to the opening of the South Atlantic. The later extrusive magmatism is represented by the Mosquito and the Sardinha Formations (Vidotti, 1997).

5.1.2 Stratigraphy

The stratigraphy of the basin is represented by five main periods: Silurian, Devonian, Permo-Triassic, Jurassic and Cretaceous. These are unconformably underlain by metamorphic basement rocks and the molasses of the Riachao and Mirador Formations (Viddoti, 1997). The total sedimentary thickness of the basin is about 3400 m near the centre of the basin with Paleozoic sediments reaching up to 2900 m and the Mesozoic and Cenozoic sediments do not exceed 600 m (Goes et al., 1993). The summary of the whole chronological stratigraphy of the basin is shown in Figure 5.2.

The Silurian sequence (Serra Grande group) unconformably overlies the metamorphic basement and the ancient sedimentary rocks (Riachao and Mirador Formations). It is mainly composed of sandstones, shales, siltstones and conglomerates with rare diamicts. It is subdivided into the Ipu, Tiangua, and Jaicos Formations. The Ipu Formation normally contains medium to coarse-grained sandstones interbedded with rare siltstones, shales and diamicts, and has an approximate thickness of 350 m. It is Lower Silurian in age. The Middle Silurian Tiangua Formation comprises extremely micaceous sandstone with some siltstone and grey shales and has a maximum thickness of 200 m. The Upper Silurian Jaicos Formation conformably overlies the Tiangua Formation and consists of medium to coarse-grained sandstones and pelites with a thickness in excess of 360 m. The Serra Grande group represents a transgressive to regressive cycle (Goes et al., 1993) and comprises lithologies favourable for the accumulation of groundwater.

It is followed by Devonian Caninde Group, another transgressive-regressive cycle and comprises mainly shales, sandstones, and siltstones. It generally overlies the Serra Grande Group, but in the eastern margins of the basin, it is in direct contact with the underlying basement rocks. It is subdivided into the Itaim, Pimenteiras, Cabecas, Longa and Poti Formations (Cunha, 1986). The Middle Devonian Itaim Formation is 260 m thick and consists of fine white sandstones and grey to dark grey shales. The Upper Devonian Pimenteiras Formation consists of thick, organic-rich, dark-grey to black radioactive shales with thin layers of very fine-grained sandstones and has been the target for oil exploration in the basin. Its maximum-drilled thickness is 320 m. The Upper Devonian Cabecas Formation contains fine sandstones and is 350 m thick.

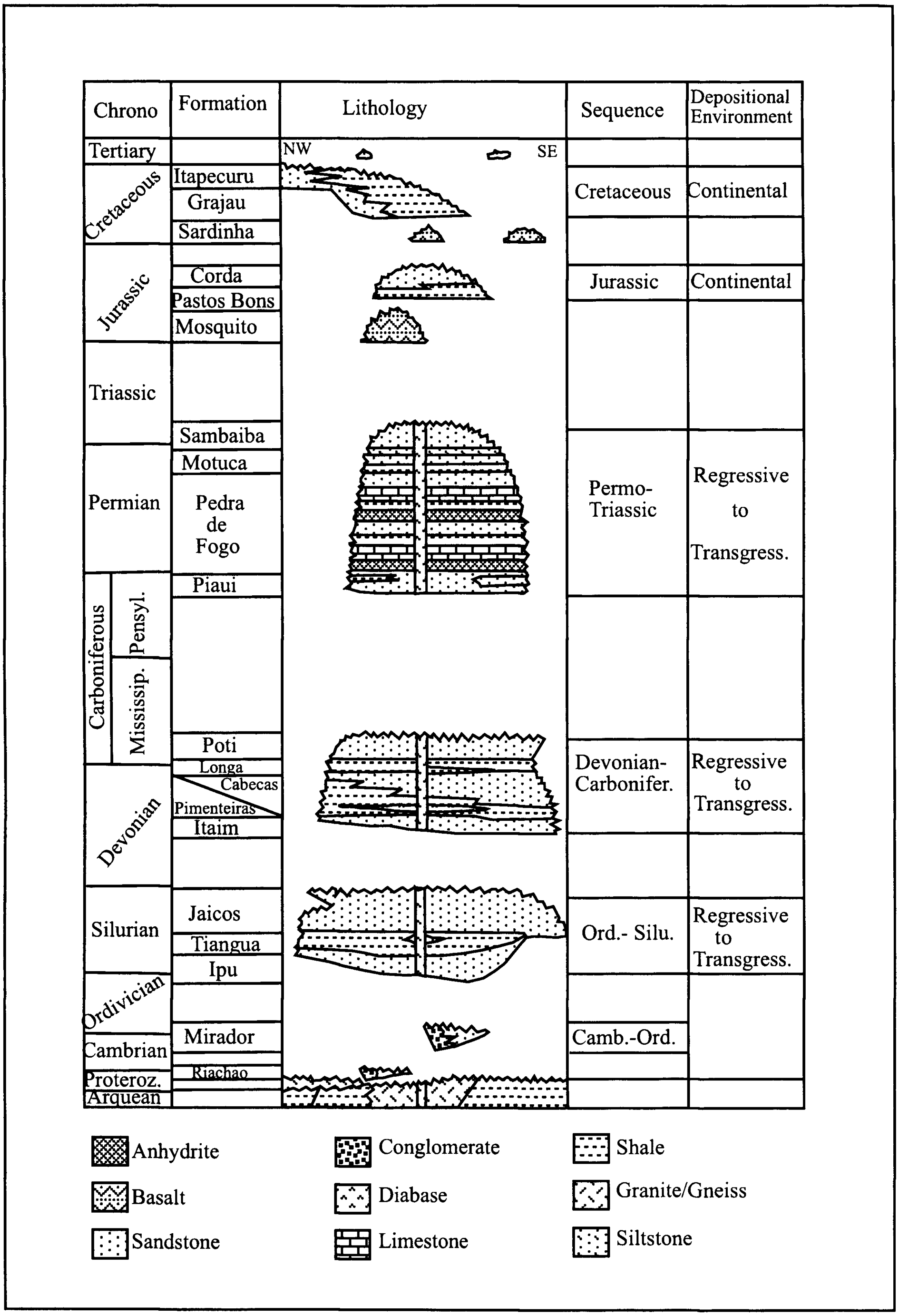

Figure 5.2: Schematic NW-SE lithostratigraphic section of the Parnaiba basin (after Goes et al., 1993).

The Longa Formation is of Upper Devonian-Lower Carboniferous age, 220 m thick, and is made up of fine-grained sandstones, shales and siltstones. The Poti Formation (the youngest member of the Caninde Group) comprises grey-whitish sandstone with intercalated conglomerate, siltstone, and red shale and has a maximum drilled thickness of 220 m. The Carboniferous-Triassic rocks comprise the next depositional sequence. These form the Balsas Group and include the Piaui, Pedra de Fogo, Motuca and Sambaiba Formations. These mainly consist of sandstones, siltstones, shales, limestones, anhydrites, and cherts with pieces of silicified wood (Goes et al., 1993). As indicated in Figure 5.2, the lithological sequence, the depositional environments record a transgressive to regressive cycle of the basin (Goes et al., 1993). The Piaui Formation comprises medium to fine-limestones. The Piaui Formation is Upper Carboniferous in age and has a maximum drilled thickness of 220 m. The lower Permian Pedra de Fogo Formation consists of silex and limestones interbedded with fine/medium grained yellowish sandstones, grey shales and white anhydrite and attains 240 m maximum-drilled thickness. The Upper Permian Motuca Formation comprises reddish and brown siltstones, fine/medium-grained white sandstones, white anhydrite and very rare limestones with maximum-drilled thickness of 220 m. The Sambaiba Formation consists of yellow to reddish, fine/medium-grained sandstones with a maximum-drilled thickness of 440 m.

The overlying Jurassic rocks indicate a continental desert-type depositional cycle and consists of sandstones, siltstones and shales (Goes et al., 1993). They include the Mearim Group which is divided into the Pastos Bons and Corda Formations. The Pastos Bons Formation consists of sandstones with a maximum-drilled thickness of 77 m. The Corda Formation is characterised by grey-whitish and reddish, fine to coarse-grained sandstones and has a maximum drilled thickness of 29 m. The Mearim Group rocks show unconformable contacts with the subjacent Mosquito and Sardinha basalts. The Cretaceous deposits comprise sandstones, mudstones, shales, carbonates and anhydrites and are represented by the Grajaú, Codó and Itapecuru Formations. This sequence was deposited in a continental environment. The Grajaú Formation comprises fine to conglomeratic, whitish sandstones interfingered with the bituminous shales, limestones and some anhydrite of the Codó Formation. The Codó sediments were deposited in a shallow marine environment and occur interbedded with littoral sediments of the Grajaú. These formations were deposited in the Middle Cretaceous and have a maximum-combined drilled thickness of 237 m. The Itapecuru Formation comprises reddish, medium to coarse-grained sandstones and brown-reddish mudstones with a thickness of < 724 m and was deposited in the Upper Cretaceous. Sedimentation cycles in the Parnaiba basin ended in the upper Cretaceous (De Sousa, 1996).

5.1.3 Previous geophysical studies

Until recently, there have been no major geophysical efforts to examine either the deep structure or the localized structure of the basin. Previous work has been on a regional scale and most of the major structures were located on geological maps using aerial photographs and aeromagnetic studies. There are 36 exploratory boreholes drilled in the Parnaiba basin by PETROBRAS, the Brazilian national oil company. Of these, twenty-two reached the basement rocks or precursory sedimentary covers. In addition, 25 wells were drilled for shallow groundwater exploration by CPRM company (Brazil) in the northeast of the basin. The density of exploratory wells is 1 /16,700 km^2. Seismic reflection studies for oil exploration focused on the central part of the basin and coverage is only 7,866 km, with a very low density of 0.013 km/km^2. The data gathered from the surface geology, geochemical surveys, exploratory wells and seismic sections were integrated by Goes et al., 1993) to produce the conventional litho-stratigraphic chart (Fig. 5.2).

The results from well data and the seismic sections indicated the existence of graben-like structures within the basin which might have acted as precursory axes of subsidence. These structures are probably the result of the activity along ancient fault lines in the Precambrian (Riachao) or Cambrian (Mirador) times (Cunha, 1986). A gravity survey carried out by PETROBRAS and processed by De Sousa (1996) suggested the following:

1) The areal extent of the Transbrasiliano lineament and NNW-SSE graben could be assessed with thicker accumulation of sediments. 2) The basin is underlain by a lens-shaped zone of dense material in the lowermost part of the crust/uppermost part of the mantle. Up to 10 km of the lower continental crust in this zone seems to be partially replaced/intruded by material intermediate in density between normal lower continental crust and upper mantle. This anomalous, dense zone may result from intrusion/partial replacement of the lower crust by mantle material, i.e. continental underplating (Furlong and Fountain, 1986) or passive upwelling of partial melt during rifting and extension of the lithosphere (Buck and Mutter, 1987). 3) A slight increase in the depth to the moho is seen at the centre of the basin. 4) Elongated NE-SW relative gravity lows indicate that sediments predating Parnaiba, and metamorphosed in varying degrees during the Brasiliano

cycle, should be found in grabens to NE, beneath the basinal sequence. 5) An anomaly in the centre of the basin has been interpreted as an independent verification that the continental lower crust beneath Parnaiba may be intruded with mantle–differentiated material.

Broad-band MT data are available along small profiles close to the centre and on the SE margin of the basin (Oliveira and Fontes, 1991; and De Sousa and Oliveira, 1995). MT soundings undertaken in the central part suggested the presence of a highly conductive layer in the deeper part of the basin (1 ohm-m) with an approximate thickness of 1000 m in the sedimentary section (Arora et al., 1999). On the other hand, the MT data undertaken in the SE margin indicated a relatively less conductive layer above the sedimentary/basement interface (10 ohm-m). In addition, geomagnetic induction data recorded in the Parnaiba basin by Arora et al. (1997) revealed a large NE-SW trending conductive anomaly (Parnaiba basin conductivity anomaly- PBCA) in the central part of the basin with an embedded resistive zone. This PBCA anomaly is in accordance with that deduced from MT data and is interpreted as a graben in the Precambrian basement filled with carbonaceous sediments. This high electrical conductivity may be due to the presence of carbon generated by thermal-controlled pyrolysis of hydrocarbon-saturated sediments (Arora et al., 1999). The embedded resistive body, also characterised by high density, is consistent with the presence of a diabase intrusive related to magmatic events. This is perhaps a manifestation of the basin-modifying tectonics caused by the Cretaceous magmatic activities. The relatively less conductive SE margin of the basin is truncated by the Transbrasiliano lineament. Aeromagnetic data are available for most of the Parnaiba basin. The qualitative interpretation of the data by Nunes (1993) suggested a complex basement configuration, including the presence of graben structures aligned with the PBCA. Also, for subsurface structural mapping and groundwater resource investigation, integrated geoelectrical methods including dc resistivity (VES), transient electromagnetic (TEM) and tensorial audio-magnetotelluric (AMT) measurements were carried out in the eastern margin of the basin (Fontes et al., 1997; Ulugergerli, 1998; and Meju et al., 1999). These indicated that the structural lineaments and faults appeared to have significant effect on groundwater distribution.

5.1.4 Current study

Although there is plenty of geophysical data for part of the Parnaiba basin, the NE and SW margins are not well covered. It is required to fully understand the subsurface structures that may affect the groundwater distribution at these margins. The present study is part of major project between Leicester University (UK) and National Observatory (Rio de Janeiro, Brazil) focusing on these two margins of the basin (see Fig. 5.1). The geological maps for the respective margins are shown in Figures 5.3 and 5.4. Note the lithological and structural trends.

As shown in Figure 5.3, the northeastern part contains rocks ranging in age from the Precambrian (basement rocks) to Quaternary cover deposits. The geology is complex and dominated by NE-SW and NW-SE structural trends. The lithological units trend NW-SE. The Quaternary and Tertiary sediments unconformably overlie the basement rocks in the north and outcrops in the form of strips trending NW-SE. Elsewhere, sedimentary formations of the Serra Grande and Caninde Groups are overlain by the Sardinha Formation. These lithologic units are affected by NW-SE structural trends. The aeromagnetic map of the basin shows a discontinuous fault running parallel to the basement arches to the west of the present study profile (see Fig. 5.1) and may be a possible basin-bounding fault. One of the objectives of the TEM-MT survey in the NE margin is to track this possible feature further to the East.

Figure 5.4 is a simplified geological map of the southeastern margin of the basin. The lithostratigraphic units are oriented approximately NNE-SSW. The Serra Grande Group is exposed in the area and unconformably overlies the Precambrian basement. The Serra Grande Group consists of the Jaicos, Ipu and Tiangua Formations (see section 5.1.2). The Jaicos Formation is the dominant unit and is also the target aquifer within this area. The Serra Grande Group is followed by the Caninde Group which is overlain by Tertiary sediments in the western regions (see Fig. 5.4). Structurally, the sedimentary cover basement contact is exposed to the east and southeast. Also, there is a major circular structural feature near the City of Picos (Fig 5.4) which is thought to be caused by faulting and magmatic activities. The Picos fault, detected by aerial photography, is also a major feature and which could play a vital role for controlling groundwater distribution in the area. All these features are the targets of the joint National Observatory-Leicester University exploration campaign in the SE margin of the basin.

5.2 Combined TEM-MT field surveys.

Electromagnetic methods are a common geophysical technique used in groundwater investigations because they directly measure the variation in the physical properties that relate to permeability, porosity, and fluid content in the subsurface. The TEM and AMT methods were utilised in the present study. It is hoped that combining the two methods will give information about shallow and deep structures. The equipments used are described in the following sections.

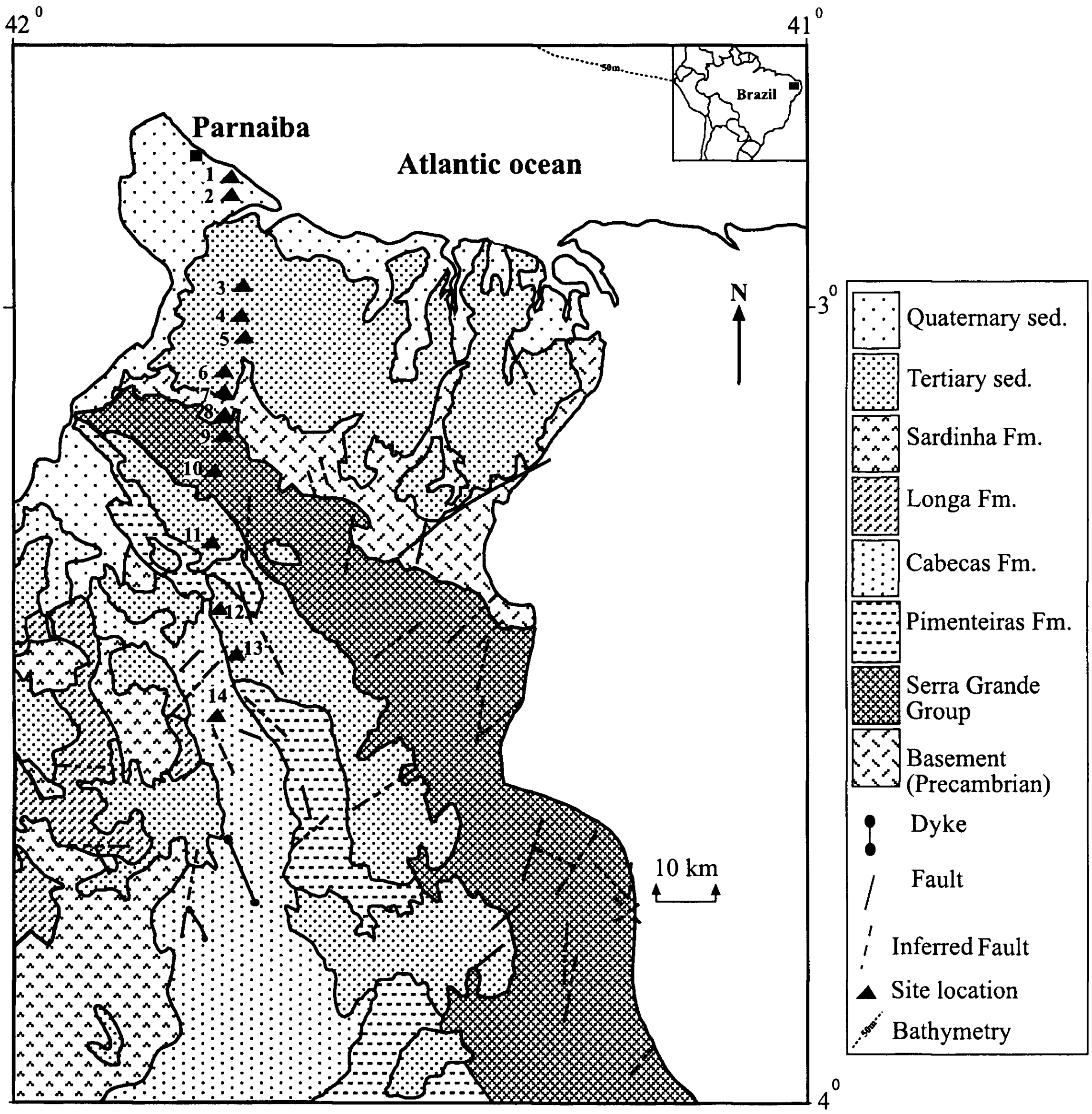

Figure 5.3: Geological map of the north-eastern part of Parnaiba basin showing the location of the TEM-MT stations occupied in 1999.

5.2.1 Magnetotelluric field instrumentation

Figure 5.5 is a schematic diagram of a typical field system configured for the collection of single-station magnetotelluric data. The equipment used in this study is the MT-1 field system developed by EMI (USA) that consists of three major components:

A) Magnetic and electric field sensors and analogue electronics,

B) The MT-1 receiver (data recorder),

C) The system computer, typically a laptop.

5.2.1.1 Electric field detectors

Electric field measurements were made by stretching a long wire connected to two electrodes at its ends and measuring the difference in voltage between two electrodes positions. The electrode separation used depends on the telluric intensity present and the sensitivity of the recording instrument. To measure the two orthogonal horizontal components of the electric field on the surface and to allow the full tensor impedances to be calculated, electric field dipoles were typically arranged in an L-shaped array with the two electric field dipole sharing a common electrode (Fig. 5.5).

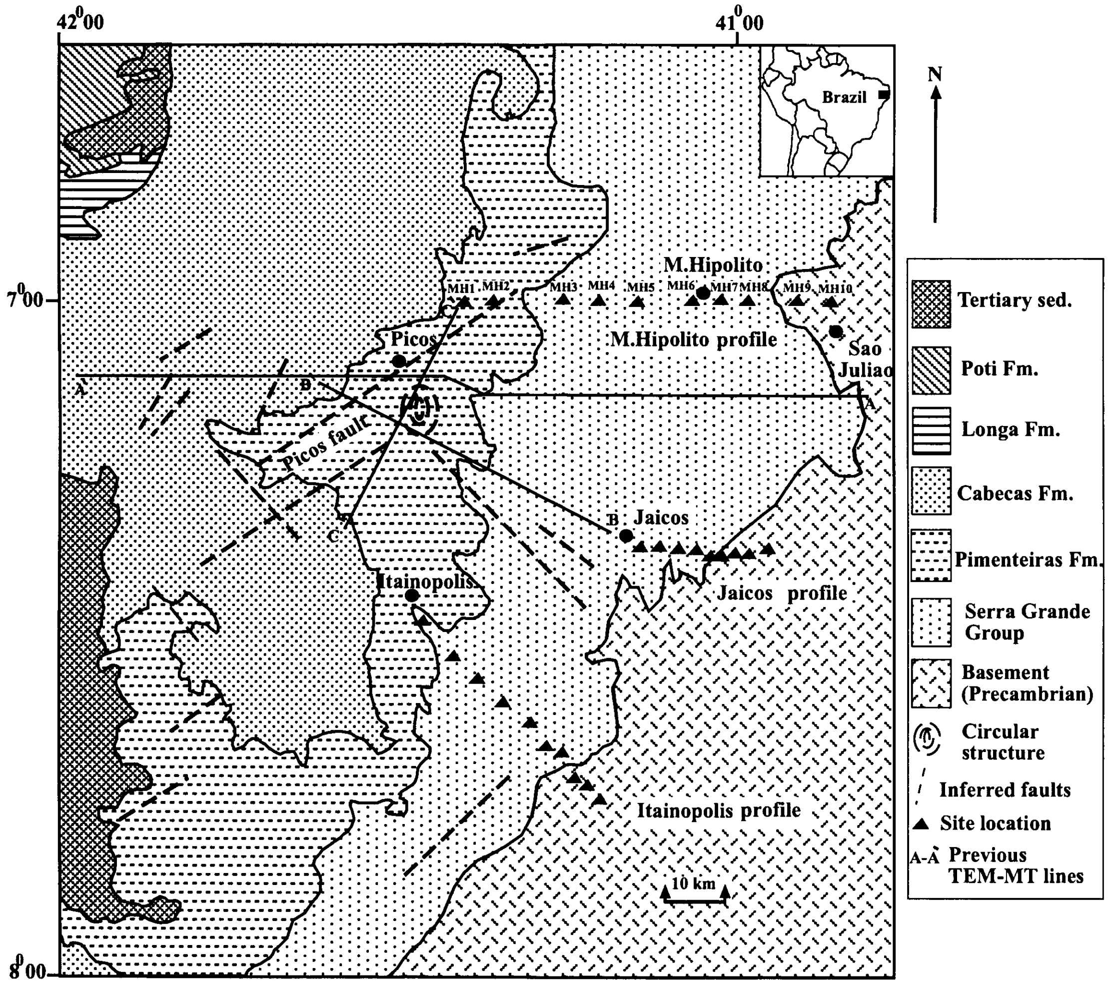

Figure 5.4: Geological map of the south-eastern part of Parnaiba basin showing the locations of the TEM-MT stations occupied in 2000 and previous survey lines.

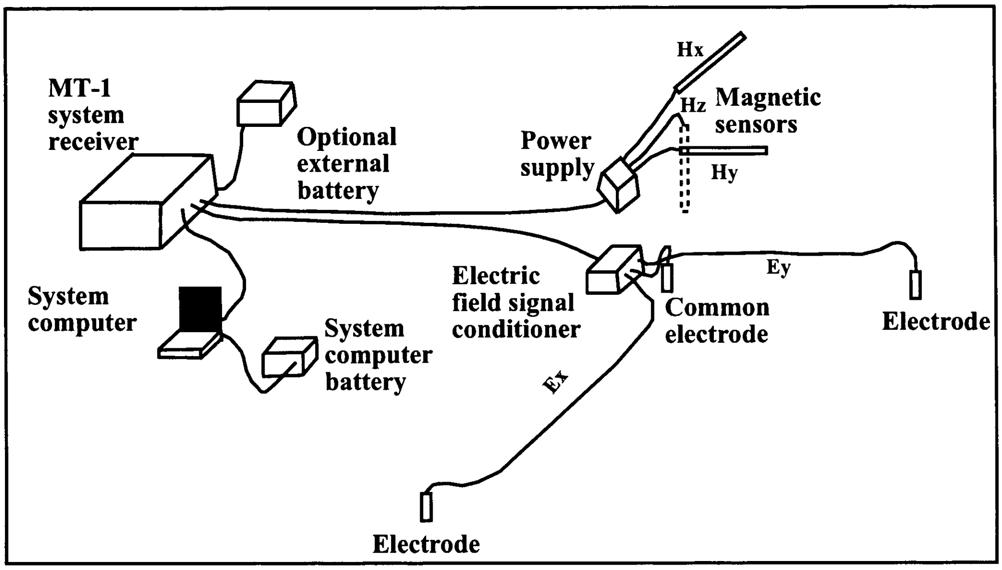

Figure 5.5: A schematic drawing depicting the EMI MT-1 magnetotelluric field equipment.

Several types of electrodes are commonly used in geophysics, and can be categorized into three groups (Petieau and Dupis, 1980; Vozoff, 1991):

(a) Metallic electrodes (brass and steel stakes), (b) graphite electrodes, and (c) non-polaisable (porous-pot) electrodes (typically made of copper, cadmium, silver, mercury, or lead rod in a supersaturated solution). Among these there are three types prepared for the EMI-MT1 system;

1) Titanium-alloy polarised electrodes. These are best suited for high-frequency electric field data acquisition and are easily driven into the ground. They do not oxidise, thus securing a good contact with the ground.

2) Lead-lead chloride $(Pb - Cl_2)$ electrodes. They posses excellent chemical stability and low DC drift which is useful for collecting long time series. They are preferred for low-frequency data acquisition.

3) Non-polarizable (porous-pot) electrodes. These have low DC drift rates and are generally adequate for most field applications.

In this study, non-polarizable electrodes were used for the electrical field measurements. They consist of metal rods (e.g. Copper, Zinc or Lead) immersed in a porous pot containing a saturated solution of their own salt $(Cu - CuSO_4, Cd - CdSO_4, Ag - AgCl, Hg - HgCl_2)$. This salt removes any sharp electrical contact resistance when the electrode is placed into the ground.

5.2.1.2 Magnetic field sensors

Three different types of sensors can be used for recording the magnetic field:

1- highly permeable induction coils or superconductivity quantum interface device (SQUID).

2- variometers with photoelectric feedback.

3- electron processing magnetometers.

The magnetic field sensors available for the EMI equipment were induction coils and SQUID. Each type of sensor has advantages and disadvantages. Induction coils are relatively noise-free but heavy while the SQUID magnetometer is easier to install and carry around because all three components are placed into a single device. However, the SQUID requires a good supply of liquid helium to provide the near absolute-zero temperature at which superconductivity is present which can be a severe limitation in some remote areas. In this study induction coils were used.

5.2.1.3 MT-1 Receiver

The MT-1 receiver is the central component of the MT-1 system (Fig 5.5). This unit accepts input from the sensors and performs the amplification, filtering, analogue to digital (A/D) conversion and the storage of time series. It also interfaces with the system computer and provides many automatic functions such as the recording of gains and the automatic setting of filters. The MT-1 receiver consists of three major components

(1) The signal acquisition board (SAB),

(2) The acquisition and processing unit (APU),

(3) The power source.

5.2.2 TEM instrumentation-Sirotem MK3b

The Sirotem equipment is an Australian built field. The system consists of transmitter and receiver components housed together and powered by two 12 v batteries; a central receiver box, external transmitter synchronisation and dual time-base facilities (powered by a SATX-1 high power transmitter for certain configurations) are also available along with the necessary cables and wire loop.

This instrument relies on EM induction where the magnetic field is transmitted into the ground via a current pulse in the form of a discrete, bipolar or square signal in a wire loop. This current pulse rises exponentially to produce a constant current, I, before it goes down linearly after turn off time, t_0 producing a ramp. The magnitude of I and t_0 is a function of the size and resistance of the transmitter loop. Maximum current output is normally 10 amps, and is regulated by loop wire resistance; an internal microprocessor regulates the current. A secondary magnetic field is generated due to the induced eddy current in the earth and can be measured in the form of a decay voltage response with time in the absence of a primary field (see section 3.2).

The received signal can be measured over up to 53 windows with the Sirotem MK3b; the interval length is defined by the time series and the number of windows selected. The Sirotem MK3b used in this study has four sampling time bands (Table 5.1); (1) composite band ranging from early times at 50 microseconds in window 1 to late times at 1.84 seconds in window 53; (2) early time band extending from 50 microseconds in window 1 to 384 milliseconds in window 53; (3) standard time which extends from 487 microseconds in window 1 to 1.94 seconds in window 50, and (4) High resolution band extending from 8 microseconds in window 1 to 92 microseconds. The Sirotem MK3b can be used for very shallow investigations but when the transmitter is turned off, the current takes a finite time to fall to zero equal to $L \times I / 24$, where L is the loop induction and I is the loop current. This means that the receiver cannot operate during this period and the early time windows may be lost. In a site where this problem is faced, an accessory heat sink device, known as the accelerator, should be used to reduce the ramp time to $L \times I / 400$ by allowing the turn-off voltage to rise to 400 volts. This permits the Sirotem receiver to measure much earlier times (about 16 times faster). The transmitter frequency is proportional to the total number of channels required to record the transient down to noise level for each time-base, but is commonly in the range of 1.4-250 Hz.

To minimize the noise as much as possible, the data can be stacked between 2^8 and 2^{11} (i.e. between 256 to 2048) times. The chosen number of stacks is a practical compromise between the acquisition time and the signal to noise ratio. By stacking n records, the signal to noise ratio improves according to $(n)^{1/2}$. The signal due to the positive and negative pulses were also averaged and considered to be one measurement stack to cancel the common noise and any DC bias. A notch filter is also provided for 50/60 Hz power line rejection. Four gain settings are provided; 0.1, 1,10 and, 100. It is important to choose an appropriate gain setting, since high gains increase the signal levels when noise levels are low, but too much gain can cause the input level to be exceeded in the early times. Lower gain settings may be necessary when early time signals are strong. In a routine field survey, multiple runs should be performed, each with different gain settings in order to choose the appropriate one. The output stacked voltage gives error statistics which can be of help for knowing the amount of errors and in deciding whether the sounding should be discarded, to select another one, or if the sounding should be repeated.

The Sirotem has a separate multi-turn receiver which can be used for central loop sounding and is useful for measuring both vertical and horizontal fields (three components). It has a fixed moment of 10000 m^2. In addition, the Sirotem can be used for deep exploration, and a transmitter current of up to 20 Amps can be achieved by linking a SATX-1 transmitter to the main Sirotem unit using high-stability oscillators.

5.3 Data acquisition

During March-April 1999 and July-August 2000, regional joint TEM and AMT surveys were carried out across the north-eastern and the south-eastern parts of the Parnaiba basin, Piaui State, Brazil. The first field survey was carried out on the N-S survey line (Parnaiba line) that extends from Parnaiba city on the Atlantic coast, into the hinterland for 95 km (Fig. 5.3). There are 14 observational stations with an average spacing of 7 km on this profile. The second field survey was carried out in the eastern part of Parnaiba basin using the same joint techniques; the survey consisted of three survey lines (M.Hipolito, Jaicos, and Itainoplis as shown in Figure 5.4). The Monsenhor Hipólito profile (line 1) is 64 km long with ten stations (9 stations measured in 2000 in addition to a site from previous survey in 1996) and an average spacing of 6.4 km. The Jaicós profile (line 2) is 23 km long and consisted of nine stations with an average spacing of 2.5 km. The Itainópolis profile (line 3) is 40 km long with ten stations spaced about 4 km apart. Note that data acquisition was hampered by numerous factors of which the obtaining permission for doing a sounding and financial constraints resulted in a wide station separation (e.g. 7 km for the northern profile). This study only focuses on the northern Parnaiba and Monsenhor Hipólito profiles which, for simplicity, were named PN and MH profiles respectively. The Jaicos and Itainoplis lines are the subject of another study.

Care was taken in selecting the sites where the MT and TEM data were collected. Generally; stations were selected away from power lines, pipelines, electric fences, radio transmitters, vehicular traffic, buildings and even pedestrian traffic. Natural features which might affect the fields (especially the electric fields) include abrupt topographic features such as sinkholes and pinnacles, small salt pools (Vozoff, 1991). Sites were thus selected

Windows number	Early time (ms)	Composite time (ms)	Standard time (ms)	High resolution (ms)
1	0.050	0.050	0.487	0.008
2	0.100	0.100	0.887	0.014
3	0.150	0.150	1.287	0.020
4	0.200	0.200	1.687	0.026
5	0.250	0.275	2.087	0.035
6	0.325	0.375	2.687	0.047
7	0.425	0.475	3.487	0.059
8	0.525	0.575	4.287	0.071
9	0.625	0.725	5.087	0.089
10	0.725	0.925	5.887	0.113
11	0.875	1.125	7.087	0.149
12	1.075	1.325	8.687	0.149
13	1.275	1.625	10.287	0.245
14	1.475	2.025	11.887	0.293
15	1.675	2.425	13.487	0.341
16	1.975	2.825	15.887	0.413
17	2.375	3.425	19.087	0.509
18	2.775	4.225	22.287	0.605
19	3.175	5.025	25.487	0.701
20	3.575	5.825	28.687	0.797
21	4.175	7.025	33.487	0.941
22	4.975	8.625	39.887	1.133
23	5.775	10.225	46.287	1.325
24	6.575	11.825	52.687	1.517
25	7.375	14.225	59.087	1.709
26	8.575	17.425	68.687	1.997
27	10.175	20.625	81.487	2.381
28	11.775	23.825	94.287	2.765
29	13.375	28.625	107.09	3.149
30	14.975	35.025	119.89	3.533
31	17.375	41.425	139.09	4.109
32	20.575	47.825	164.69	4.877
33	23.775	57.425	190.29	5.645
34	26.975	70.225	215.89	6.413
35	30.175	83.025	241.49	7.181
36	34.975	95.825	279.89	8.333
37	41.375	115.03	331.09	9.869
38	47.775	140.63	382.29	11.405
39	54.175	166.23	433.49	12.941
40	60.575	191.83	484.69	14.477
41	70.175	230.23	561.49	16.781
42	82.975	281.43	633.89	19.853
43	95.775	332.63	766.29	22.925
44	108.58	383.83	868.69	25.997
45	121.38	460.63	971.09	29.069
46	140.58	563.03	1124.7	33.677
47	166.18	665.43	1329.5	39.821
48	191.78	767.83	1534.3	45.965
49	217.38	921.43	1739.1	52.109
50	242.98	1126.2	1943.9	58.253
51	281.38	1331.0		67.469
52	332.58	1535.8		79.757
53	383.78	1843.0		92.045

Table 5.1: Recording times for Sirotem MK3b. Each value represents the middle of a recording window.

in areas that are sheltered from wind, and away from large trees and steep topography. Winds can degrade the data quality because the motion of the sensors and cables in the earth's DC magnetic field induce noise that is not easily differentiated from the signal from the motion of trees. In areas of steep topography, it is difficult to accurately layout electric field lines and becomes harder to orient and level magnetic sensors.

The TEM and MT soundings were centred on the same positions. The horizontal co-ordinates for each station were determined using a portable GPS receiver but the vertical resolution is not satisfactorily accepted and instead the station elevations were taken from the existing topographic maps.

The Sirotem MK3b system (as described in section 5.2.2) was used for the TEM soundings. Central-loop and single-loop TEM data were acquired at these sites using 50 or 100 m-sided transmitter loops depending on the geometrical constraints of the site. The time window band selected was either the high resolution (an accelerator was used when needed) or the early time series and the recording number of windows selected varied depending on the quality of data. Sferics effect (atmospheric disturbance) and noise originating from local main power supplies (60 Hz in Brazil) were rejected.

The MT recording consisted of the conventional five components (three magnetic and two electric fields). Three magnetic field components were recorded such that two were measured in the magnetic east-west and north-south directions, respectively dubbed the YX and XY polarizations. The other magnetic field component was recorded in the vertical direction. These induction coils were placed in shallow trenches and buried to eliminate wind vibration noise. They were accurately oriented and levelled such that there were no measurements of the significant component from the other directions. The electric dipoles were oriented in the magnetic east-west and north-south directions and were 50 or 100 m long depending on the site constraints. The non-polarized electrodes utilised were buried in shallow holes at the end of telluric lines to ensure temperature stability and protection from any other interference, and were kept moist at all times by placing mud inside the holes. At the same time, the telluric cables were kept fixed on the ground to reduce the effect of wind-induced disturbances. The contact resistance between each electrode pair (N-S or E-W) was checked before the measurement started. Values greater than 10 kΩ were not acceptable and effort was made to wet the ground to improve contact.

Previous MT investigations in the south-eastern part of the basin (Ulugergerli, 1998, and Meju et al., 1999) have indicated that the base of the sedimentary sequence could be resolved by MT observations at frequencies greater than 1Hz. This was also consistent with the theoretical depth of penetration of EM fields calculated from the skin depth equation and/or Bostick depth. However, the recording bandwidth was 0.01 to 176 Hz for the PN profile and each site was recorded overnight for repeatability. As high frequency EM data can be recorded much more quickly than low frequency data, the signals were not recorded simultaneously over the entire frequency band but were instead measured in three overlapping bands (band 3; 167-5.5 Hz; band 2; 12-0.3 Hz; band 1; 0.7-.0098 Hz). The recorded bandwidth for the eastern profile was 336 to 0.14 and recorded in two overlapping bands (band 1: 336-3.66Hz; band 2:13.45-0.14). Only band 1 was recorded at site 10 which was located on outcropping basement rocks.

The signal from each electrode pair is connected to a preamplifying and filtering instrument (electric field signal conditioner in Figure 5.5). This unit also isolates the input signal from the output signal to eliminate ground loops through the MT-1 receiver. Input signals to the signal acquisition board (SAB) are first passed through a differential amplifier to reduce common mode noise due to possible system ground loops. Following the front-end differential amplifier is a high-pass filter that eliminates DC voltage offsets. The resulting output is then passed through a first amplification stage. Once amplified, input signals are notch filtered at 60/50 Hz and 180/150Hz to minimise any noise associated with either the utility power grid or a nearby AC generator. A second amplification is applied to the filtered signals. After this amplification stage, the signals are routed to an anti-alias low pass filter and then a processing diversion occurs using Fast Fourier Transformation (***FFT***). A third and final amplification stage is applied to the signals. The APU executes all the acquisition and processing operations instructed by the user through the system computer. It controls the entire analogue and digital electronic processes applied to the input signals. This starts with arrival at the SAB and ends with the transmission of sampled time series data to the system computer for further processing and analysis.

After the signals are filtered and amplified, they are converted to digital time series. A Fast Fourier transformation is then performed on these time series and cross-power spectra are calculated for the various channels. The cross powers were then used in the computation of the MT interpretative parameters.

A total of 100 time series data windows were recorded for each band in order to minimize any noise errors and to get good quality data. In-field analysis enables a very quick appraisal of the data being collected, and involves converting the data into apparent resistivities, phases and other vital information as a function of frequency. A flow chart of MT data acquisition is shown in Figure 5.6.

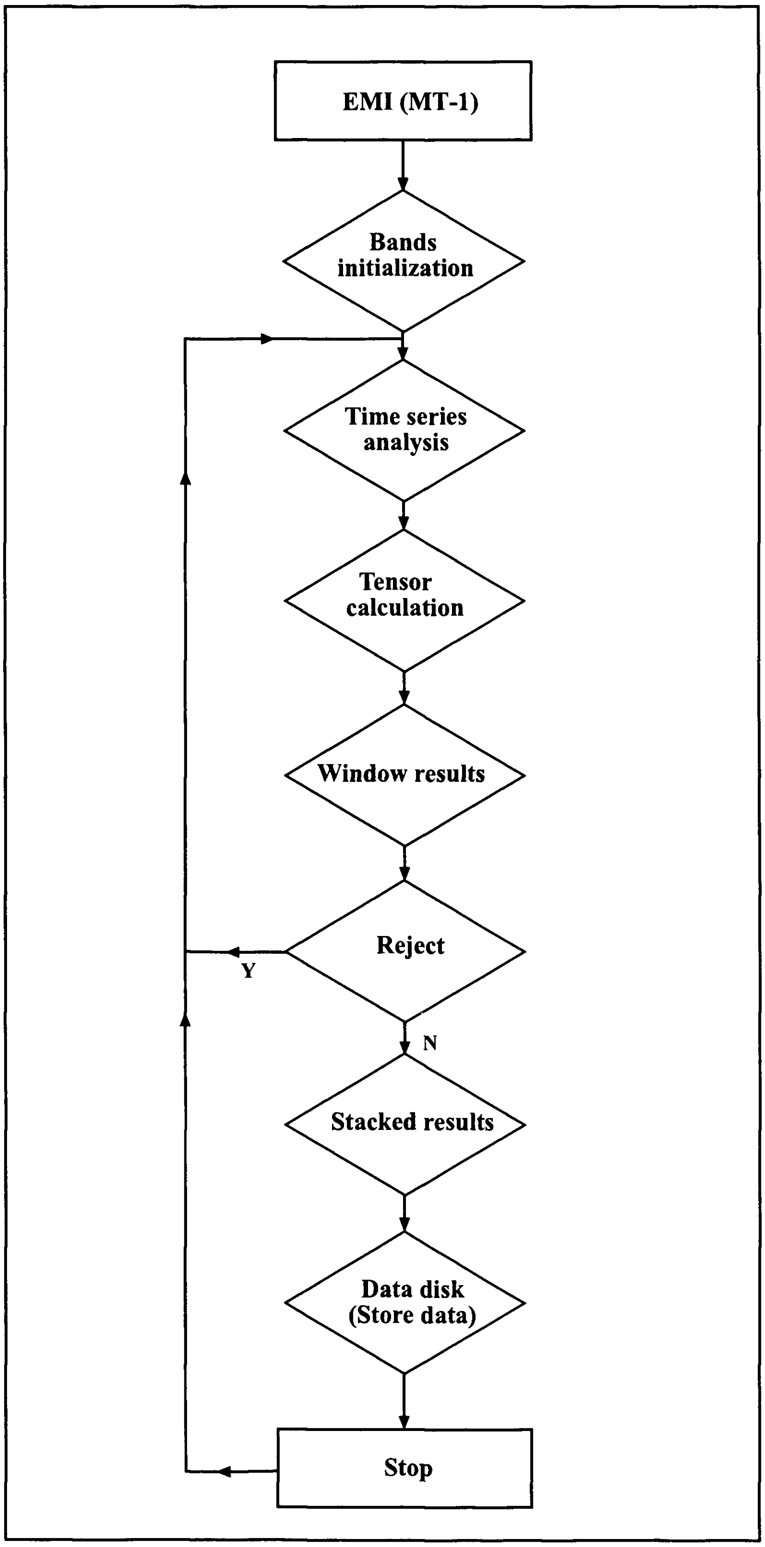

Figure 5.6: Simplified flow chart of the in-field system.

5.4 MT data processing

The reprocessing of MT data essentially involves the conversion of the time series recorded for the five electric and magnetic field components to give more accurate earth response functions such as the apparent resistivities and other qualitative and quantitative information. After the raw field data were originally filtered and amplified and stored in the form of time series, they were transferred to a personal computer for processing. The recorded time series were analysed using a software package (MTR93) developed by a commercial company, EMI. In the first step of the processing, the windows for time series were checked for acceptance or rejection. Accepted windows must have low noise. Coherence was found to be the most useful criterion for rejecting poor quality data window. However, at some locations, the noise level was either two high or the signal strength was too low to allow rigid acceptance criteria to be applied. After selecting the appropriate windows time series, Fast Fourier Transformation was performed and cross–power spectra were calculated for the five channels. Impedance tensor was obtained and several parameters were then computed as a function of frequency. They include the apparent resistivities and phases (un rotated, major and minor), the azimuth of the principal impedance axes, Swift skew values, and coherency. A typical example of the magnetotelluric data for the PN profile (station 2) is shown in Fig 5.7. The data presented are the apparent resistivity and the phase response along the measuring and principal directions with error bars, which are the standard deviations from the mean value. The coherency, the impedance skew and the Swift azimuth are also plotted. The MT response functions (resistivities and phases) show a continuous response in all frequencies. The data show a similar trend at high frequency (>10 Hz) in apparent resistivities in xy and yx directions and also with the major and minor responses; the phases also have the same shape in both directions. There is a good coherency between electric and magnetic components up to a frequency of 1 Hz, the Swift skew value is low (<0.12) and the azimuth is consistent around a value of -20^0 (except for the first few points). Note that the azimuth is measured from the magnetic north, which is 23^{0}W from the geographic north. Beyond frequency 1Hz, the response functions are relatively different in the two directions (xy and yx), the data are not highly coherent, the skew value is around 0.25, and the azimuth is not consistent. This may generally suggest a simple structure at shallow depth and become more complex as we go deeper. The data show small error bars particularly at high frequencies that increase at low frequencies but remain within a limited range, implying the collection of high quality data at this site.

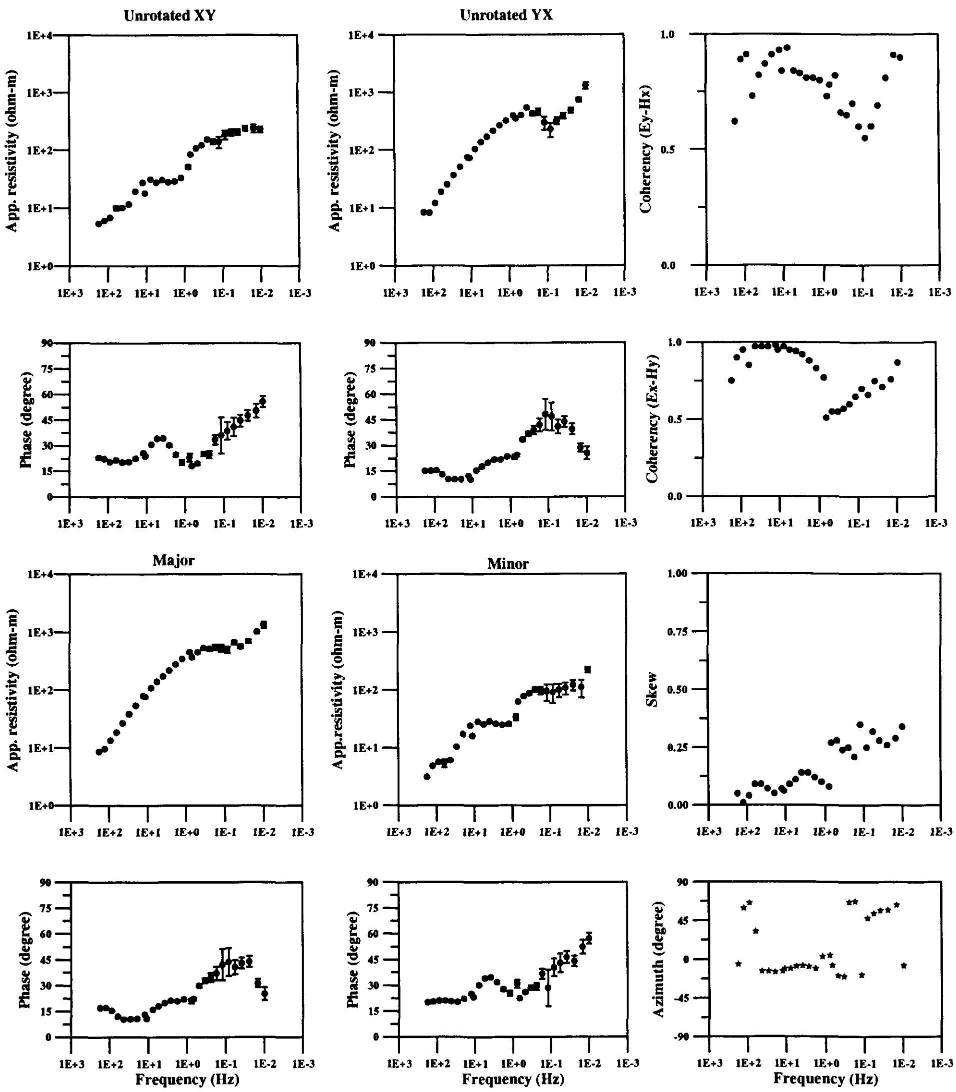

Figure 5.7: Response curves for station 2 from PN profile.

Figure 5.8 is a representative example for the MH profile (station MH3). All the parameters displayed show a continuous response at all frequencies. The response functions, especially apparent resistivities are consistent at high frequencies (>10Hz). The data are highly coherent up to frequency of 1Hz, with a low value of skew (<0.25) suggesting a simple structure. At low frequency (<1 Hz), the coherencies are below a value of 0.75 and the skew values are greater than 0.25. The values of Swift azimuth are continuous and increase linearly with decreasing frequency. These also indicate the complexity of structure at greater depths as expected from previous studies in Parnaiba basin (see Ulugergerli, 1998). The error bars are too small at all frequencies indicating the recording of high quality data.

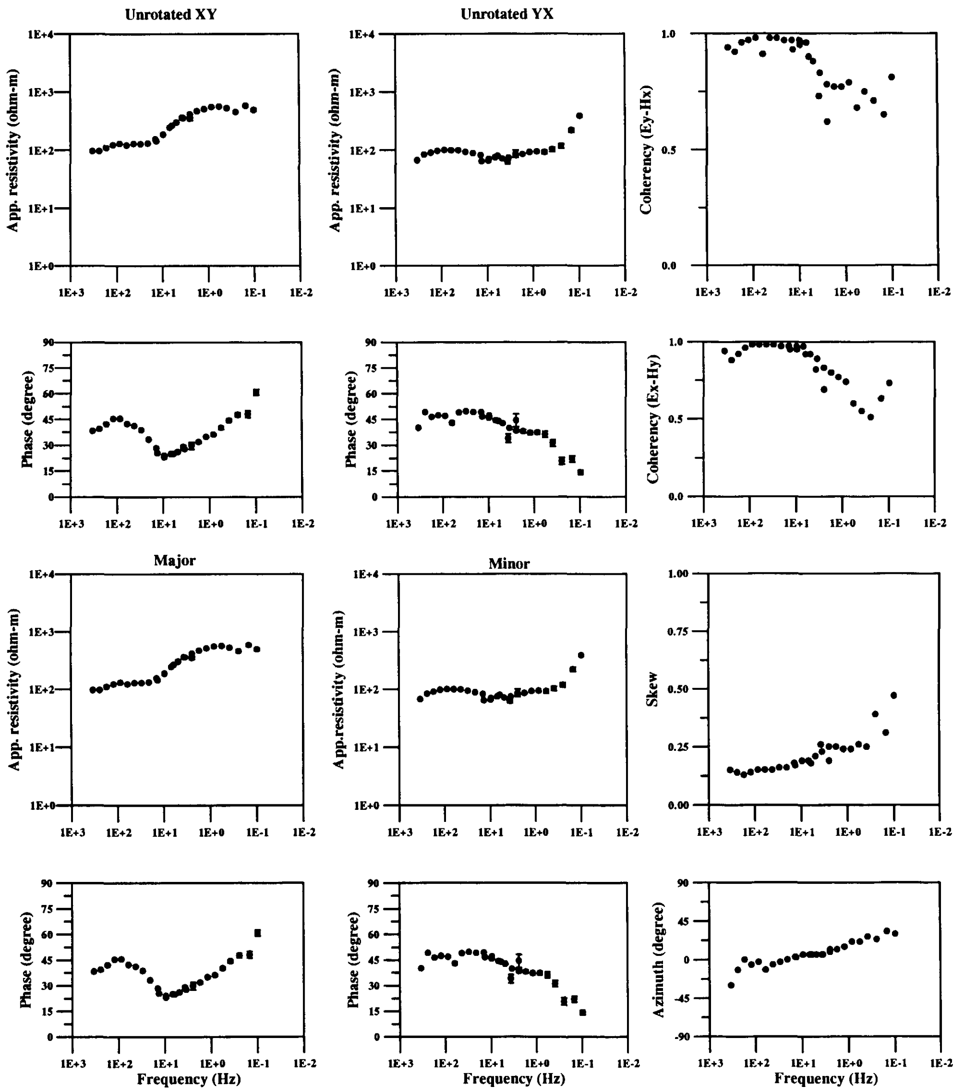

Figure 5.8: Response curves for station MH3 from MH profile.

5.4.1 Computation of induction arrows (sea coast effect)

The measurement of the vertical component can help in understanding the conductivity distribution. This can be performed by calculating the induction arrows. In the time domain, variations in vertical magnetic field may be related to variation in the horizontal magnetic fields by the equation (Parkinson, 1983; Hobbs, 1992)

$$z(t) = ax(t) + by(t), \quad (5.1)$$

where x, y and z represent magnetic field variations in north, east and downward directions respectively, and a and b are real numbers. In the frequency domain, equation 5.1 becomes

$$Z(w) = A(w)X(w) + B(w)Y(w), \tag{5.2}$$

where X, Y and Z are the Fourier transform of x, y and z. The quantities of A and B are complex with

$$A = A_R + iA_I \text{ and } B = B_R + iB_I. \tag{5.3}$$

These complex quantities may be combined to form the two-dimensional vector (A, B) called the magnetic response function. The real parts of A and B and the imaginary parts of A and B may be combined to form $\pm(A_R, B_R)$ and (A_I, B_I). These parts may be drawn as lines on a geographic map and can be termed induction arrows (Hobbs, 1992). These induction arrows either point towards areas of higher conductivity (Parkinson convention) or point away from areas of high conductivity (Wiese convention). The definition of induction arrows differs for Parkinson and Wiese as shown in Table 5.2. The real induction arrows magnitude may be indicative of a conductivity contrast, where the largest values are usually close to it and the smallest values are indicative of increasing distance from the boundary. Moreover, the direction of the conductivity gradient is often indicated by the azimuth of induction arrows. In a two-dimensional structure, conductivity anomalies often occur in the form of elongated features that extend a great distance in one direction. Near a truly two-dimensional structure both real and imaginary induction arrows point in the same direction for all frequencies (Parkinson, 1983). The direction of the gradient of conductivity or induction arrows can be drawn on geographic maps so that the arrows point at right angles to the current concentration in high conductive zone (Gregori and Lanzerotti, 1980). Imaginary parts are relatively smaller and show a frequency dependence markedly different from those of the real parts.

The induction arrows (Parkinson convention) were used in this study to detect the presence of linear zones of anomalous current concentrations in the subsurface, and to investigate if there is any coastal effect along the PN profile. Figure 5.9 shows examples of induction response calculated (real and imaginary parts) for station 3 on PN profile. In this figure, induction vectors seem scattered and there is no single consistent direction for both the real and imaginary data at all frequencies. This may suggest that the area has an increasingly complicated structure at depth.

The real parts of the induction arrows are selected at two frequencies (8 Hz and 40 sec) sampling different depths and they are superimposed on the known geological features along profile PN in Figure 5.10. The difference in the magnitude and azimuth of the

Convention	Real arrow		Imaginary arrow	
	Magnitude	Azimuth	Magnitude	Azimuth
Parkinson	$\sqrt{A_R^2 + B_R^2}$	$\pi + \arctan\left[\frac{B_R}{A_R}\right]$	$\sqrt{A_I^2 + B_I^2}$	$\arctan\left[\frac{B_I}{A_I}\right]$
Wiese	$\sqrt{A_R^2 + B_R^2}$	$\arctan\left[\frac{B_R}{A_R}\right]$	$\sqrt{A_I^2 + B_I^2}$	$\arctan\left[\frac{B_I}{A_I}\right]$

Tale 5.2: The definition of induction arrows from Parkinson (1959) and Wiese (1962) convention.

induction arrows for both frequencies suggests the presence of lateral and vertical variations in subsurface resistivity. However, some other interesting deductions can be made from this figure. At low frequencies, the so-called coast effect (e.g. Lilley and Bennett, 1972) appears to influence the measurements at the first four stations from the coastline; but interestingly at the high frequencies (>1 Hz), only the induction arrows for the two northernmost sites point toward the coast which may indicate that the coast effect at shallow depth is restricted only to the first two sites. The induction arrows at high frequency point towards the northeast at stations 12, 13 and 14, indicating the presence of a linear NW-SE trending conductive zone in this region. This may indicate the presence of a concealed fault-zone, or it may be the effect of the linear outcrop of the marine Pimenteiras Formation that is known to be conductive (see Meju et al. 1999, Fig. 2). This response pattern does not persist at low frequencies which may suggest that the causative body does not extend to great depths.

5.4.2 Application of tensor decomposition techniques

The presence of charges or galvanic distortion in magnetotelluric data can lead to the misinterpretation of the measured impedance tensor, so it is vital to separate the galvanic effects from induction responses within the data. Bahr (1988) and others (Groom and Bailey, 1989; Groom and Bahr, 1992) attempted to separate regional and local information by means of tensor decomposition using a physical model. In their approach, they assumed that the inductive response is restricted to regional 1D or 2D body with an overlying inductively-small local body on a regional host, where the distortion of telluric and magnetic fields by inductively weak bodies are negligible. However, the conductivity structure might be more or less complex than assumed. For this reason, Bahr (1991) has showed that this method could be employed only if the data satisfy certain conditions which they categorized into seven classes of general model of increasing complexity (see section 2.7). Thus in order to evaluate the necessity of applying Groom and

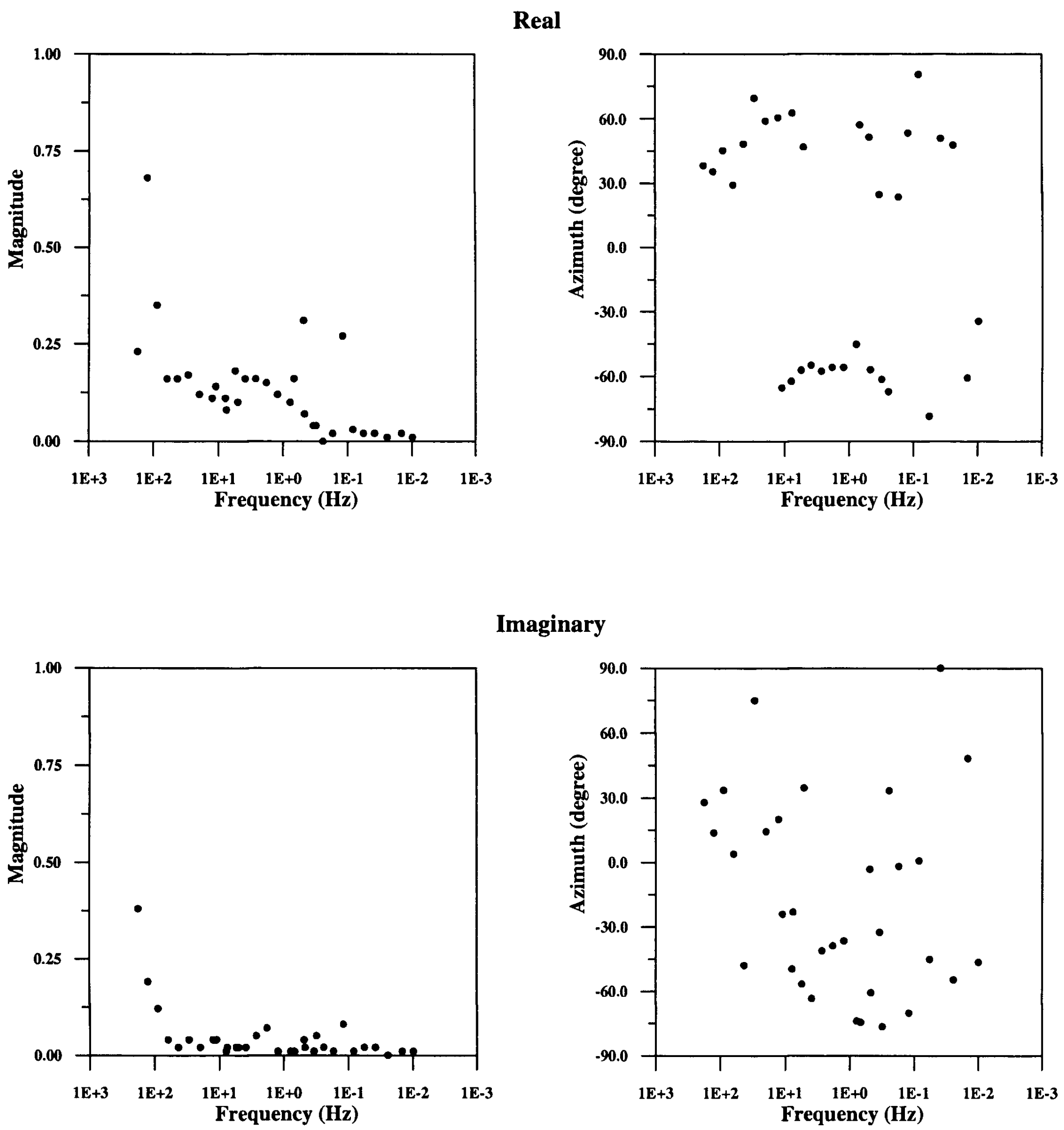

Figure 5.9: Parkinson induction arrows computed at station 3 (PN profile).

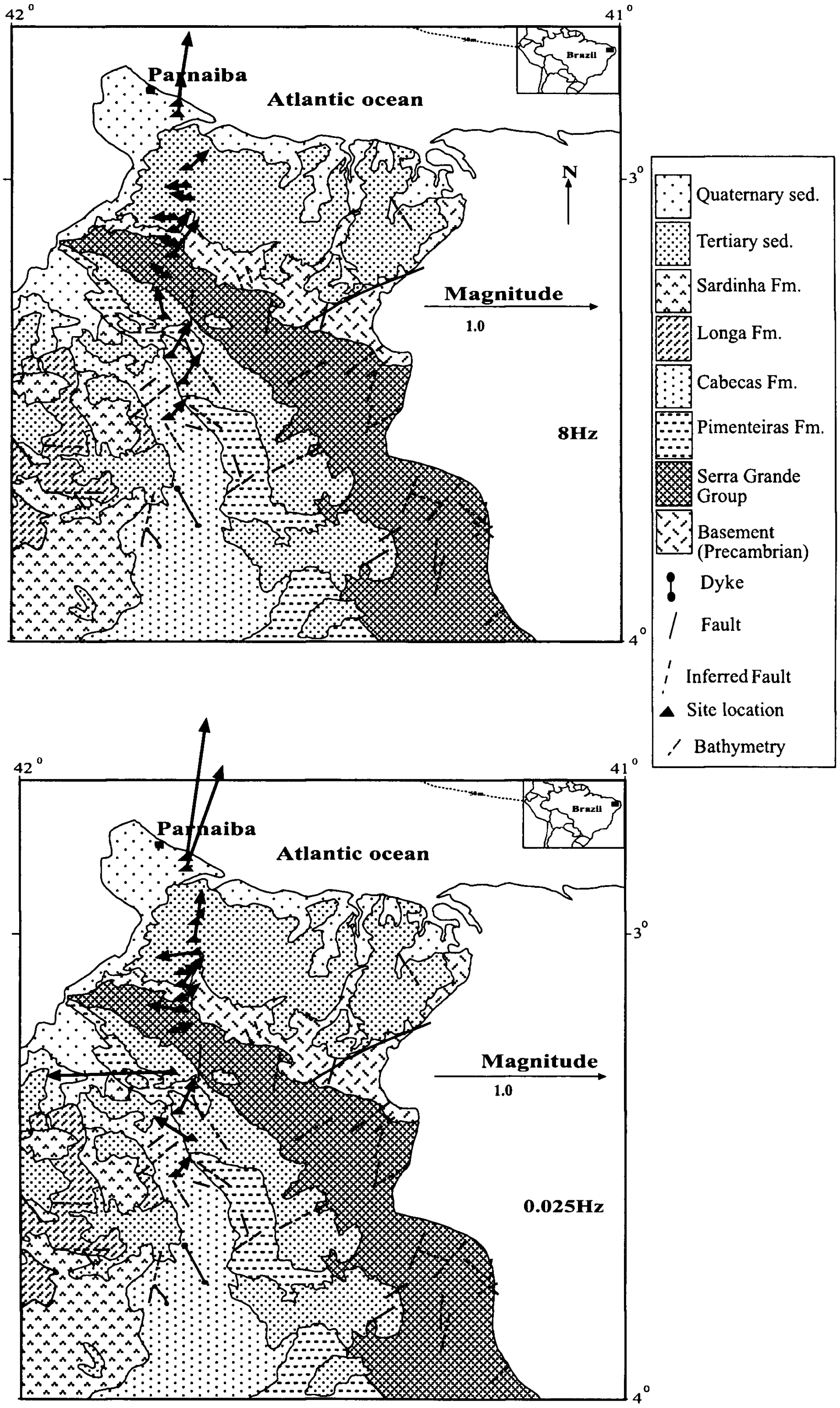

Figure 5.10: Real component Parkinson induction arrows for two frequencies superimposed on the geological map for comparison.

Bahr classes			
Station	Band 1 (176-5 Hz)	Band 2 (5-0.3 Hz)	Band 3 (0.3-0.0098 Hz)
1	1	2	7
2	1	2	7
3	1	1	7
4	1	1	7
5	1	7	7
6	1	7	7
7	3	2	7
8	1	7	7
9	1	1	7
10	7	7	7
11	3	7	7
12	1	1	7
13	1	1	7
14	1	1	7

Table 5.3: Summary of results of analysis of the PN profile using the Bahr (1991) method for seven classes of telluric distortion.

Bahr classes		
Stations	Band 1 (336-3.4 Hz)	Band 2 (3.4-0.147)
Site 1	-	-
Site 2	7	1
Site 3	3	7
Site 4	1	1
Site 5	3	7
Site 6	1	7
Site 7	7	7
Site 8	3	7
Site 9	3	7

Site 10	7	-

Table 5.4: Summary of results of analysis of the MH profile using the Bahr (1991) method for seven classes of telluric distortion.

Bailey (1989) tensor decomposition of the Parnaiba basin, the data at each station were first analysed using Bahr classes (1991). The data at each frequency were grouped into one of the seven-classes. Then the average value for each band was calculated. Tables 5.3 and 5.4 respectively give the summary of the results of this analysis for PN and MH profiles.

Some interesting points relating to the nature of the induction problem arise from this analysis. In the PN profile (Table 5.3) and at the high frequency band, most of the sites (10 sites) fall into class 1; the remaining three sites were categorized into higher classes which are class 3 (characterizing an area of weak local distortion) for two sites and class 7 for the other. This indicates that the tensor can be described mostly by the conventional method.

The data measured in frequency band 2 show fluctuations between classes 1,2 and 7, suggesting a 2D/3D regional conductivity structure. In the low frequency band (band 3), the data fall mainly into class 7 suggesting that Z describes a regional 3-D conductivity anomaly, for which the superimposition model is not appropriate. For the MH profile, Table 5.4 shows that in the high frequency band, the data fall into classes 1, 3, and 7 suggesting an approximately 2D regional structure with weak local distortion. In the low frequency band, the data suggests a mainly 3D regional conductivity structure for which it is not valid to apply the Groom-Bailey decomposition. Nevertheless, if the decomposition methods yield a regional strike that is coincident with the regional strike of neighbouring sites, then the regional structure can be considered to be approximately 2-D (Groom and Bailey, 1989; and Bahr, 1991).

In order to demonstrate the decomposition of Groom-Bailey, data sets from 2 sounding sites (station PN12 on the PN profile and MH9 on the MH profile) were selected as shown in Figures 5.11 and 5.12. Station PN12 is chosen because of its close location to an expected concealed fault that may possibly represent the northern margin of Parnaiba basin. Station MH9 (MH) is located near the contact between the basement and sedimentary rocks and also shows that the impedance tensor has been distorted (class 3 at high frequency). In both figures, the observed data, predicted data, and the principal axes response are presented in the form of Cagniard apparent resistivity. The upper part in the left hand side illustrates the results of unconstrained decomposition, while in the lower part of the diagrams, the regional strike has been constrained to -30^0 for station PN12 (Fig. 5.11) and to 30^0 for station 8 (Fig. 5.12). The reason for the selection of these angles to constrain the data was based on the dominant strike direction and also the lithologic trend in both profiles (a more detailed explanation of the selection of the strike angle is presented in the next section). The distortion parameters (shear and twist) and the regional strike (from the Groom-Bailey and Swift methods) are also plotted on the extreme right hand side. As shown in these figures, and due to the complicated structure in both profiles, the dominant strike direction rotates from higher to lower frequency, or from shallower to deeper structure. The difference between the observed and decomposed data were insignificant at high frequency. This may be due to the decomposition method requiring certain conditions such as a strong 2D host and 3D scatterer which may not be the case at these sites. However, differences become more significant for both stations (particularly phase) at low frequency for which the data have been categorized into class 7, and the superimposition model of Groom-Bailey was no longer valid. A possible 3-D regional structure (class 7 for all sites at low frequencies) makes the physical model of Groom-Bailey unwarranted and could lead to erroneous results. Moreover, the presence of static shift which is not resolved by physical decomposition, may not help in recovering any more reliable decomposed data. In the light of these results, it was decided that the Groom-Bailey decomposition process was not necessary in this study. Interestingly, the Groom-Bailey decomposition was applied for the previous MT profile located near Picos city in Parnaiba basin (Ulugergerli, 1998) and it did not work.

5.4.3 Geoelectric strike determination

In the magnetotelluric method, it is critical to define the dominant regional trend, as any error in the rotation of the data will cause the TE and TM responses to be mixed. There are many approaches developed to obtain the regional geoelectric strike (e.g. Swift, 1967; Bahr, 1988; and Groom and Bailey, 1989). The Swift method does not take into account noise and local distortion and therefore may not give accurate results in the presence of the effect of static shift to the data. The Bahr and Groom-Bailey methods have been developed to overcome such distortion problems.

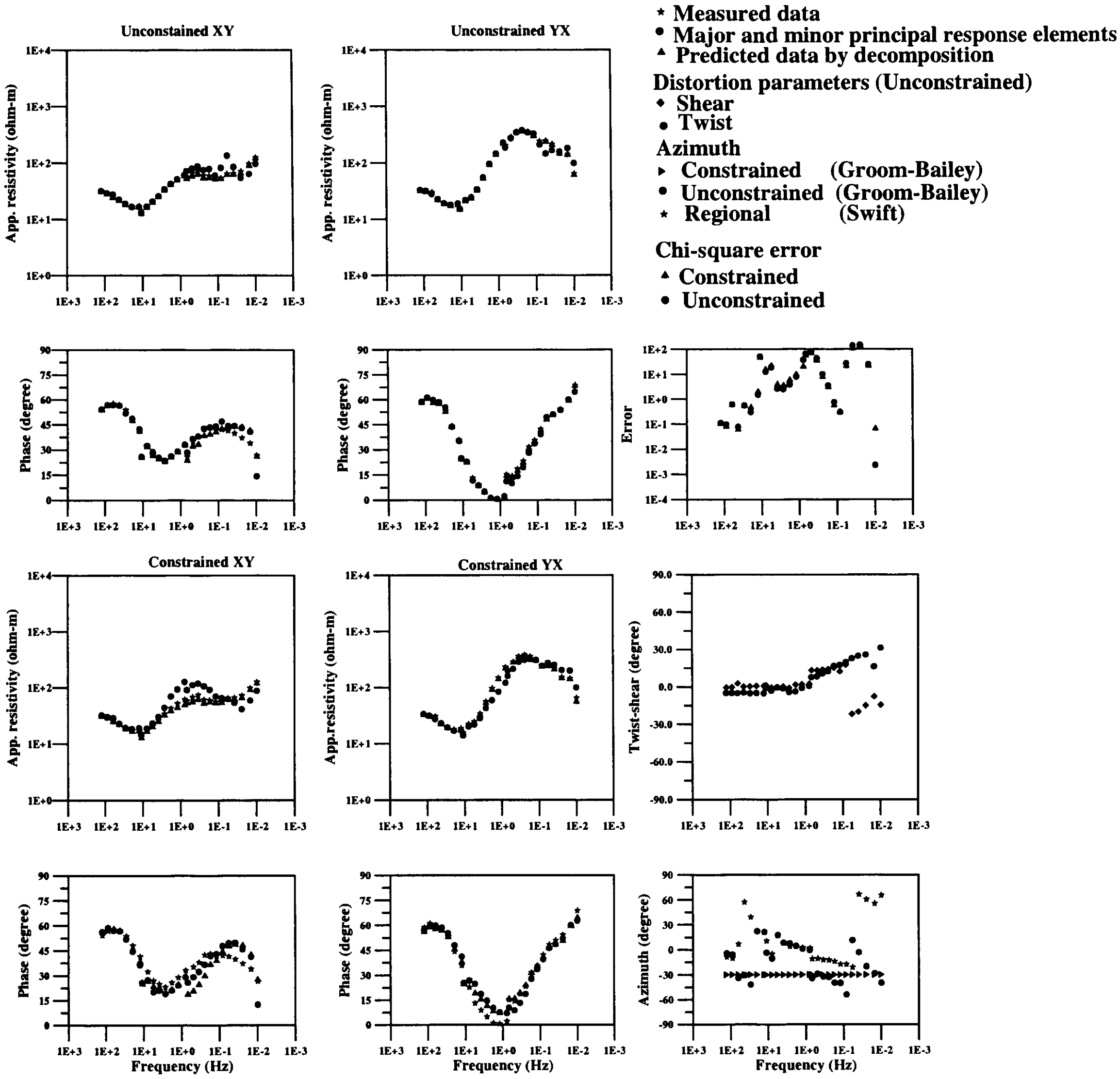

Figure 5.11: MT parameters obtained by using the procedure of Groom-Bailey (1989) for site 12 on the PN profile.

In this study, the regional azimuths were obtained using the Swift method and an unconstrained Groom-Bailey decomposition at each station (see appendix A.1 and B.1). However, since conductivity anisotropy may exist and the gross structure is most likely complex particularly when three dimensionality enters and local 3-D distortion and noise are present, surface geological information may be needed to assist in determining the dominant structural strike.

In an effort to estimate the dominant strike direction in both profiles, the regional azimuths were calculated and plotted on the geological map at representative frequencies using an unconstrained Groom-Bailey decomposition technique which accounts for distortion effects and is considered to be more convenient than the Swift method. Figures 5.13 and 5.14 show the azimuths of Groom-Bailey decomposition for both profiles. For

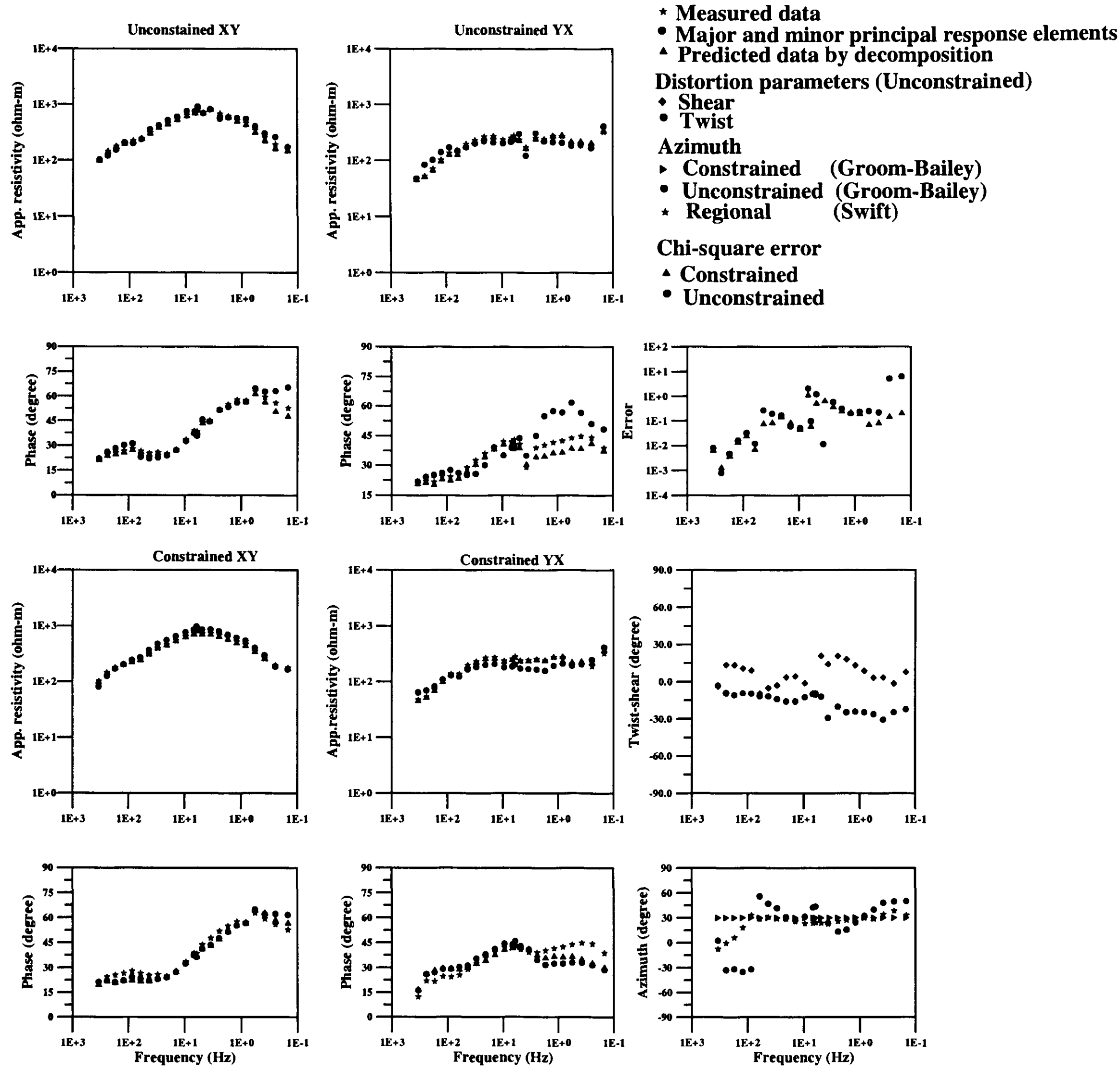

Figure 5.12: MT parameters obtained by using the procedure of Groom-Bailey (1989) for site MH9 on the MH profile.

the PN profile, the Groom- Bailey strike is plotted for four characteristic frequencies (32 Hz, 8 Hz, 0.5 Hz, and 0.025 Hz). It was found that the dominant strike is approximately WNW-ESE at most of the sites which is closely consistent with the lithological trend. On the other hand, the computed azimuths at some selected frequencies along the MH profile (30Hz, 8Hz, 0.5Hz, and 0.25 Hz; Fig. 5.14) suggest two dominant strikes trending NNE-SSW and NNW-SSE. The main geologic units in the area trend nearly NNE. Overall, it has been observed that there is a consistency in the azimuths obtained from Swift and Groom–Bailey at some sites at most frequencies for both profiles (see Appendices A and

B, taking into account that there is $\pm 90^0$ ambiguity in strike direction). These figures show that the dominant strike is nearly -30^0 for the PN profile and 30^0 for the MH profile.

In the light of these investigations, the MT data were rotated -30^0 from the measurement direction (i.e. -53^0 from the geographic north since the declination is 23^0W) for the PN profile yielding the TE and TM mode data required for 2-D modelling; while the data for the MH profile were rotated 30^0 from the measurement direction yielding the TE and TM modes along approximately north-south and east-west geographic directions, respectively.

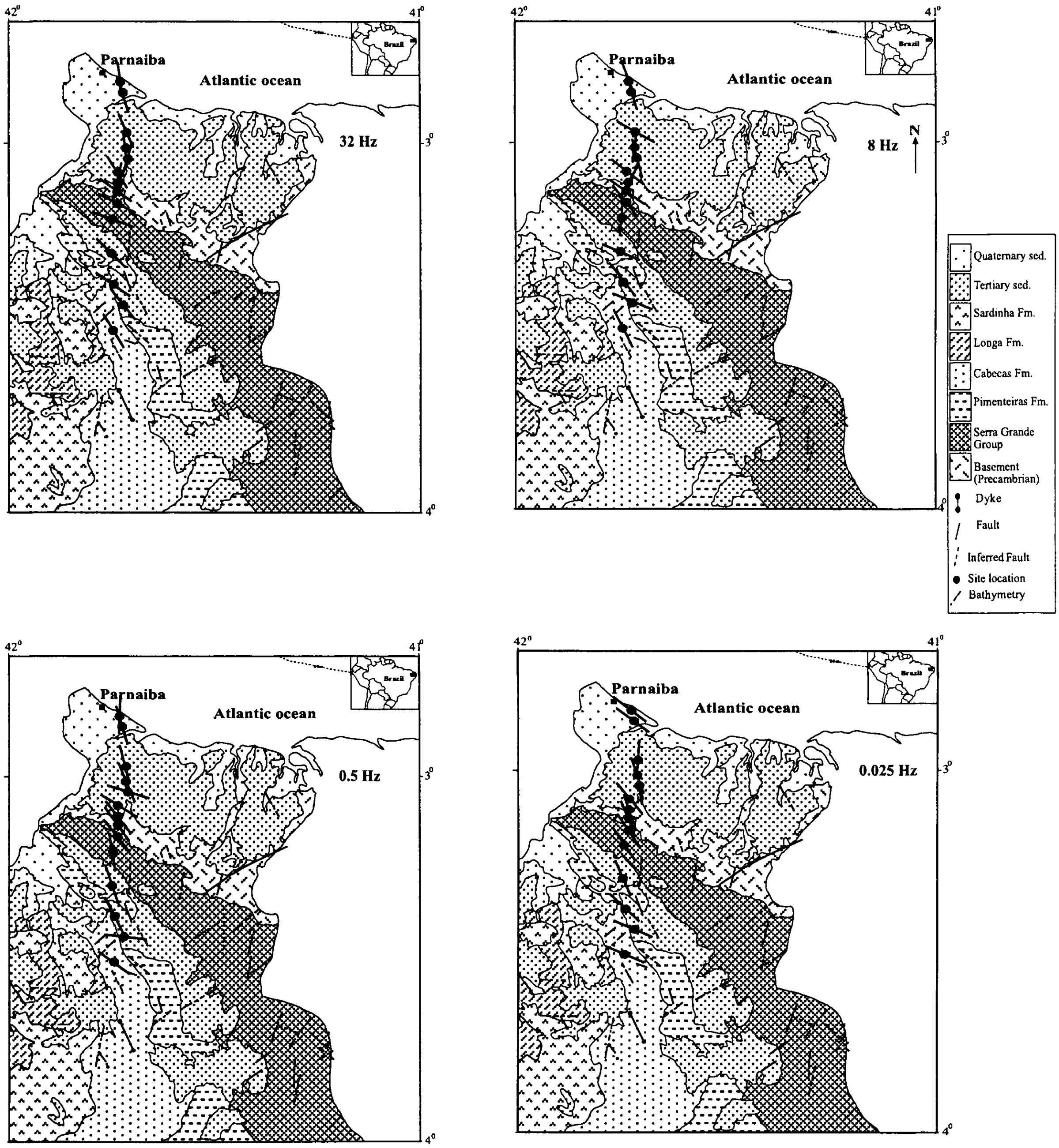

Figure 5.13: Regional azimuth defined using the unconstrained Groom-Bailey (1989) decomposition from four selected MT frequencies along PN profile.

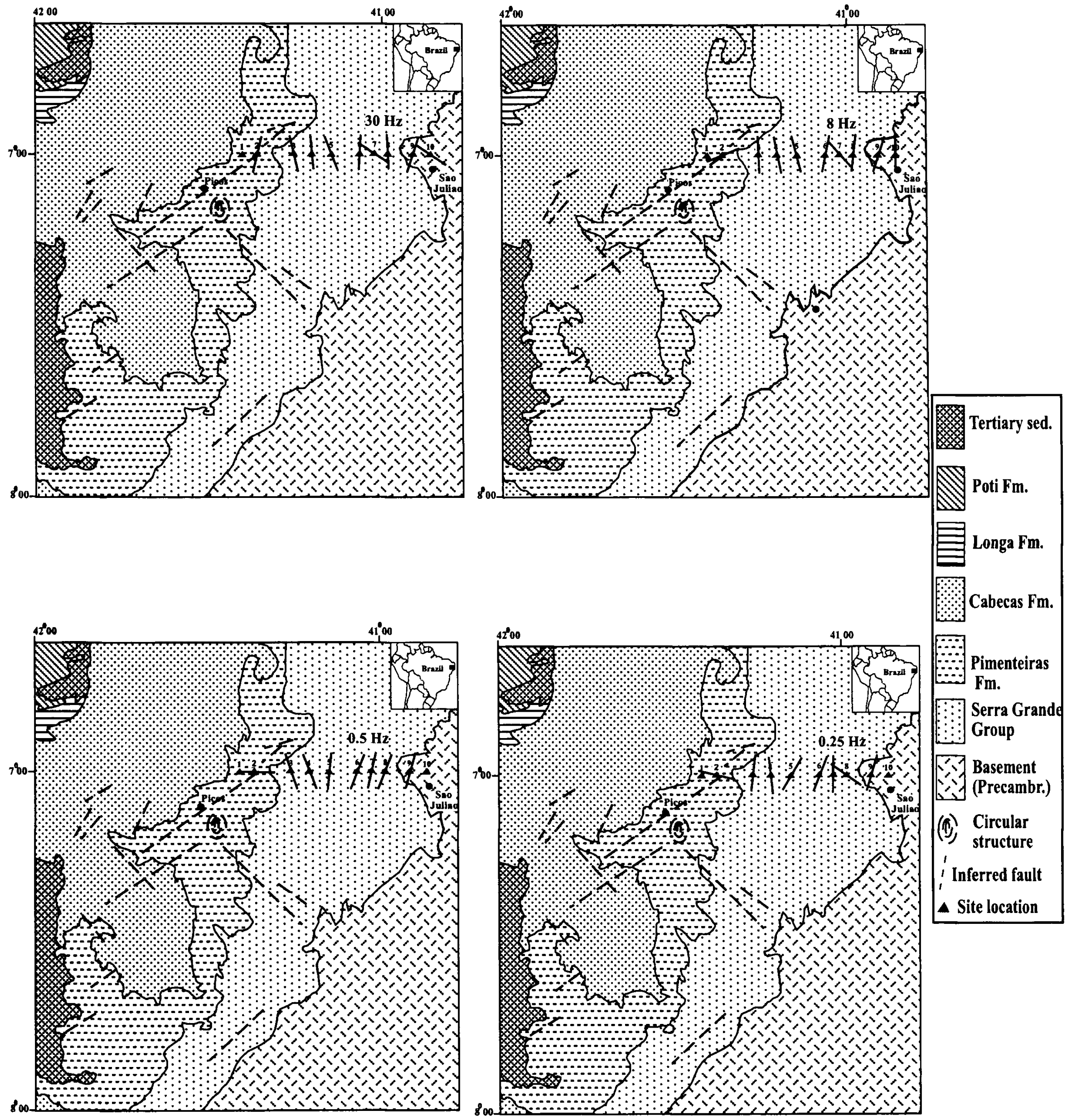

Figure 5.14: Regional azimuth defined using the unconstrained Groom-Bailey (1989) decomposition from four selected MT frequencies along MH profiles.

5.4.4 Static shift correction

Small-scale inhomogeneities can shift the magnetotelluric apparent resistivity data vertically. This effect is called static shift (see section 2.7.1). Several methods have been suggested for correcting MT data for this effect, but none of these techniques has proven to work consistently in every geological environment (Groom and Bahr, 1992). The most reliable method is based on the use of independent data set provided by a complementary induction method that uses the magnetic field (Larsen, 1977). Studies have shown that

TEM data are well suited for static correction (Sternberg et al., 1988; Pellerin and Hohman, 1990; Meju, 1996; Meju et al., 1999).

In this study, the MT data have been corrected using TEM data. Following Meju et al. (1999, Fig. 6), the TM mode MT apparent resistivity curves were corrected using the single-loop TEM data while the TE mode apparent resistivity curves were corrected using central-loop data. However, some single loop TEM data were very noisy at some stations and also strongly affected by IP effect at late times; in these cases only the central loop data were used. This is in addition that the strength of the induced voltage response is highest in the centre of the loop and less affected by lateral variations. Representative examples of the MT and TEM data are shown in Figures 5.15 and 5.16 for PN and MH profiles, respectively. The MT data are shown (without error bars for simplicity) with the TEM data in these figures. The MT curves show a parallelism with some vertical shift in the overlapping segments. This may indicate shallow 1-D features, and that the MT curves were affected by static shift. The MT resistivity data were shifted upward or downward to match the relevant TEM curve and the MT error bars were eventually multiplied by the correction factor. These figures also show that the TEM data are coincident with the MT resistivity curves at some sites (e.g. site PN13 and MH2) for which there is no need for static shift corrections. Notice in Figure 5.16 that MT data for site MH5 are affected by static shift and both TM and TE modes were corrected (using only central loop TEM data) because the single loop data were very noisy. Some of TEM data showed negative response at late times and these data channels were deleted such that there is no overlap between the TEM and MT sounding curves (see appendix A.2 and B.2). However, since the area exhibits shallow 1-D conditions, non-overlapping TEM data may suffice for MT static shift correction (see Meju, 1996).

5.5 Qualitative interpretation of the MT data

After rotating and correcting the data for static shift, they were prepared for interpretation. Qualitative interpretation is typically the first stage of any interpretation, and can provide prior information prior to modelling. This section gives a brief description of the quality of the MT data followed by presentation of pseudosections.

At high frequencies (up to 10 Hz), the quality of data based upon the smoothness of data points, the size of error bars, and the coherency between electric and magnetic fields

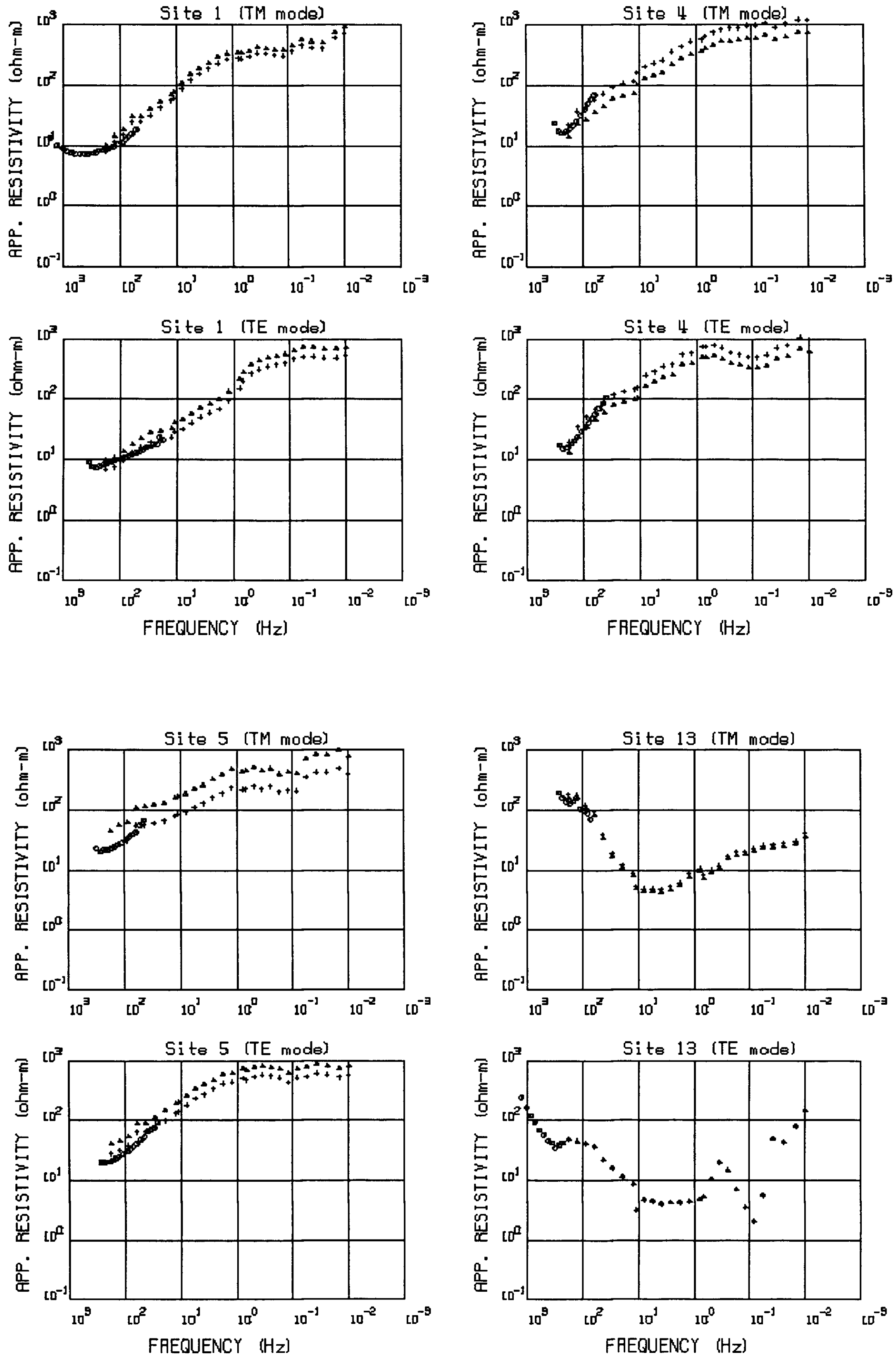

Figure 5.15: Sample illustration of MT data before (triangular ornaments) and after (cross symbols) static correction for four stations along the PN profile.

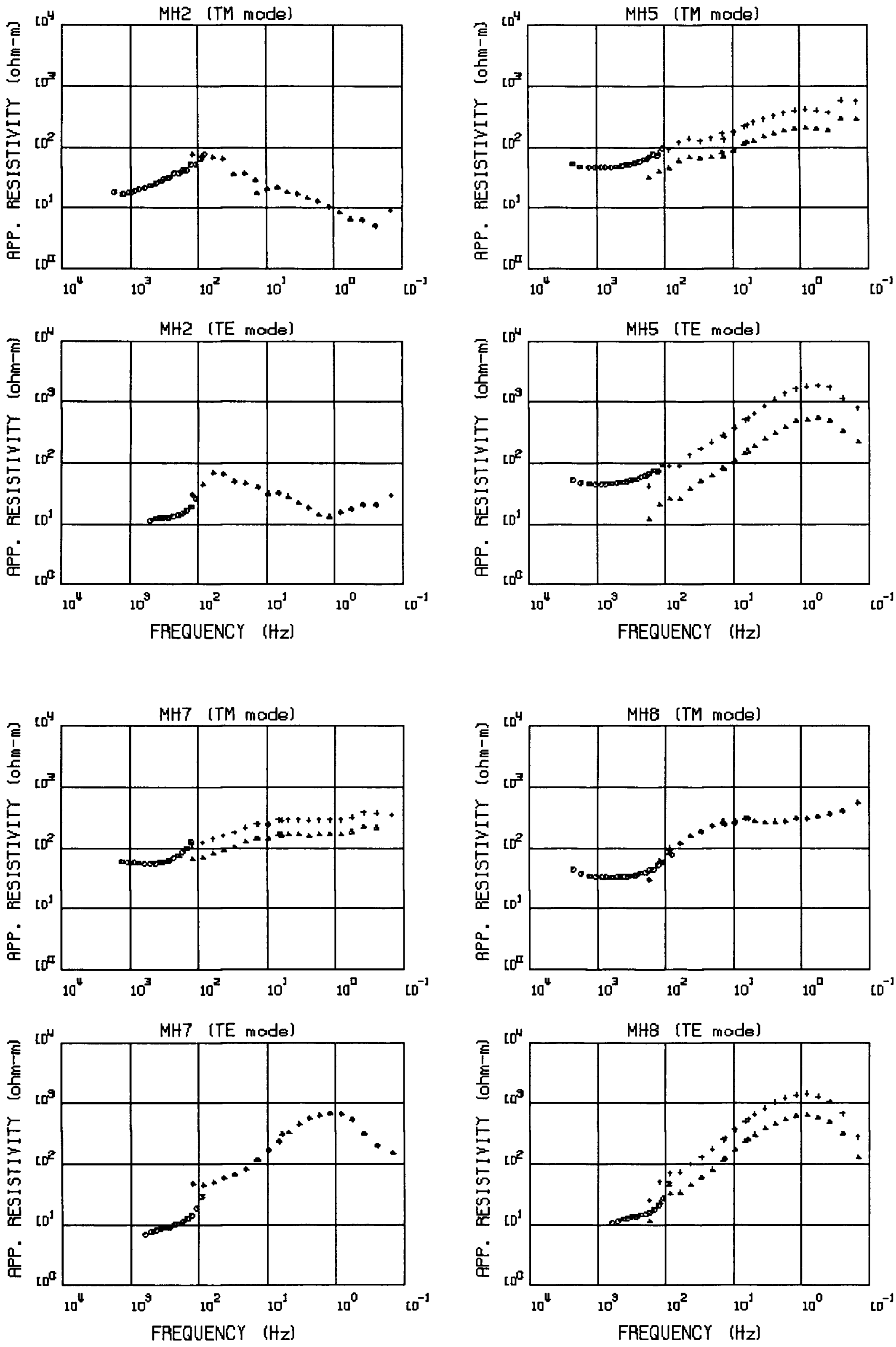

Figure 5.16: Sample illustration of MT data before (triangular ornament) and after (cross symbols) static correction for four stations along the MH profile.

is generally good at most of the sites, particularly along MH profile (Appendix A.1). The trends of apparent resistivities and phases of the principal directions are similar, suggesting the presence of shallow 1-D conditions. This is emphasized by skew values with an average of 0.2. At low frequencies, the quality of data appears relatively more scattered and noisy. At many stations the apparent resistivity curves are anisotropic, the phase data are different in the two principal directions and the skew values increase to more than 0.4, suggesting a 2- or 3-D environment. Figures 5.17 and 5.18 show pseudosections of the TM and TE mode responses for the two profiles. These pseudosections are important and illustrate the lateral changes in conductivity distribution with frequency. Note the lateral and vertical variations of apparent resistivity and phase in both TM and TE modes. The PN profile can be classified into three zones: moderately resistive zone (site1 to site 5), highly resistive zone (site 6 to site 8) and less resistive zone (site 9 to the end of the profile). For the MH profile, there are also lateral and vertical resistivity and phase variations in both modes; the eastern part appears more resistive than the western part. There is an obvious change in resistivity and phase responses between stations MH8 and MH9 in both modes, and a conductive zone is also shown at low frequency underneath stations MH1 and MH2. More information can be obtained by quantitative interpretation and modelling of data as shown in chapter 6.

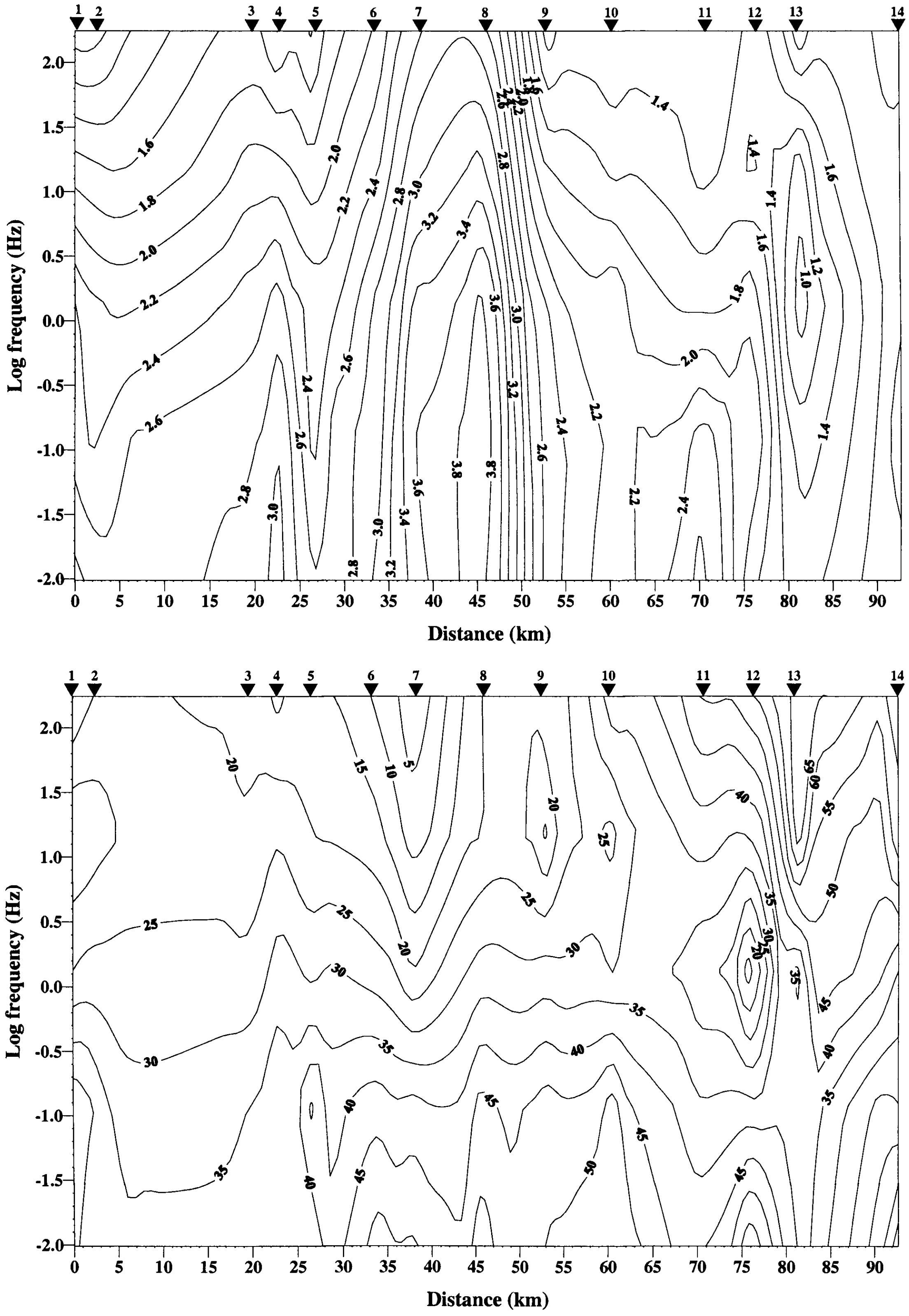

Figure 5.17a: Pseudosections of shifted apparent resistivity and impedance phase of TM mode for PN profile. The apparent resistivity values $(\Omega.m)$ have been contoured on a logarithmic scale. The phases are in degrees.

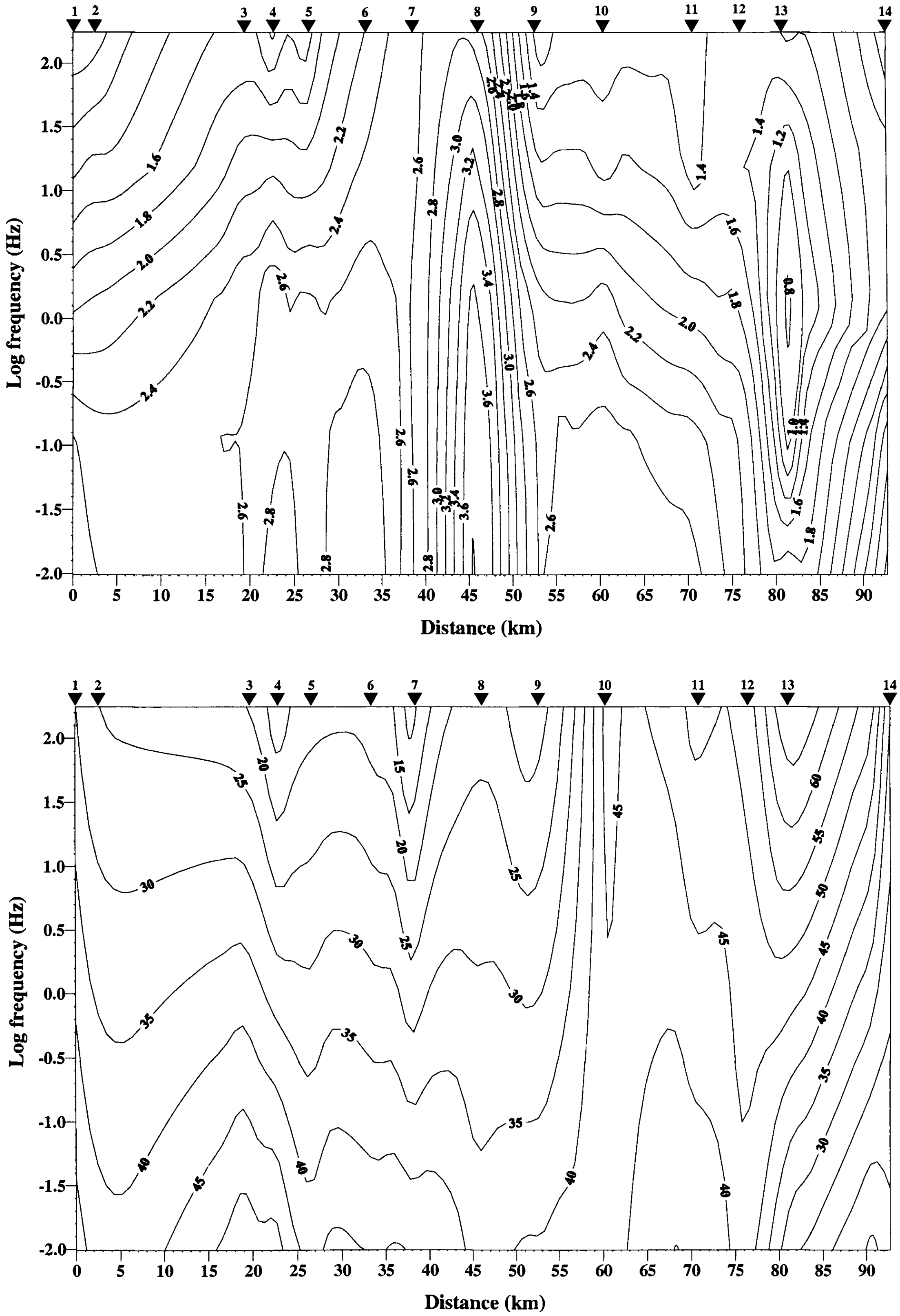

Figure. 5.17b: Pseudosections of shifted apparent resistivity and impedance phase of TE mode for PN profile. The apparent resistivity values ($\Omega.m$) have been contoured on a logarithmic scale. The phases are in degrees.

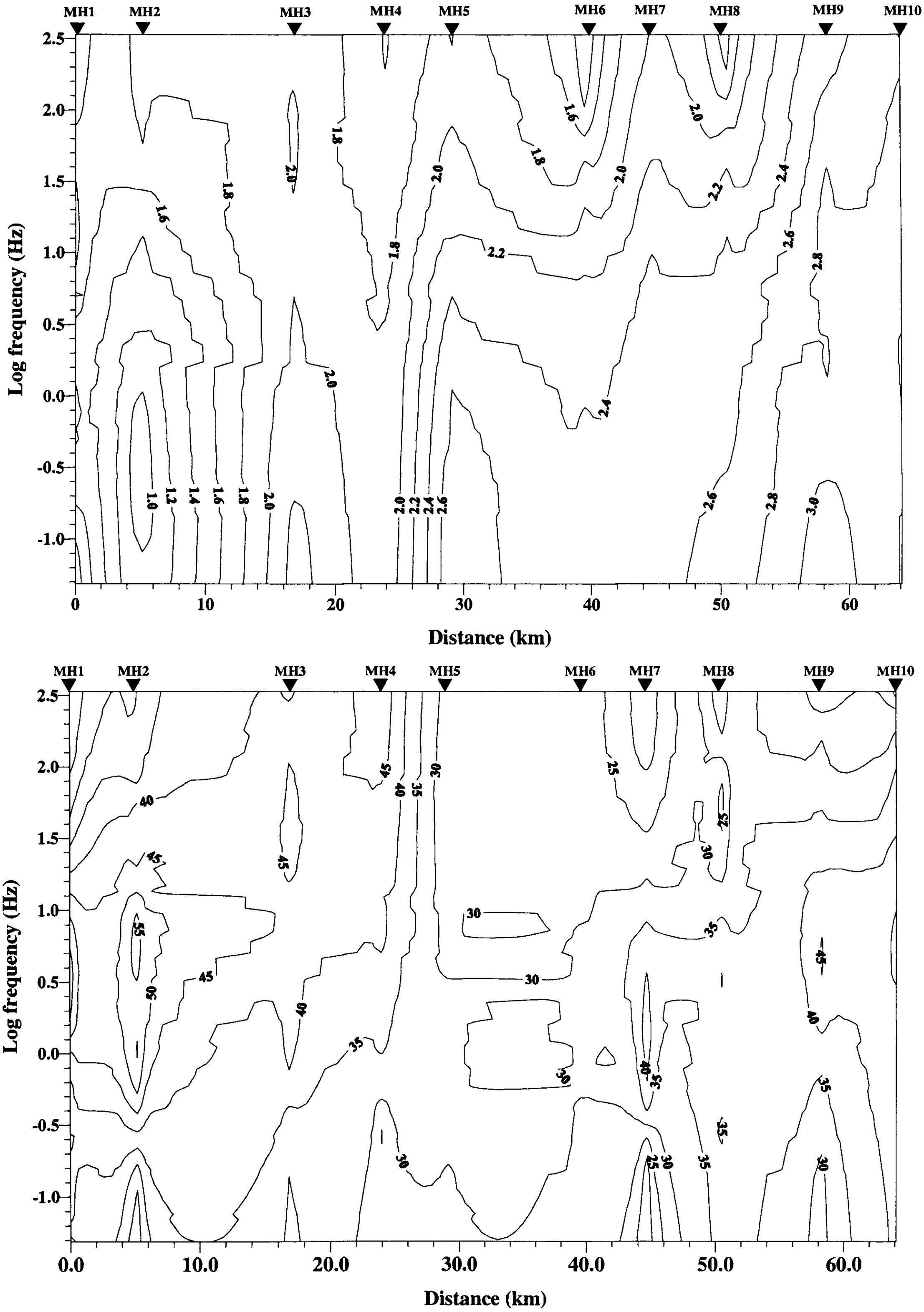

Figure 5.18a: Pseudosections of shifted apparent resistivity and impedance phase of TM mode for MH profile. The apparent resistivity values ($\Omega.m$) have been contoured on a logarithmic scale. The phases are in degrees.

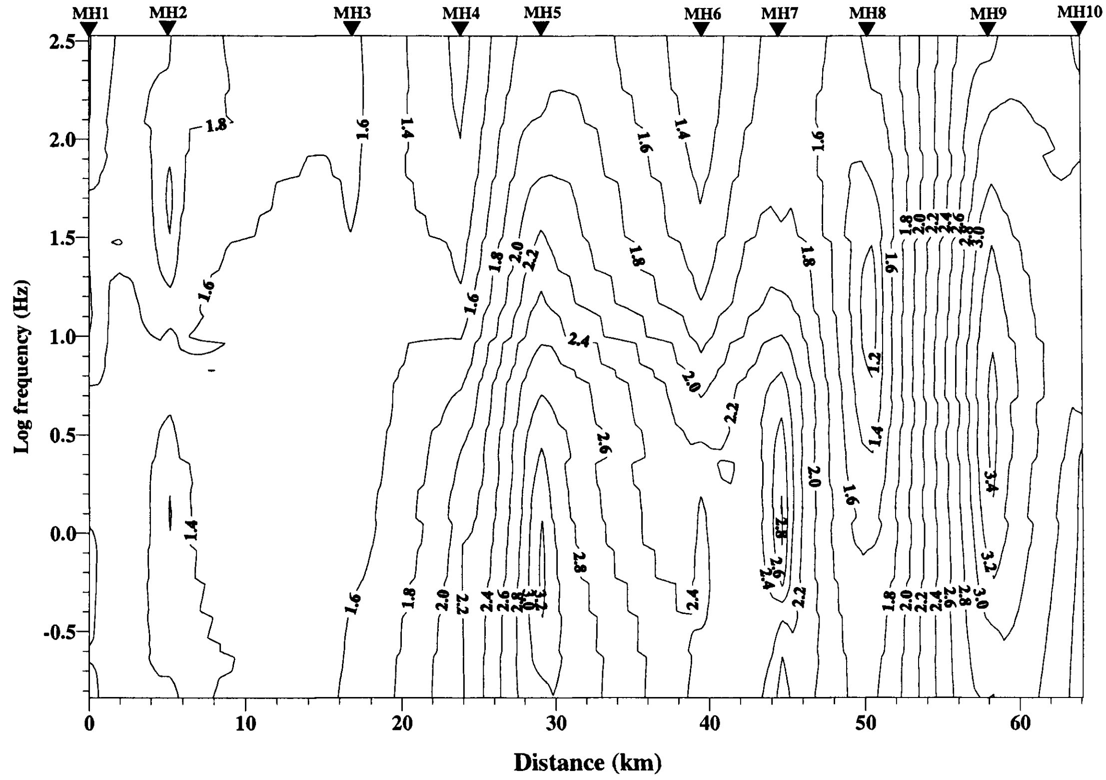

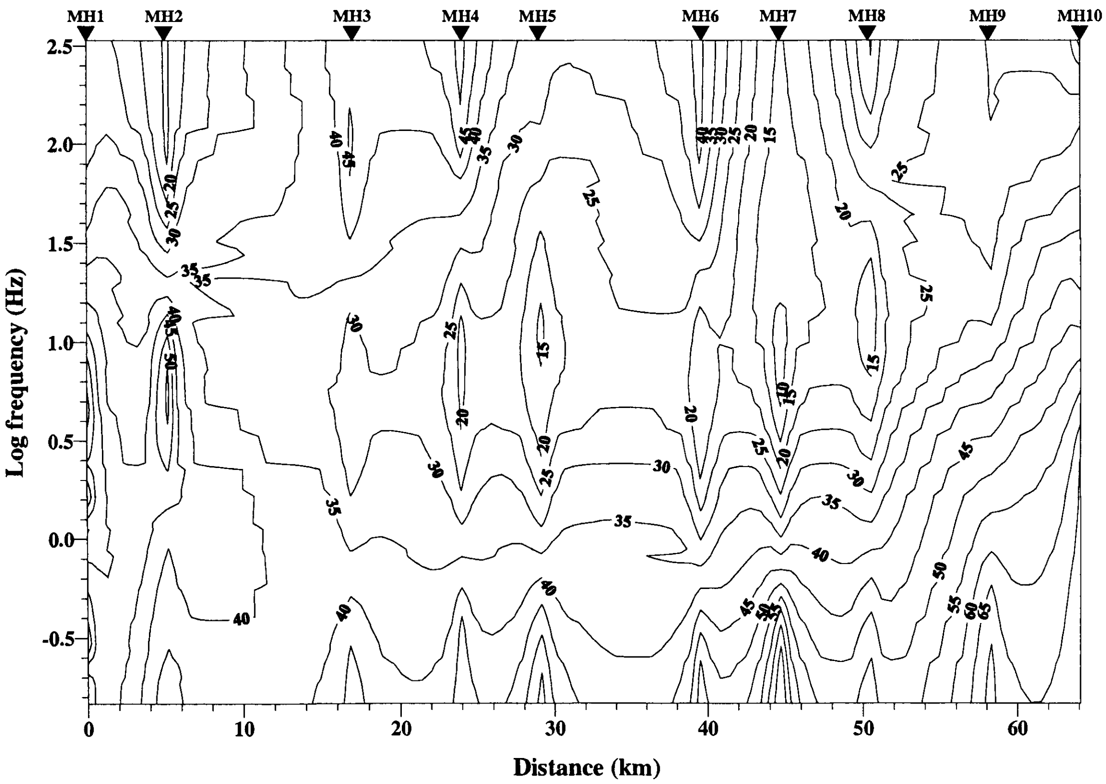

Figure 5.18b: Pseudosections of shifted apparent resistivity and impedance phase of TE mode for MH profile. The apparent resistivity values ($\Omega.m$) have been contoured on a logarithmic scale. The phases are in degrees.

6. Modelling of Parnaiba data

Quantitative interpretation of data can be performed to obtain a realistic conductivity structure in the form of a resistivitity depth map or geoelectric section. The results of 1-D and 2D inverse modelling of Parnaiba data are discussed in this chapter.

6.1 Invariant resistivity Bostick sections

The determinant of the impedance tensor is invariant under rotation and hence is independent of the orientation of the measuring coordinates. The invariant resistivity is one of two parameters which can be derived from the determinant of the impedance tensor (invariant phase is the other; Ranganayki, 1984). It reduces four resistivitites to a single resistivity (equation 2.65) and thus is considered a scalar average.

The unrotated apparent resistivity and phase curves and also the calculated parameters such as skew (see appendix A.1 and B.1) for the two profiles of study indicate that one dimensional structure data may be valid at high frequencies at most of the sites. However, the character of the curves at lower frequencies (<1Hz) suggests more complex structure as shown in chapter 5. Despite that, the invariant resistivity from the effective impedance was considered in this study to be useful for a first-pass interpretation. The invariant resistivity was therefore calculated and then corrected for static shift using central-loop TEM data which are less affected by lateral variation and then mapped onto their approximate depths using the Niblett-Bostick transformation (Bostick, 1977) to yield a simple image of the subsurface for each profile. Figure 6.1 shows the invariant apparent resistivity section for the PN profile to a depth of 20 km. The lateral and vertical variations in resistivities are obvious. High resistivity values are apparent at stations 7 and 8 located on outcropping basement rocks. Low resistivity values are shown at the north and south of the zone of outcropping basement corresponding to the areas where there is a cover of sedimentary rocks. Based on the resistivity distribution, the sedimentary cover appears thicker south of station 12 (e.g. near stations 13 and 14). The abrupt change in resistivity in the top 3 km at this locality would appear to suggest the presence of a fault near station 12. A thin conductive cover unit is also seen underneath stations 2 and 3. The invariant resistivity section for the MH profile is presented for the top 5 km of the subsurface in Figure 6.2. The western part of this profile is located outcropping sedimentary rock while the extreme eastern part is located on basement rock. Strong lateral and vertical resistivity variations are seen in the invariant section.

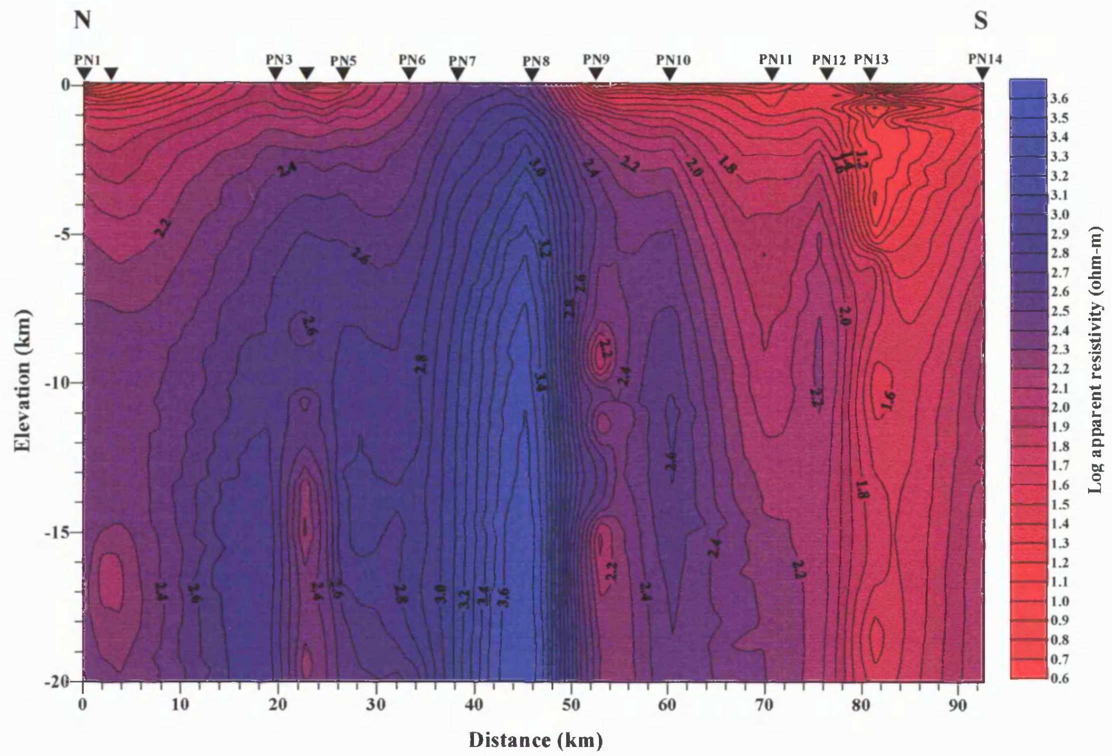

Figure 6.1: The corrected invariant resistivity values from static shift are plotted against the elevations (i.e. depths) calculated using Niblett-Bostick transformation for PN profile (note the vertical axis is exaggerated from the original given below for detailed display).

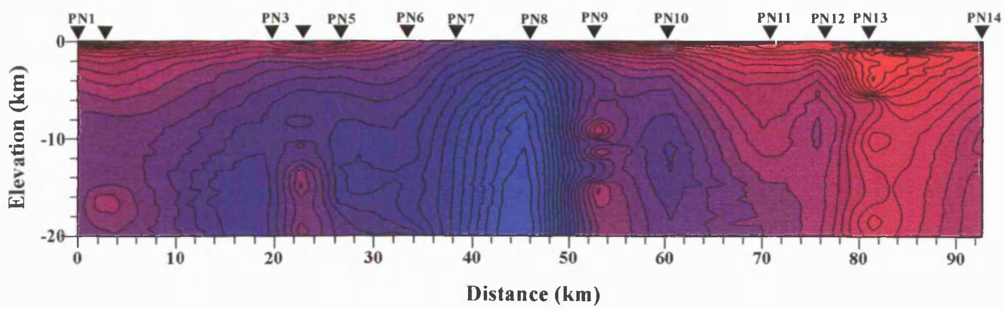

High resistivity values are displayed at stations MH9 and MH10 situated on outcropping basement rocks. Cover units of less than $150\,\Omega.m$ resistivity extend laterally from stations MH8 to MH1 and these extend vertically to depth of 1 km between MH8 and MH5 and possibly correlate with the outcropping Serra Grande Formation. These cover units extend to a greater depth at station MH4 and at stations MH2 and MH1 where graben-like structures may be present. The cover sequence is much thicker and of lower resistivity (< $50\,\Omega.m$) underneath stations MH2 and MH1. This particular conductive signature may be indicative of possible faulting in this locality related to Picos fault that may represent the edge of major graben structure along the profile of study.

6.2 1-D MT inversion results

Since the MT data at most of the sites are approximately 1-D at high frequencies, one-dimensional inversion was undertaken as a second approach to the interpretation of the measured responses. It also serves as a guide when constructing a starting model for eventual 2-D modelling.

The 1-D inversion program used in this study was developed by Meju (1992, 1996) for joint interpretation of TEM and MT data. The code requires an initial guess model. If the starting model is correctly specified, the non-uniqueness of the inverse problem is greatly reduced and so the final model may be a good representation of the Earth's conductivity distribution (Oldenburg, 1990). The Niblett-Bostick depth transformation for MT data and the Meju (1998) transformation for TEM data were used for generating the initial models.

The steps for performing 1-D inverse modelling were as follows: (1) deduce a starting model from the approximate transform model, (2) calculate its response function, (3) compare this with the observed data and its associated errors and then (4) iteratively adjust the model parameters to reduce the misfit between the field and computed data. After getting the optimum model parameters, the quality of the solution was assessed with the aid of the misfit error, model resolution matrix, or parameter covariance matrix (Meju, 1992, 1994). The 1D inversion models for all sites were then collated to produce geoelectric sections. Figures 6.3 and 6.4 show examples of the results of 1-D inversion of TEM and MT data for PN and MH profiles respectively. In each figure, the result of simple data transformation (initial model) and the 1-D layered-earth inversion are shown on the right hand plot while the field data and the calculated response of the constructed model are plotted together on the left hand side for comparison.

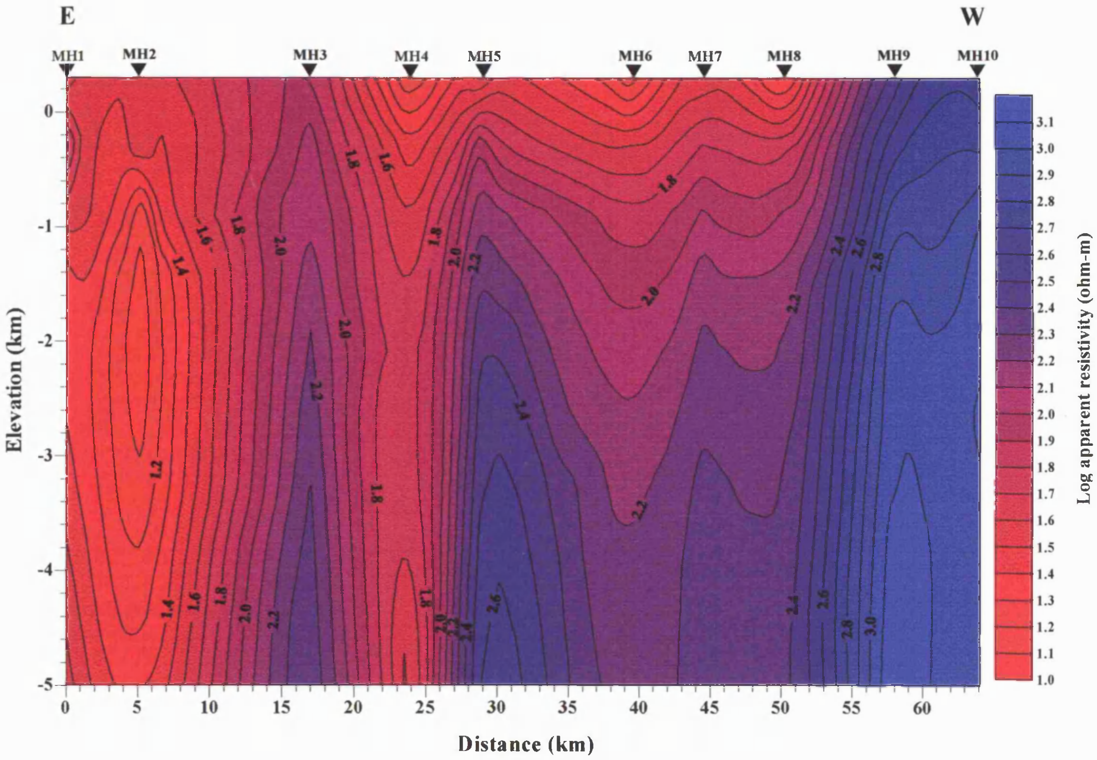

Figure 6.2: An E-W invariant resistivity section for the MH profile (note the vertical axis is exaggerated).

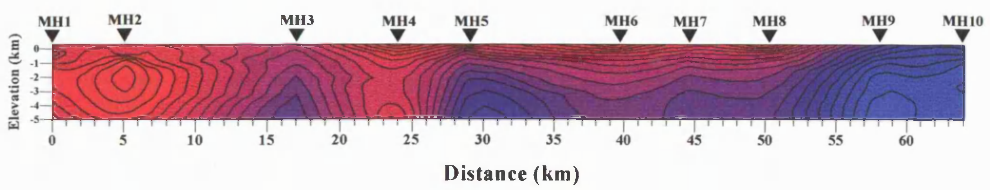

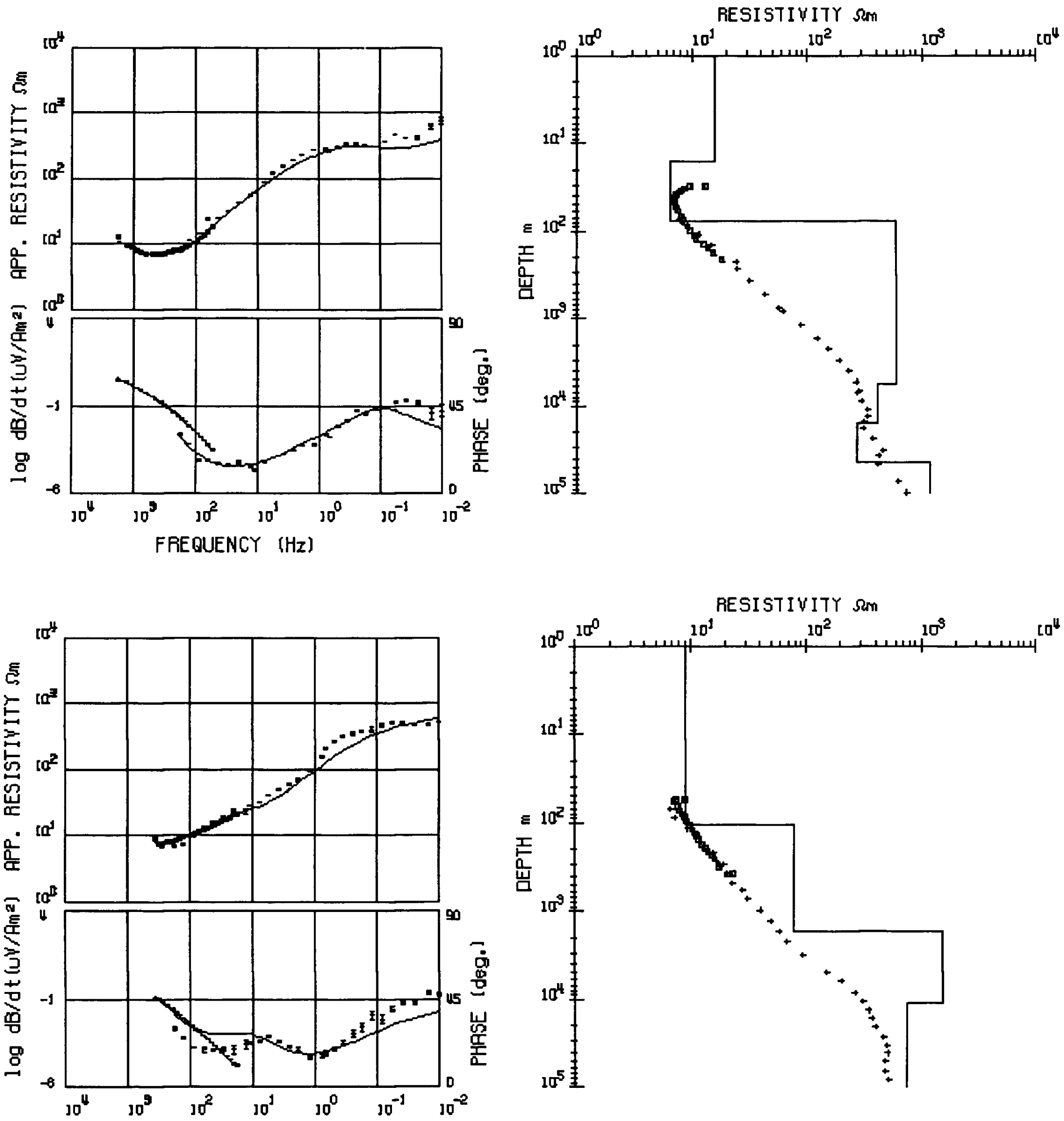

Figure 6.3: Results of joint inversion of TEM and MT data for the two polarization modes for station PN1. The upper figure shows the results for TEM single loop data (square symbol) and TM mode MT data (cross symbol). The bottom figure shows the results for central loop TEM data and TE mode MT data.

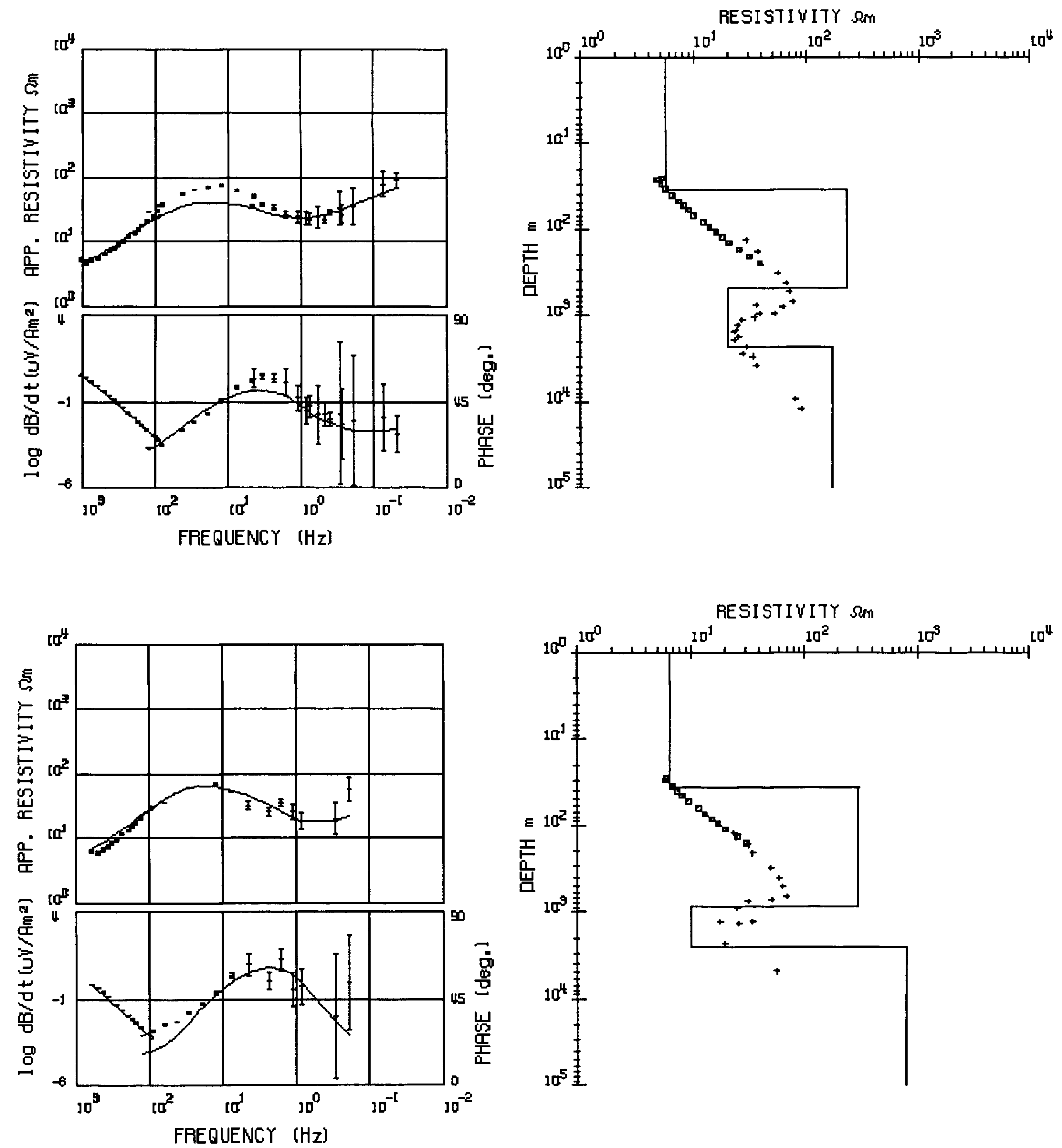

Figure 6.4: Results of joint inversion of TEM and MT data for the two polarization modes for station MH1. The upper figure shows the results for TEM single loop data (square symbol) and TM mode MT data (cross symbol). The bottom figure shows the result for central loop TEM data and TE mode MT data.

6.2.1 Geoelectric section for PN profile

The 1-D results for the PN profile have been collated into a geoelectric section and are presented in Figure 6.5. Only the results for the top 5 km are plotted because the resistivity values are too high beyond that depth and suggest the presence of basement.

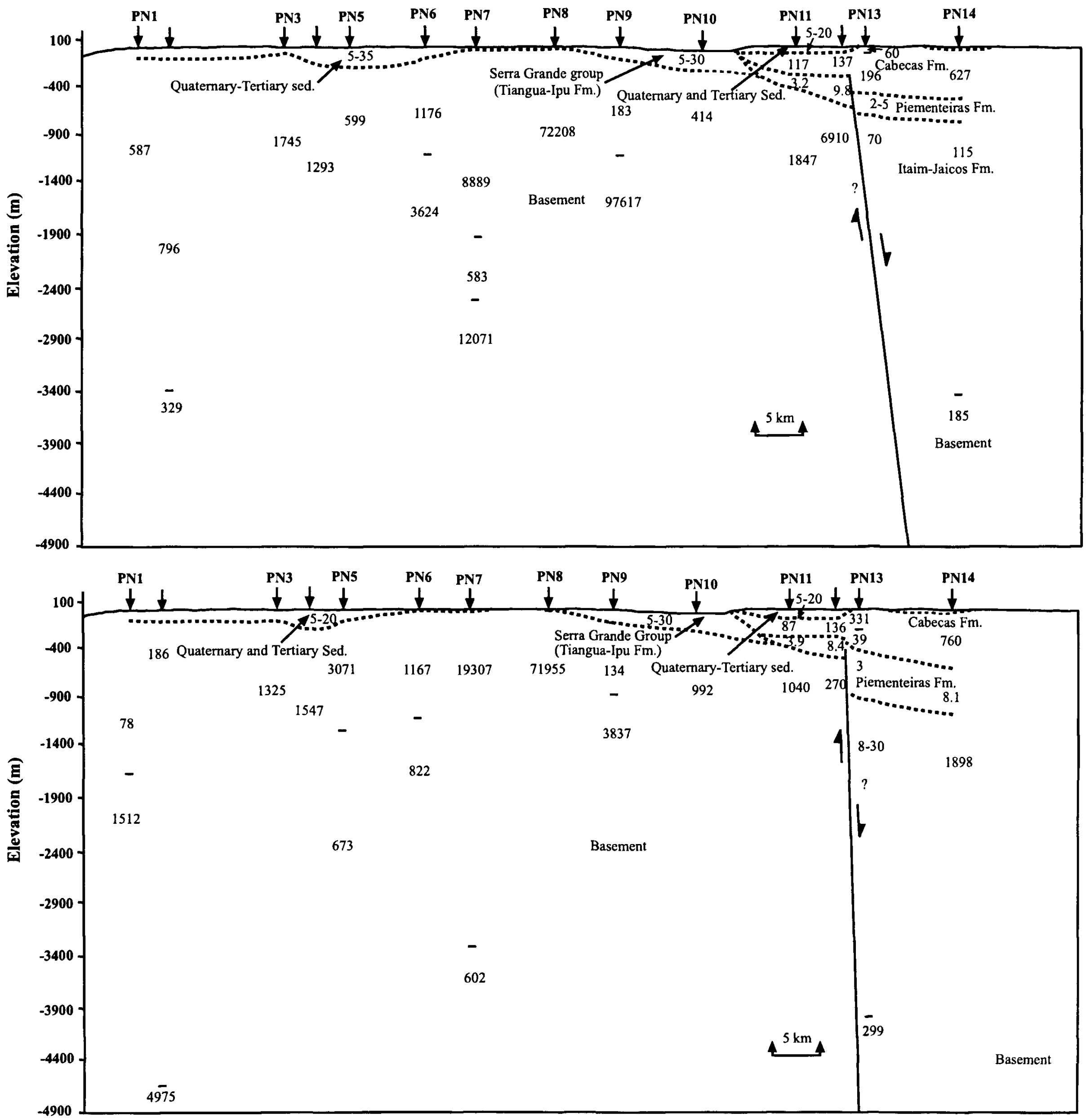

Figure 6.5: Interpretative geoelectric sections for the PN profile derived from collating 1-D models for the TM mode (top diagram) and TE mode (lower diagram) data. Resistivity is in ohm-m.

Also, this study is mainly concentrating on determining the thickness of sedimentary cover for hydrogeological purposes. It was found that the 1-D results for the TE and TM models are approximately similar at most of the stations on the PN profile (from PN1 to PN12) with only slight differences in resistivities and depths suggesting that 1-D modelling may be valid for the top 5 km along this profile. The resistivity section was compared with the lithologic variations inferred from the geological map to see if there is any realistic correlation. It would appear that the resistivity values are highly correlated with lithologic units. Relatively conductive sedimentary rocks appear to increase in thickness away from the zone of basement outcrop at stations 7 and 8 in agreement with the geological map. The cover units have resistivities of 5-35 $\Omega.m$ and can be traced from stations 1 to 6; these probably correspond to Quaternary and Tertiary sediments. Southward from station 8, the basement cover would seem to consist of different strata and a fault may be present near station 12. These cover units exhibit a general gentle dip to the south in agreement with the expected dip direction from the geological map. These units comprise a low resistive layer of between 5 and 20 $\Omega.m$ at stations 11 and 12 which based on the geological map possibly corresponds to Quaternary and Tertiary sediments. A unit with relatively high resistivity outcrops between stations 13 and 14 and may be correlated with the Cabecas Formation. The next underlying unit is probably Piementeiras shale and has a low resistivity (<10 Ω m). The Serra Grande group outcrops on the surface between stations 9 and 10 as shown in the geological map and which may be represented by low resistivity (5-30 Ω m). Tectonically, the abrupt change in resistivity values at station 12 at a depth of >500 m may suggest the presence of a major fault in this locality. Note that a fault was inferred on the tectonic and aeromagnetic maps, as possibly extending across the location of the MT-TEM profile.

The geoelectric section derived only from the 1-D central-loop TEM inversion for the first six stations is shown in Figure 6.6. This has more relevance to seawater intrusion problem mentioned in chapter 1. This geoelectric section shows a conductive (5-10 Ω m) body, sandwiched between an upper layer of 12-26 Ω m resistivity and a bottom layer of 80-140 Ω m resistivity that extends about 23 km from the coast in this model. Considering the standard hydrogeological model for seawater intrusion shown in chapter 4 (Fig. 4.4), we would expect seawater flow to be downward and not in an upward direction as implied by the TEM resistivity model. This may suggest that there might not be any significant seawater intrusion on land in this coastal section of the study area. However, the wide spacing and the undersampling in the horizontal direction with distance particularly between stations 2 and 3 may preclude inferring accurate hydrogeological model (salt water intrusion). In order to get more realistic information about possible seawater intrusion, intensive TEM field survey with a combination of other geophysical techniques like resistivity method may be strongly needed.

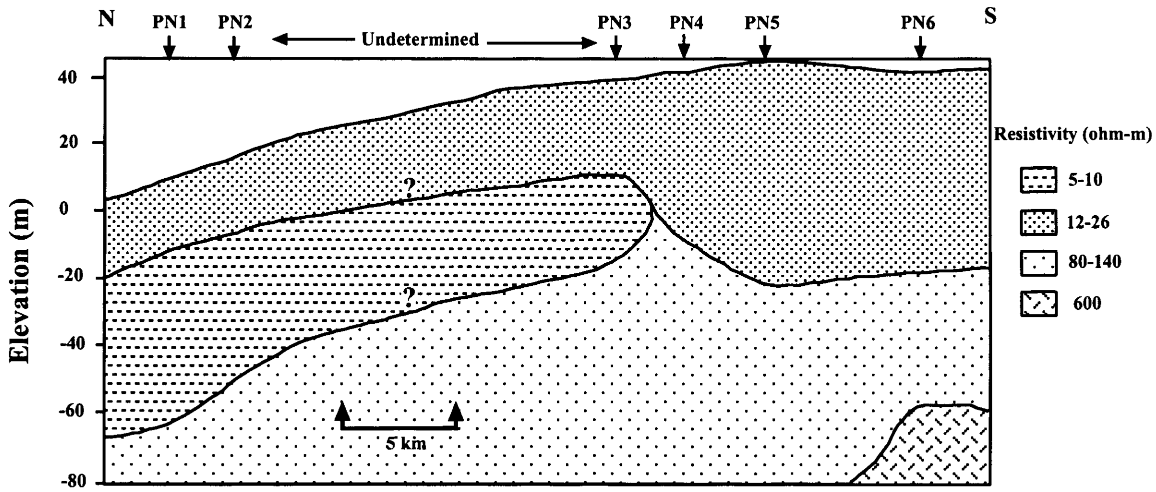

Figure 6.6: Interpretative resistivity section derived from collating central-loop TEM 1D inversion results for the first six stations on the PN profiles.

6.2.2 Geoelectric section for MH profile

The interpreted geoelelectric sections of the MH profile deduced from joint 1-D TEM-MT models are shown in Figure 6.7. The geology along the profile is made up of a sequence of sedimentary rocks resting on a crystalline basement. According to the geological map, the sedimentary rocks outcropping along most of the profile (from sites MH3 to MH10) belong to the Serra Grande group, with the Jaicos Formation being considered to be the dominant unit. The Piementeiras Formation outcrops at stations MH1 and MH2 and may rest on the Serra Grande Group. The geoelectric section for both modes (TM and TE) generally consists of two geoelectric units between stations MH5 and MH10; the top conductive unit probably belongs to the Serra Grande group. The underlying resistive unit is possibly basement rock and nearly outcrops on the surface at sites MH9 and MH10 in agreement with the basement outcrop on the geologic map. The region near stations MH1 and MH2 is underlain by anomalously thick conductive materials extending to 2.1 km depth in TM mode and 2.3 km in TE mode at site MH1 and greater depth at MH2. A fault is inferred to be present between stations MH4 and MH5. The lateral resistivity changes at this location are more clearly appropriate in the TM mode section. These complex structures along this profile suggest the necessity for more sophisticated modelling such as 2-D inversion.

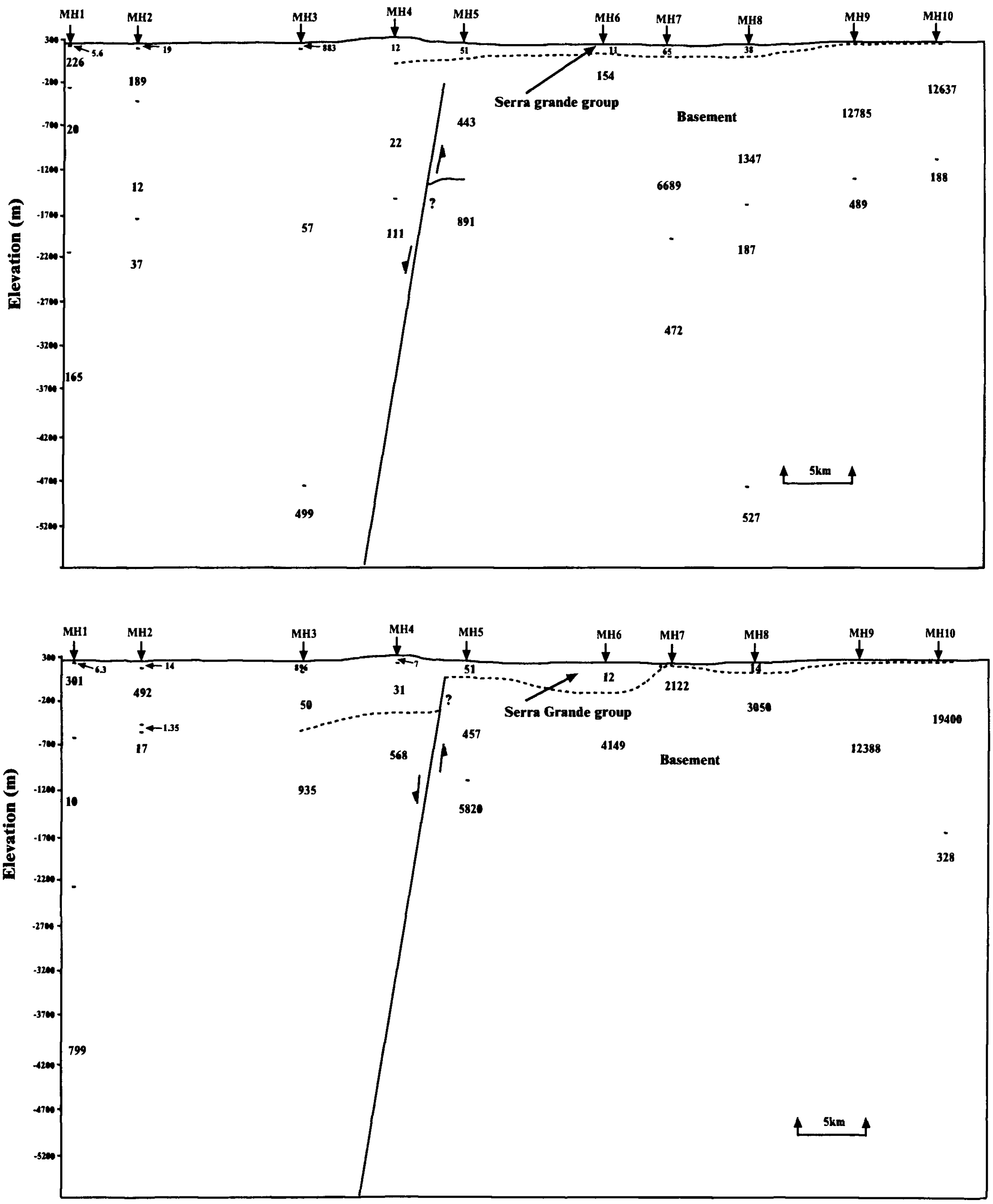

Figure 6.7: Interpretative geoelectric sections for the MH profile derived from the collating 1-D models for the TM (top diagram) and TE mode (lower diagram) data. Resistivity is in ohm-m.

6.3 Two dimensional inversion

The 2-D inversion-modelling program used in this study was written by Randal Mackie (1996). This program uses Tikhonov's method that defines a regularized solution of the inverse problem to be a model m that minimizes the objective function

$$S(m) = (d - F(m))^T R_{dd}^{-1}(d - F(m)) + \tau[L(m - m_0] , \quad (6.1)$$

where d is the observed data vector, F is the forward operator, m is the unknown model parameter vector, R_{dd} is the error covariance matrix, L is a laplacian operator, m_0 is the vector of a priori model, and τ is the regularization parameter.

The algorithm used to minimize the objective function, S, is the non-linear conjugate gradient method. The forward algorithm uses a finite-difference technique based on a network formulation of Maxwell's equations. Operationally, the region to be modelled is divided by a number of horizontal and vertical lines forming a mesh of rectangular cells of variable sizes. The intersections of the horizontal and vertical lines form the nodes of the grid. Madden and Mackie (1989) mentioned some factors that must be taken into consideration when preparing the grid. Firstly, the spacing has to adequately describe the important electrical parameter of the area of interest. Secondly, the errors in the approximation resulting from the discretization have to be at an acceptable level. Thirdly, limits have to be imposed on the computational efforts involved in obtaining the solution.

Proper design of the model based on these factors is very important in calculating a realistic response in 2-D. For instance the target area of magnetotelluric response should be confined to the order of a skin depth, and this applies to the horizontal as well as to the vertical distances. This is correct in ordinary circumstances, but very different situations can occur when dealing with anisotropic media (Madden and Mackie, 1989). The extension of the model allows the inversion to incorporate the effect of nearby structures on the predicted impedance. Thus, the columns near the centre of the model should be grided in a finer mesh than the columns near the edge. In vertical distance and for boundary conditions, several grided air layers are added on the top of the earth model to account for perturbations in the H fields from lateral current gradients. All the H field perturbations are required to be damped out at the top of the air layer. At the bottom of the earth model, 1-D impedance for a layered earth is used to relate the E field to the H field. Broadly speaking, proper mesh design is something acquired with experience, but rules of thumb concerning the element dimensions can be used as a guide line (see Wannamaker et al., 1985) as follows:

1- Near a conductivity boundary, element dimensions should not exceed a quarter of the skin depth in the medium where the element is situated.

2- A resistivity medium is defined by at least 3 elements horizontally and 2 elements vertically.

3- About 2 to 3 skin depths away from a conductivity boundary, element dimension may be increased up to the skin depth of the medium.

4- Because the fields decay exponentially, vertical element dimensions may be increased exponentially downward from the air-earth interface.

5- Because of the long wavelengths of the field in the air, 7 to 10 element rows increasing upward exponentially are recommended for the air layer.

6- Near the bottom (basement), element dimensions are kept essentially uniform.

There are four input files needed to run the inversion program used in this study. These are the data files, the model file, file containing the input parameters, and the last one includes model parameters to be fixed, if desired. Either TE or TM mode data or both of them can be used as the input file to the inversion. If both modes are used as prepared in this study, they should include the apparent resistivities, phases, and errors for each frequency at each station. The input required by the inversion program includes the expected *rms* error, the smoothing factor TAU, and the noise floor. The program terminates if the *rms* error reached before the maximum number of inversion iterations (60 in this program). The program typically stops once convergence has been attained and the error could not be reduced further. The *rms* error is defined as

$$rms = \sqrt{\frac{(d-f(m))^T R_{dd}^{-1}(d-f(m))}{ndpts}}, \tag{6.2}$$

where *ndpts* is the number of data points and the other parameters have been defined previously. TAU is the regularization parameter that controls the trade-off between fitting the data and adhering to the model constraint. Larger values cause a smoother model at the expense of a worse data fit. The value of TAU should optimally be chosen such that the *rms* error for the inversion is between 1 and 1.5. Nevertheless, it is not an easy task to get the target *rms* error values for noisy and non 2-D data. The noise floor is defined as the parameter that controls the error such that the input error below this parameter will be reset to this value.

For the PN profile, the design of the 2-D calculation mesh was optimised for the top 30 km of the subsurface to investigate if there is any interesting anomaly beyond the top 5 km of hydrogeological interest; on the ocean-side, the 2-D grid made use of the available bathymetric data and incorporated a surface conductive slab of 2.5 Ω m representing the seawater layer (cf. Arora et al. 1999). For the MH profile, the mesh design was optimised for the top 15 km despite the suggested presence of a conductive zone at some stations (MH1, MH2, and MH4) which may have limited the resolution to about 5 km.

As a simple way of addressing the problem of non-uniqueness, two sets of initial models were adopted in the inversion studies, viz: (1) featureless (half-space) models and (2) structured models derived from joint 1-D inversion. The first approach was considered to provide further constraints for the initial model for the second approach.

6.3.1 Results of 2-D inversion using half space initial models

6.3.1.1 PN profile

For 2-D inversion, MT stations have been projected onto a profile perpendicular to the adopted strike (i.e. trending N 37^0 E) so that the distances between the stations are different from those shown on the actual site location map (Fig 5.3). Since there is no subsurface or any borehole information for the northern profile, preliminary 2-D inversion was performed using a blind interpretation or smooth model (e.g. Constable et al., 1987; Bai et al., 2002), in which the subsurface is divided into several blocks of constant resistivity (half space). This profile was modelled using a mesh size of 55 x 46 as shown in Table 6.1. The grid was extended down to a depth of 30 km. It was finer for the top 3 km and became coarser with increased depth. Care was taken to add more grid elements in the anomalous area. Although the topography does not change sharply (maximum 100 m above sea level), it has been included in the modelling. Initially, inversion runs were performed (using half space 500 $\Omega.m$) to determine the best value for TAU parameter (in terms of model smoothness and data fit). Based on the initial results, a value of 5 was used for TAU. Additionally, the noise floor in the data was arranged to be 5 %. Then the desired *rms* error was set to 0.5 and the maximum number of iterations to achieve these criteria was set to 60. However, as mentioned above, the program automatically stops when the minimization converged and could not reduce the error further.

In the case of inversion with smooth initial models, the responses of the resulting model matched the field data satisfactorily only for half-spaces of resistivity >50 Ω m. The optimal models constructed from initial models of 250, 500, 750 and 1000 Ω m resistivities show similar features as can be seen in Figure 6.8. A relatively conductive trough-like feature is clearly apparent between stations 12 and 14 in the top 4 km of the subsurface and there is a high resistivity zone underneath stations 6 to 8. The trough-like feature occurs in the expected subcrop region of the elusive major fault seen to the west of the survey line on the tectonic map (see Fig. 5.1). The highly resistive body beneath stations 6 to 8 coincides geographically with the zone of basement outcrop on the geological map. This useful information can be used in conjunction with 1-D modelling to produce more realistic initial model for the final 2D inversion.

```
Number of X-grid =55 and Z-grid =46

X-Block width (m)

100000 30000 10000 3000 1000
500 1000 1000 700 5250 5250 1000 1000 1175
1000 1375 1375 1000 2000 2000 1500 1600 1200 2000
2000 2825 2825 2000 2250 2250 2000 2815 2815 2000
3700 3700 2000 900 1000 1000 1000 550 500 500 500
1850 2000 2000 2000 2000
1000 3000 10000 30000 100000

Z-Block thickness (m)

5 20 20 20 20 20 20 20 50 50 100 100 100 100 100 100 100
100 200 200 200 500 500 500 1000 1000 1000 1000
1000 1000 1000 1000 1000 1000 1000 2000 2000 2000 2500
2500 2500 2500 10000 30000 100000 200000

Site location

6 9 12 15 18 22 25 28 31 34 37 41 45 50
```

Table 6.1: Grid size used in the 2-D modelling for PN profile.

6.3.1.2 MH profile

This profile has shown interesting features in the invariant and 1-D results. Therefore, more grid elements were added in the anomalous area, so it was modelled using a mesh design of 55 x 48 blocks as shown in Table 6.2. The grid was extended down to a depth of 15 km. The topography was also included in the initial model. Fixed parameters were not added to this grid. Based on the initial results of inversion using half space 500 $\Omega.m$, the TAU value of 5 has also been decided. Also a value of 5% was considered for the noise floor. The desired *rms* error was set to 0.5 and the maximum number of iterations to achieve these criteria was set to 60. As before, the calculated response also matched the field data satisfactorily only for half-spaces of resistivity >50 Ωm. The models constructed from initial models of 250, 500, 750 and 1000 Ωm resistivities are shown in Figure 6.9. The resistive zone near station MH1 is apparent in the three models (500, 750, and 1000 ohm- m) and may be interpreted as possibly correlating to shallow resistive sill-like intrusive body. The conductive trough-like feature at stations MH1 and MH2 may be related to the Picos fault that may be part of a major graben in this area. A trough-like feature occurs between stations MH3 and MH4. The high resistivity values underneath stations MH6 to MH10 are related to basement rocks which are covered by a relatively thin conductive geoelectric layer. It is obvious from these geoelectric sections that 2-D inversion using a half space initial model can give a geologically feasible model of the subsurface.

Number of X-grid =55 and Z-grid =48

X-Block width (m)

```
100000  30000  10000  3000  1000
  1000   1000   1000  1000  1000   1000   1500   2500  2500
  2500   1000   1000  1000  2000   2000   1000   1000  1000
  1000   1000   1000  1000  2000   2000   2000   2000  2200
  1500   1000   1000  1000  1000   1500   1800   2000  2000
  2000   1000   1000  1600  1500   1200   1000   1000  1000
  1000   3000  10000 30000 100000
```

Z-Block thickness (m)

```
 50   50   50   50   50   50   50   50   50   50   100   100
100  100  100  150  150  150  150  200  200  200   250   250
250  250  250  350  350  350  500  500  500  500   500   500
500 1000 1000 1000 2000 3000 3000
1000 3000 10000 30000 100000
```

Site location

```
6 11 16 21 26 32 36 40 45 50
```

Table 6.2: Grid size used in the 2-D modelling for MH profile.

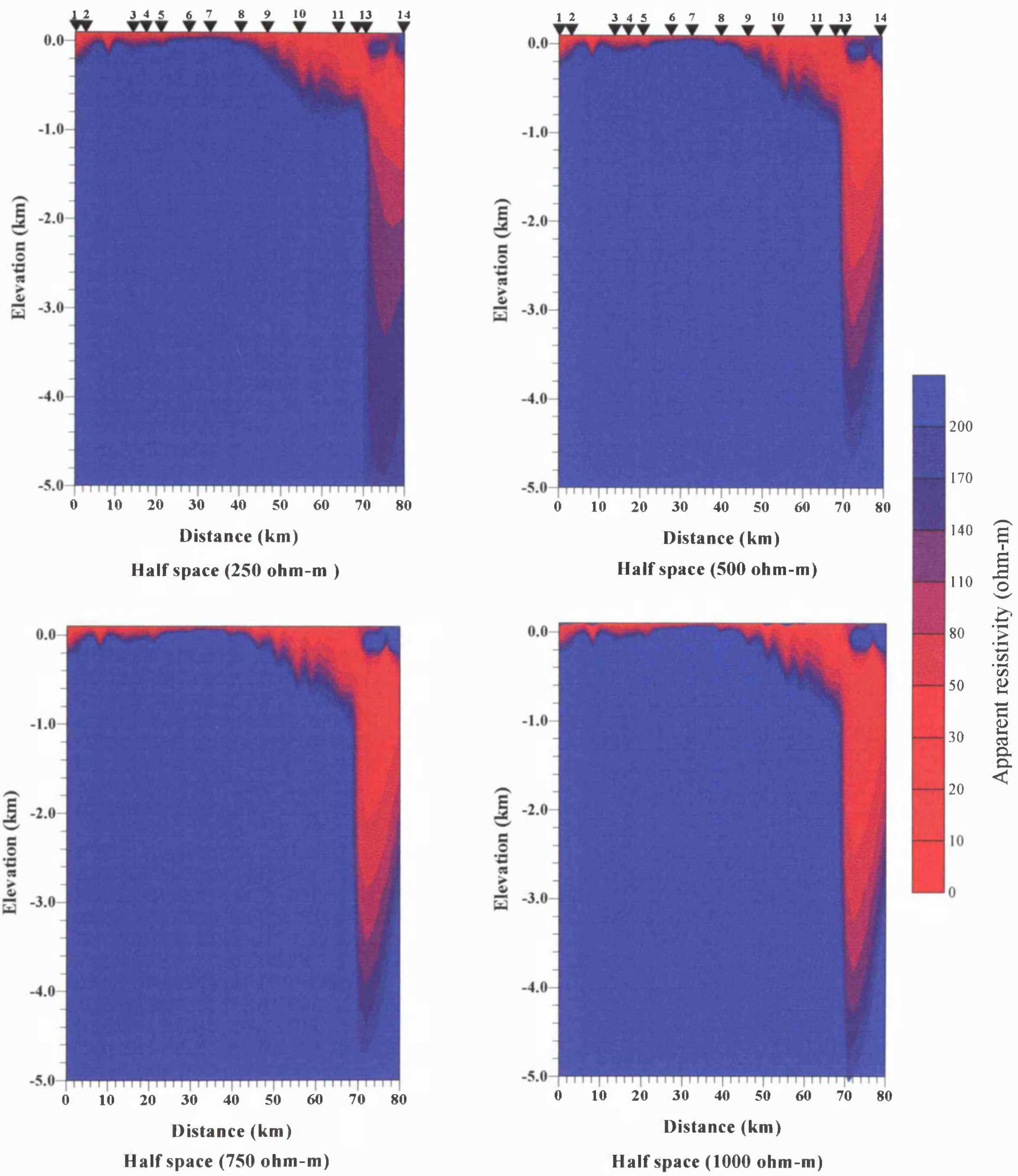

Figure 6.8: 2-D inversion models generated using different initial half space models for PN profile (note the vertical axes are exaggerated from the original given below).

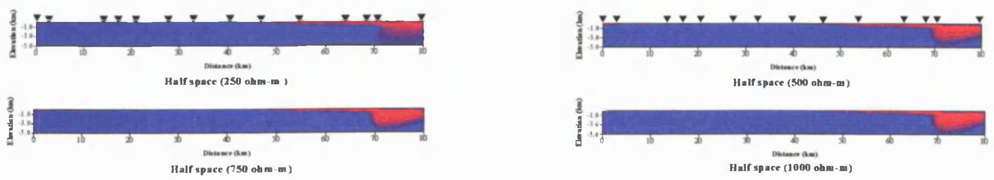

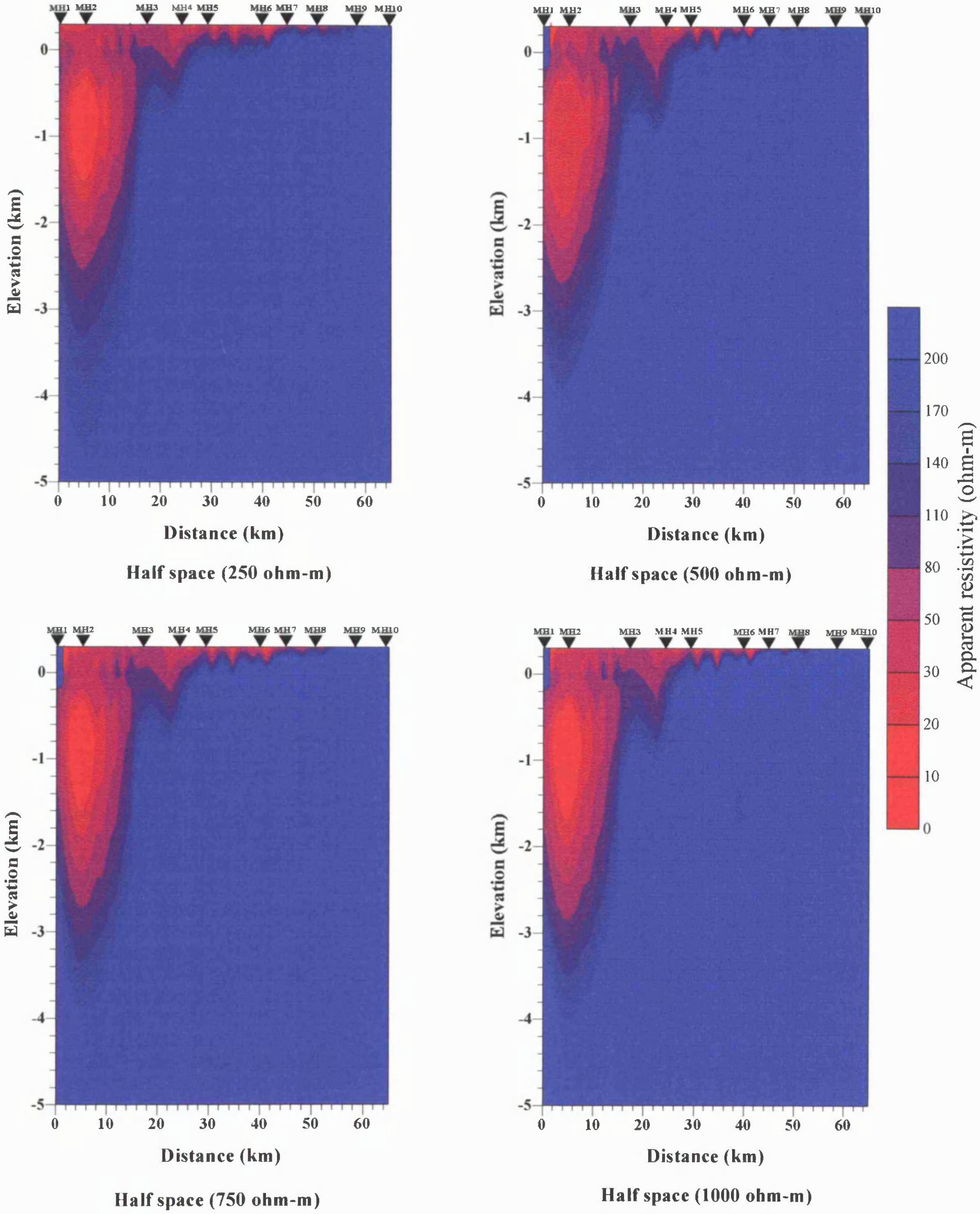

Figure 6.9: 2-D inversion models generated using different initial half space models for MH profile (note the vertical axes are exaggerated from the original given below.

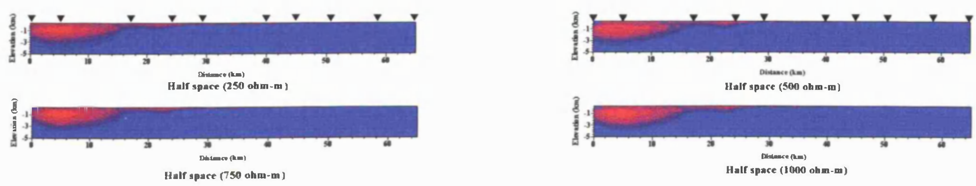

6.3.2 2-D inversion final model

6.3.2.1 2-D final model for PN profile

A structured initial model was constructed using a combination of the 1-D geoelectric sections using joint TEM and MT (TM and TE modes) data, significant features from 2-D modelling from half spaces, and information from the geological map. The above-mentioned parameters used in the half space modelling (TAU and noise floor) were put in the input file and also the same mesh size was employed. The inversion results were assessed after a number of iterations by evaluating the misfit between the observed and calculated response. Then a modification was also employed manually to some initial model parameters (resistivities and depths) such that, over a number of iterations, a better set of the model parameters can be found that minimize the error between the model response and the observed data. This approach was repeated for more than 20 different models to get a reasonable model based on the minimum misfit and minimum *rms* error and also agreed with the available geological information. The final result of 2-D inversion along PN profile is presented in Figure 6.10 (only the top 5 km is shown for hydrogeophysical convenience). The output model statistics are presented in Table 6.3. It can be seen that that after 51 iterations, the program automatically stopped when the minimization converged and could not reduce the error further. The fit between the calculated model responses and the observed data is shown in Figure 6.11 and is satisfactory especially at high frequencies of interest in this hydrogeological work since the calculated response shows mostly the same trend of observed data. At low frequencies, the fit is not good at some sites and may be attributed to the 3-D regional structure at depth. This 2-D model is nearly similar to those constructed using featureless initial models and may thus be accepted as a plausible model of the subsurface geology. It would appear that the unweathered crystalline basement in the area of study is generally highly resistive with a minimum value of 200 Ω m and may be traced to the north and south from the part of the model coinciding with the zone of basement outcrop in the geological map (stations 7 and 8). Relatively conductive sedimentary cover rocks appear to increase in thickness away from the zone of basement outcrop as expected from geology; the cover units extending from stations 1 to 6 probably correspond to Quaternary and Tertiary sediments with the uppermost section being very conductive (≤ 10 Ω m) underneath stations 1 to 3 in accord with TEM data (see Fig. 6.6). Southward from station 8, the basement cover units show

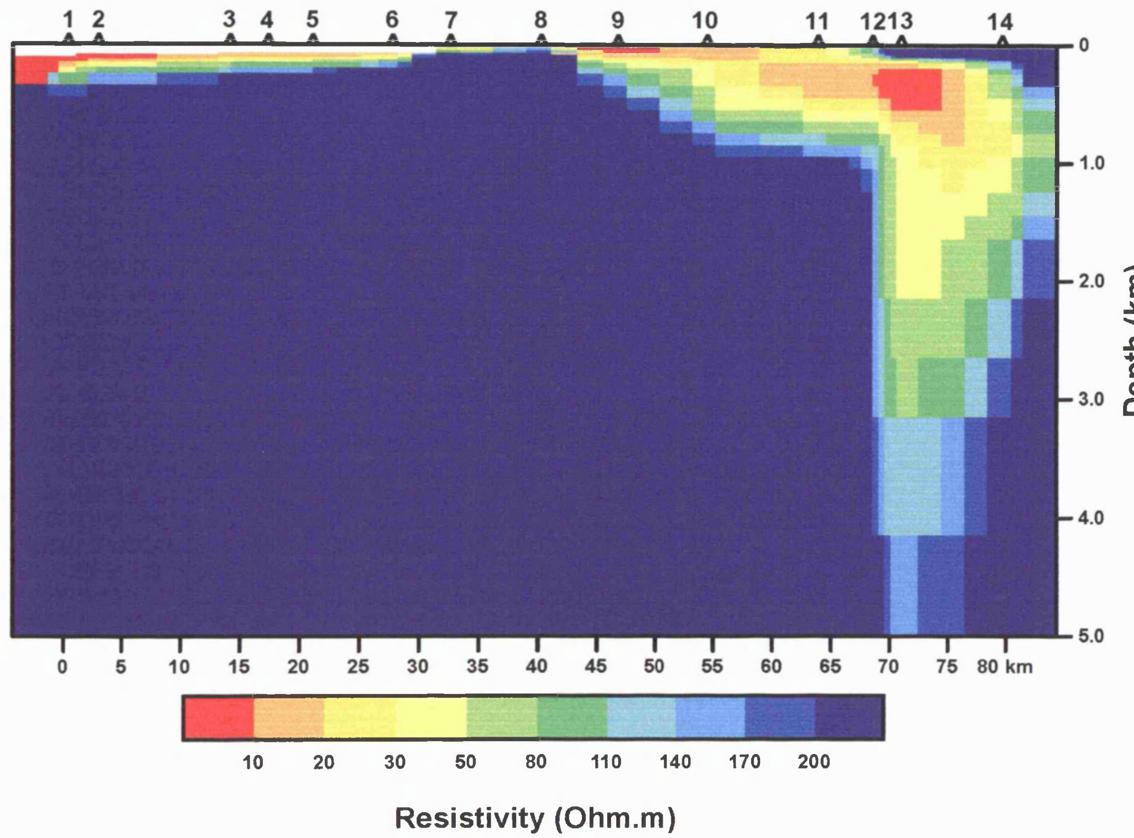

Figure 6.10: A geoelectric structure derived from 2-D inversion with a structured initial model for PN profile. Only the top 5 km is shown to stress the shallow features evinced by the inversion.

TAU 5 Chi 1568

Iter.	S1	S2/t	S2	S3	S
0	151083.	0.	0.	0.	151083.
1	14661.3	820.186	4100.93	1.33166E-06	18762.2
2	7652.32	850.166	4250.83	2.12061E-05	11903.2
3	5037.46	546.101	2730.51	2.53870E-04	7767.97
4	3951.90	468.744	2343.72	5.67244E-04	6295.62
5	3123.33	377.702	1888.51	9.73756E-04	5011.84
6	2619.84	295.466	1477.33	1.60565E-03	4097.17
7	2324.20	271.173	1355.87	2.04639E-03	3680.07
8	1741.33	261.560	1307.80	3.04844E-03	3049.13
9	1604.99	256.424	1282.12	3.12121E-03	2887.11
10	1435.64	224.956	1124.78	3.23977E-03	2560.42
11	1415.56	181.911	909.555	3.35485E-03	2325.12
12	1392.43	147.433	737.164	3.46147E-03	2129.60
13	1317.61	104.5380	522.690	3.63824E-03	1840.30
14	1248.16	92.3714	461.857	3.68520E-03	1710.02
15	1215.33	86.7740	433.870	3.70086E-03	1649.21
16	1110.01	77.1469	385.735	3.73767E-03	1495.75
17	1078.51	72.8583	364.291	3.75497E-03	1442.80
18	1032.65	69.8628	349.314	3.77654E-03	1381.96
19	982.511	68.1078	340.539	3.81238E-03	1323.05
20	935.597	68.7557	343.779	3.85105E-03	1279.38
21	891.210	69.3641	346.820	3.90484E-03	1238.03
22	843.388	68.5380	342.690	3.99129E-03	1186.08
23	821.473	65.9645	329.823	4.07623E-03	1151.30
24	789.372	63.2370	316.185	4.21848E-03	1105.56
25	770.903	61.2687	306.343	4.35037E-03	1077.25
26	745.543	60.0594	300.297	4.50909E-03	1045.84
27	722.445	58.8936	294.468	4.71500E-03	1016.92
28	700.603	57.4436	287.218	4.94477E-03	987.826
29	690.779	56.3690	281.845	5.08372E-03	972.629
30	685.123	54.4975	272.488	5.24304E-03	957.616
31	680.255	53.4354	267.177	5.37623E-03	947.437
32	668.970	52.9239	264.620	5.56848E-03	933.595
33	658.651	52.2151	261.075	5.81565E-03	919.733
34	653.791	51.6782	258.391	5.96458E-03	912.188
35	649.633	49.6284	248.142	6.30384E-03	897.781
36	645.532	48.5136	242.568	6.56630E-03	888.107
37	642.371	47.4842	237.421	6.83233E-03	879.799
38	639.498	46.5651	232.826	7.10438E-03	872.331
39	637.804	46.1654	230.827	7.26493E-03	868.638
40	631.182	45.7891	228.946	7.68846E-03	860.136
41	627.399	45.4609	227.304	8.01264E-03	854.711
42	623.554	44.9203	224.601	8.44412E-03	848.164
43	623.293	44.0261	220.131	8.82430E-03	843.432
44	623.216	43.0311	215.155	9.28834E-03	838.381
45	621.889	41.9773	209.886	1.00042E-02	831.786
46	617.856	41.9153	209.576	1.05006E-02	827.443
47	614.651	41.9395	209.697	1.08834E-02	824.359
48	611.222	41.9914	209.957	1.13289E-02	821.190
49	607.713	41.9391	209.695	1.19316E-02	817.420
50	605.369	41.8918	209.459	1.23806E-02	814.840
51	605.273	41.3918	206.959	1.28966E-02	812.245

Table 6.3: Statistics for the inversion of PN profile. TAU is the smoothing factor, chi is the desired chi square or the number of data used in the inversion, S1 is chi square, S2 is the model roughness, S2/t is the model roughness divided by smoothing factor, S3 is the closeness of the fixed parameters, S is the sum of S1, S2, and S3.

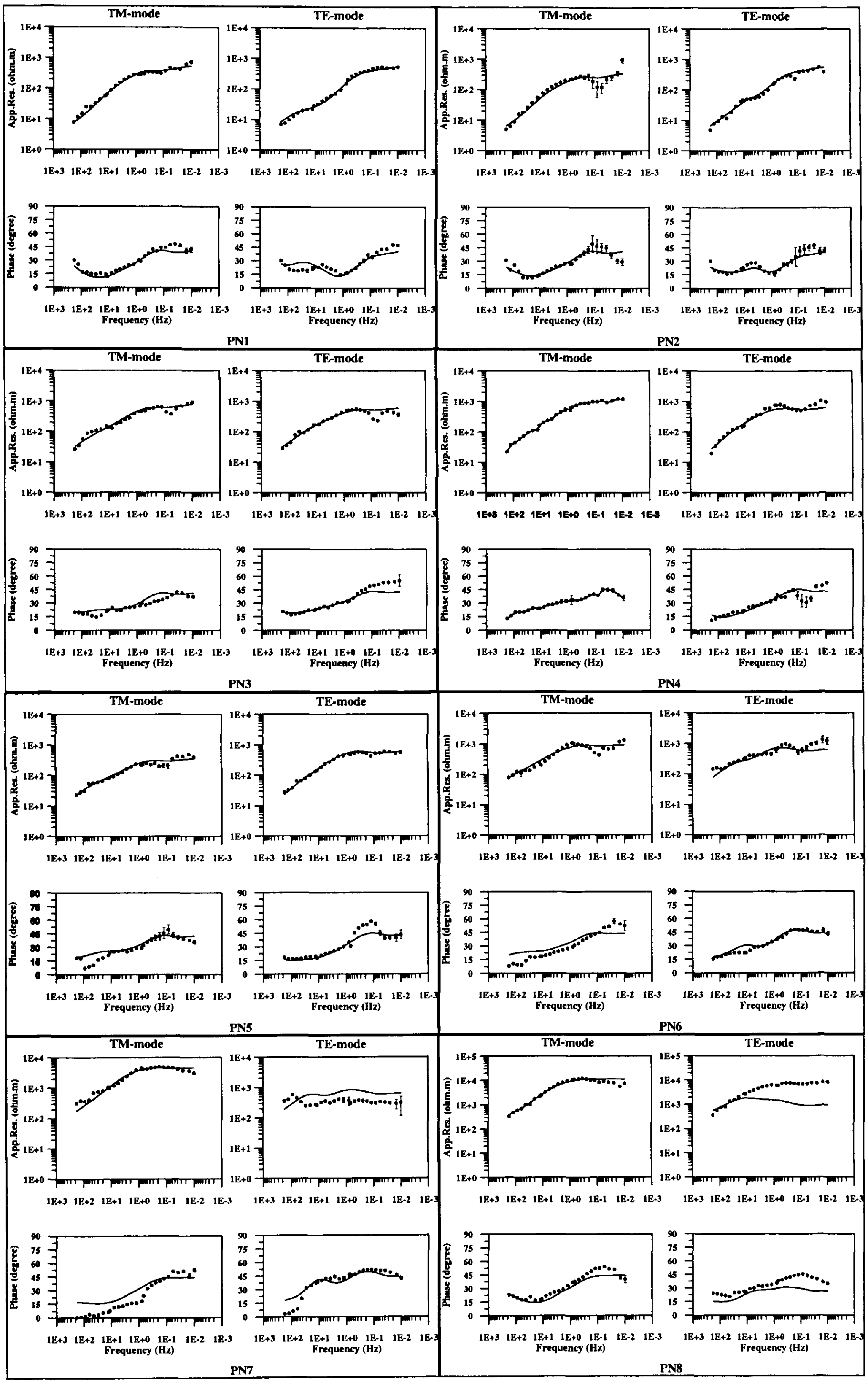
TM-mode
TE-mode
App.Res. (ohm.m)
Phase (degree)
Frequency (Hz)
PN1
PN2
PN3
PN4
PN5
PN6
PN7
PN8

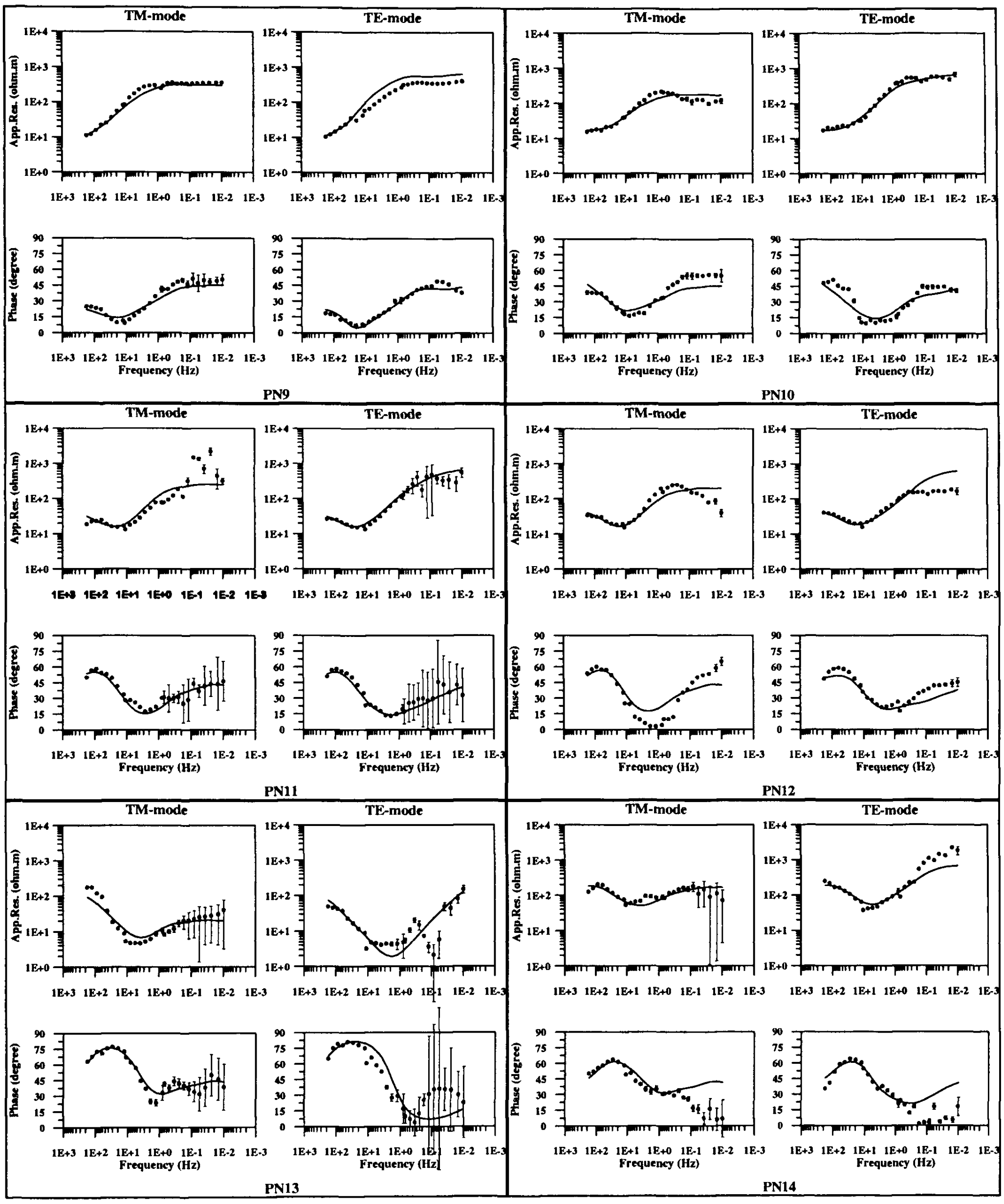

Figure 6.11: The fit between the MT observed data and the 2-D model response for PN profile. The apparent resistivity and phase information are presented for the TE and TM modes at each station starting from the north to the south on the profile. The error bars of the data are one standard deviation.

anomalous thickening starting from station 10 and attaining a maximum thickness of about 3 km underneath station 13.

These cover units exhibit some stratification consisting of an uppermost resistive (>150 Ω m) sliver starting near station 12 (and correlating with the zone of outcropping Cabecas sandstone), an underlying Conductive unit of <20 Ω m (correlated with the Pimenteiras shale which is draped over by Quaternary sediments at station 11), and a basal unit of moderate resistivity (ca. 20-80 Ω m) that may represent thickened segments of the

Serra Grande formations which outcrop at stations 9 and 10 or a combination of the Serra Grande group and pre-Silurian sediments of Riachao and Mirador Formations as suggested for deep grabens found elsewhere in the basin (see De Sousa 1996; Ulugergerli, 1998; Arora et al. 1999; Meju et al. 1999).

It may be possible to interpret this model tectonically and hydrogeologically. A major fault could be expected to lie at depth near stations 12 and 13. This may be part of a block-faulted structure marking the main edge of the basin. Based on the studies conducted further south by Goes et al. (1993) using data gathered from surface geology, geochemical surveys, exploratory wells and seismic sections, the projected sedimentary cover thickness would be about 1 km just south of station 14. The presence of thickened (ca. 3 km) conductive geoelectric units near stations 12 and 13 in this MT model (inferred to be sedimentary cover rocks) is therefore anomalous; it is best explained by the existence of a hitherto undiscovered graben-like structure. The Serra Grande group contains the most important aquifer in the Parnaiba basin and this anomalously thickened zone may thus have hydrogeological implications. From the available lithostratigraphic sections of the central and southeastern parts of the Parnaiba basin (see De Sousa 1996; Arora et al. 1999; Meju et al., 1999), the crystalline basement rocks are inferred to be directly overlain in some areas by the Riachao and Mirador Formations of Cambrian-Ordivician age. These units contain carbonatic facies which have high geothermal conductivity (De Sousa 1996); it is logical to expect that these will be associated with relatively high electrical conductivity. Based on the current 2-D resistivity models, it is suggested that Cambro-Ordovician sediments may be present in the deep trough-like structure in the study area and may therefore not be restricted to the central and southeastern parts of the basin as previously believed.

6.3.2.2 2-D final model for MH profile

The initial model was also prepared using the 1-D inversion results of joint TEM and MT (TM and TE modes) data in addition to the information from previous geoelectric studies in the area, and the major features from the 2-D models from half space. The inversion results were assessed also after a number of iterations. Then, a modification was employed to some initial model parameters before getting the final model. This approach was repeated over 30 different models for the same purpose as discussed for PN profile.

The final result of the 2-D inversion is presented in Figure 6.12 for the top 5 km. The model statistics are presented in Table 6.4. It shows that after 52 iterations, the program automatically stopped when the minimization converged and could not reduce the error further. Also the fit between the calculated model response and the observed data is shown in Figure 6.13 and is reasonably good particularly for high frequency data at most of sites. The 2-D model suggests the presence of strong lateral changes in resistivity in the top 4.5 km of the subsurface. The basement rock units are generally highly resistive and a value of ≥ 200 ohm-m appears to be appropriate as shown in the PN profile. These units outcrop on the surface at stations MH9 and MH10. The relatively conductive zone near the surface at station MH9 may thus indicate the presence of highly weathered basement rocks. The basement appears to be of irregular topography and is overlain by thickened sedimentary cover at stations MH1 and MH2 and between stations MH3 and MH5.

The contact between the basement and its sedimentary cover may be traced eastward along the profile starting from between stations MH8 and MH9 (in agreement with the basement-sediment contact on the geological map). The Serra Grande group aquifer outcrops at stations MH3 to MH8 and is well imaged by the resistivity inverse model. This segment of the model is the recharge area. The Pimenteiras Formation forms the aquitard west of this recharge zone. There appears to be a resistive sill-like intrusive body underneath stations MH1 and MH2 in agreement with previous MT models of the region (see Meju et al., 1999). The 2-D model also shows other interesting geological features; a major fault is suggested near station MH2 and extends vertically into the basement. The fault appears as a highly conductive zone and may represent the edge of a major graben structure. The smaller graben suggested between stations MH3 and MH5 agrees with that seen on the Jaicos-Picos line (Ulugergeli, 1998; see also Meju et al., 1999). This particular graben appears to contain thick sedimentary materials, possibly of the Serra Grande Group. This possible graben has the optimum potential for drilling for groundwater since the deeper graben-like zone at stations MH1 and MH2 may contain highly saline groundwater as shown by the high conductivity along the presumed Picos fault that may act as an impermeable barrier to the groundwater flow leading to the concentration of salt to the west. The presence of this conductive zone may also be interpreted in terms of the geothermal activity in the area. The circular magmatic structure shown on the geologic map (Fig. 5.4) is very close to the Picos fault and there may be a link between them underneath the ground surface; so this fault can be a zone of weakness for spreading hydrothermal fluids.

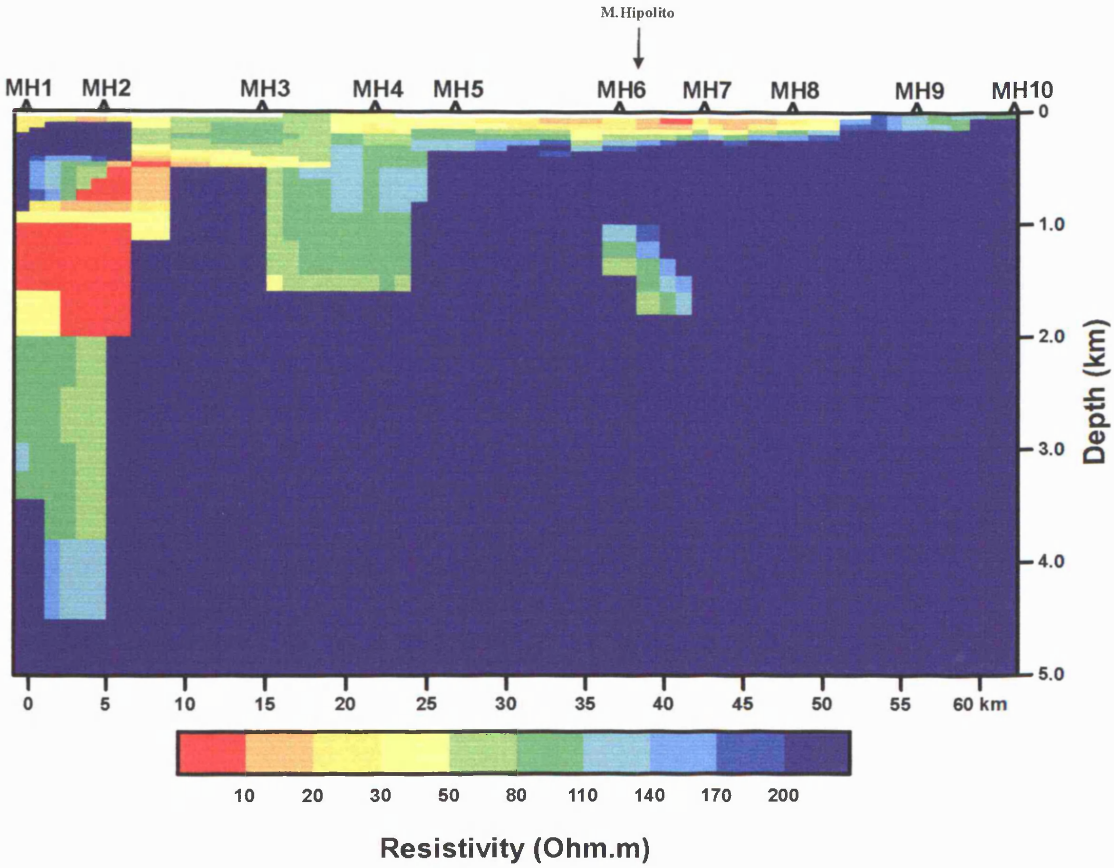

Figure 6.12: A geoelectric structure derived from 2-D inversion with a structured initial model for MH profile. Only the top 5 km is shown to stress the shallow features evinced by the inversion.

TAU 5					Chi 876
Iter.	S1	S2/t	S2	S3	S
0	5760.29	0.	0.	0.	5760.29
1	3165.29	0.116656	0.5832	0.	3165.87
2	2128.29	0.806009	4.0300	0.	2132.32
3	1914.20	1.16913	5.8456	0.	1920.04
4	1735.22	1.89997	9.4998	0.	1744.72
5	1667.64	1.94772	9.7386	0.	1677.38
6	1559.35	2.25964	11.2982	0.	1570.65
7	1463.72	3.14661	15.7330	0.	1479.46
8	1409.94	4.04584	20.2292	0.	1430.17
9	1391.55	4.38811	21.9406	0.	1413.49
10	1348.70	5.46482	27.3241	0.	1376.03
11	1325.83	5.90937	29.5469	0.	1355.38
12	1292.44	6.53952	32.6976	0.	1325.14
13	1273.16	7.24195	36.2097	0.	1309.37
14	1237.91	8.80168	44.0084	0.	1281.91
15	1182.43	11.8524	59.2620	0.	1241.70
16	1157.50	13.6133	68.0667	0.	1225.57
17	1130.45	16.3944	81.9718	0.	1212.42
18	1124.26	16.3599	81.7995	0.	1206.06
19	1107.04	16.2667	81.3333	0.	1188.37
20	1078.26	16.0098	80.0488	0.	1158.31
21	1073.54	15.9571	79.7856	0.	1153.32
22	1045.93	15.4898	77.4491	0.	1123.38
23	1033.95	15.3520	76.7601	0.	1110.71
24	1028.89	15.3068	76.5342	0.	1105.42
25	1008.03	15.3264	76.6319	0.	1084.66
26	1004.347	15.4529	77.264	0.	1081.61
27	1001.751	15.5740	77.869	0.	1079.62
28	967.909	18.1819	90.909	0.	1058.82
29	953.815	19.3780	96.890	0.	1050.70
30	928.147	22.1295	110.64	0.	1038.79
31	925.246	22.2019	111.010	0.	1036.26
32	901.845	23.0862	115.431	0.	1017.28
33	893.452	23.5112	117.556	0.	1011.01
34	891.787	23.6027	118.013	0.	1009.80
35	885.294	24.0550	120.275	0.	1005.569
36	882.505	24.2642	121.321	0.	1003.826
37	877.589	24.6363	123.182	0.	1000.771
38	866.753	25.4594	127.297	0.	994.050
39	864.997	25.5994	127.997	0.	992.994
40	862.118	25.8664	129.332	0.	991.450
41	854.164	26.6912	133.456	0.	987.620
42	830.147	29.2959	146.479	0.	976.626
43	817.674	31.0156	155.078	0.	972.752
44	810.263	31.8802	159.401	0.	969.663
45	802.844	32.7736	163.868	0.	966.711
46	785.132	34.3475	171.737	0.	956.869
47	778.186	35.0297	175.149	0.	953.334
48	777.095	35.1363	175.682	0.	952.777
49	768.893	35.9674	179.837	0.	948.730
50	766.682	36.2374	181.187	0.	947.869
51	759.508	37.1090	185.545	0.	945.053
52	755.938	37.5812	187.906	0.	943.844

Table 6.4: Statistics for the inversion of MH profile.

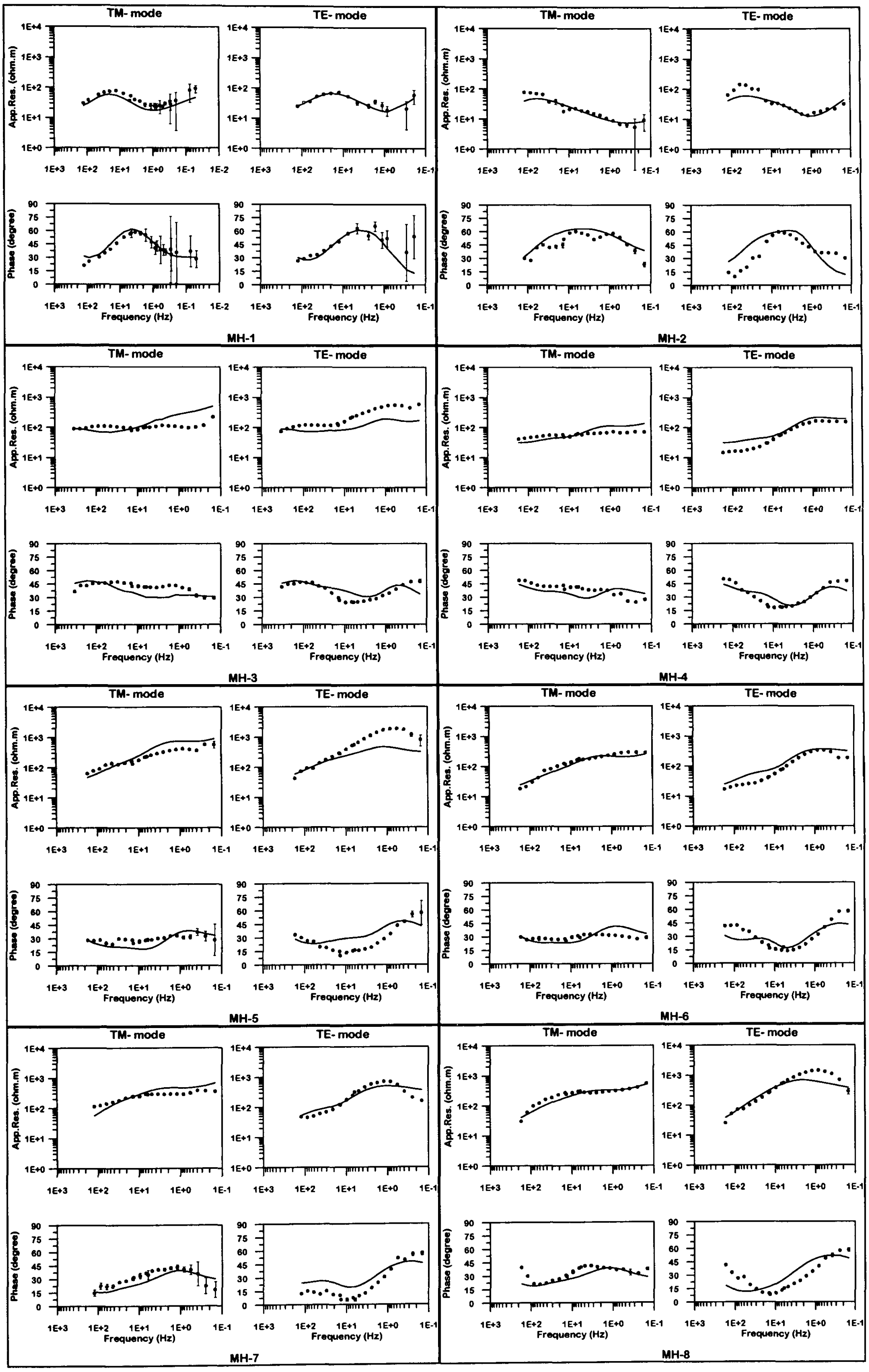
TM- mode
TE- mode
App.Res. (ohm.m)
Phase (degree)
Frequency (Hz)
MH-1
MH-2
MH-3
MH-4
MH-5
MH-6
MH-7
MH-8

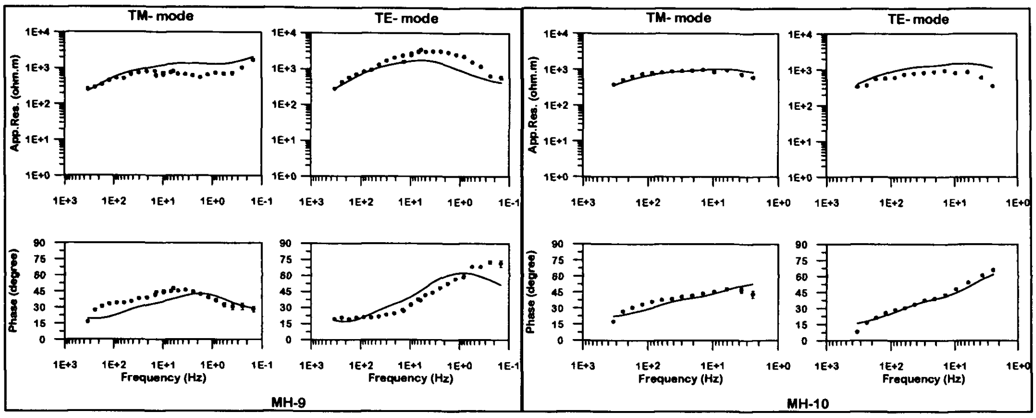

Figure 6.13: The fit between the MT observed data and the 2-D model response for MH profile. The apparent resistivity and phase information are presented for the TE and TM modes at each station starting from the west to the east on the profile. The error bars of the data are one standard deviation.

6.4 Prediction of aquifer properties

It is beginning to emerge that aquifer properties are highly correlated with electrical resistivity measurement (see Ebraheem et al., 1990; Aristodemou and Thomas-Betts, 2000; Meju 2000) as both relate to the pore space structure and heterogeneity. Empirical relationships between these properties and non-invasive geophysical information may be used to predict their values as an alternative approach to pumping tests or laboratory experiments with core samples. For instance, porosity can be determined through the use of Archie (1942) equation, see chapter 4. However, this requires that fluid resistivity, ρ_f should be determined in a clean matrix (i.e. a clay-free medium). If there is no borehole data or laboratory measurements through which we can obtain accurate value of *m*, ρ_f, and also *n* when the pores are not fully saturated by fluid, then we cannot determine these parameters reliably.

In this study, since there is no information about the hydraulic properties of the main aquifer, the total dissolved solids (TDS) were predicted using the schemes suggested by Meju (2000) and Ebraheem et al. (1990) equations, chapter 4. The main aquifer in the eastern and northern margins of Parnaiba basin is the Serra Grande group. Based on the results from 2-D inversion of PN profile, a huge thickness of this group may exist at stations 12 and 13 with resistivity of 20-80 ohm-m as described above. If a value of 30 ohm-m was taken to represent the top of the saturated zone of aquifer, then according to Meju (2000), the predicted value of the total dissolved solids is 398.36 mg/l. However, based on Ebraheem et al. (1990), the predicted TDS value is 753.1 mg/l. This big difference is attributed to the fact that Meju scheme was developed for highly saline aquifers but Ebraheem equation was derived for use in acid mine drainage problems. Since there is no evidence for the presence of highly saline water, fluid resistivity was calculated based on Ebraheem et al. (1990) equations. The fluid resistivity computed has a value of $14.25\,\Omega.m$. On the other hand and for the MH profile, total dissolved solids and fluid resistivity are predicted for two selected locations; the first is between stations MH1 and MH2 and Meju (2000) equations were applied to that location of probably highly saline water. The other is in the graben structure between stations MH3 and MH4 where Ebraheem et al. (1990) equations were employed. These areas of study are characterised by the Serra Grande aquifer. Table 6.5 shows the estimated aquifer properties.

Site / Parameter	(PN profile)	Site (MH1-MH2) (MH profile)	Site (MH3-MH4) (MH profile)
Total dissolved solids (mg/l)	**753**	**3850**	**164.426**
Fluid resistivity $(\Omega.m)$	**14.25**	**1.79**	**51.36**

Table 6.5: Some predicted aquifer parameters at selected sites on PN and MH profiles.

The highest TDS and the lowest fluid resistivity values are obtained for the first location on the MH profile where saline water may be expected. Having determined ρ_b and ρ_f as above, Archie (1942) equation may be applied to predict the porosity, assuming a relatively homogeneous medium. For most of the rocks the cementation exponent m lies between 1.3 and 2.5 (Schopper, 1982) and an average value of 1.9 can be adopted in this study. Also full pore saturation may be assumed, i.e. $S=1$. As an example, the predicted porosity value at the first location (MH1-MH2) on MH profile is 53% which is anomalously high and may indicate that this hydrogeological property can assist for accumulation of a huge amount of groundwater in that area.

The main disadvantages and limitations of the technique used to derive porosity are the following; these equations are empirical and require certain conditions to relate bulk resistivity to TDS; for instance, the scheme suggested by Meju (2000) was developed specifically for relatively homogeneous porous formations fully saturated with a highly saline pore fluid. So the applications of these equations for the prediction of hydrogeological parameters under different conditions may yield erroneous result. Also the porosity value predicted from Archie (1942) equation may be unrealistic since the assumed parameters should be precisely determined based on borehole information. Moreover, as discussed above, Archie's equation is valid only for clay-free and clean sediments. Any deviations from these assumptions make the equation invalid as discussed by Worthington (1993). In this study, the aquifer system consists mainly of sandstone with intercalations of clay and silt materials, so a modified representation of the Archie's equation might be required to obtain appropriate value of porosity (cf. Worthington, 1993; Aristodemou and Thomas-Betts, 2000). However, the above equations may demonstrate an approximate estimation especially if there is no hydrogeological or borehole information.

7. Application of TEM method for rapid mapping of a buried hillside in Quorn: Comparison with conventional methods.

7.1 Introduction

Geophysical techniques have shown their effectiveness in mapping the subsurface structure of crystalline basement terrains overlain by sedimentary overburden. Seismic and magnetic techniques are the most common methods used in mapping basement topography. Magnetic method is particularly suitable for mapping basement features such as lineaments, faults, shear zones, lithologic contacts, etc. which may be hidden from direct view because of overlying sedimentary cover (Sharma, 1997). Seismic reflection has been applied to detect a thick zone of intense fracturing (e.g. Gendzwill et al., 1994). The electrical (resistivity) methods also have been applied successfully to these targets (e.g. Barker et al., 1992). Palacky et al. (1981) have shown that HLEM, VLF electromagnetic, and DC profiling techniques combined with aerial photography or remote sensing are effective techniques for detecting fracture zones in Precambrian crystalline basement terrains (see also Wright, 1992; Pedersen et al., 1994). Azimuthal DC resistivity variations have been used to characterize fracture systems in both bedrock and unconsolidated sediments (Leonard-Mayer, 1984; Taylor and Fleming, 1988; Carpenter et al., 1991; Watson and Barker, 1999). Ground penetrating Radar has been used for mapping fracture zones (e.g. Seol et al., 2001). Recently, transient electromagnetic (TEM) method has been employed for this task because it has a good potential for penetrating thick conductive overburden overlying resistive bedrock targets (Meju et al., 2001). TEM is also widely used for hydrogeological, engineering, and environmental applications (e.g. Sandberge, 1993; Christensen and Sorensen, 1994; Shtivelman and Goldman, 2000). Meju et al (2001) successfully combined single-loop TEM and HLEM profiling methods for detecting fracture zones in a granitic terrain in Brazil. They also suggested that central-loop TEM can be applied to this problem and that the TEM method could effectively be used as the sole tool for such tasks in deeply weathered terrains. It will be interesting to see if the TEM method can be equally successful in mapping shallow fractured crystalline bedrock such as present in Quorn (the subject of this chapter) and would be the case in some engineering investigations.

According to Meju et al., (2001), the TEM model for a fracture zone in granite (Fig. 7.1) is analogous to a relatively conductive dyke emplaced within a resistive host covered by conductive overburden. The expected TEM response consists of single peak anomalies over zones of thickened saprolitic overburden at early times, and twin peak anomalies consisting of peaked response near each edge of the fracture-zone with depressed field values over the centre at late-times representing the signature of the steep fracture-zone with possible clay alteration products (Fig. 7.1). It was demonstrated that small loop TEM profiling has the ability to detect fracture zones in granite even underneath > 50 m overburden. As a further development and for engineering-type surveys, a novel small loop, short offset, azimuthal TEM technique has been suggested as a cost-effective approach for the 3D mapping of fracture zones in shallower bedrock. This TEM azimuthal survey technique could correspond to DC azimuthal resistivity surveys applied in detecting fracture zones. The present study aims to evaluate the applicability of this novel approach in characterising fractured shallow bedrock.

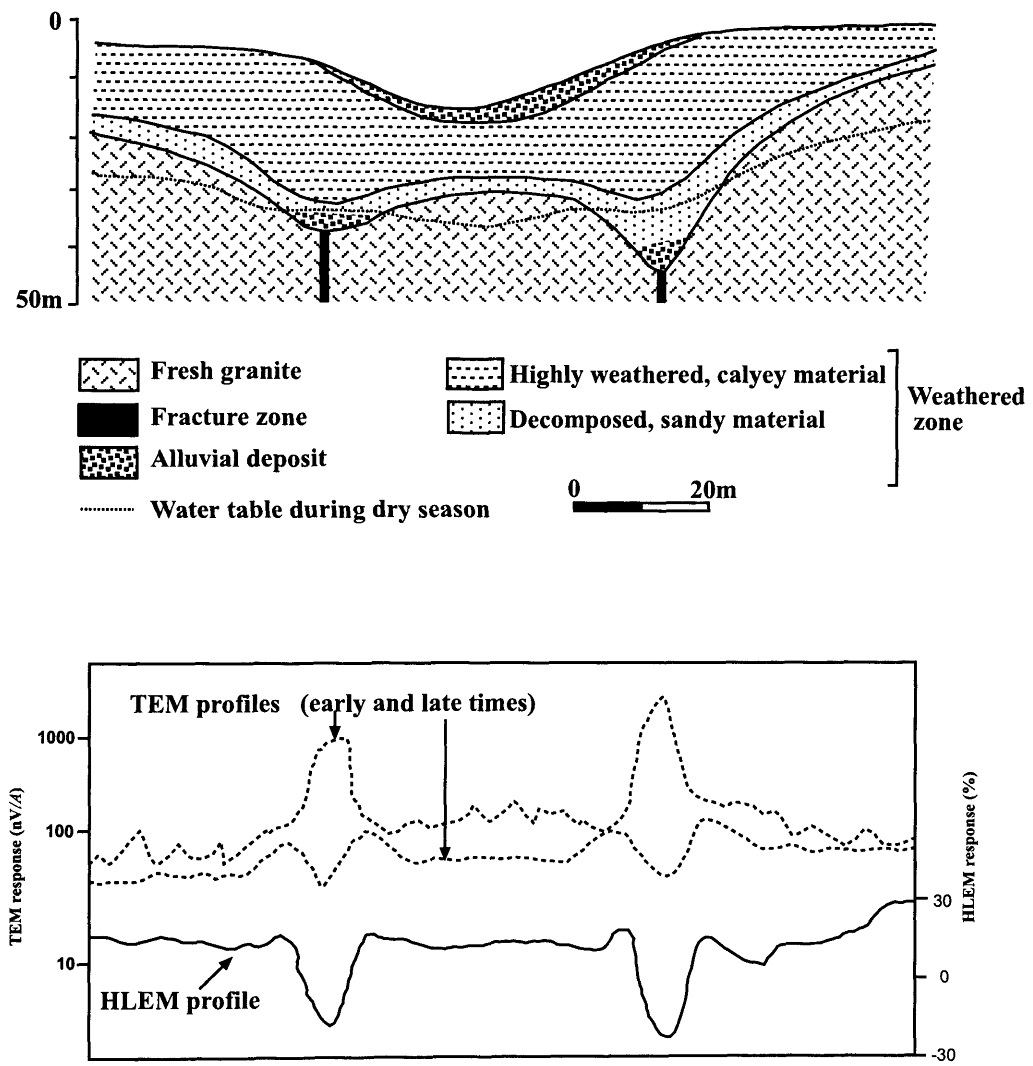

Figure 7.1: Idealized weathering profile and transient electromagnetic responses over a fractured granitic basement (after Meju et al., 2001).

7.2 Area of study

This study centres on a granodiorite body of Quorn Park, 10 miles north of Leicester, England (Fig. 7.2). The park is a large pasture field north of the Redland Quarry exploiting the Mountsorrel granodiorite. The ground is generally flat, but slopes at a very low angle towards the north. During Permo-Triassic times, the granodiorite formed an inselberg feature standing above a desert plain with deep wadis cut into its surface. This basement might be fractured or faulted and the zones of intensive fracturing are more susceptible to weathering and this could cause some problems to the Mountsorrel quarry. This basement topography was buried by a sequence of mudstones and sandstones known as the Mercian Mudstones; ~ 30 m thick. The determination of the nature of the granodiorite upper surface and its fractured/faulted zones are of primary importance from an industrial viewpoint and for engineering geophysical interest and could influence the design of future extensions of the Mountsorrel quarry. In this study area, the depth to the basement is not deep <30 m depth (Ahmed, 1993) so that shallow-depth TEM sounding equipment such as the Geonics PROTEM47, the Sirotem MK3 and others may be applicable. In this study, the Geonics TEM47 was used to track target geological features such as fractures or fault zones. The dip direction of these features can be approximately estimated from the shape of twin-peak anomalies (Weidelt, 1983). The TEM results will be compared with conventional techniques (VLF and DC resistivity methods) to determine its effectiveness for mapping the dissected bedrock.

The specific tasks in objectives of this study are:

1) Evaluation of a rapid Azimuthal TEM surveying technique for locating fracture zones.

2) Evaluation of TEM in mapping the thin cover sequence (drift and mudstone) over the site of study.

3) Comparison of TEM and established VLF and DC resistivity methods of bedrock mapping.

7.3 Description of the available data

Large amounts of TEM, VLF, and DC resistivity data have been recorded over the Quorn Park test site and have not been previously analysed. The survey lines are shown in Figure 7.2. DC resistivity soundings and profiling using Schlumberger and Wenner arrays in addition to VLF were conducted along most of the survey lines. A seismic refraction study was performed along one of the profiles (Ahmad, 1993), and will be useful for comparison with TEM and DC results.

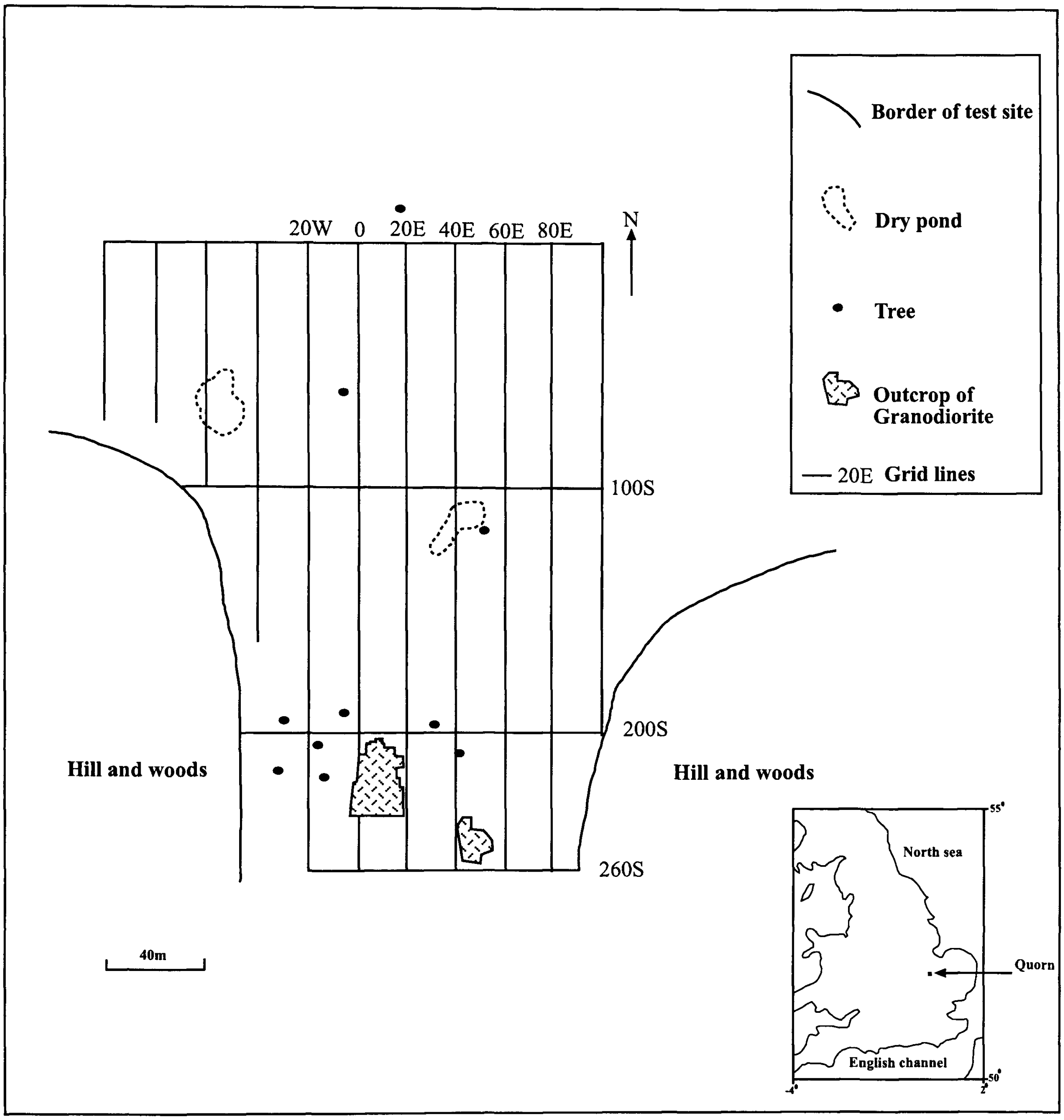

Figure 7.2: Location map of Quorn Park showing geophysical survey lines and site details.

7.3.1 TEM survey technique

The TEM survey employed a short-offset configuration with 20 m sided contiguous square loops as the transmitter. For every transmitter (Tx) loop position, multi-channel data were recorded at four locations using a roving receiver; the receiver (Rx) is sequentially positioned 10 m away from each of the four sides (instead of a single position per loop) as illustrated in Figure 7.3. A total of 96 soundings were recorded over 4 hours. The main motivation was to cover the whole area in a relatively short time period while obtaining

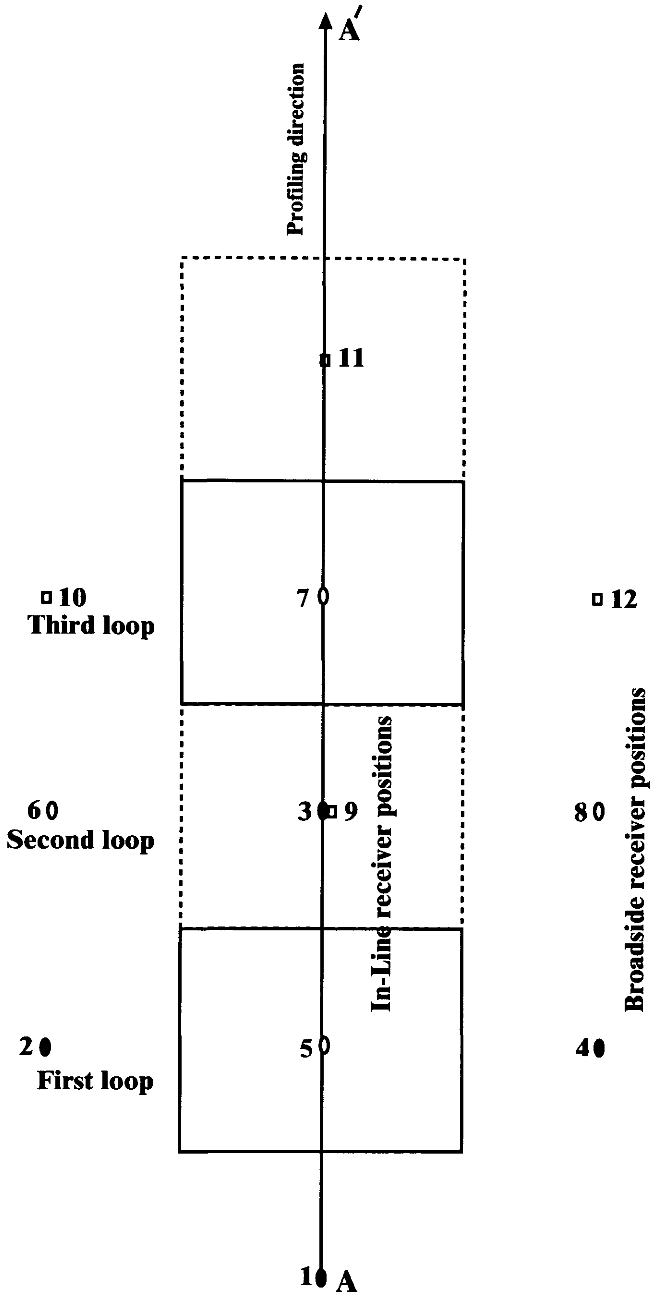

Figure 7.3: Sketch map showing azimuthal TEM survey design. For each transmitter (Tx) loop position, readings are made at 4 different azimuths, with the receiver positioned 20 m from the Tx loop centre.

data with the Rx in different azimuths. As shown in Figure 7.3, the azimuthal TEM soundings (1, 2, 3 and 4) were measured using the first transmitter loop; the next soundings (5, 6, 7, and 8) employed the second loop, while the next four soundings (9, 10, 11, and 12) related to the third loop position and so forth. Note that the two soundings labelled 3 and 9 represent the same site occupied by the receiver but for different Tx loops. Any differences between such coincident soundings might be suggestive of heterogeneity at the site which is one of the advocated advantages of this surveying strategy (M. Meju, 2000, private comm.). This TEM grid–type surveying can be termed a contiguous loop azimuthal sounding method. Eleven conventional central loop TEM soundings were also recorded along profile 20W for comparison with the azimuthal TEM data.

The various TEM data were acquired using the Geonics PROTEM 47 equipment to obtain information at very shallow depths, and at least two soundings were measured at each site using different gains for consistency checks. To overcome random noise problems as much as possible, several decay curves were stacked per sounding. The instrument consists of a small, lightweight, battery-operated transmitter with a very fast turn-off time to enable the near surface response to be measured. It can be used with three different base frequencies of 25, 62.5 or 262.5 Hz for 50 Hz power line frequencies. The maximum current output is 3 A, the turn-off time for this current and for a 20 m loop is $2\,\mu s$. The PROTEM receiver measures the rate of decay of the induced field in nV/Am^2. It can measure all three components of the magnetic field but only the vertical component was recorded in this study. It has 20 time gates geometrically spaced throughout the time range of each base frequency, and a solid-state memory for storing up to 3300 data sets. At a higher base frequency (262.5 Hz), the effective time gate starts at 0.0069 ms. The gain is controlled from the console unit. The Rx coil is a multi turn cable encased in a solid insulating material with its own preamplifiers on a vertical limb. It is about 0.75 m across but has an effective area of 31.4 m^2.

7.3.2 DC resistivity and VLF surveys

Thirty-six DC resistivity soundings were recorded along survey lines 20W, 20E, 40E, and 60E (8, 6, 10, and 6 soundings, respectively) using a conventional Schlumberger array with maximum AB/2 of 80 m, and E-W electrode spreading axis (which might be the dominant strike direction). Six soundings were also performed along profile 20W using a maximum AB/2 of 80 m but with N-S electrode spreading axis. Additionally, resistivity data were collected along profile 20E in the form of resitivity profiling using Wenner array with electrode spacing and station intervals of 10 m. VLF data were recorded using the Geonics EM16 instrument along survey lines 20E, 40E, and 60E with a station interval of 10 m. The location of these TEM/VLF/DC survey lines is shown in Figure 7.2.

7.4 Processing and simple interpretation of the TEM data

The short offset azimuthal TEM (SoTEM) field data are presented in the form of stacked voltage profiles, contour maps, and quasi–3D maps of apparent resistivity and voltage response for selected channels. The SoTEM data were initially plotted with respect to the receiver position and also at the mid point between the transmitter and receiver and compared with the other available data. It was found that the location of the anomalous zones (probably fracture zones) in the SoTEM profiles for data plotted at the receiver position, rather than midpoint between the transmitter and receiver, coincide with the position of the anomalous zone deduced from central-loop TEM and the conventional methods (VLF and DC resistivity soundings and profiling) used in this study and which are known to be effective techniques for detecting fracture zones in crystalline basement terrains (Pedersen et al., 1994). Therefore, it was decided to present the SoTEM field data at the receiver position rather than the midpoint between the transmitter and receiver as shown in the following sections. The conventional central-loop data were transformed into resistivity versus depth sections. In addition, the results from 1-D modelling are presented for the central-loop TEM method.

7.4.1 Line 20W

The voltage responses at all channels for all profiles were plotted first in a logarithmic scale against distance. It was found that the TEM anomalies do not extend beyond the first six channels and vanished after channel number 6 (0.0263 ms). Figure 7.4 shows a selected example of this response pattern for the first nine channels along line 20W. It shows an anomaly at profile position 120 m. This is clearly seen only at the first six channels and therefore, only these channels have been selected for presentation in linear scale in order to see these features in more detail. The voltage responses for both central loop and part of the azimuthal (broadside) configurations are shown respectively in Figures 7.5 and 7.6. Notice that the voltage response values and anomaly patterns are very similar for both configurations, and this may indicate that the broadside short offset sounding data are valid for subsurface investigation at this site. There is a characteristic symmetric twin-peak TEM anomaly with depressed field values at the profile position 120 m. Based on the symmetry pattern (Weidelt, 1983), the anomaly may be interpreted as indicative of the presence of a vertical conductive zone (fracture-zone). The absence of a single peak anomaly at the earliest times (cf. Meju et al., 2001) suggests the absence of a thick

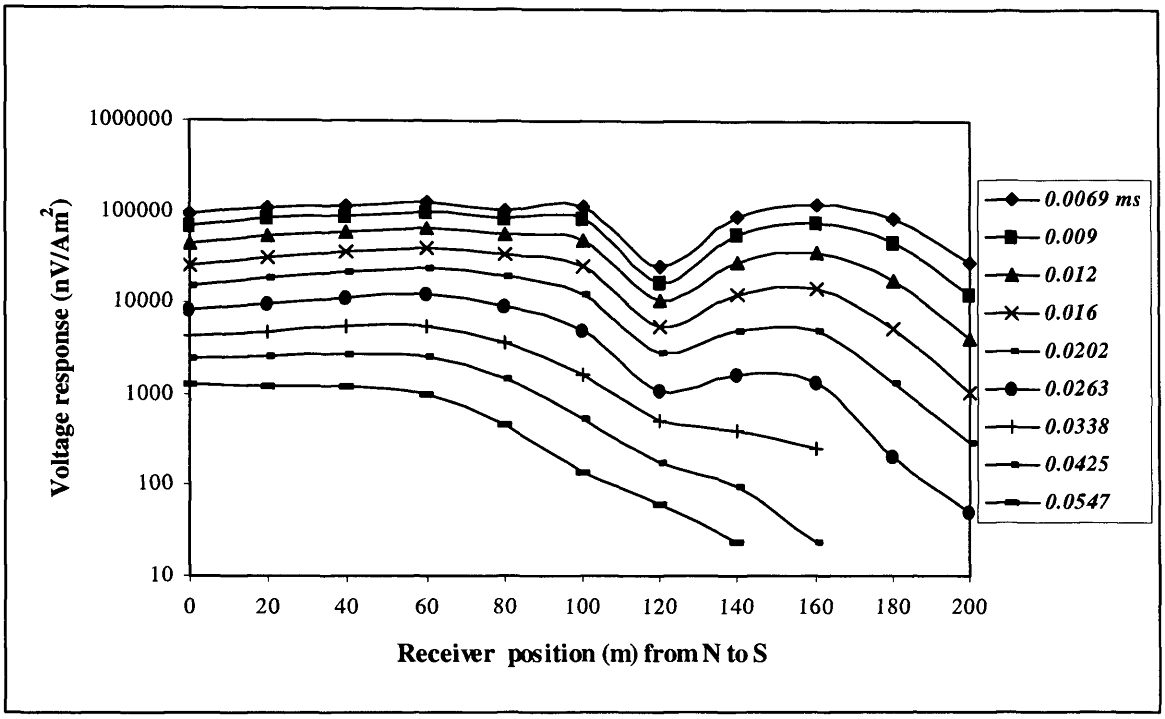

Figure 7.4: Broadside azimuthal TEM short-offset data for line 20W. The voltage decay data for the first nine channels are shown. The data were plotted in the receiver positions, which are 20 m away in the left hand side from the centre of the transmitter loop.

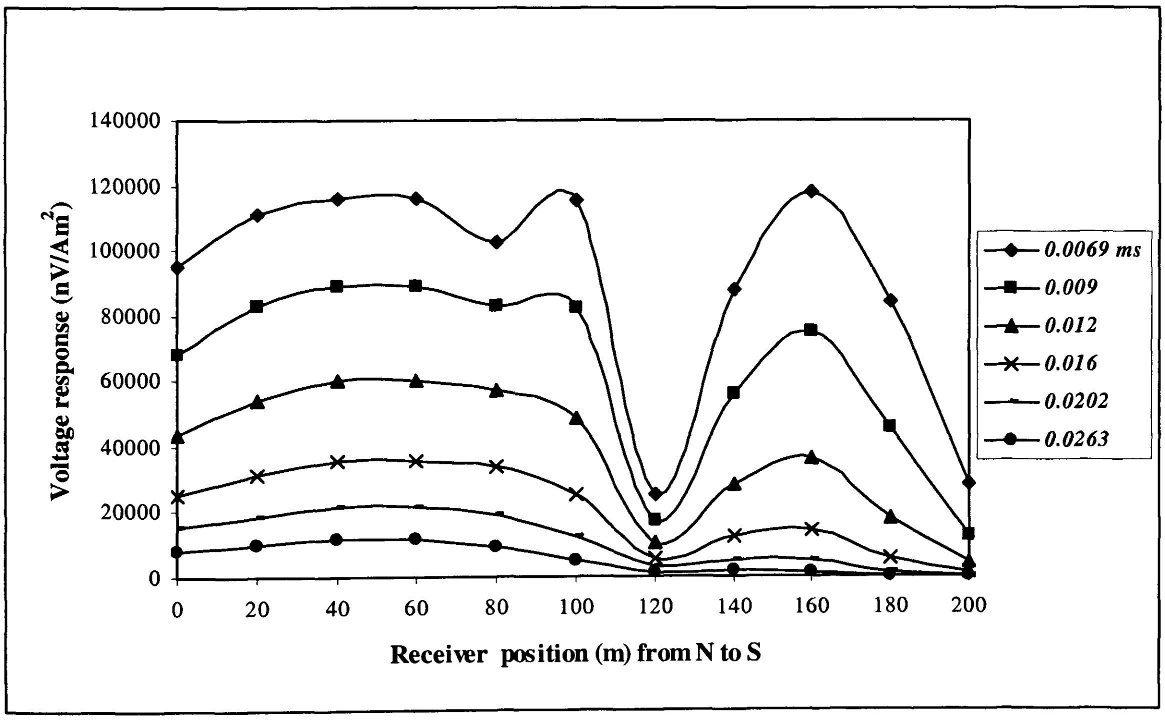

Figure 7.5: Central-loop TEM data for line 20W. Only the voltage decay data for the first six channels are shown. The receiver position is located in the centre of the transmitter loop.

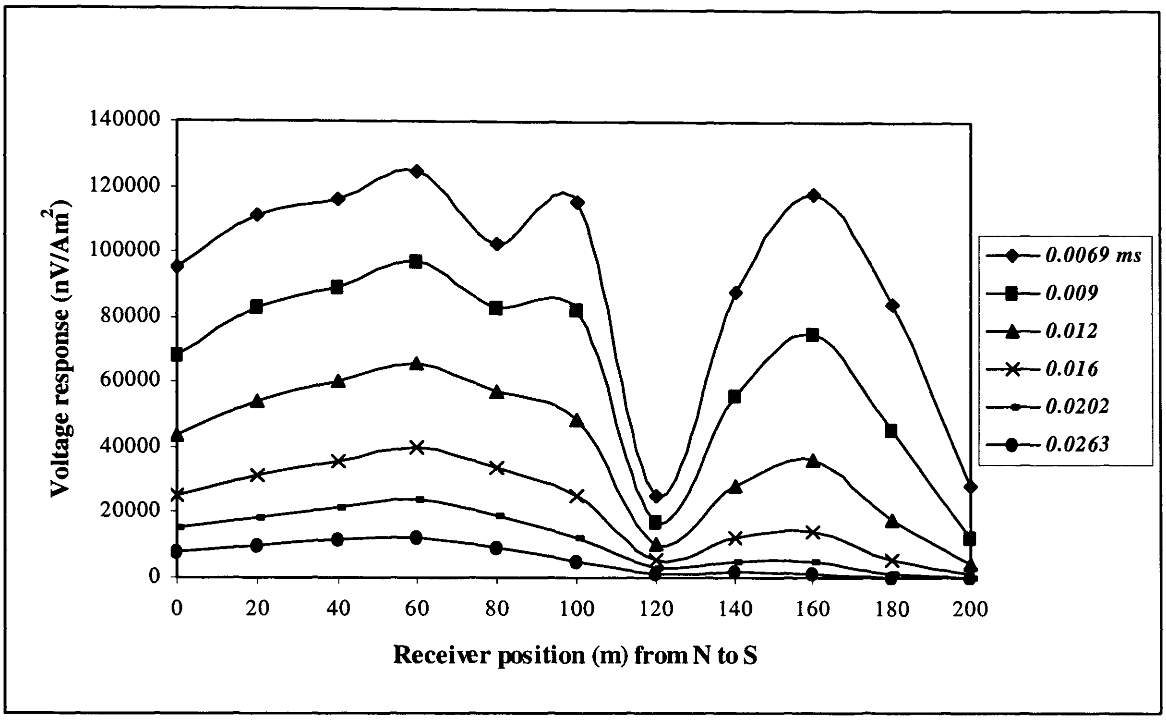

Figure 7.6: Broadside azimuthal short-offset TEM data for line 20W. Only the voltage decay data for the first six channels are shown. The data were plotted in the receiver positions, which are 20 m away in the left hand side from the centre of the transmitter loop.

overburden at this site. The voltage response values decrease dramatically towards the south since the basement outcrops at the area around line position 200 m (see Fig. 7.2).

The depth-transformed apparent resistivity data for central loop soundings (Meju, 1998) are shown in Figure 7.7; note the resistive vertical zone at site 120 m between two ambient low resistive zones equivalent to the twin peak anomaly at the same location. The contour lines generally slopes towards the north which is the dipping direction of the basement, except for the site of 120 m, the position of the expected fracture zone. The resistivity values increase with depth, particularly from south to north, which is the same dip direction of the granodioritic bedrock in the area of study.

The central loop data were inverted (Meju, 1992, 1994, 1996; Meju and Hutton, 1992) and the results are given in appendix D. An example of the inversion models is shown in Figure 7.8. The 1-D inversion results have been collated to form an approximate geoelectric section (Fig. 7.9). It shows two geoelectric layers; a low resitivity layer (29-90 ohm-m), correlated with mudstone and an underlying high resistivity layer (>770 ohm-m) interpreted as basement. The resistive basal layer slopes towards the north which is in agreement with the dip direction of the granodiorite at this site. An abrupt change in resistivity occurs at site location Q7 (120 m) and suggests the presence of a possible fracture zone. Note that the top layer suggested by 1-D modelling (e.g. Fig. 7.8) is not presented in this geoelectric section since there is a lack of data at the shallow depth (<10 m).

7.4.2 Line 0

Twenty-one soundings were conducted along line 0 using the azimuthal short offset loop configuration. The Tx loop was laid out along the survey line and each sounding was recorded twice from different loop locations as illustrated in Figure 7.3. One of the two soundings at each Rx station is for when the Tx loop is positioned north of the Rx position and the other is for when the Tx loop is positioned to its south. The voltage responses for were plotted in two profiles (Tx north and Tx south of Rx) for the first six channels for comparison. It is of interest to see, in addition to anomalous zones, if any differences can

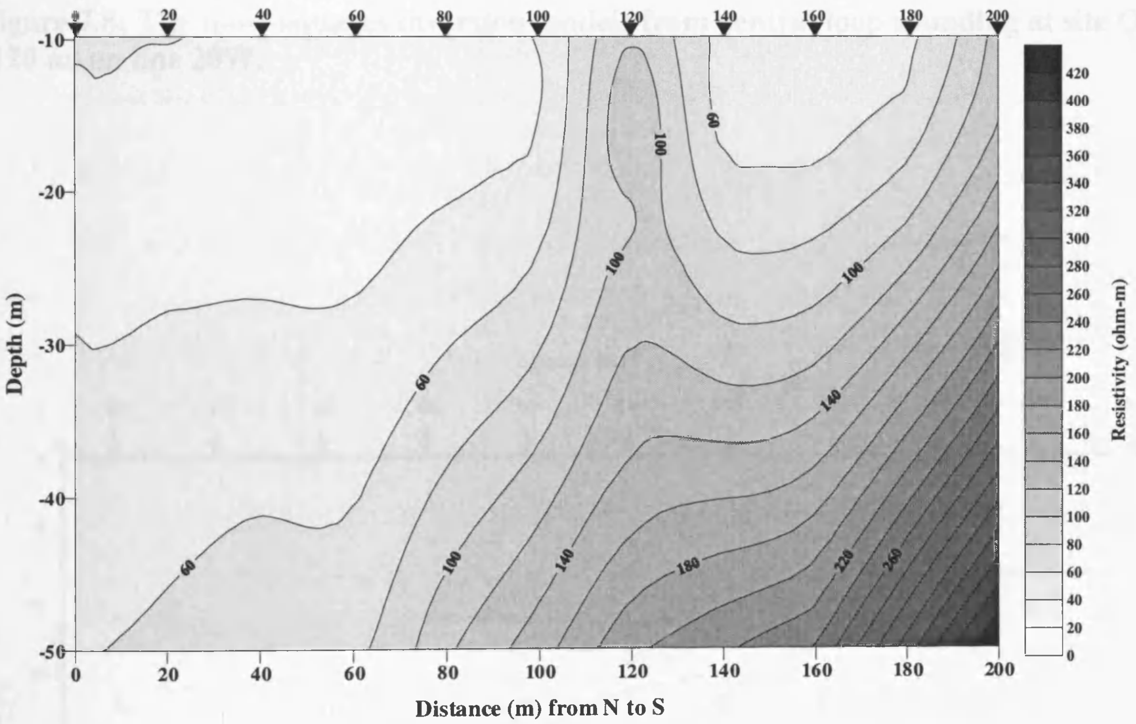

Figure 7.7: Resistivity contour map for central loop configuration for line 20W.

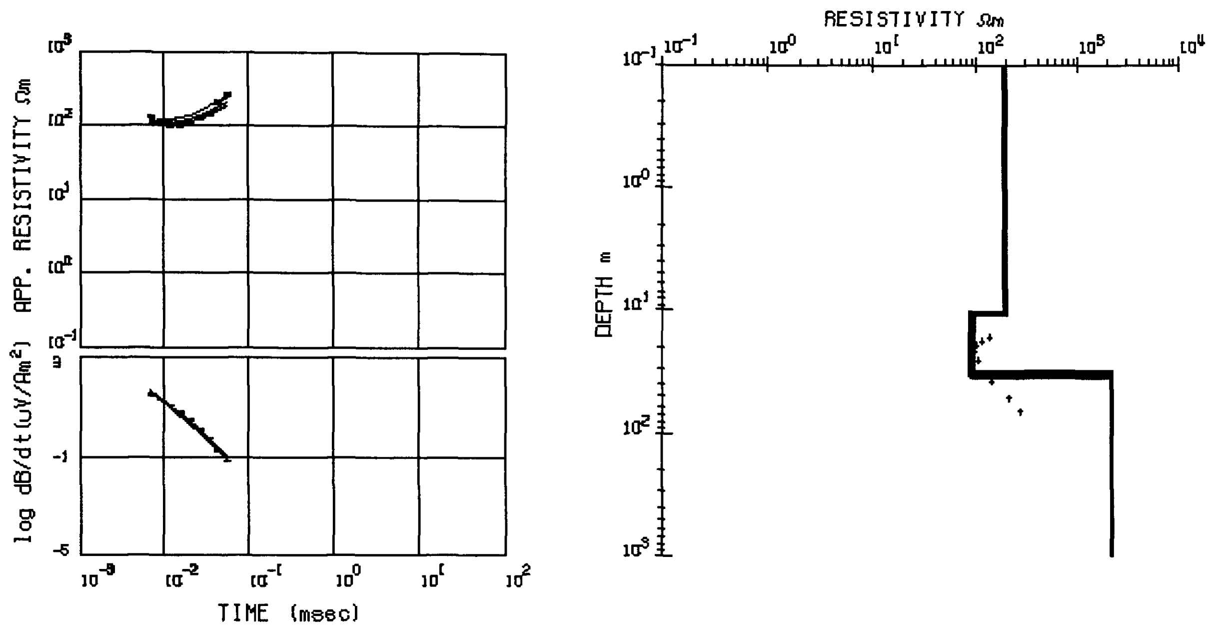

Figure 7.8: The most-squares inversion models from central loop sounding at site Q7 (120 m) on line 20W.

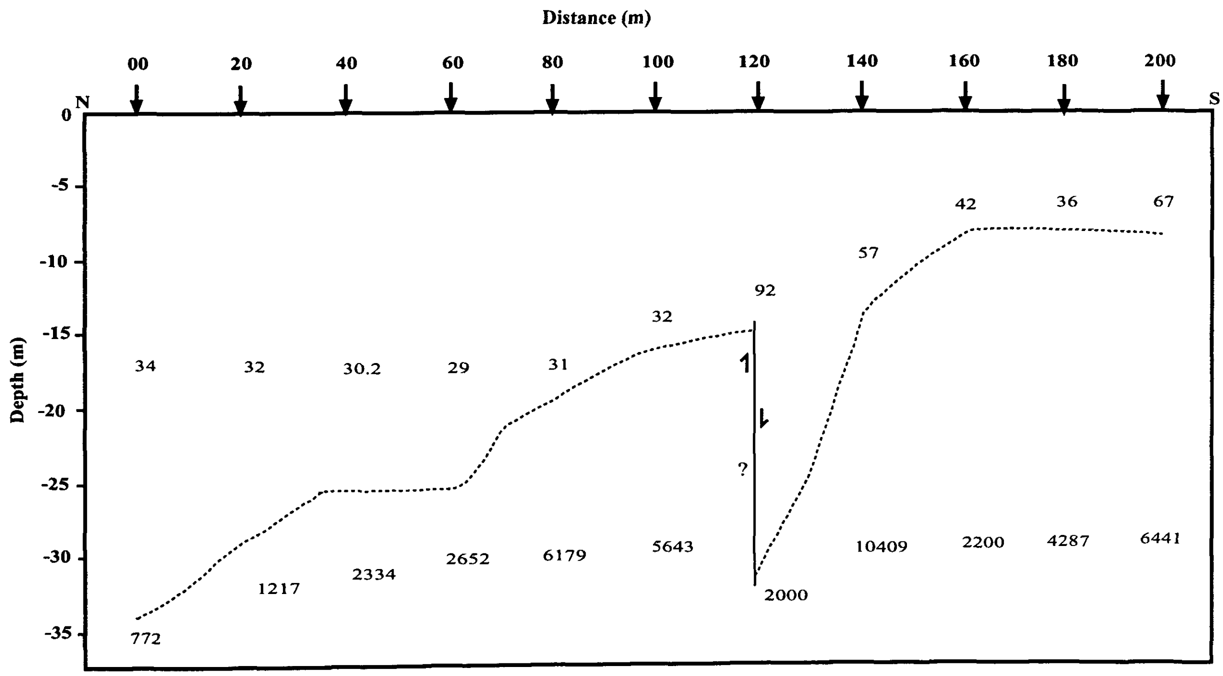

Figure 7.9: 1-D geoelectric section deduced from TEM central loop data for line 20W.

be detected in these two data sets that might suggest a heterogeneous subsurface. Figure 7.10 shows the TEM responses profile for which the transmitter loop was located north of the receiver position. An asymmetrical twin peak anomaly occurs with a depression centred at a line position between 100 and 120 m. Another anomalous zone (twin peak) is also seen at line position 60 m. The voltage response was affected by lithological variations and then diminished at line position 180 m where the contact between the basement and sedimentary rocks might appear near the surface. Figure 7.11 shows the voltage response along the same line 0 but with the transmitter loop located south of the receiver loop. The anomalous zone seen between line positions 100 m and 120 m (Fig. 7.10) was displaced to line position 120 m. In addition, the twin peak anomaly at line position 60 m is not clearer when compared to that shown in Figure 7.10. This may be interpreted to the effect of measurement from different transmitter position. This is in addition to the effect of lateral heterogeneities and the complex structure. The near surface sedimentary-basement contact is displayed at line position 200 m but with a close agreement or similarity with the basement outcrop (Fig. 7.2).

7.4.3 Line 20E

Figure 7.12 shows the TEM data collected on line 20E for eleven sounding positions. Only the voltage responses of the first six channels are plotted because the responses beyond these channels are nearly flat. An asymmetric twin-peak anomaly with a depressed value occurs at line position 100 m. This feature may be an extension of the anomalous zone seen at position 120 m on lines 20W and 0. Another small twin peak anomaly is apparent in the first three plotted channels at position 40 m and may be attributed to a small conductive zone or shallow inhomogeneities at this location. The voltage response reduces and becomes flat beyond line position 160 m, suggesting the closeness of basement to the surface.

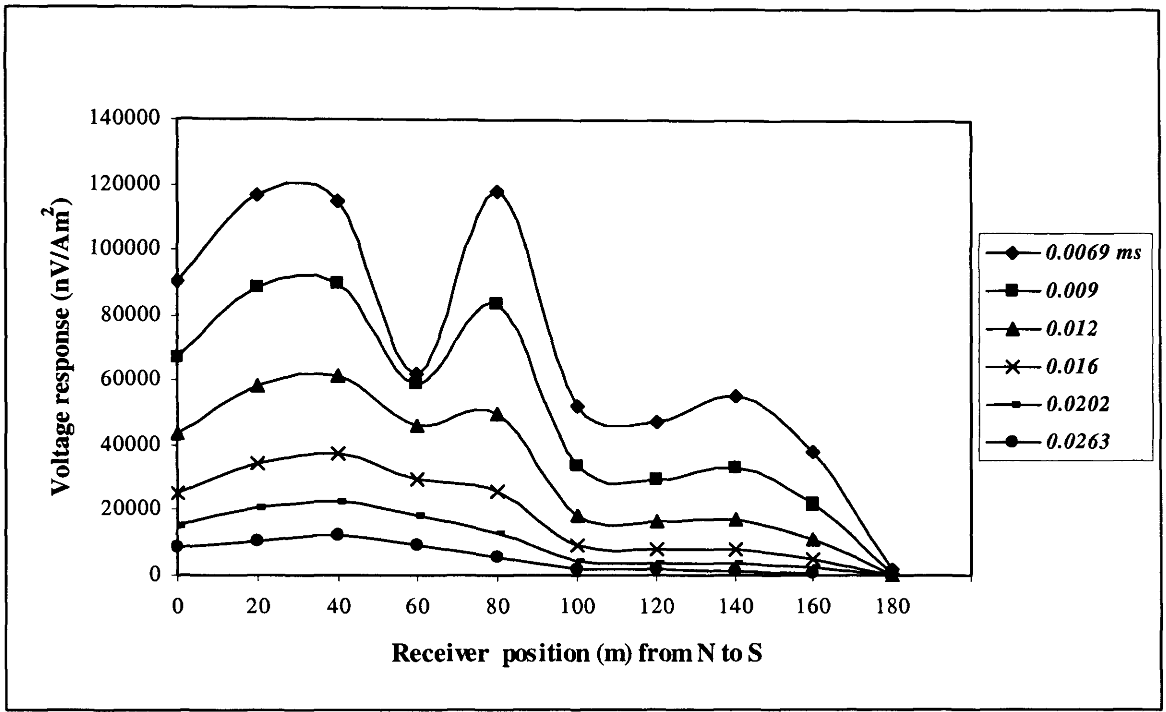

Figure 7.10: In-line azimuthal short-offset TEM data for line 0. The centre of the transmitter loop was located 20 m away north of the receiver position.

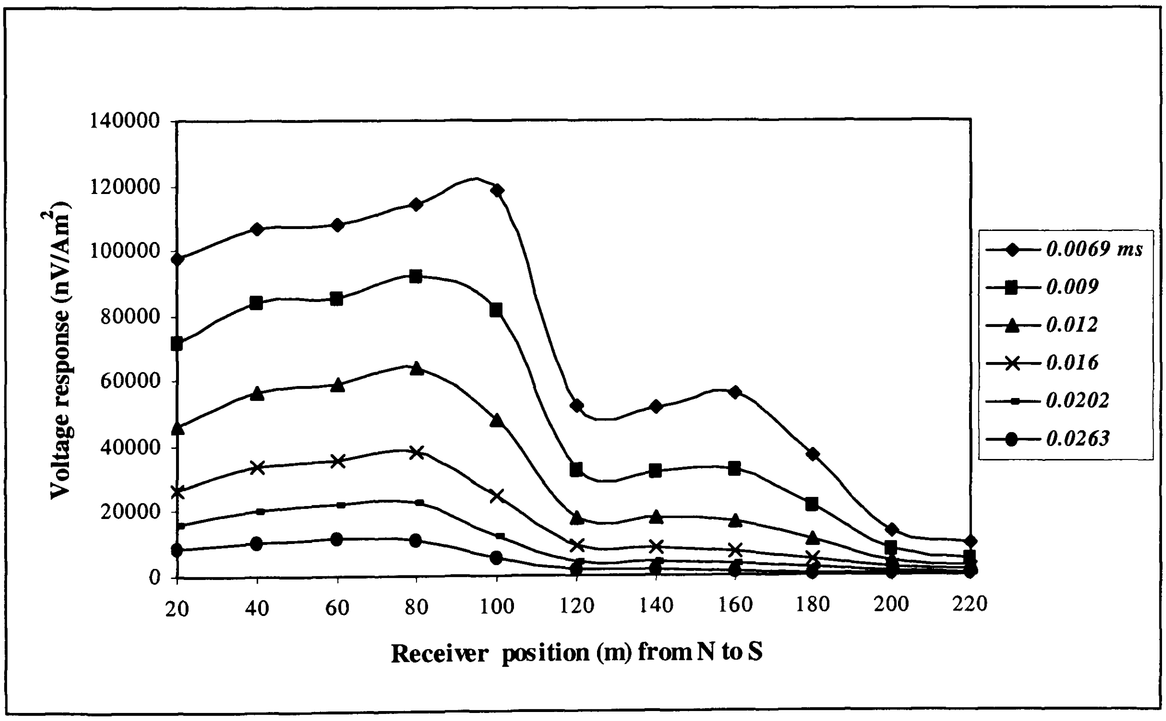

Figure 7.11: In-line azimuthal short-offset TEM data for line 0. The centre of the transmitter loop was located 20 m away south of the receiver position.

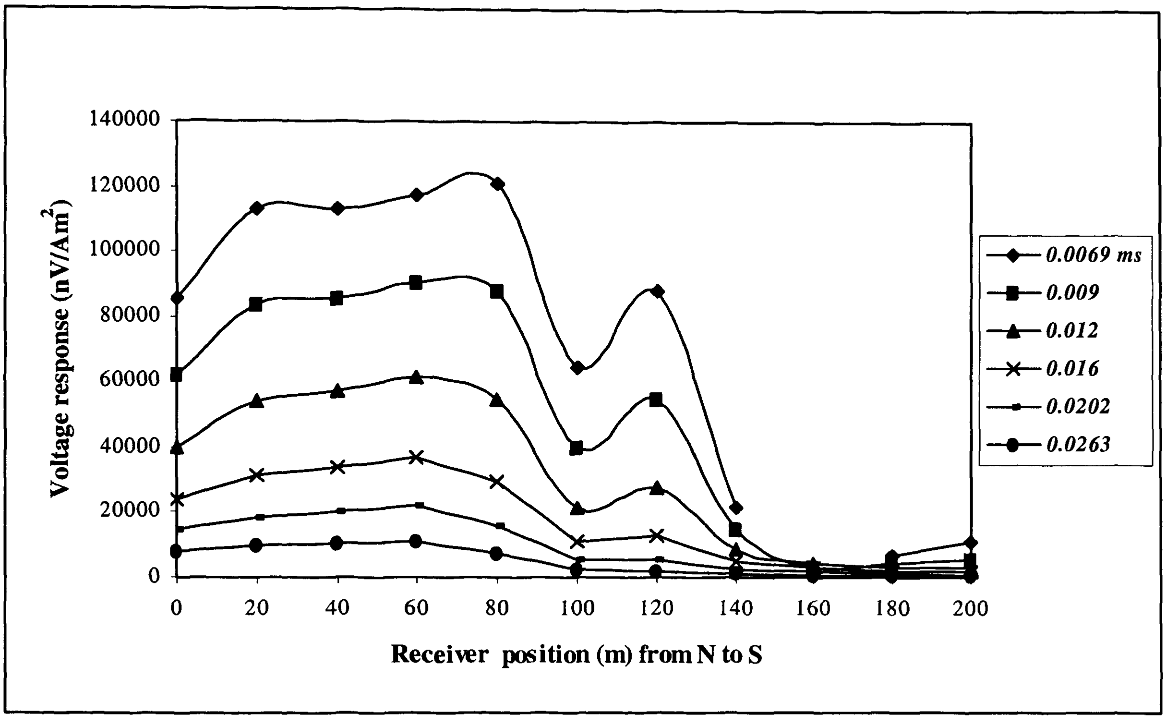

Figure 7.12: Broadside azimuthal short-offset TEM data for line 20E. The data were plotted in the receiver positions, which are 20 m away in the right hand side from the centre of the transmitter loop.

7.4.4 Line 40E

The voltage profiles for line 40E are shown in Figure 7.13. An interesting anomaly is the twin-peak feature occurring at profile position 140 m which may be related to the anomalous feature seen in the previous lines. Further south, the response decreases at line position 180 m suggesting a possible location of sedimentary-basement contact near the surface. A relatively more conductive zone is better illustrated at position 60 m than the adjacent positions. This response may suggest the presence of a more conductive overburden at this location.

7.4.5 Line 60E

The Tx loop was laid out on line 60E for azimuthal soundings to yield two data sets in the in-line configuration. Figures 7.14 shows the in-line voltage responses for which the transmitter loop was located north of the receiver position. As shown in this figure, a major fracture zone, indicated by twin-peak anomaly, is apparent close to line position 120 m. This feature might be an extension to the anomalous zone seen on the other profiles. There are also two twin-peak anomalies at line positions 20 m and 60 m. However, when the transmitter loop was located south of the receiver loop (Fig. 7.15), the expected fracture-zone located near 120 m was displaced to 140 m. In this configuration, the two conductive zones (positions 20 m and 60 m) displayed in Figure 7.14 disappeared. Note that there is no repetitive sounding at position 0 m to indicate whether the twin-peak anomaly at position 20 m (Fig. 7.14) can be confirmed. The differences between the two plots might be attributed to the effects of the heterogeneities and the complex structure of the area.

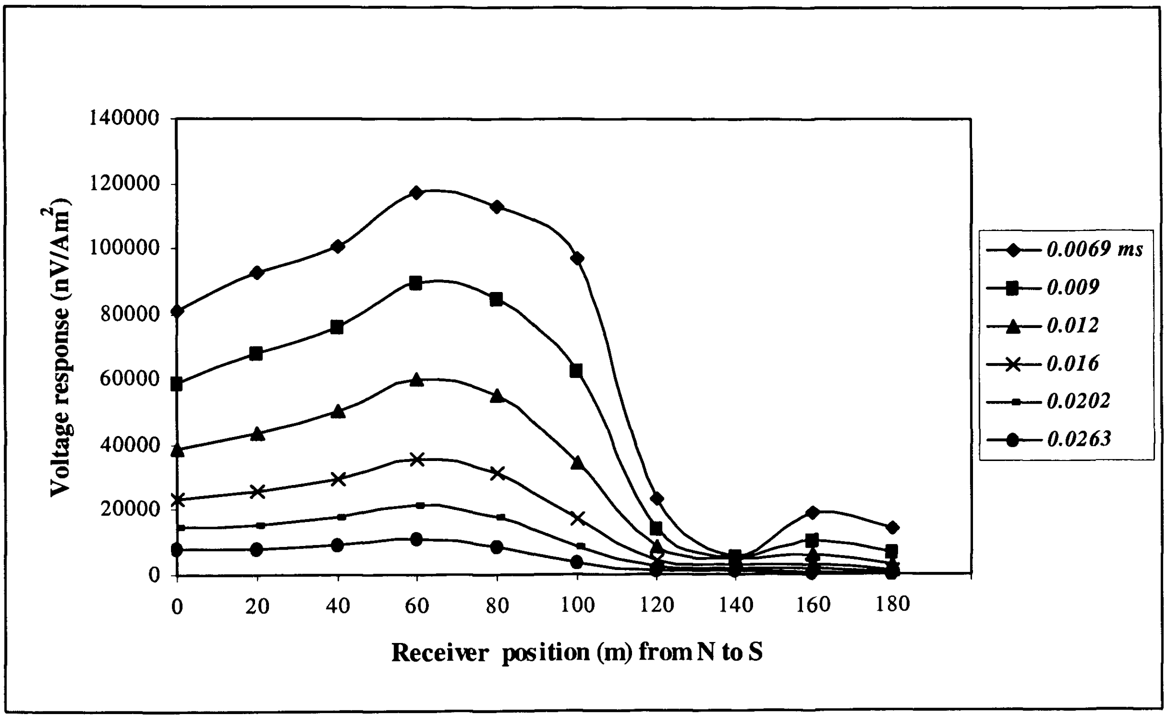

Figure 7.13: Broadside short-offset TEM data for line 40E. The data were plotted in the receiver positions, which are 20 m away in the left hand side from the centre of the transmitter loop.

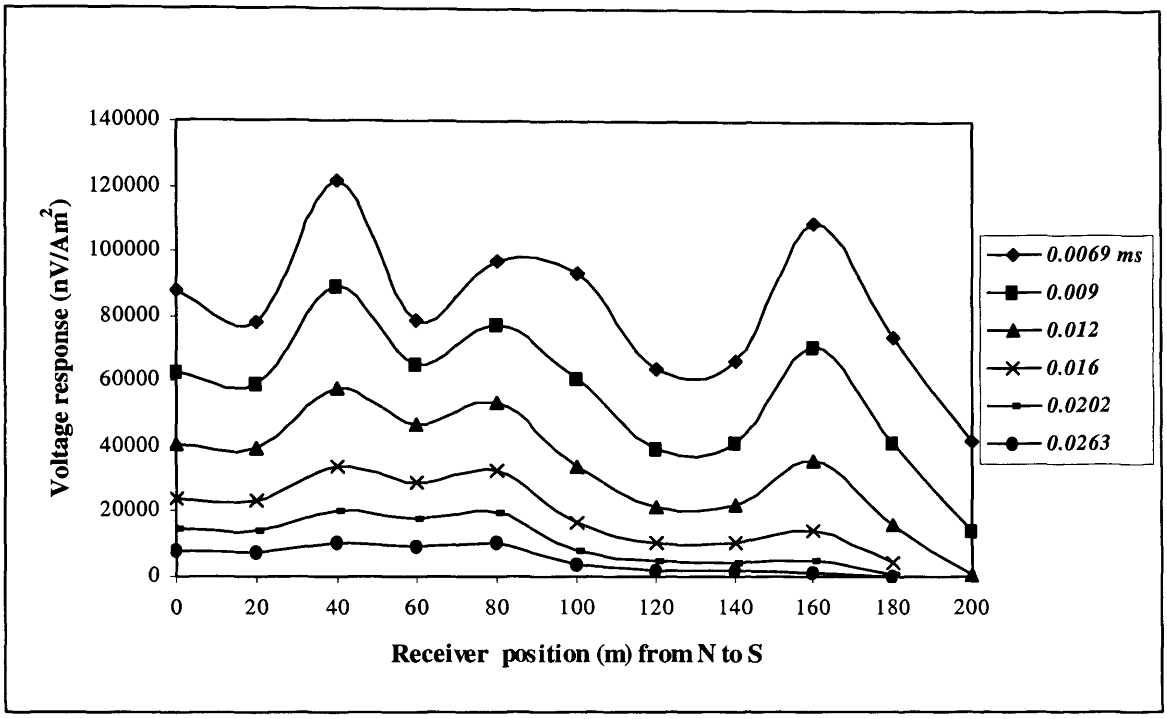

Figure 7.14: In-line azimuthal short-offset TEM data for line 60E. The centre of the transmitter loop was located 20 m away north of the receiver position.

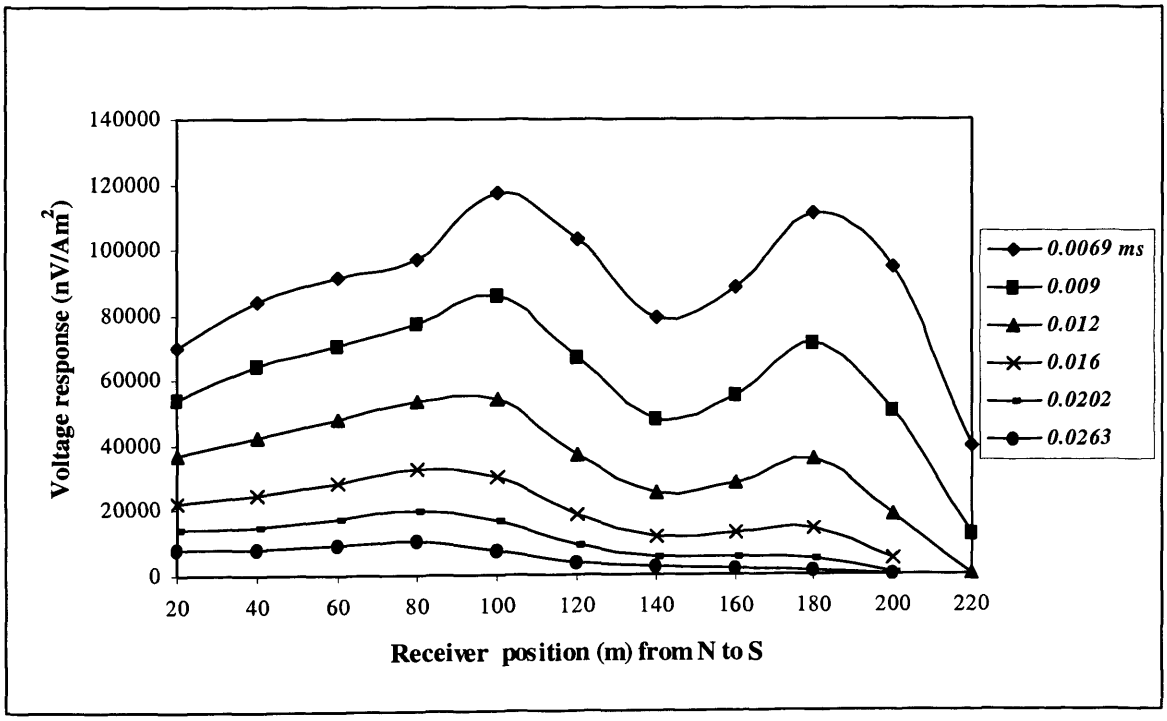

Figure 7.15: In-line azimuthal short-offset TEM data for line 60E. The centre of the transmitter loop was located 20 m away south of the receiver position.

7.4.6 Line 80E

TEM voltage profile for line 80E did not display any significant anomalies (Fig. 7.16) suggesting that the bedrock is not affected by significant fracturing along this line. Note that conductive zones appear at site positions 60 m and 160 m.

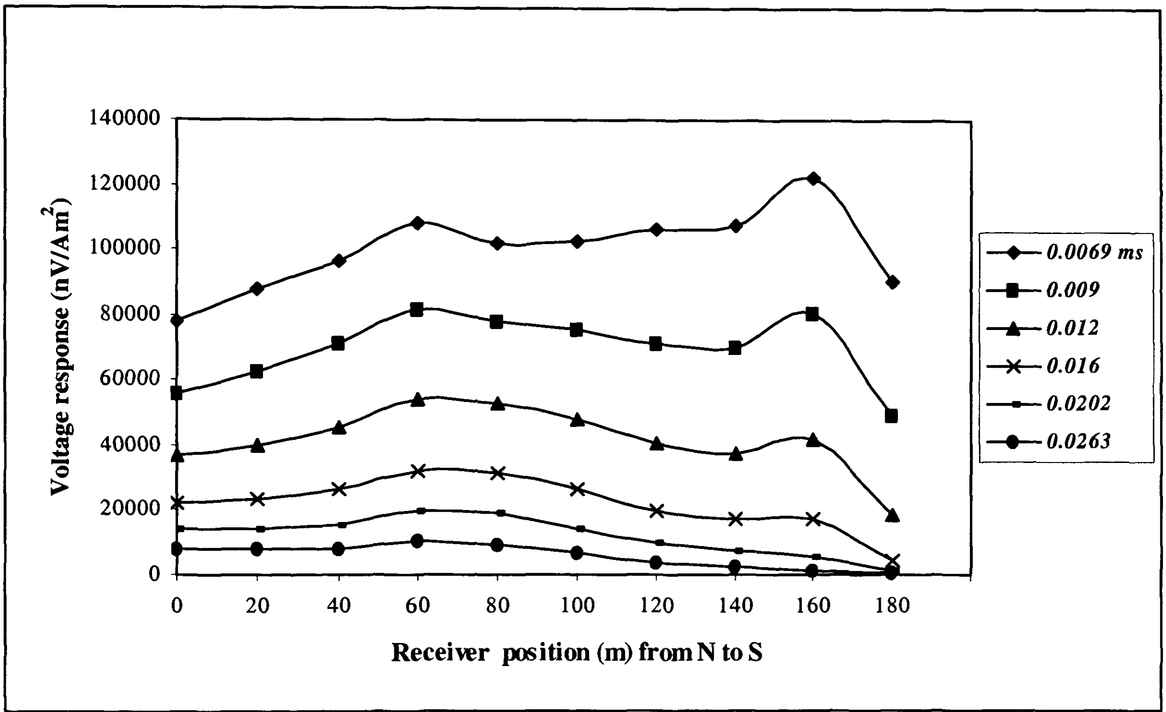

Figure 7.16: Broadside azimuthal short-offset TEM data for line 80E. The data were plotted in the receiver positions, which are 20 m away in the right hand side from the centre of the transmitter loop.

7.4.7 3D Contour maps of time slices

The voltage responses were converted to apparent resistivity using the late-time approximation (Kaufman and Keller, 1983). Both voltage responses, and their apparent resistivities are presented in the form of contour maps and quasi three-dimensional images at the same time windows to trace the anomalous zones all over the area and to see whether there might be an improved visual trend identification. Figures 7.17a and 7.17b are contour maps of the voltage responses and apparent resistivities for channel 2 (0.009 ms). The contoured voltage values decreases towards the south where the basement outcrops or is very near from the surface (e.g. at position 180 m on profile 0), and generally increase towards the north, where sedimentary cover increases. According to the low response of the outcropping basement, a possible near surface sedimentary/basement contact is shown (solid lines). The bedrock surface appears to be dissected by a fracture zone as indicated by a lower voltage response between two highs. This zone is possibly located between positions 100 and 140 m on lines 20w to 60E. The trajectory of this fracture zone (dashed lines) is also shown. On the other hand, the resistivity map displays high resistivity values between two low resistivities correlating with the inferred fracture zone. The expected outcropping granodiorite/sediment contact is also shown by varying resistivities. The 3-D view maps of voltage response and apparent resistivities for the same channel (0.009 ms) are shown respectively in Figures 7.18a and 7.18b. The fracture zone appears in the voltage response in the form of a trough between two peaks. However, major troughs appear to mark the contact between the cover rocks and the bedrock (e.g. position 180 m on profile 0), while the fracture zone in the 3-D view map of resistivities appears as peaks. In the same way, and to trace these anomalous features at greater depth, the voltage responses, apparent resistivities, and their 3-D view are presented respectively in Figures 7.19a, 7.19b, 7.20a, 7.20b for channel 4 (0.016 ms). These figures illustrate the same features discussed above, and suggest an extension of the fracture zone to a greater depth. It was found that the presentation of data in the form of resistiviy or voltage response yielded equivalent structural images at this site. However, the 3-D view maps differed for both responses types, with the voltage responses giving a clearer image than their equivalent apparent resistivities.

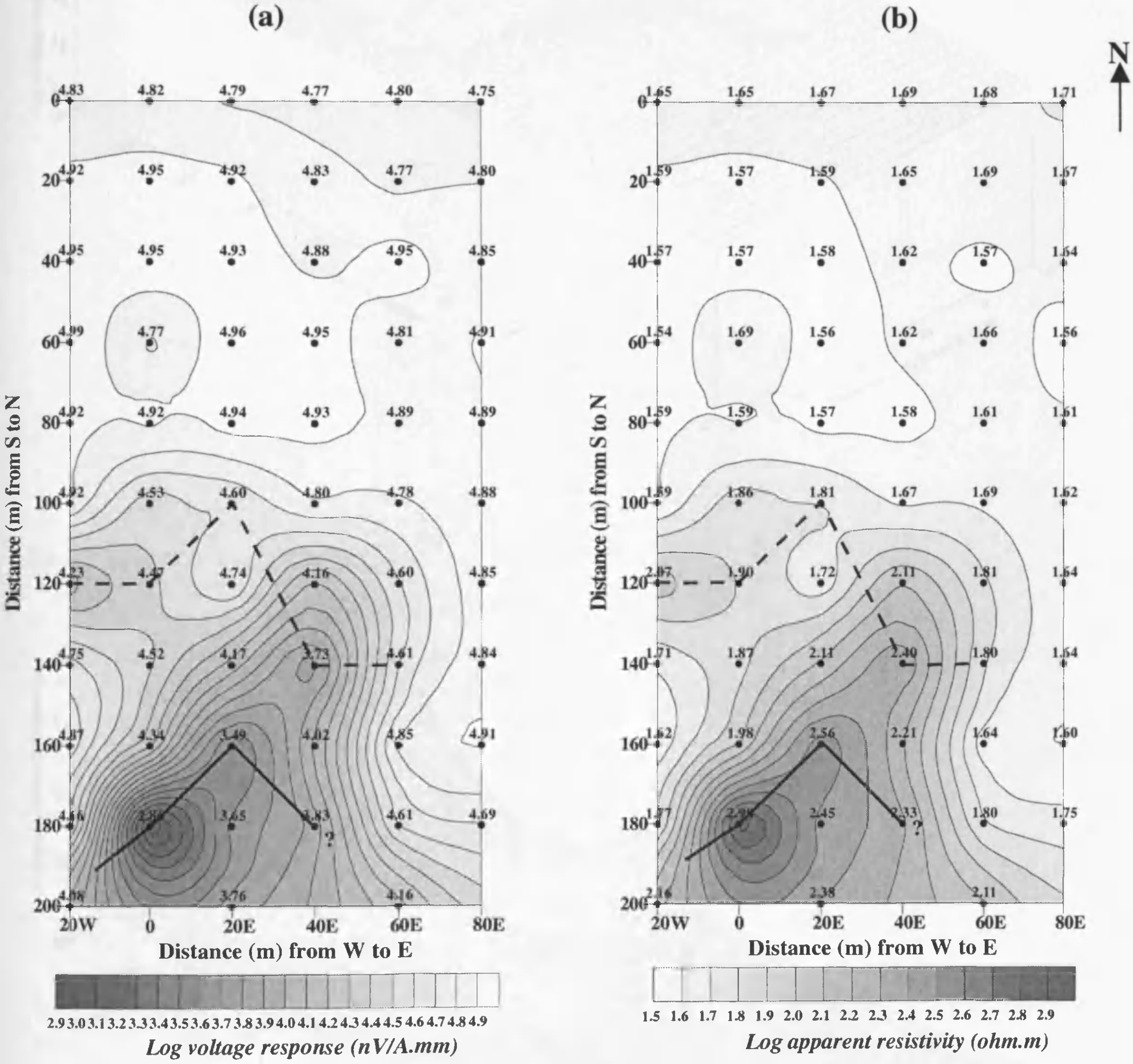

--------- *Inferred trace of major fracture zone*

——— *Inferred trace of near surface sed./bas. Contact*

Figure 7.17: Contour map (plan view) of voltage responses (a) and apparent resistivities (b) from azimuthal configuration for 0.009ms.

a)

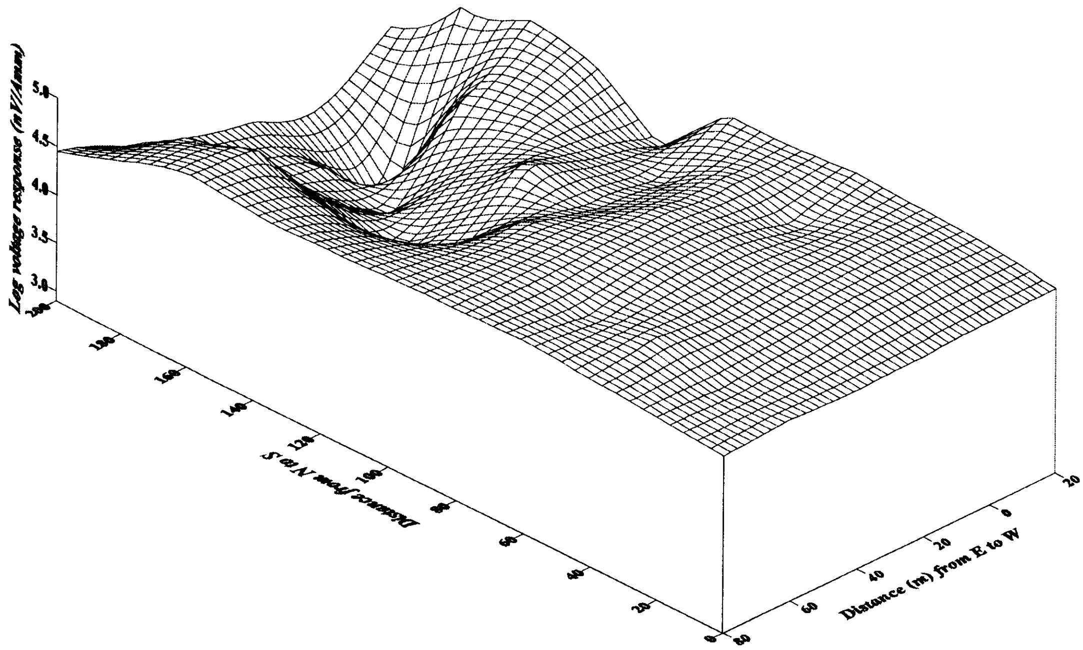

b)

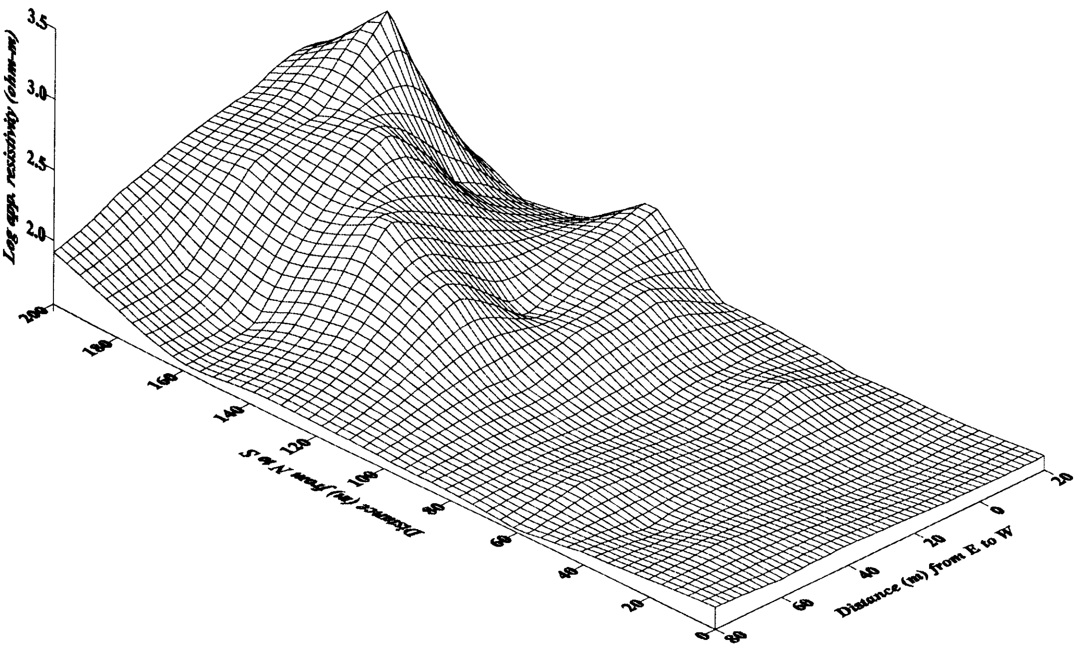

Figure 7.18: Quasi three-dimensional view maps of voltage responses (a) and apparent resistivities (b) from azimuthal configuration for 0.009 ms.

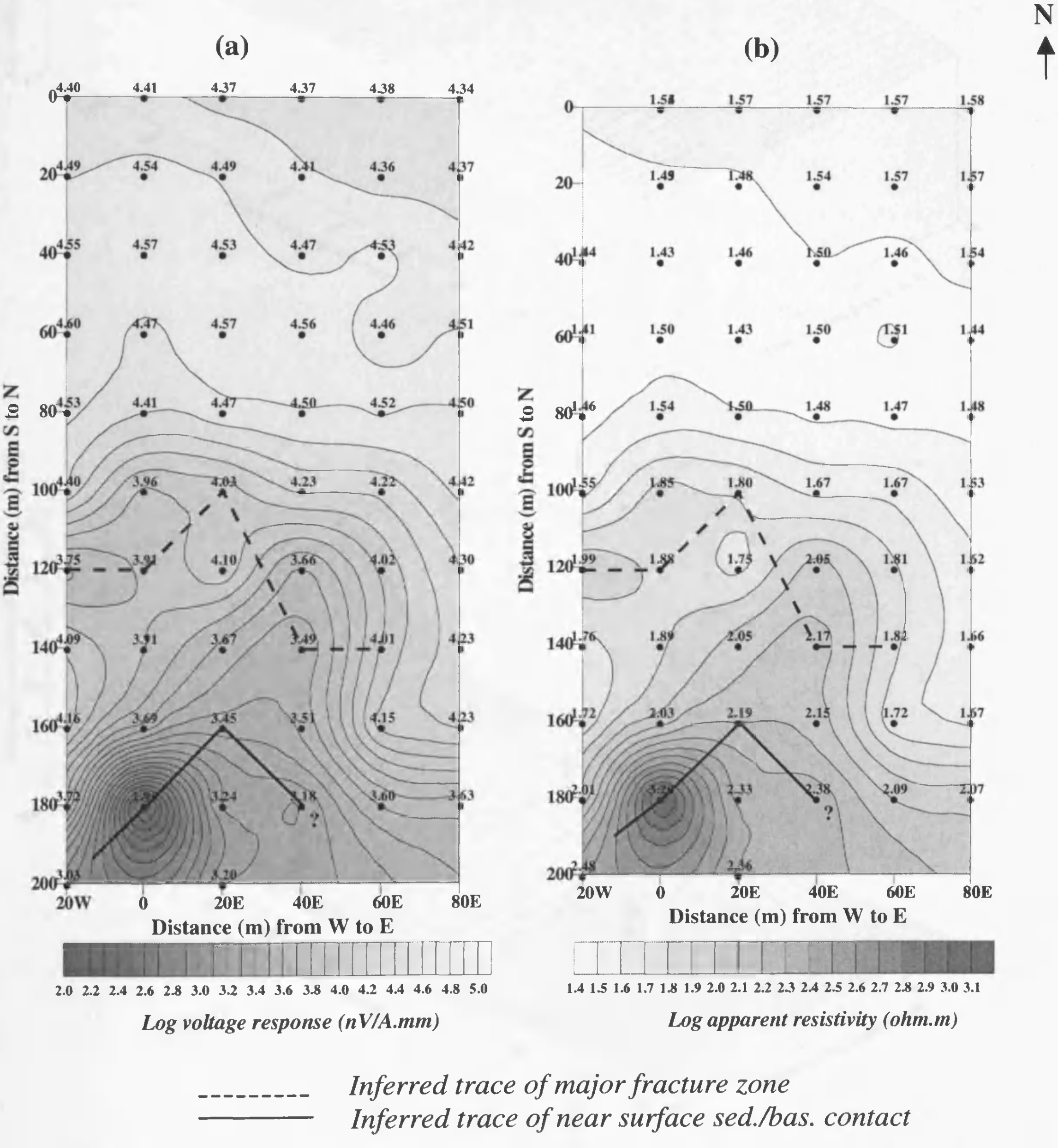

Figure 7.19: Contour map (plan view) of voltage responses (a) and apparent resistivities (b) from azimuthal configuration for 0.016 ms.

a)

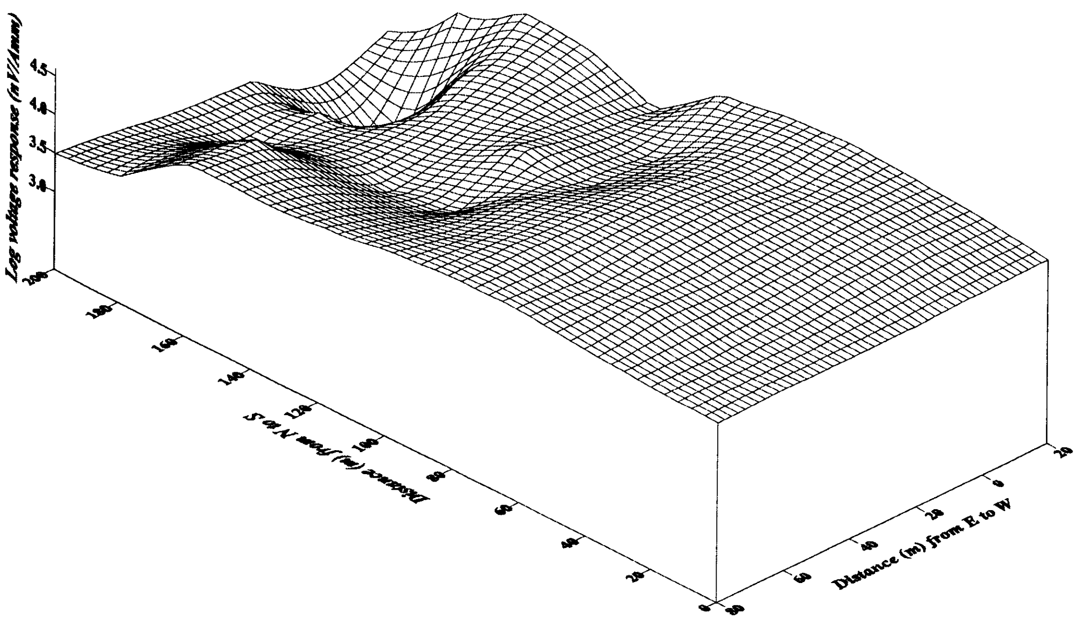

b)

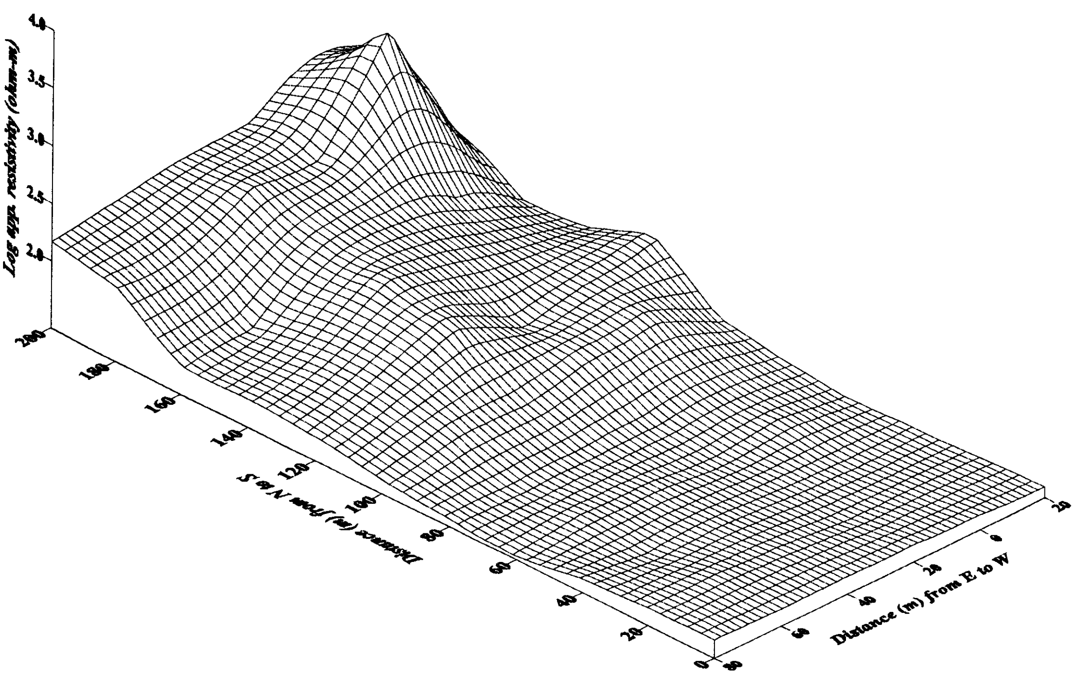

Figure 7.20: Quasi three-dimensional view maps of voltage responses (a) and apparent resistivities (b) from azimuthal configuration for 0.016 ms.

7.5 DC resistivity (1-D inversion) and VLF analysis

The VES data measured with E-W electrode expansion axes (and N-S in the case of line 20W) were inverted using a 1-D scheme (Meju, 1992) to reveal the subsurface resistivity distribution at each site (see appendix C). These 1-D inversion results have been collated to form geoelectric sections. The damped most-square inversion scheme (Meju and Hutton, 1992) was also applied to the DC resistivity data for line 20W to account for non-uniqueness. Figure 7.21 shows the typical inversion models for two stations (Q15 , Q50 on line 20W; the rest is in appendix C). As shown in Figure 7.21, the most-squares range of parameters is small due to the small observational errors. Notice that the 1D models agree with the resistivity-depth transformation (Meju, 1995), from which the starting models were generated. This is often the case over 1-D stratified formations and may suggest that layered sediments overlie the granodiorite at these positions. Figure 7.22 shows the geoelectric section for line 20W for Schlumberger soundings with a N-S spreading axis. The geoelectric section for soundings with an E-W spreading axis is shown in Figure 7.23. The two geoelectric sections show three geoelectric layers of variable thicknesses; 1) a possible topsoil or drift deposits with high resistivity values (> 200 $\Omega.m$) and a maximum thickness of 1.5 m; 2) an underlying low resistivity layer (7.8-49 $\Omega.m$) possibly mudstone with a maximum thickness of 20 m at the northern segment; and 3) a resistive basal layer (basement) with irregular topography which is more or less flat towards the south from the profile position 120 m. These sections also show a lateral change in resistivity structure around line position 120 m, and since there are no DC resistivity soundings between line positions 105 m and 150 m, an inferred fault was constrained at line position 120 m according to the results from TEM data along the same line (see Fig. 7.9). This anomaly is evident along the 1-D model of N-S spreading axis when compared to that deduced from the geoelectric section of E-W spreading trend (the expected dominant strike direction).

The results from the previous seismic refraction survey (Ahmad, 1993) along the same line (Fig. 7.24) indicate three distinct velocity layers; 1) drift deposits of 490-700 m/sec, 2) mudstone layer of 1700-2000 m/sec, and 3) bedrock (granodiorite) of 4200 m/sec. The thickness of the drift deposits is relatively similar in both models (seismic and electrical) with some difference at the southern segment. The depth to the basement varies due to the variation in dip, with subsequent variations in the thickness of mudstone in both seismic and electrical models. The approximate dip direction of the basement topography derived from seismic section at position 55 m, directed towards the north, is similar to that inferred from the 1-D geoelectric model with N-S spreading axis but has a slight difference in depth. In addition, at position 120 m, the seismic section shows an abrupt change in the gradient of dip towards the south which is inferred from DC and TEM data as the position of a fault or fracture zone. However, the outcropping basement to the south (see Fig. 7.2) indicates that the bedrock is dipping towards the north contrary to that derived from seismic section and to some extent agrees with TEM-DC results.

a)

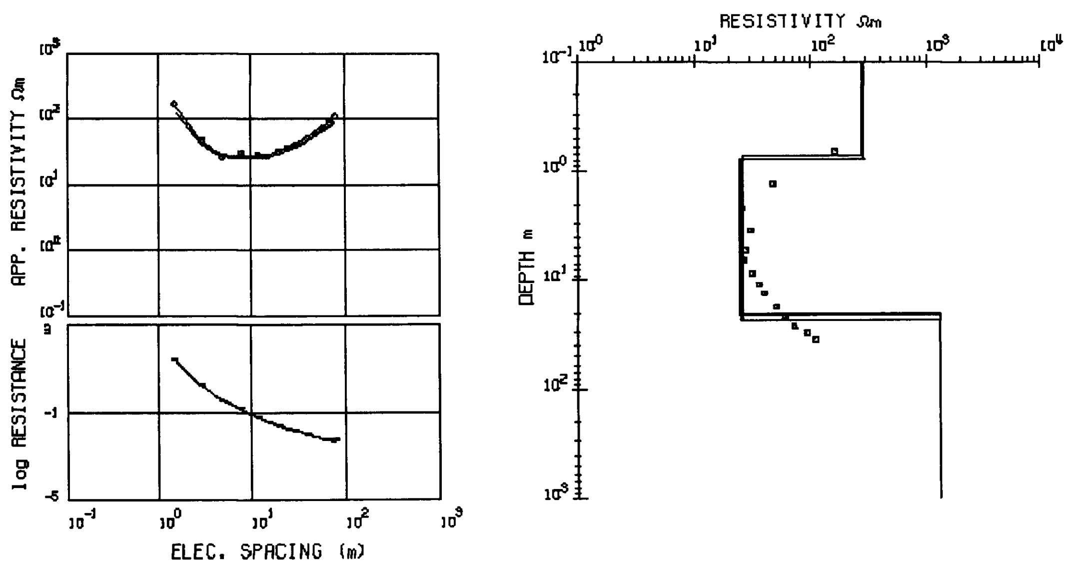

b)

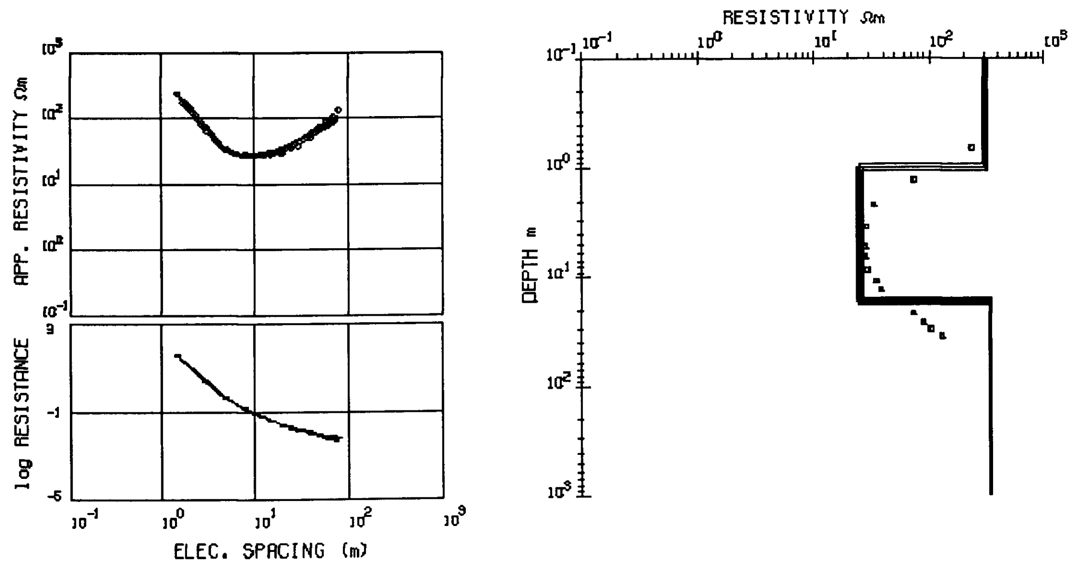

Figure 7.21: The most-squares inversion results for DC resistivity data at position 15 m (a) and 50 m (b) on line 20W (N-S electrode spreading axis). The square symbols in the right hand plot represent the results of simple resistivity-depth transformation (Meju, 1995).

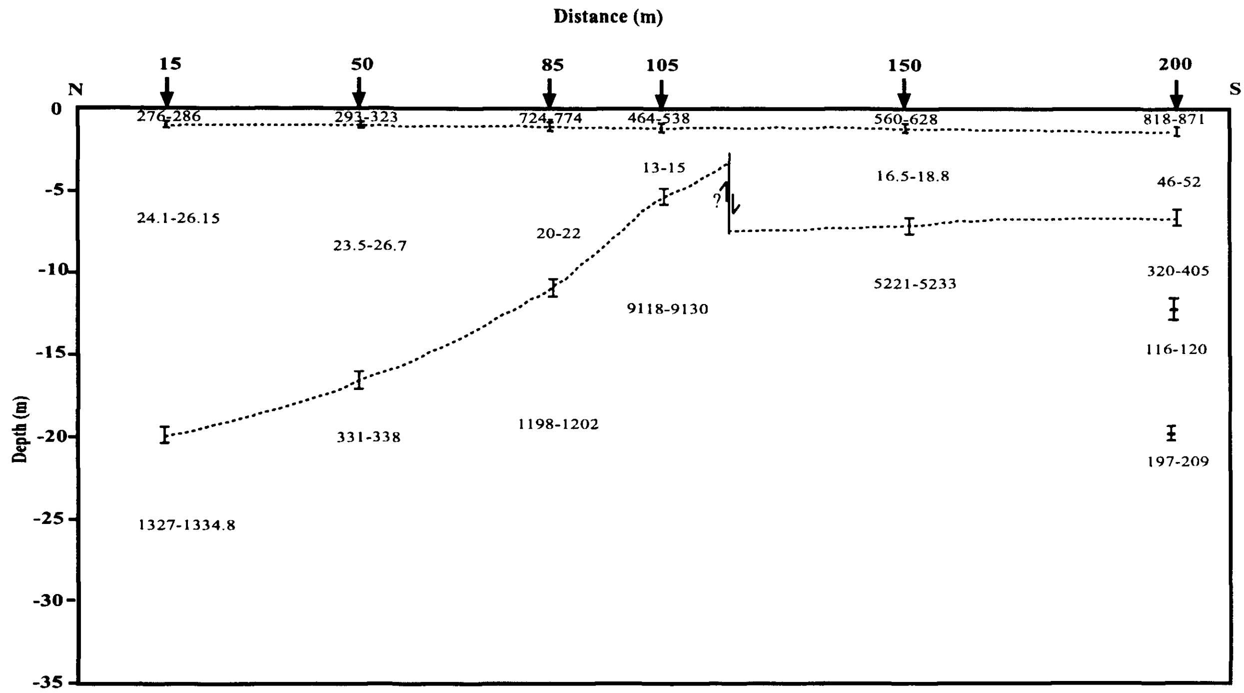

Figure 7.22: Interpretative geoelectric cross-section for line 20W (N-S electrode spreading axis).

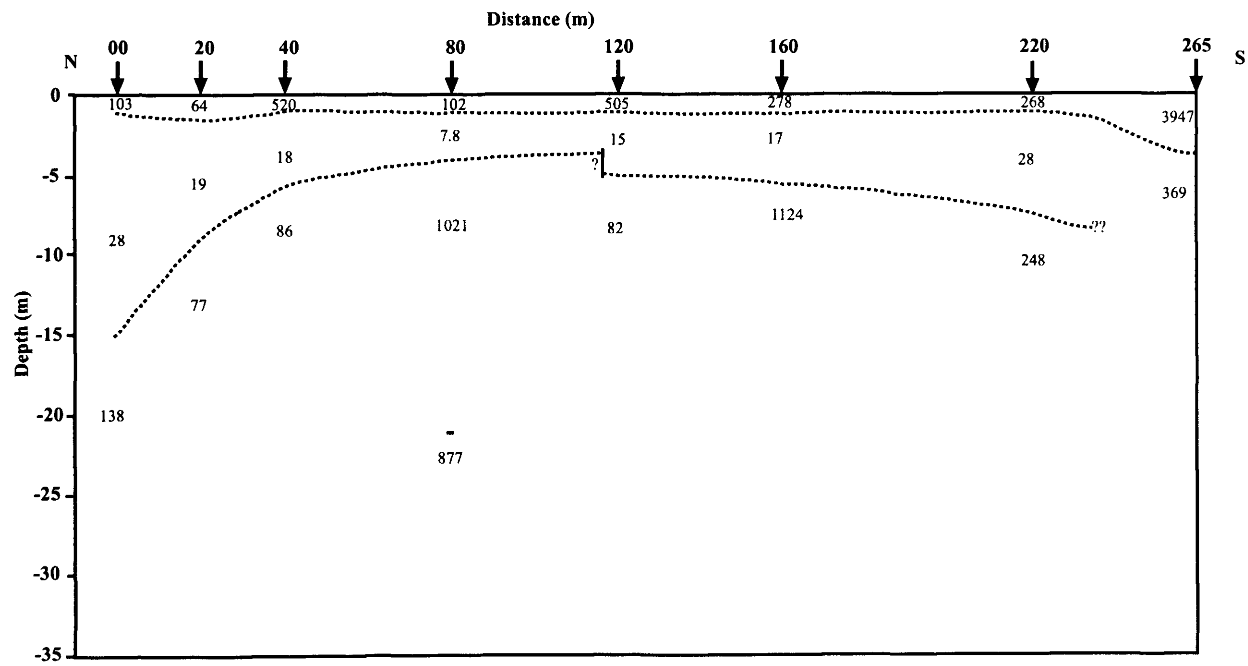

Figure 7.23: Interpretative geoelectric cross-section for line 20W (E-W electrode spreading axis).

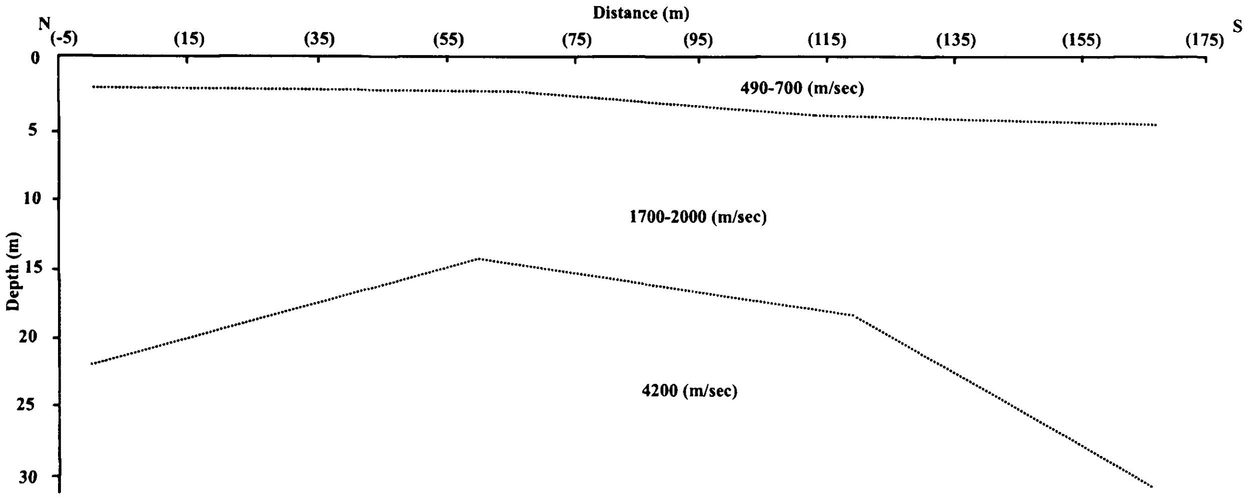

Figure 7.24: Depth to bedrock under line 20W based on seismic refraction interpretation (Ahmad, 1993).

The geoelectric section from the 1D models for line 20E is presented in Figure 7.25. It consists of three geoelectric layers; a top layer of moderate resistivity (>88 $\Omega.m$) interpreted as possible drift deposit, a second layer of lower resistivity (29-201 $\Omega.m$) interpreted as mudstone, and the highly resistive (>500 $\Omega.m$) basement. Two fault- or fracture-zones are inferred along this line; the first is at a line position 40 m and the other is at line position 100 m. These two anomalous zones correlate with those deduced from TEM profiling (Fig. 7.12). The result of Wenner resistivity profiling using a constant separation of 10 m (Fig. 7.26) along this line shows a change in resistivity at positions 100 m and 190 m, but not at position 40 m, where there might be a change at greater depth. The higher resistivity at position 190 m may be interpreted as the effect of near-surface granodiorite.

The geoelectric section for line 40E (Fig. 7.27) identifies three possible disrupted zones near positions 30 m, 60 m and 100 m which correspond to the region of highest TEM voltage response in Figure 7.13. However, this 1-D model does not indicate the presence of a significant feature at line position 140 m, as in the case of TEM profiling. This may be due to the lack of resistivity soundings between positions 120 m and 160 m. Notice that the geoelectric section exhibits some layering (see Fig. 7.27) as in the other lines.

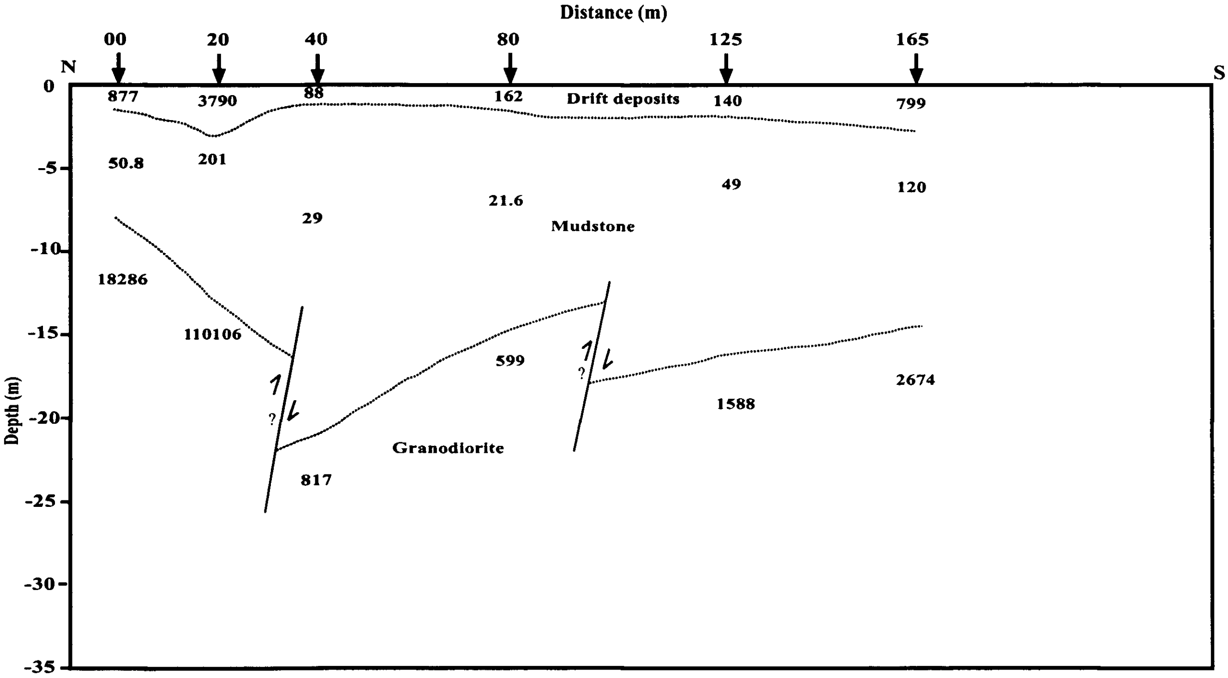

Figure 7.25: Interpretative geoelectric cross-section for line 20E.

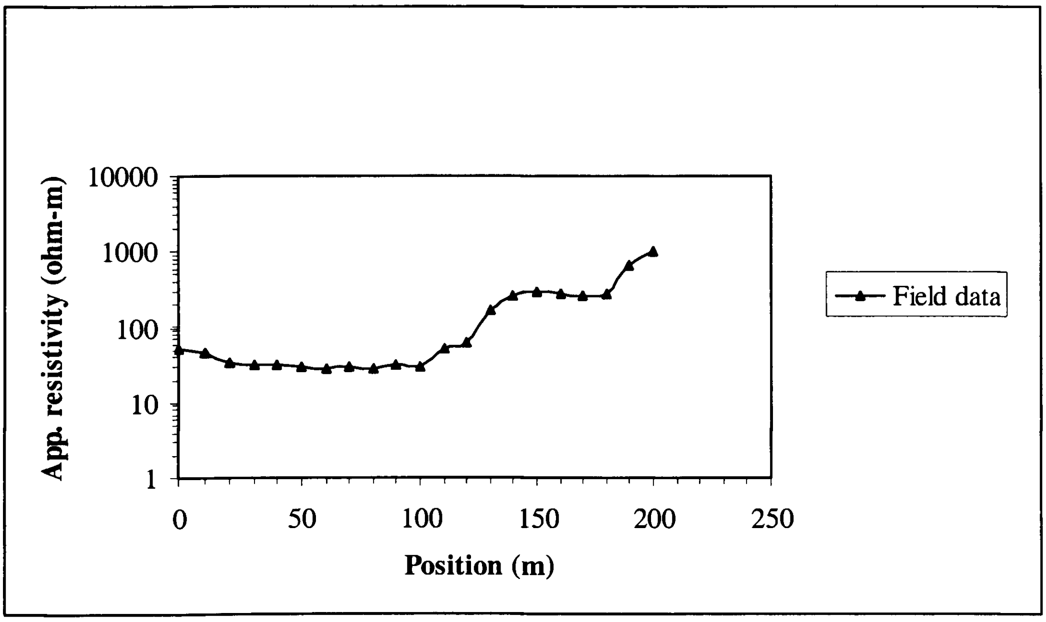

Figure 7.26: Result of dc resistivity profiling using Wenner array (a=10 m) on profile 20E.

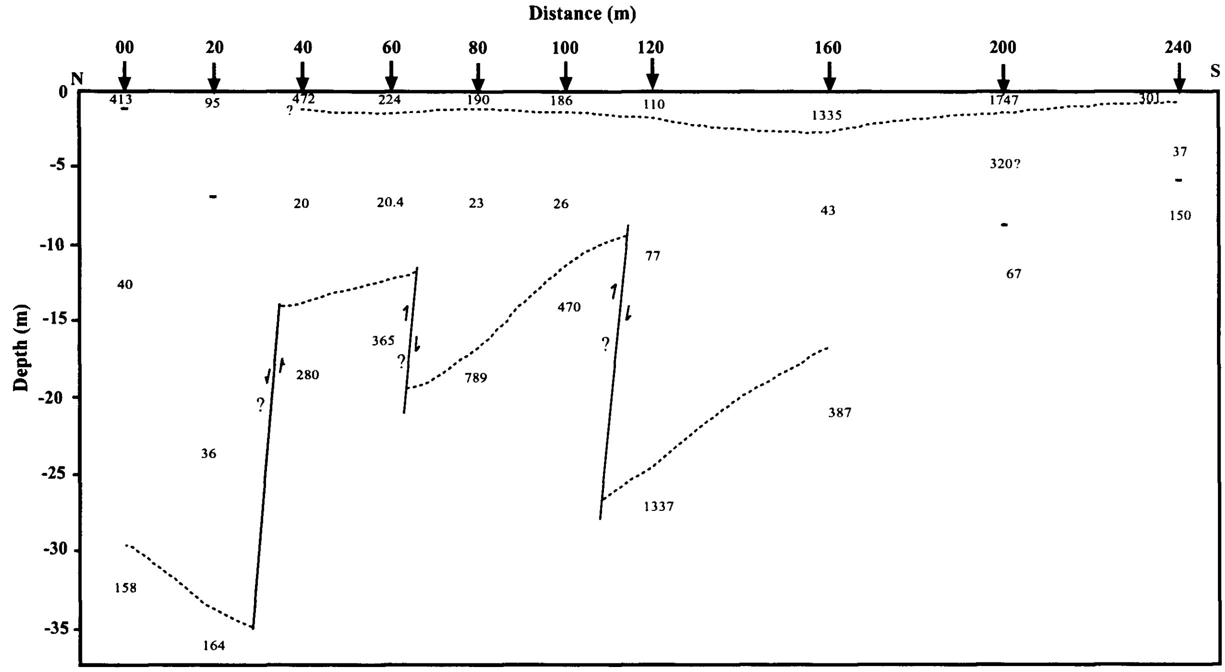

Figure 7.27: Interpretative geoelectric cross-section for line 40E.

The geoelectric section for line 60E (only 100 m long) is presented in Figure 7.28 and indicates that there might be two anomalous zones at line positions 20 m and 60 m. This agrees only with TEM data for the case where the Tx loop was located north of the receiver coil (Fig. 7.14). The three-geoelectric layers are present in all the 1D models; the top layer is sub-horizontal with an average thickness of 2.5 m; the second layer (possibly mudstone) has a variable thickness depending on the underlying basement disruption pattern.

The available VLF (inphase and out-of-phase) data for the three profiles were compared with the previous results from TEM and DC resistivity profiling. The VLF profiles for the inphase and out-of-phase components for line 20E (Fig. 7.29) show a cross-over close to profile position 100 m in accord with the TEM results at that location. The VLF profiles for the inphase and out-of-phase components for line 40E (Fig. 7.30) show a cross-over at line position 140 m in agreement with TEM data at that location. The VLF profiles for line 60E (Fig. 7.31) do not show any cross-over. The Fraser (1973) filter was calculated and contoured for the three profiles as shown in Figure 7.32. Note that there is an anomalous zone which trends from SE to NW. Comparing the VLF map with TEM contour maps (voltage response and resistivity), an agreement between the two methods is seen except for line 60E where the TEM maps show an anomalous zone at line position 140 m. However, the VLF Fraser filter map displays this anomalous zone centered at line position 160 m; this difference might be due to the complex structure and heterogeneity particularly along profile 60E as discussed above.

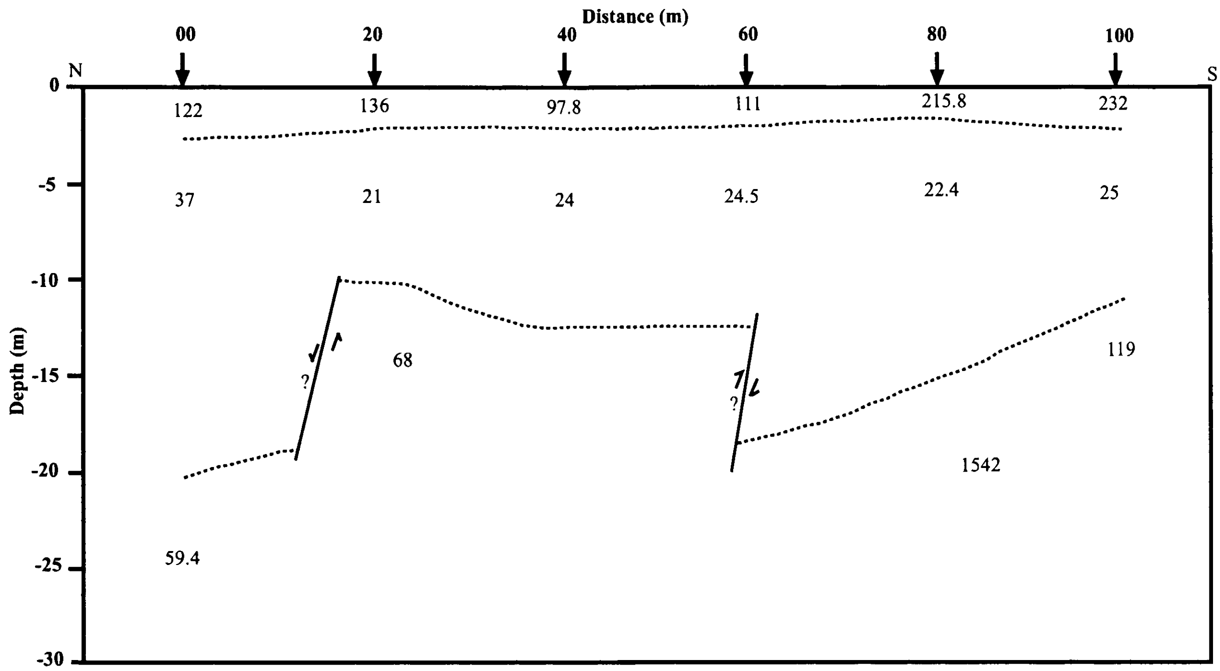

Figure 7.28: 1-D geoelectric cross-section for line 60E.

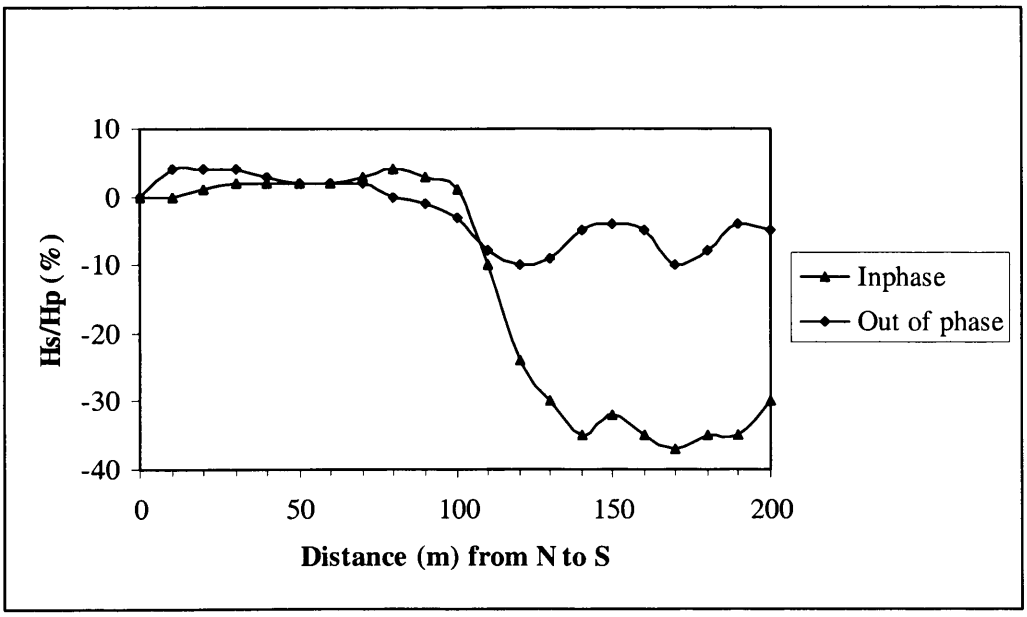

Figure 7.29: VLF profile for line 20E.

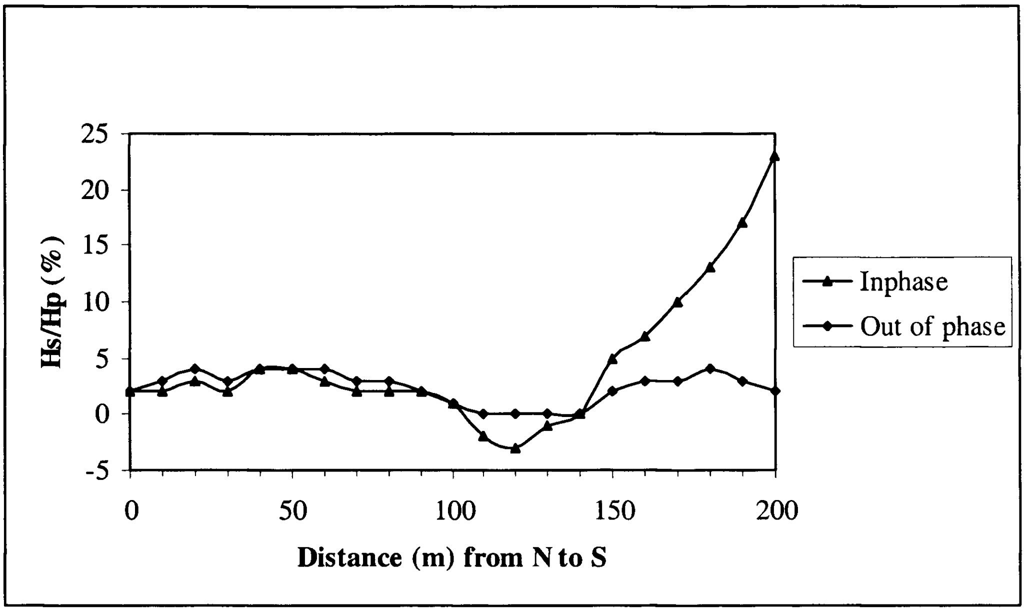

Figure 7.30: VLF profile for line 40E.

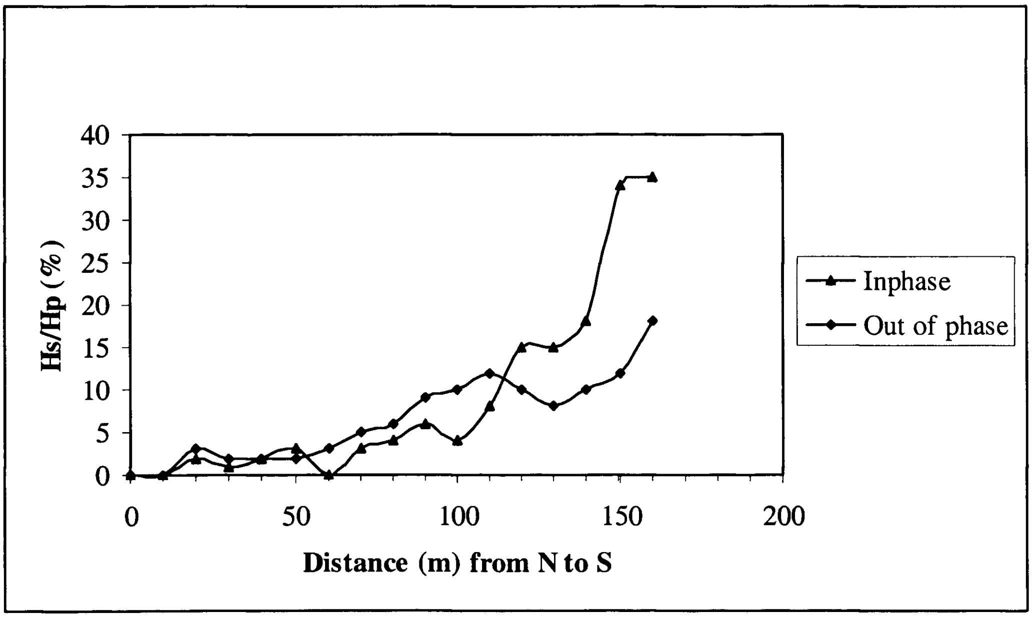

Figure 7.31: VLF data for profile 60E.

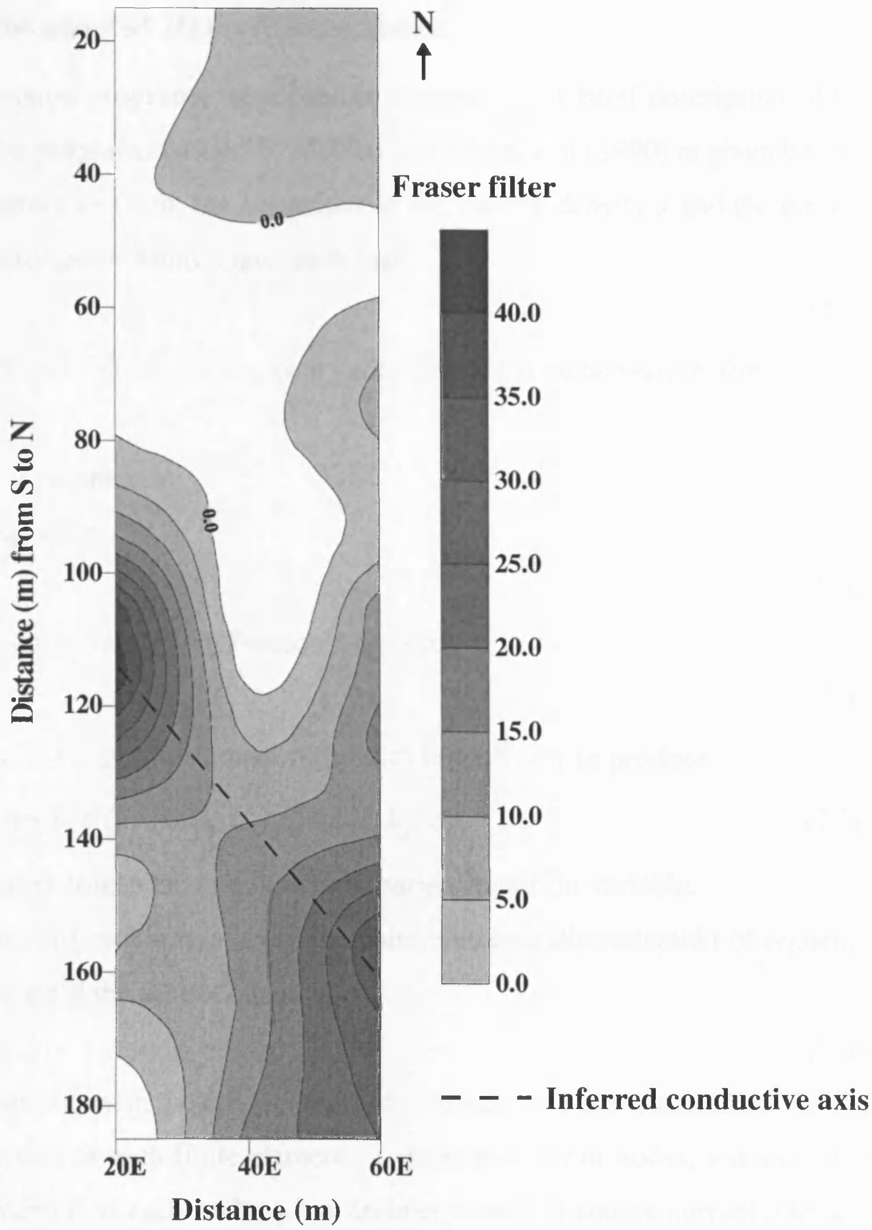

Figure 7.32: VLF Fraser filter contour map for the available data.

7.6 2-Dimensional Schlumberger inversion

It is well known that in complex environments, resistivity not only varies with depth, but also along with horizontal direction, which should be parallel to the survey line. 2-D modelling was carried out in this study in order to compare and improve the results of the 1-D resistivity modelling which is taking into account only the variation of resistivity with depth. 2-D modelling is also applied to assess whether any extra information about the subsurface structure could be obtained.

7.6.1 Description of the adopted 2D inversion schemes

Two different 2D inversion programs were used in this study. A brief description of the theory and of one of the programs written by Uchida and Murakami (1990) is given below. In an isotropically conductive earth, the behaviour of the current density J and the electric field intensity E is controlled by Ohm's law, such that

$$J = \sigma E, \tag{7.1}$$

where σ is the conductivity. Since the stationary electric field is conservative, then

$$E = -\nabla V, \tag{7.2}$$

where V is the electrical potential.

Using the continuity equation,

$$\nabla . J = I, \tag{7.3}$$

where I is the current source, we obtain Poisson's equation,

$$-\nabla .(\sigma \nabla V) = I. \tag{7.4}$$

In case of 2D, equation 7.4 is Fourier transformed with respect to y to produce

$$\nabla .[\sigma(x,z)\nabla \hat{V}(x,k_y,z)] + k_y^2 \sigma(x,z)\hat{V}(x,k_y,z) = \hat{I}(x,k_y,z), \tag{7.5}$$

where ^ means the Fourier transform and k_y is the Fourier transform variable.

The solution to the forward problem is given by finite elements discretization of equation (7.5) (Sasaki, 1981) to yield the matrix equation

$$Kv = s, \tag{7.6}$$

where K is an LxL matrix with positive symmetric values that are determined by the geometry and conductivity of each finite element. L is the number of nodes; v is a column vector of unknown potential at each node; s is a column vector of source current intensity at each node. The potential V in the real 3-D domain can be obtained by applying inverse Fourier transform.

Apparent resistivity is then obtained for Schlumberger array using the equation,

$$\rho_a = G \, {}^{\Delta V}\!/_{I}, \tag{7.7}$$

where

$$G = \pi \frac{(AB/2)^2 - (MN/2)^2}{2(MN/2)}.$$

The forward calculation depends on the position of the current electrodes because at these two positions the source current is not zero. By using the reciprocity theorem which states that a source and a receiver may be interchanged and the same field will be observed, means that apparent resistivities for all *AB/2* of the sounding can be obtained by one forward calculation.

The inverse problem is solved using the conventional damped non-linear least square schemes or Marquardt's method. A brief description of this method is given in chapter 2 and, and further details are available in Uchida and Murakami (1990).

Two different kinds of meshes are used in Uchida and Murakami (1990) program: a calculation mesh and a model mesh as shown in Figures 7.33a and 7.33b. The model mesh describes a 2-D resistivity structure along the survey line by initially dividing the subsurface medium into many rectangular blocks: 30 blocks vertically and 2 times the number of sounding stations horizontally. Resistivity values can be assigned to each block of the model mesh individually. However, the number of blocks would be too large for the inversion if we assign different resistivities to all of them. Accordingly, several neighbouring blocks are grouped into a resistivity block within which the resistivity is constant. These block resistivities are treated as unknown in the inversion, while the boundaries of these blocks are kept unchanged. A finite-element calculation mesh is used for each sounding which consists of 2400 rectangular elements: 80 elements horizontally and 30 elements vertically. Each rectangular element is divided into two triangular parts to get a more accurate modelling of the irregular interface. In order to handle almost three decades of AB/2 with a single calculation mesh, the element size is increased gradually further away, both horizontally and vertically, from the centre of the mesh as shown in (Fig. 7.33b). When the calculation mesh has been constructed, it is superimposed onto the model mesh by placing the centre point of the calculation mesh on the location of the corresponding sounding station on the model mesh. The resistivity values are substituted into all elements of the calculation mesh from the corresponding blocks of the model mesh. Note that the two meshes have the same block boundaries in the vertical direction. These boundaries are placed at the position of each station and at the mid-point of two adjacent stations. Therefore, the number of horizontal blocks is twice the number of sounding stations. During 2-D analysis, the model holds its block boundaries during the inversion and only the resistivity within each block changes through the iteration procedure. Surface topography is taken into account by shifting all the nodes of the calculation mesh vertically according to the elevations of the surface points. However, the electrode spacing is measured by the horizontal distance in the modelling rather than the distance along the ground.

7.6.2 Application of Uchida and Murakami's code to Quorn data

The grid generated for the line 20W is shown in Table 7.1. There are 12 horizontal blocks because there are 6 surveyed sites along the profile; the vertical blocks numbers 30; and the total number of blocks is 109. While the block size can affect the resolution of the results (Sasaki, 1992), the thicknesses of the vertical blocks are finer at the shallow depth (i.e. top 40 m), which is the main interest of this study.

The 2-D inversion used the VES data with N-S spreading axis. Two types of initial models were used: 1) results of 1D inversion and 2) featureless half spaces (50, 100, 300, and $500\,\Omega.m$). The 2-D model results from half spaces gave the same models, and one of them is presented in Figure 7.34a (half space $50\,\Omega.m$). The results of 2-D inversion using 1D-based initial models is shown in Figure 7.34b. The model response is compared with the field data in Figure 7.35 for the inversion with a half space (50 ohm-m) model. The match has an acceptable fit at most sites except site Q6 which may be affected by 3-D structure at the depth corresponding to AB/2 greater than 10 m. The r.m.s error was 0.2. The 2-D inversion models show geoelectric sections consisting of three geoelectric layers; a near surface layer of high resistivity ($\geq 100\ \Omega.m$) and maximum thickness of 2 m is underlain by low resistivity layer which rests on a high resistive layer (granodiorite?). These layers have resistivities and thicknessess different to those from the 1-D inversion. This would suggest that the result of 1D inversion in this study can only be taken as approximate models.

(a)

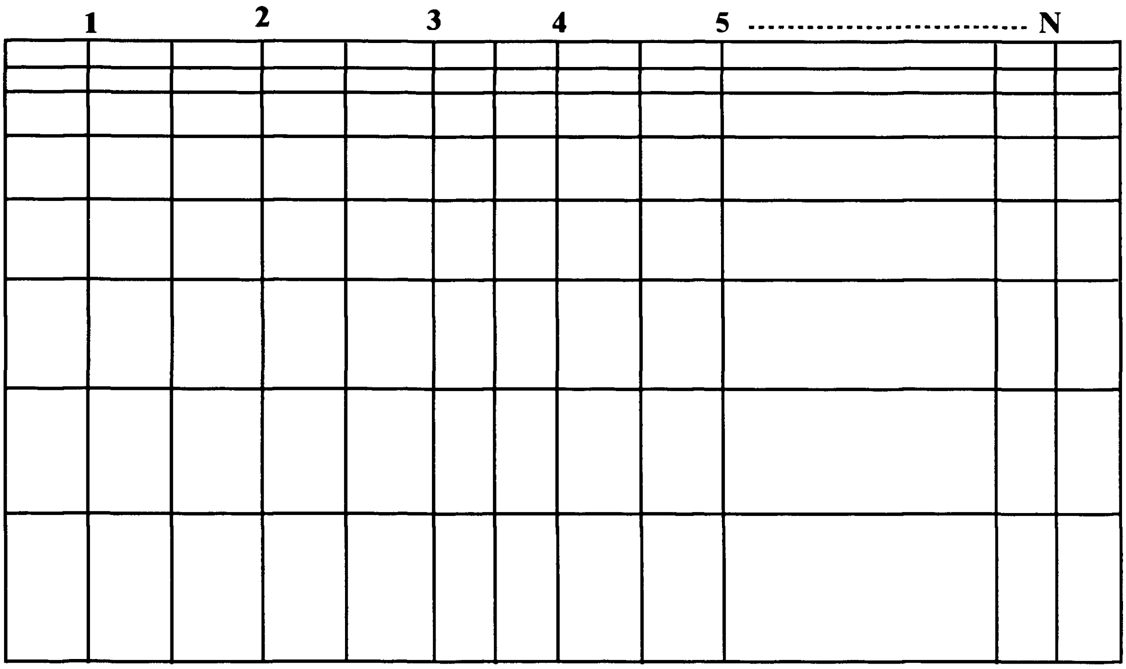

(b)

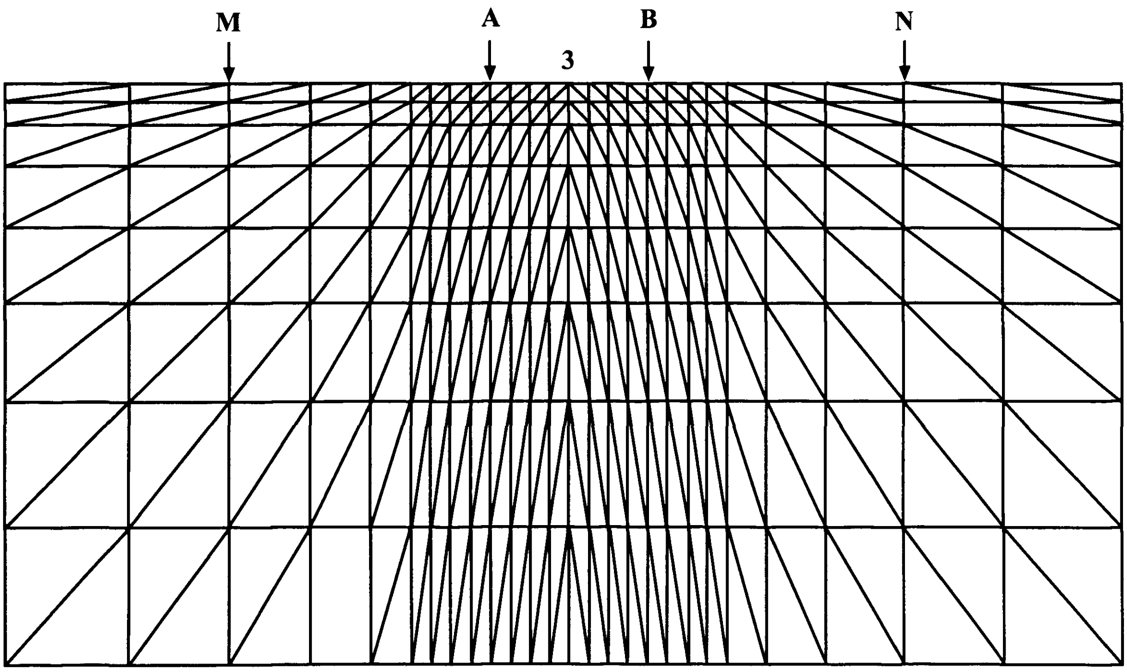

Figure 7.33: Schematic view of a model mesh (a) and a calculation mesh (b). Only 8 of the 30 vertical blocks are illustrated in both (a and b).

NV2 = 12
NZ = 30
NBLK = 109

Vertical thicknesses of the blocks:
0.3 0.3 0.4 1.0 1.5 1.5 1.5 2.0 2.0 2.0 2.0 2.5 2.5 2.5 3.0 3.0 3.5 3.5 3.5
10.0 10.0 10.0 10.0 10.0 10.0 20.0 40.0 80.0 150.0 600.0

Grid design:

1	1	2	2	3	3	4	4	5	5	6	6
1	1	2	2	3	3	4	4	5	5	6	6
7	7	8	8	9	9	10	10	11	11	12	12
7	7	8	8	9	9	10	10	11	11	12	12
13	13	14	14	15	15	16	16	17	17	18	18
19	19	20	20	21	21	22	22	23	23	24	24
25	25	26	26	27	27	28	28	29	29	30	30
31	31	32	32	33	33	34	34	35	35	36	36
37	37	38	38	39	39	40	40	41	41	42	42
43	43	44	44	45	45	46	46	47	47	48	48
49	49	50	50	51	51	52	52	53	53	54	54
55	55	56	56	57	57	58	58	59	59	60	60
61	61	62	62	63	63	64	64	65	65	66	66
67	67	68	68	69	69	70	70	71	71	72	72
73	73	74	74	75	75	76	76	77	77	78	78
79	79	80	80	81	81	82	82	83	83	84	84
85	85	86	86	87	87	88	88	89	89	90	90
91	91	92	92	93	93	94	94	95	95	96	96
97	97	98	98	99	99	100	100	101	101	102	102
103	103	104	104	105	105	106	106	107	107	108	108
109	109	109	109	109	109	109	109	109	109	109	109
109	109	109	109	109	109	109	109	109	109	109	109
109	109	109	109	109	109	109	109	109	109	109	109
109	109	109	109	109	109	109	109	109	109	109	109
109	109	109	109	109	109	109	109	109	109	109	109
109	109	109	109	109	109	109	109	109	109	109	109
109	109	109	109	109	109	109	109	109	109	109	109
109	109	109	109	109	109	109	109	109	109	109	109
109	109	109	109	109	109	109	109	109	109	109	109
109	109	109	109	109	109	109	109	109	109	109	109

Table 7.1: Grid size used in the 2-D modelling for DC resistivity data (20W, N-S electrode spreading axis).

(a)

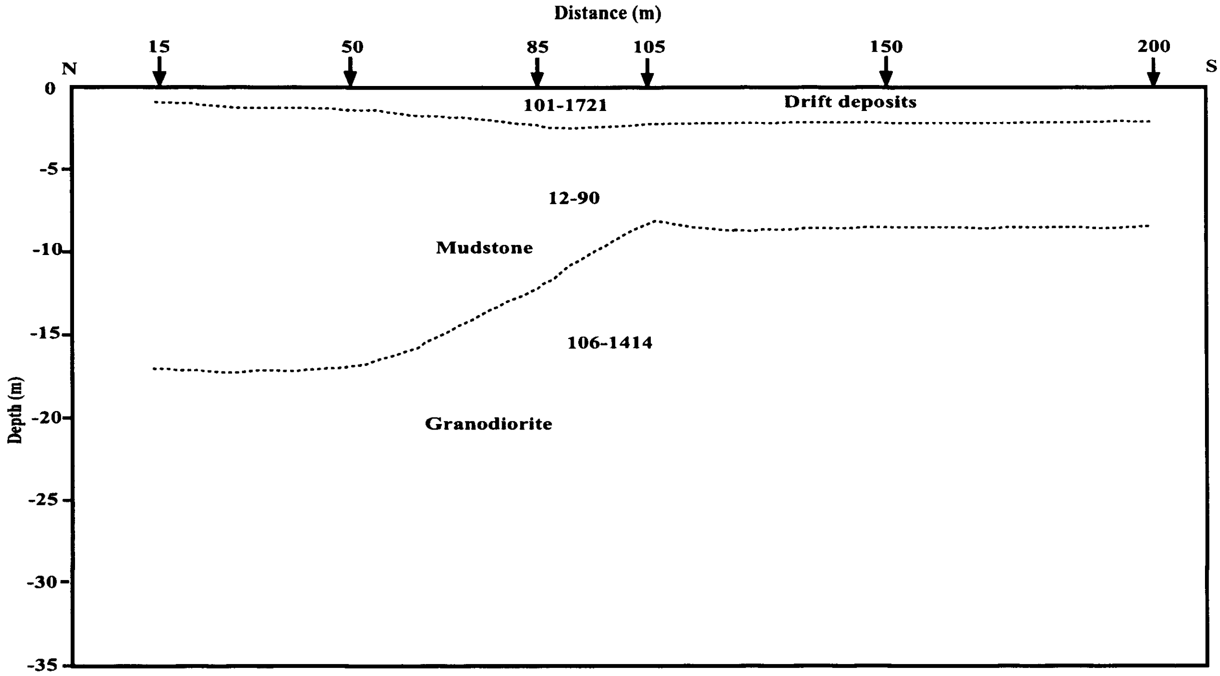

(b)

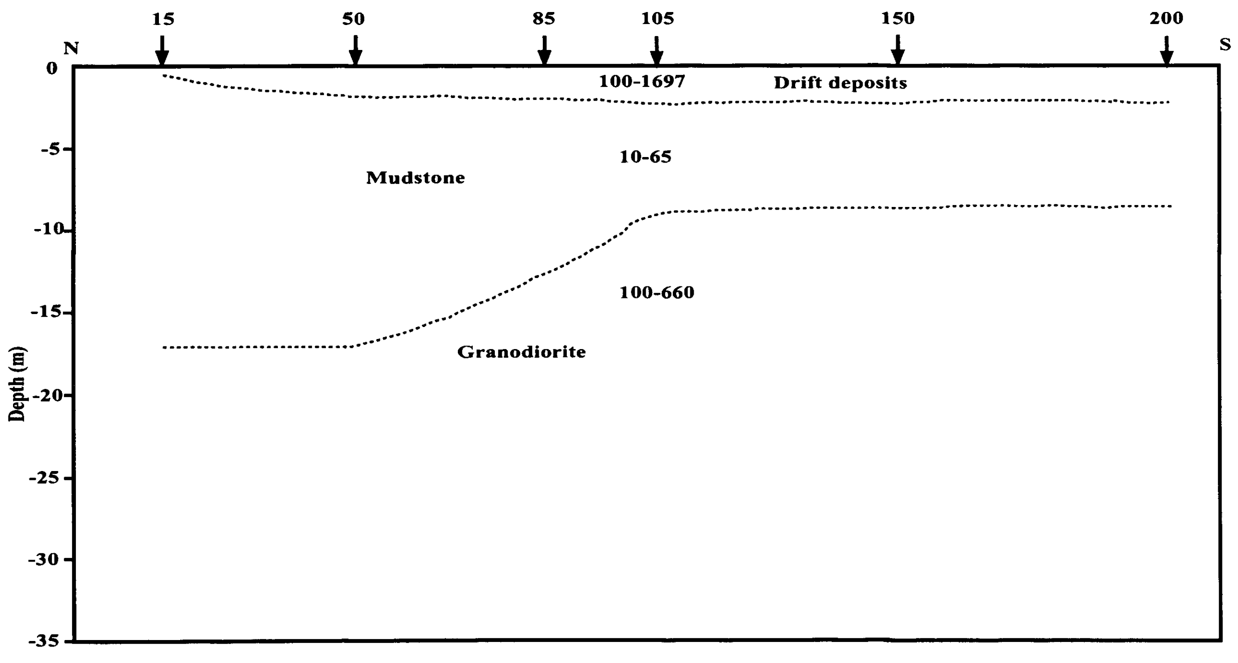

Figure 7.34: Interpretative 2-D geoelctric section derived by 2-D inversion using (a) half space of 50 ohm-m as the starting model; (b) 1-D results as initial model.

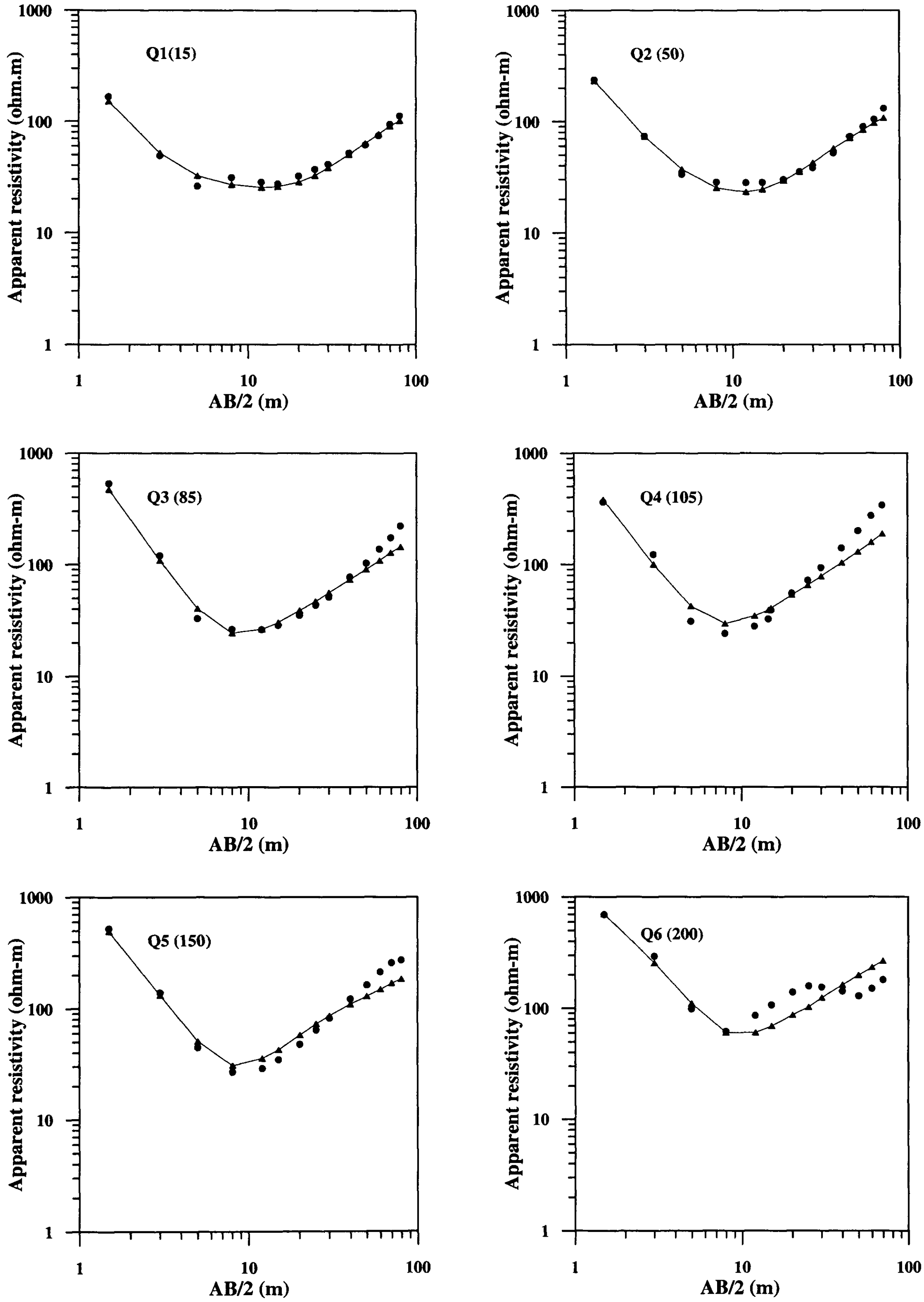

Figure 7.35: The fit between the observed apparent resistivity data and the 2-D model response for line 20W (N-S spreading): the data are presented at each station starting from the north to the south. The 2-D inversion used a half space of 50 ohm-m as the starting model.

7.6.3 Alternative 2D inversion scheme for line 20W

The 2-D inversion program of Perez-Flores in 1995 (see also Perez-Flores et al., 2001) was applied to the data. The scheme assumes a 2-D structure of a constant resistivity (Gomez-Trevino, 1987) and minimizing the sum of the square of the residuals as well as the derivatives of resistivitivies. The solution is obtained using a constrained Quadratic programming. The grid design is shown in Figure 7.36a. The 2-D inversion results are also shown in Figure 7.36b. The 2-D theoretical responses of this model are plotted with the observed data in Figure 7.37. The fit is satisfactory. The model shows roughly similar features to the model shown in Figure 7.34, except for minor differences in changes in resistivities, thicknessess, and the dip of the base layer. The top geoelectric layer of high resistivity ($\geq 65\,\Omega.m$) and of a maximum thickness of 2.5 m (drift deposit) is readily seen on this model; it is underlain by the relatively conductive layer extending to a maximum depth of 18 m at the northern end. This layer is disrupted near VES stations 5 and 6 (150 m and 200 m). It is underlain by the resistive layer which dips towards the north in agreement with the general trend deduced from the outcrop of the granodiorite. There is a noticeable change in the trend of contour lines at the positions of 120 m and 200 m. These abrupt changes (trough-shape) may be interpreted as the presence of fracture or fault zones. The former change agrees with the anomalous zone along the TEM profile. In comparison with the interpreted seismic section (Fig. 7.24), the two models show a drift deposit of relatively the same trend and thickness. The thickness of mudstone and the depth to the bedrock is nearly similar in both models starting from position 15 m until position 55 m; but after this there is no agreement between them. The abrupt change in dip direction of the bedrock starting at position 120 m is seen in both models but beyond 140 m there is a disagreement between the two models. Overall, the 2-D resistivity model provides more acceptable features that agree with the geology of the area and with the other geophysical survey (TEM results) along the same profile.

(a)

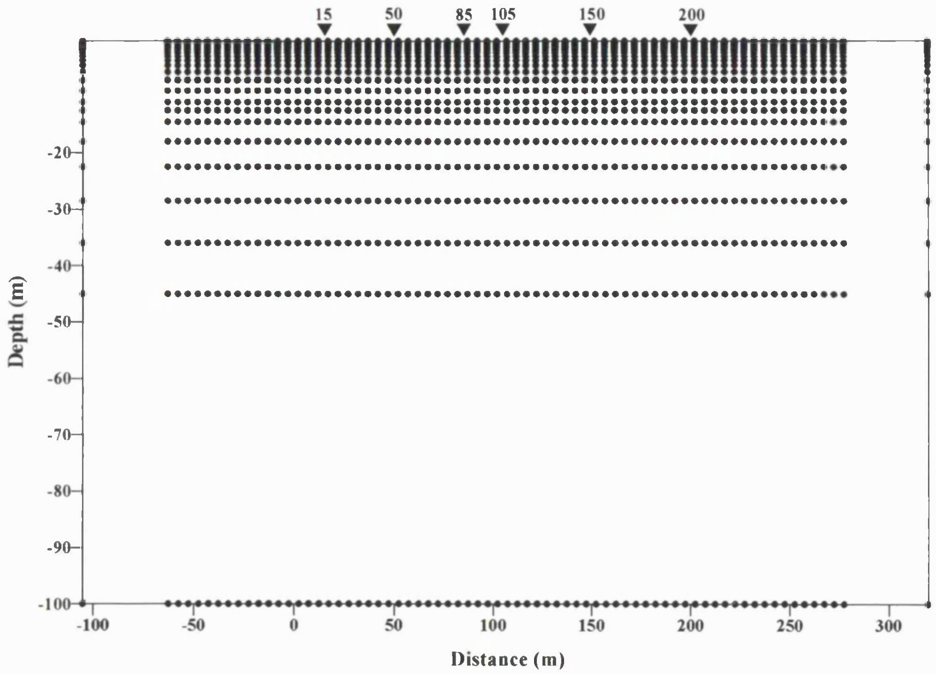

(b)

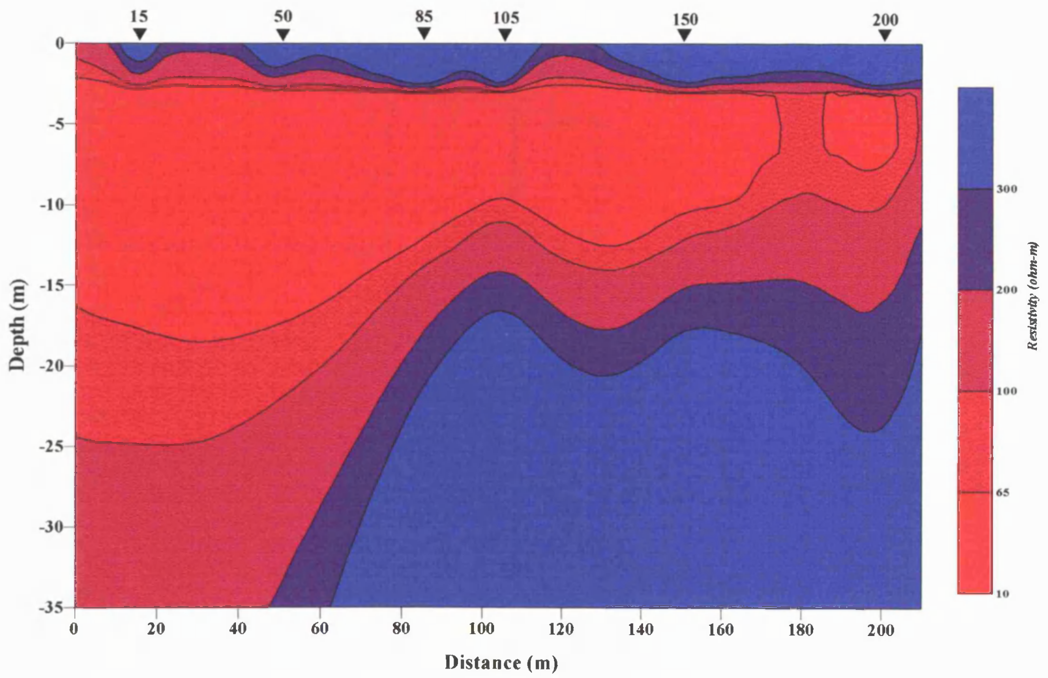

Figure 7.36: Mesh design (a) and 2-D VES inversion result (b) for line 20W (N-S electrode spreading axis). Note the vertical axis is exaggerated from the original given below.

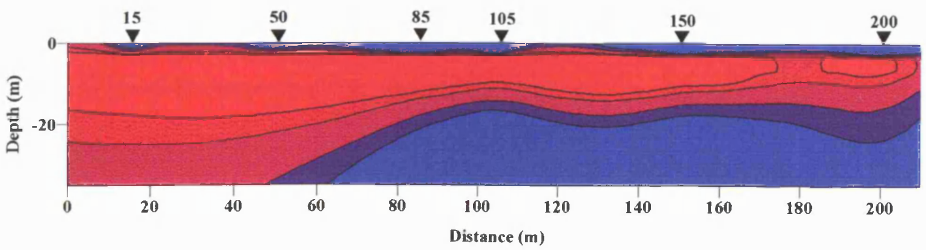

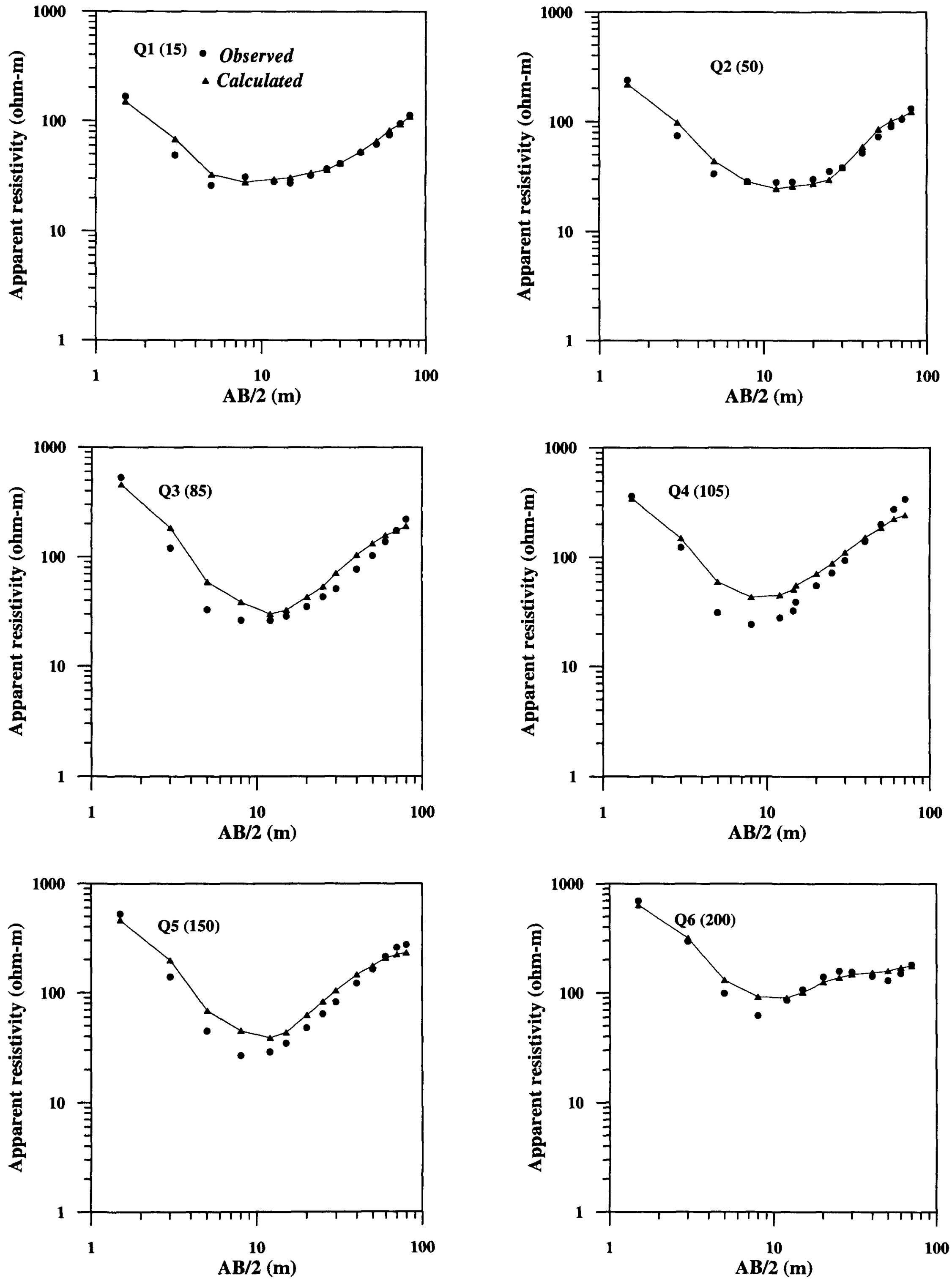

Figure 7.37: The fit between the observed apparent resistivity data and the alternative 2-D model response for line 20W (N-S spreading).

7.7 Discussion

The azimuthal short offset TEM field survey at Quorn Park area has shown that the method is effective as a rapid field survey technique, since 96 soundings were performed in just four hours. TEM central loop data collected along profile 20W gave similar results with short offset TEM data used to validate the technique.

The main objective of applying this technique was to locate any fracture/fault zones in the granodioritic terrain. The TEM results have pointed out twin peak anomalies as expected in an area of thin, weathered overburden. The positions of these anomalous zones have been compared with those seen on conventional geophysical (VLF and DC) profiling and sounding results. It was found that almost all of these zones yielded coincident anomalies in all the methods used. This may suggest that the azimuthal rapid field survey technique can be used independently. In addition to mapping possible fracture zones, the heterogeneity of the area was studied for geophysically coincident recordings from different transmitter loop positions shown on lines 0 and 60E. More detailed information about an inhomogeneity may be obtained by making further soundings between the four receivers soundings collected from each transmitter loop.

Previous TEM studies elsewhere indicated that the 1-D TEM results are adequate for structural mapping in complex terrains (cf. Cooper and Swift, 1994). In this study, the 1-D TEM results along profile 20W have illustrated the method's capabilities for detecting the major lithological boundaries. However, there are discrepancies between the depths and resistivities obtained from inversions by DC and TEM soundings along this profile. This variation in depth may be due to the difference in the current flow system and the effect of complex structure in the area.

In this study the tracking of possible fracture/ fault zones over the whole area was achieved by presenting the TEM data in the form of contour maps and 3-D view plots at selected channels. These illustrated the position of the fracture zones. There are two other suggested ways for presenting such data and identifying the fracture zone in a corresponding way to the DC resistivity method; the first is to plot resistivity data as a function of azimuth in Cartesian coordinates (e.g. Num et al., 1983). The second and most common form of data presentation is to use polar coordinates as either apparent resistivity values (e.g. Taylor and Fleming, 1988) or as percentage variations about a mean or maximum value (e.g. Sauck and Zabik, 1992). A selected example of the second method by presenting the data in logarithmic apparent resistivity values is shown in Figure 7.38; the apparent resistivities of the four TEM data set conducted at 90^0 interval from the transmitter loop centred at position 120 m on profile 0 are presented on polar coordinates. In this diagram, the TEM stations recorded are as follows, two over profile 0 at line positions 100 and 140 m and presented respectively in the bottom and top from the centre of circles; the other two stations are obtained from profiles 20E and 20W at the same position 120 m and presented in the left and right respectively. Note that only the apparent resistivities from channels 2 and 4 (0.009 ms and 0.016 ms) are plotted. An anomalous zone (a fracture- zone or any anisotropy) can be identified as the resistivity changes with rotation. The highest and abrupt change in resistivity values is recorded from the receiver loop located in the right hand side (line position 120 m on profile 20W) at the two channels. This anomalous zone has been suggested before as a possible location of a fracture/ fault zone (see Fig. 7.17) and it is easily read on this polar diagram. However and as shown in Figure 7.38, only four recorded TEM data collected from each transmitter

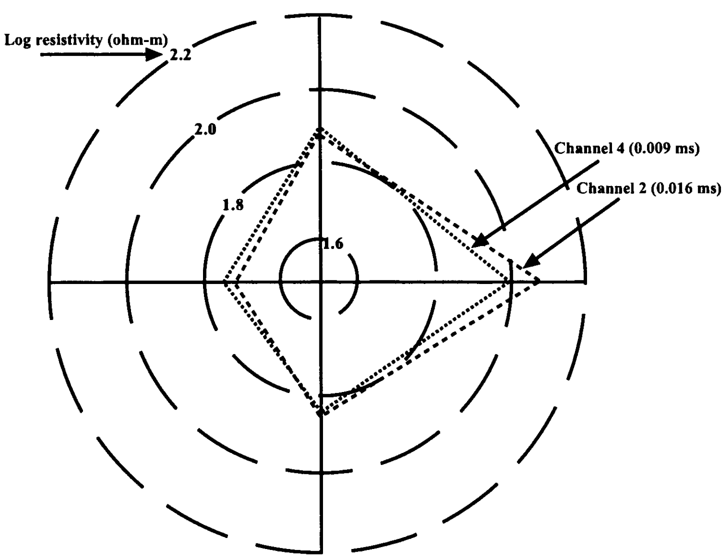

Figure 7.38: Polar azimuthal graph showing variations of resistivity with rotation.

loop are plotted and this is not enough for getting more detailed information about lateral change of resistivity with rotation angle; since a typical azimuthal resistivity survey is conducted at intervals of between 10^0 and 20^0 (through either 180^0 or 360^0, see Carpenter et al., 1991) not at interval of 90^0 as carried in this study. Therefore, more data are needed between the four-recorded data. Also, the position of a fracture/fault zone (Fig 7.38), which is confirmed by additional central loop TEM data and DC Schlumberger soundings, could be interpreted as the maximum dipping direction in dipping stratigraphy or the direction of lateral change in formation resistivity. This is possible if there is no additional geological and/ or geophysical information available. In DC resistivity method, the distinction between the above solutions is conducted by using the short offset array as described by Watson and Barker (1999). In this case, more information might be needed with this contiguous short offset TEM survey to obtain a unique solution.

8. Conclusions and recommendations for further work

This chapter summarizes the main results of work done in Parnaiba basin, Brazil and Quorn Park in Leicestershire, UK. The results are itemized in the form of concluding remarks; the relations between the results obtained and the geological information and the previous geophysical studies are highlighted; the effectiveness of the joint MT/TEM methods in structural mapping that may control on groundwater distribution and lithological mapping are also discussed; the short offset TEM technique as a rapid technique for mapping fracture zone is evaluated. Recommendations for further work are given at the end.

8.1 Executive Summary

The first part of this research comprised shallow as well as deep methods for structural mapping of portions of the Parnaiba basin, Brazil. Magnetotelluric soundings together with transient electromagnetic measurements were performed at 24 sites, 14 of them in the northern margin and 10 in the southeastern part of the basin. The MT frequency range varied from 176 to 0.01 Hz for PN profile and 336 to 0.14 Hz for MH profile.

The recorded TEM voltage decay data have been processed to yield apparent resistivities after adjustment for transmitter turn-off effects (Raiche, 1984). The 1-D results from central loop TEM data for the first 6 sites on the PN profile were collated in the form of geoelectric section and detected a conductive horizon (80 m maximum depth) extending inland from the coast for about 20 km. This horizon may represent a clayey formation rather than intruded seawater.

The MT data were analysed using standard tensorial techniques. The ratios of vertical to horizontal magnetic fields or the so-called induction arrows (Parkinson 1959) were calculated for the MT sites at the PN profile. The real parts of the induction arrows at two frequencies (8 Hz and 40 sec) selected to sample different depths suggested the presence of lateral and vertical variations in resistivity structure in agreement with geological map. The so-called coast effect appears to influence the measurements at the first two stations from the coastline at the high frequencies (>1 Hz) that are important for hydrogeophysical investigations.

The Groom and Bailey (1989) analysis of the MT data indicated that there is generally no improvement on the data at high frequencies (>1Hz). The regional azimuth derived from the decomposition indicated a N53^0 W regional azimuth for the PN profile, which is fairly consistent with the WNW-ESE lithological trend in the geological map.

The regional azimuth for MH profile is $N7^0$ E and is also concordant with the dominant geologic trends. The effect of local near-surface inhomogeneities which caused pronounced static shifts of the absolute levels of many MT apparent resistivity curves were accounted for using the dual mode TEM method suggested in Meju et al. (1999).

The resulting MT apparent resistivity and phase were plotted in the form of pseudosections and used for obtaining gross geoelectric variations. The invariant maps appeared to be effective for tracing lateral and vertical changes of resistivities along both profiles, although the response function and dimensionality indicator (e.g. Swift skew) indicated the requirements of applying multi dimensional modelling. Joint one-dimensional inversion results of TEM-MT data produced acceptable information in terms of lithology and subsurface structure. These inversion models were used as initial models for the final two-dimensional MT inversions.

It is argued that the use of a 2-D resistivity model to represent the geoelectric structure along the two profiles in Parnaiba basin is valid for the high frequency data or the top geoelectric structure (~3 km depth); the strike from Groom-Bailey tensor decomposition at selected frequencies is consistent with the geological trends and the results from Bahr (1991) distortion classification pointed out the validity of using 2-D interpretation techniques. The 2-D inversion models started with using different half spaces as initial model. Then final 2-D models were based on constructed initial models derived from the results of 1-D joint TEM-MT inversion and 2-D MT initial inversion using half space starting models in addition to information from geological maps. The resulting 2-D geoelectric models revealed features which may have influence on groundwater distribution in the area of study. The main sedimentary sequences, graben structures, faults, and general topography of basement were delineated clearly. The discontinuous fault previously suggested from aeromagnetic study in the PN profile was inferred to extend across the PN profile. It is suggested that this fault may be part of a block-faulted structure marking the main edge of the basin. On the MH profile, the Picos fault which is one of the major structures in this locality was delineated; the graben near Picos that was suggested from previous studies (Ulugergerli, 1998; Meju et al., 1999) are also shown on the relevant 2-D geoelectrical model. It is of exploration significance that the boundary between sedimentary and basement rocks both in the lateral and vertical directions are defined in both profiles by MT inversion. Moreover, most of lithologic units that outcrop on the geologic maps (e.g. Serra Grande group and Piementera Formation) are successfully delineated on the final 2-D model.

Based on the above summary, it is shown that MT/TEM methods revealed a geoelectric models that are in agreement with the available geological and geophysical information. These techniques were useful in the determination of the locations of fault zones in this type of environment particularly where varying resistivity units occur on adjacent sides of the fault. The TEM method has been shown to be an effective tool for correcting MT data from static shift; it has also had the potency for delineating conductive zones in resistive environment.

The second part of this research is considered to be a shallow study to evaluate a rapid TEM field survey technique for mapping fractured/faulted zones in areas of little or no weathered overburden. A new short offset TEM field technique was applied in this study to locate fracture zones in the village of Quorn in Leicestershire, UK. The more conventional methods (VLF, central loop TEM and DC resistivity soundings and profiling) were developed for comparative study. The rapid TEM field survey technique covered the area efficiently, since 96 soundings were performed in four hours. This is opposed to the single loop or central loop TEM field techniques which require relatively longer time to cover the whole area. TEM central loop data collected along profile 20W gave similar results with short offset TEM voltage responses as indication of the usefulness of this technique.

The results of TEM profiling show the presence of twin peak anomalies characteristic of near-vertical conductive zones. The positions of these anomalous zones have been correlated with the available conventional methods (VLF and DC profiling and soundings). It was found that most of these zones gave the same anomalies over all the methods used. Despite that, the 1-D geoelectric sections have displayed some inferred faults not detected by TEM field data; for instance, along line 40E, there are three inferred fault patterns close to profile coordinates 20, 60, and 100 m. These faults are close to each other and this may require intensive field survey to detect them by using 10 m instead of 20 m sided transmitter loop. According to the model described by Meju et al. (2001), there should be a single peak anomaly at early time for a deeply weathered terrain and twin peaks at later time. The lack of single peak anomalies suggests the thin nature of the overburden at this site.

In addition to mapping the fracture zone, the heterogeneity of the area was evidenced from the repeated soundings measured on each site from different transmitter loops along profiles 0 and 60E. The results have shown near surface inhomogeneities at some localities at early times. The 1-D TEM results along profile 20W have shown the capability of this method for detecting the boundary between the conductive overburden and the bedrock; the abrupt change in resistivity at profile position 120 m which is the expected position of the fractured or faulted zone, may indicate that the 1-D TEM results are adequate for structural mapping in this terrain and defining the lithological boundaries across the area. Nevertheless, the near surface layer of drift deposits (~2 m) mapped by DC resistivity is inaccessible to TEM at this site. The discrepancies between the depths and resistivities obtained from inversions of DC resistivity and TEM soundings may be attributed to the difference in the current flow system; also the near surface inhomogenities, the deviation from a horizontally layered earth, and the effect of 3-D environments represented by the outcropping basement rocks will differently affect the responses of the two methods. Moreover, in DC resistivity sounding, increasing the depth of investigation depends on increasing the distance between the current electrodes, this makes the measured response more affected by subsurface inhomogeneities along the area of current electrodes; while the depth of investigation for TEM system is determined by maximum recording time, the source moment and ground resistivity (Spies, 1989) so that the measured TEM response is less affected by lateral resistivity changes since it only samples the area underneath the transmitter and receiver loops.

In this study the tracking of fracture zones along the whole area were performed using presenting the voltage responses and the apparent resistivities in the form of contour maps and 3-D view plots at selected time channels. These presentations have marked the fracture zones. However, it was found that it is easy to define these anomalous zones in 3-D plan using voltage responses instead of apparent resistivities. The TEM data can also be well presented in polar coordinates as discussed above (section 7.7).

8.2 Conclusions

The main implications of the results are summarized in this section.

- The use of the multi geometry transient electromagnetic technique (TEM) to correct for static shift in the magnetotelluric responses eliminated one of the major problems of the MT technique in Parnaiba basin environments. Central and coincident loop TEM data respectively provided the right level for the MT TE and TM apparent resistivity curves. One of the drawbacks in TEM responses addressed in the literature is the IP effect through it the late time channels of coincident and central loop soundings are negative (Smith and West, 1989). In this study, the collected data suffered from this effect particularly the single loop TEM data. The late time channels were therefore truncated to get rid of IP effect and this resulted in no overlapping between TEM and MT data at some sites (e.g. station MH10). However, since the static shift changes the level of the MT apparent resistivity curve, these few TEM data points were sufficient for a correction scheme (see Meju, 1996).

- The values of MT structural and dimensionality indicators such as skew, impedance regional strike, and Bahr distortion parameters implied that it is possible to use 2-D interpretation method for the two MT profiles especially at high frequencies (>1 Hz) that correspond roughly to the top 3 km which is the main depth of interest for hydrogeophysical study in this basin. Below 1 Hz, the dimensionality indicators almost show 3D complex structure.

- The 2-D geoelectric models revealed features that the simple 1-D inversion failed to detect and which are consistent with the geological information and previous geophysical results. This is particularly evident on the MH profile and suggests that 1D interpretations are untenable in the area of study. However, 1-D inversion results were used for getting an initial model particularly if there is no enough geological information as it is obvious in PN profile.

- This study has shown the capability of joint TEM-MT methods for mapping the architecture of the sedimentary cover units and the underlying basement. This study has demonstrated the potency of MT for demarcating the main faulted margins of the basin along both profiles. The notable zone of basement truncation at the inferred basin margins in the 2-D MT model may play an important role in groundwater transport and accumulation in the graben structures (which have the optimum potential for drilling for groundwater in this basin). However the wide station separation limited the lateral resolution of the geoelectric structure, and hence the uniqueness of some of the features present in the model; this is evident between stations 1 and 2 of PN profile and the wide station spacing (7 km for PN profile and 6.4 km for MH profile). The noisy data at some sites (e.g. station 13, PN profile) also affect the resolution of 2-D MT model.

- Although 3-D MT modelling would be appropriate for detailed interpretation, the use of a 2-D approximation imaged the gross features of the area. In addition, the conventional 3-D trial and error forward modelling of these limited soundings on a single survey lines may not lead to unequivocal model in the absence of accurate quantified a priori information.

- The TEM data do not show any significant evidence of seawater intrusion in the coastal region of the PN profile. However, more densely sampled survey data are greatly required.

Closer station spacing will be able to provide the desired lateral resolution in the model and minimize the degree of non-uniqueness in the TEM model. The area between stations 1 and 2 for instance (PN) profile is the place where the lack of high-density observations generated uncertainties.

- In the past, combined HLEM-VLF-DC resistivity techniques have been used in the location of fracture-zones in crystalline rocks. Recently TEM method has also been used but for deep targets (Meju et al., 2001). The situation in Quorn Park is different and the target is considered to be small compared to the size of the transmitter loop. This study has illustrated not only the capability of central loop TEM for this task (small conductive zone) but also the rapid TEM field survey technique termed contiguous loop azimuthal sounding method. The azimuthal field survey method has been successful for locating most anomalous zones seen on the other conventional methods (DC resistivity profiling and soundings and VLF methods). The inferred zones suggested by conventional methods and not detected by qualitative interpretation of TEM data evoke to apply quantitative interpretation using multidimensional modelling (2D/3D) which is not available in Leicester University.

8.3 Suggestions for further studies

The Parnaiba basin is a complex environment. The 2-D inversion results gave plausible information when compared with the previous studies and the geological information. However, a more detailed investigation of the resistivity variations in the subsurface will help to improve our understanding of the deep structure. This will require 1) further field measurements, and 2) further mathematical modelling of the MT data. Electromagnetic induction soundings could be performed at various locations in order to improve the 2-D inversion results. Closer station spacing in anomalous zones, if not possible along the entire profiles, will be able to provide the desired lateral resolution in the model and minimize the degree of non-uniqueness in the MT models. Furthermore, 3-D modelling is required to provide a more complete image to trace the whole structure in the area especially the south-eastern part of the basin which has a complex terrain.

The results from Parnaiba basin showed high conductivity-fault zones. These conductive zones could be related to any geothermal potential. This may be evident along MH profile that has a conductive zone along the interpreted Picos fault which is very close to the circular structure shown in the geologic map (Fig. 5.4) and which is thought to be related to a magmatic activity in the area of study. Therefore, further geothermal study could also be investigated.

This study attempted to estimate some hydro-chemical parameters (e.g. total dissolved solids) and the petrophysical property of porosity from the EM models. Since there is no available borehole data or laboratory measurements through which we can obtain accurate value of some parameters (e.g. m, ρ_f, and also n, chapter 4), the calculated values at selected zones may be a rough approximation. However, detailed approach should be made to estimate more petrophysical properties, hydrochemistry, and other hydrogeological parameters especially if there is any available borehole data which can be used for correlation and obtaining accurate values of the parameters needed.

The rapid TEM field survey used at Quorn was successful in locating most of the anomalous fractured/faulted zones. However for getting more information in highly dissected area such as Quorn area and for resolving the cover unit, 2D imaging as demonstrated for DC resistivity profiles should be developed for TEM. This was a major deficiency in this study. Loops size of 10 m x 10 m sided may also be recommended and TEM equipment with very rapid primary field turn-off ($<2\,\mu\,sec$) is needed. Also, measuring the three (vertical and two horizontal) TEM components may give more information to the presence of the fractures zone. It may also be suggested that a more sophisticated array (TEM azimuthal survey) corresponding to azimuthal DC resistivity is suggested for detecting fracture zones and their azimuthal parameters in highly dissected fractured/faulted zones. The fault zones, defined by DC resistivity soundings and not detected by TEM, may also suggest the usefulness of using a combined DC-TEM approach. Incorporating other conventional methods (HLEM and VLF) is recommended for full detailed study.

Appendix A

Appendix A.1

The MT data obtained at 14 stations for PN profile in Parnaiba basin, Brazil (Figure 5.3). For each site, the data shown are: the apparent resistivity and phase curves of the off diagonal elements of the unrotated impedance tensor, the major and minor apparent resistivity and phase, the regional azimuth (Swift and Groom-Bailey methods) measured positive clockwise from magnetic north), skew, and coherency. The error bars are one standard deviation.

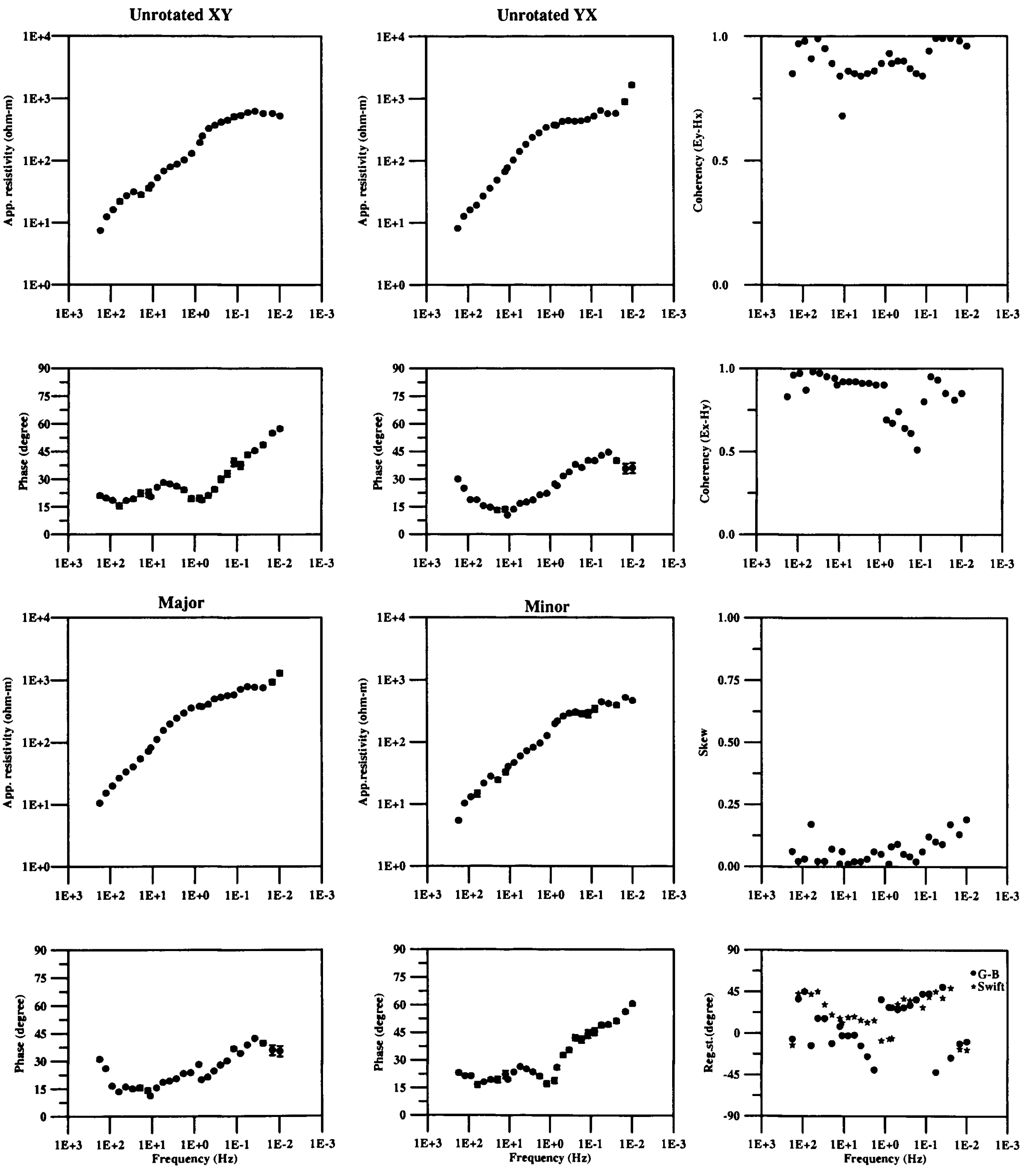

Station 1

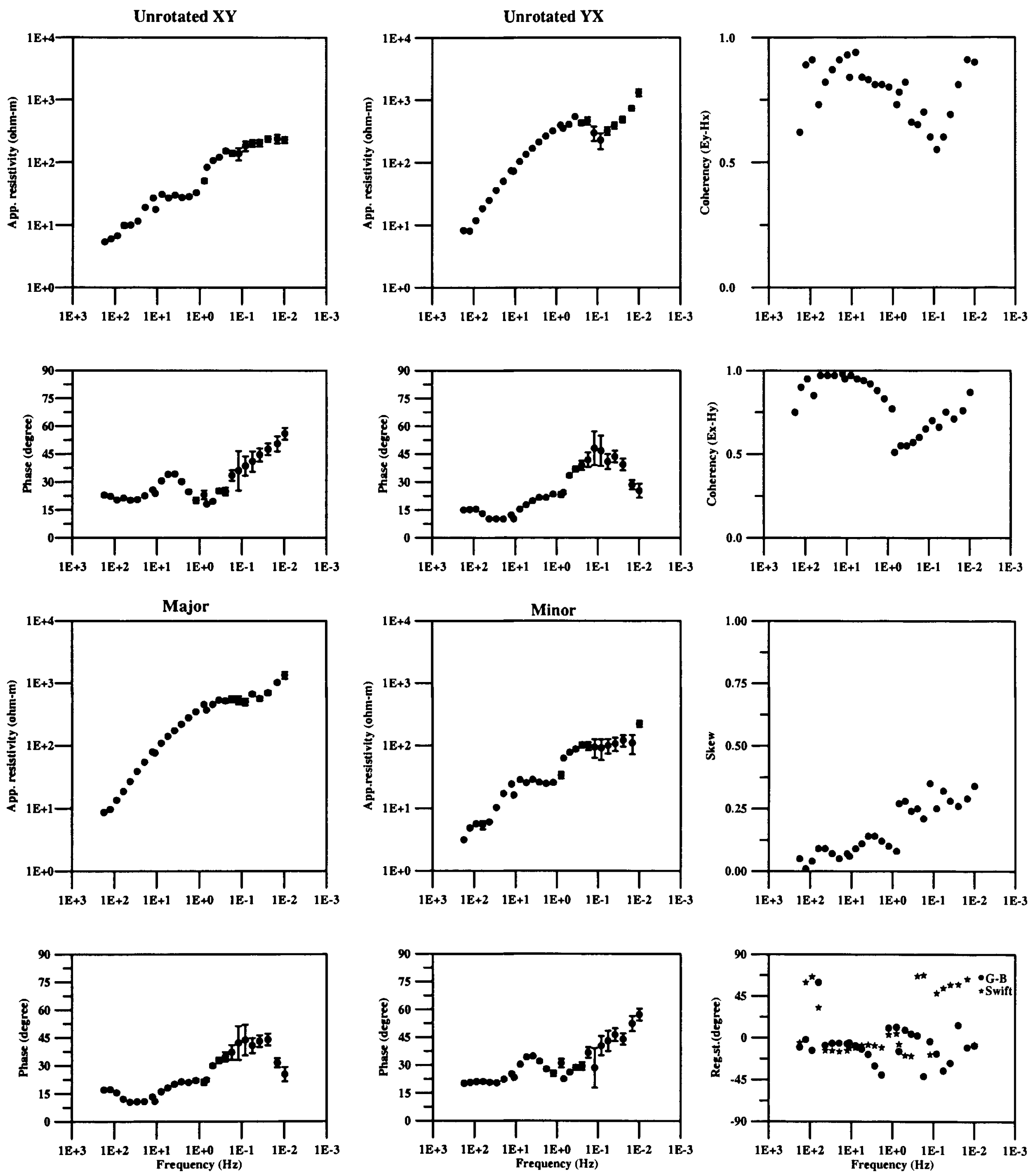

Unrotated XY
Unrotated YX
Major
Minor
App. resistivity (ohm-m)
Phase (degree)
Coherency (Ey-Hx)
Coherency (Ex-Hy)
Skew
Reg.st.(degree)
•G-B
*Swift
Frequency (Hz)

Station 2

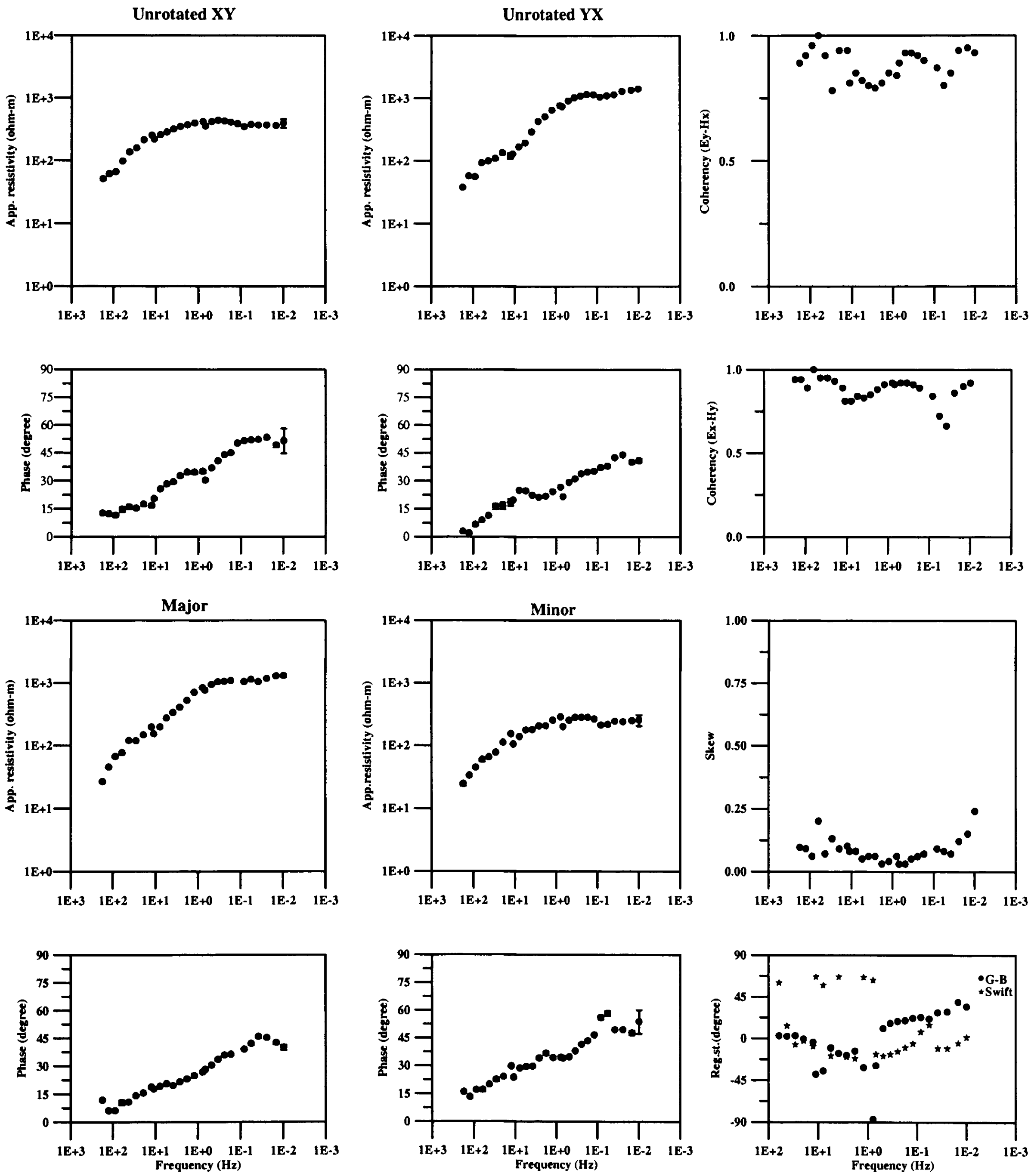
Unrotated XY
Unrotated YX
Major
Minor
App. resistivity (ohm-m)
App.resistivity (ohm-m)
Phase (degree)
Coherency (Ey-Hx)
Coherency (Ex-Hy)
Skew
Reg.st.(degree)
•G-B
*Swift
Frequency (Hz)

Station 3

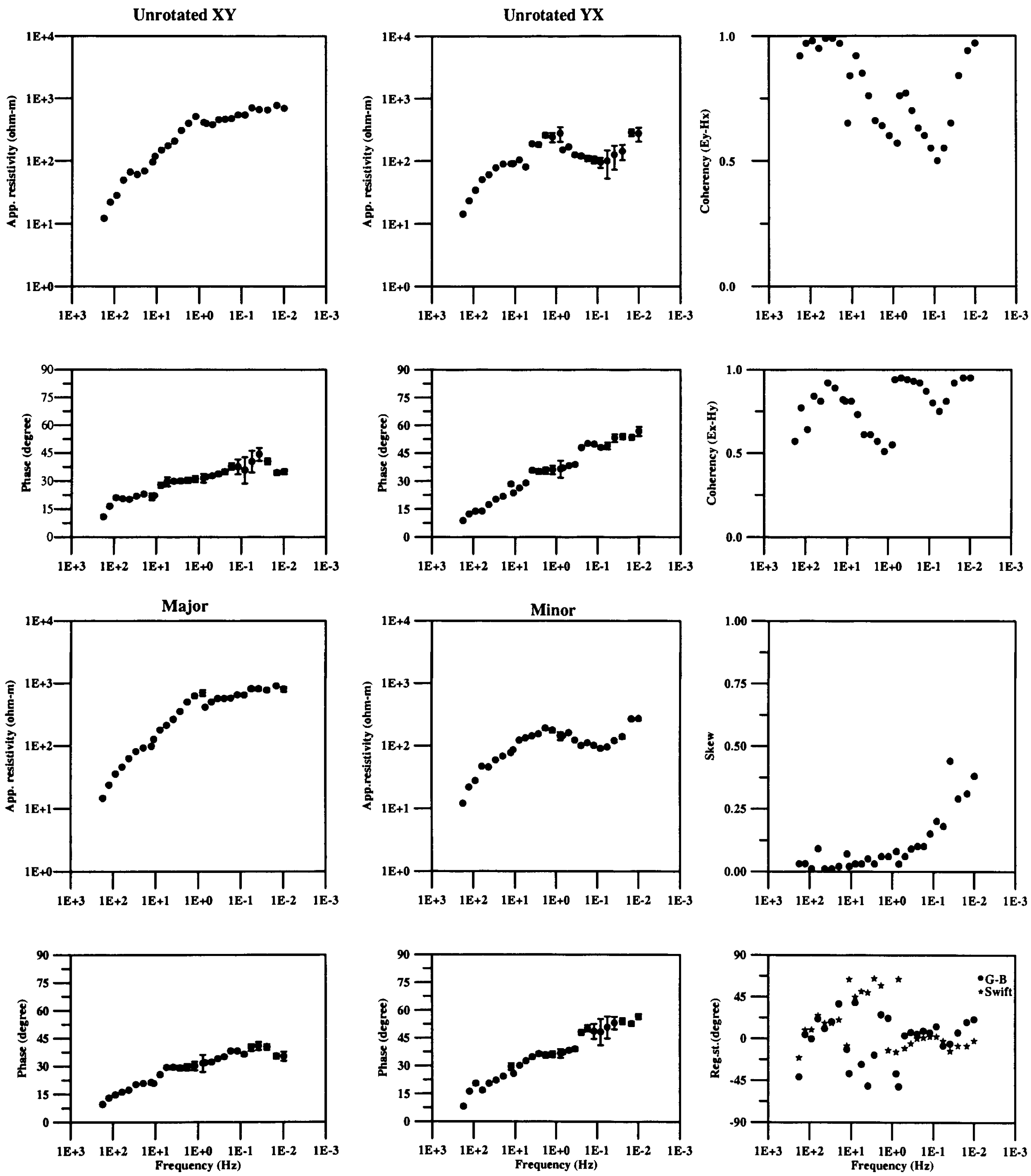
Unrotated XY
Unrotated YX
Major
Minor
App. resistivity (ohm-m)
App.resistivity (ohm-m)
Phase (degree)
Coherency (Ey-Hx)
Coherency (Ex-Hy)
Skew
Reg.st.(degree)
•G-B
*Swift
Frequency (Hz)
1E+3 1E+2 1E+1 1E+0 1E-1 1E-2 1E-3

Station 4

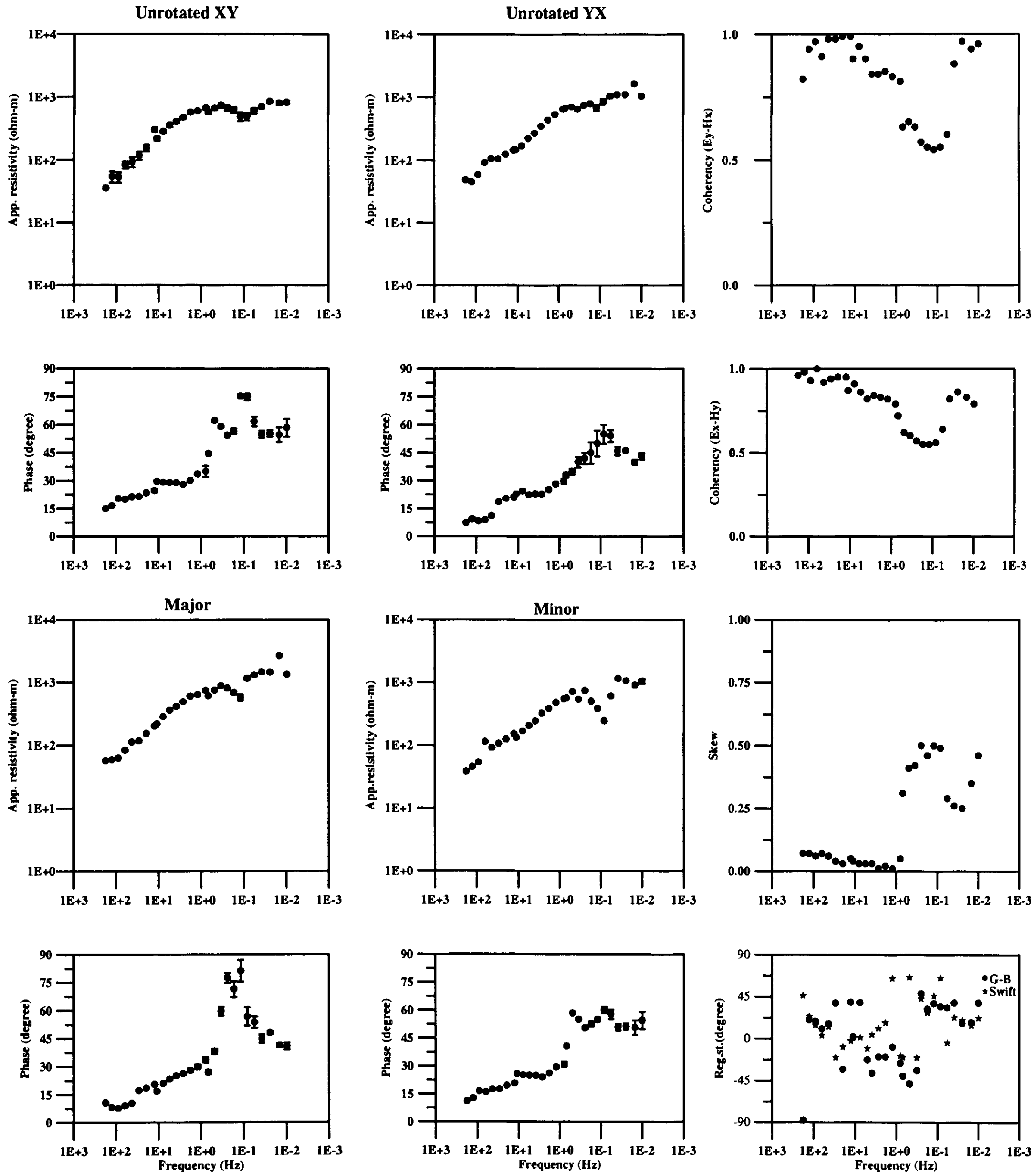
Unrotated XY
Unrotated YX
Major
Minor
App. resistivity (ohm-m)
Phase (degree)
Coherency (Ey-Hx)
Coherency (Ex-Hy)
Skew
Reg.st.(degree)
G-B
Swift
Frequency (Hz)

Station 5

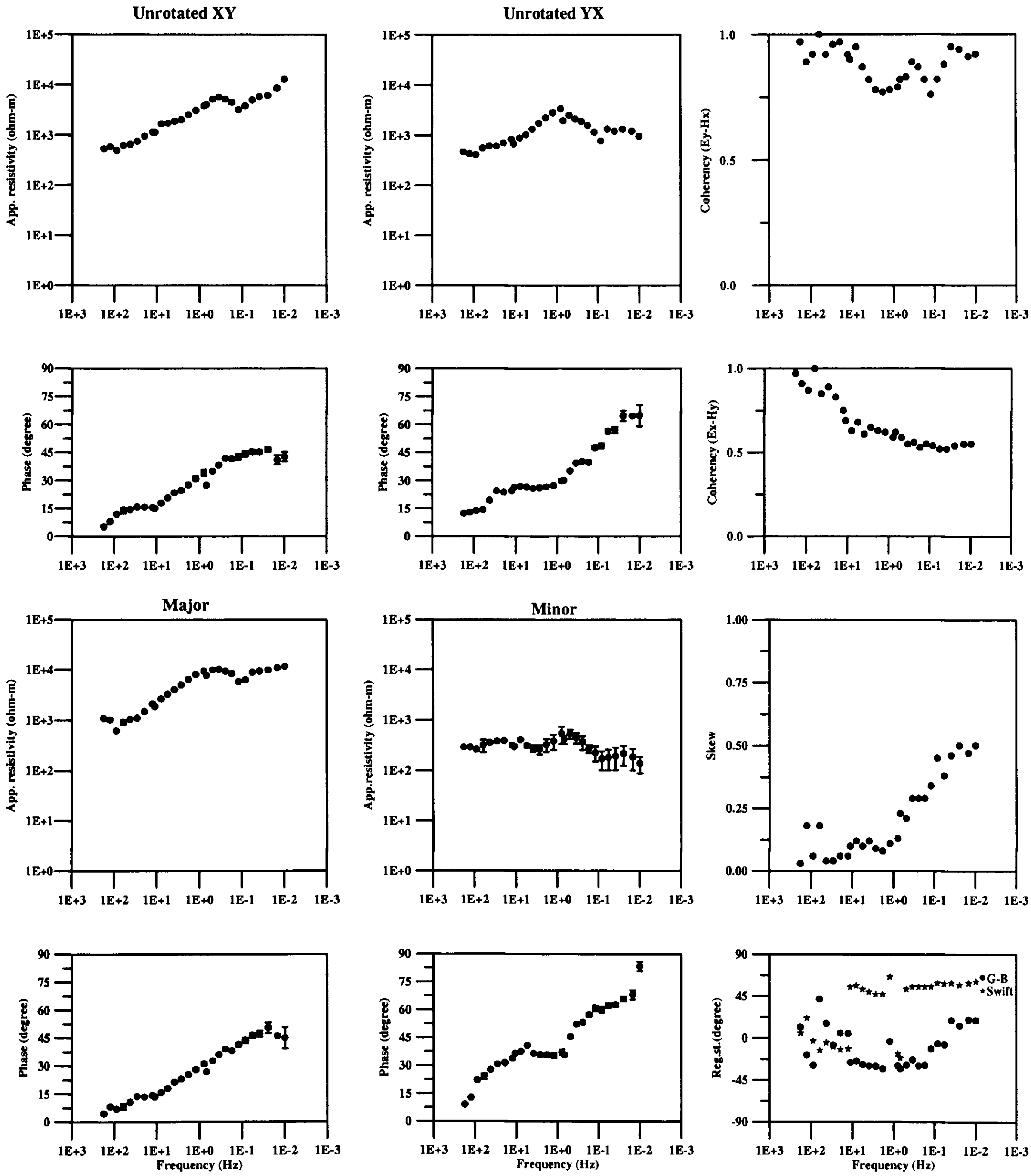
Unrotated XY
Unrotated YX
Major
Minor
App. resistivity (ohm-m)
App.resistivity (ohm-m)
Phase (degree)
Coherency (Ey-Hx)
Coherency (Ex-Hy)
Skew
Reg.st.(degree)
G-B
Swift
Frequency (Hz)
1E+5
1E+4
1E+3
1E+2
1E+1
1E+0
1E-1
1E-2
1E-3
90
75
60
45
30
15
0
-45
-90
1.0
0.5
0.0
1.00
0.75
0.50
0.25
0.00

Station 6

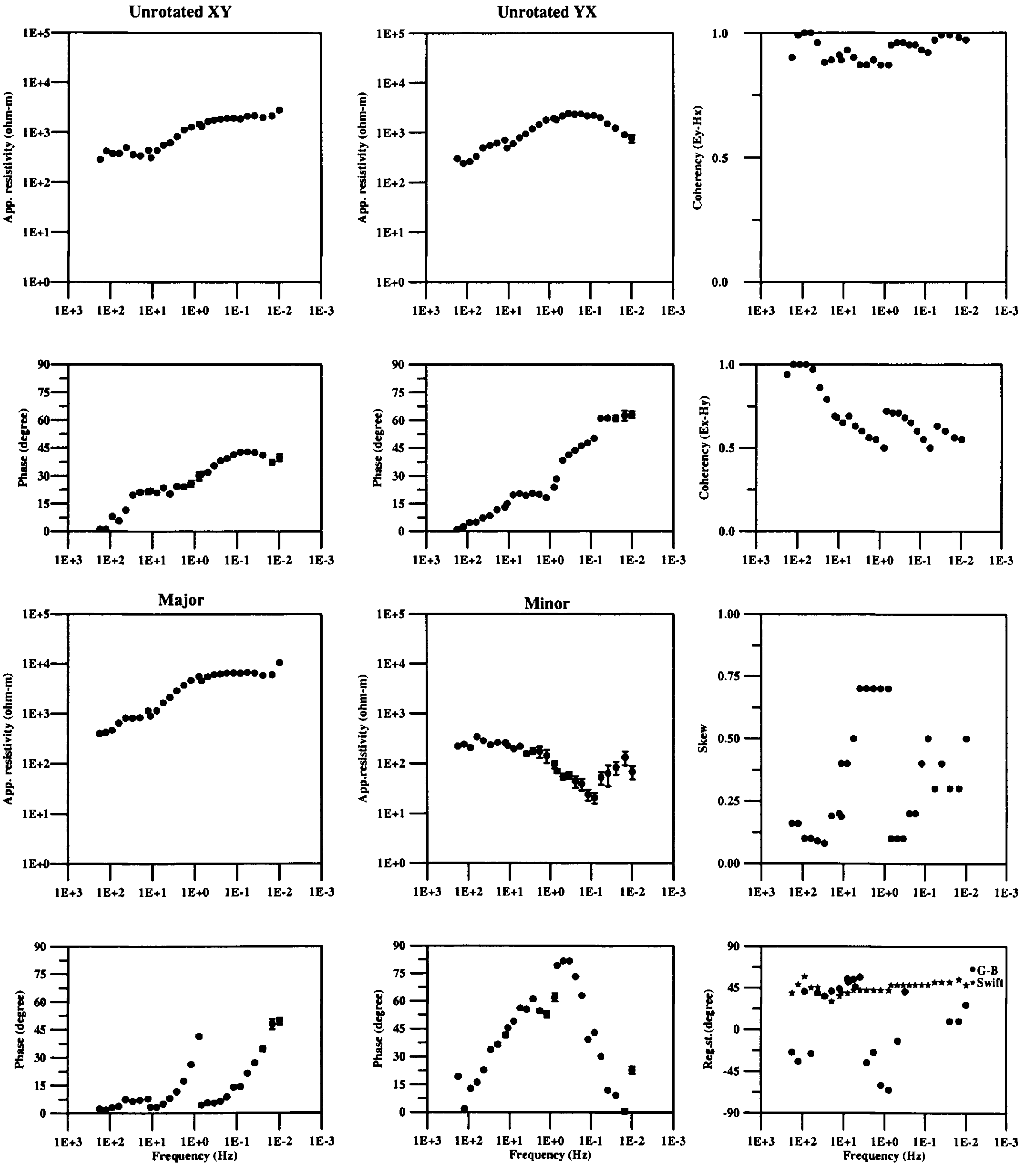

Unrotated XY
Unrotated YX
Major
Minor
App. resistivity (ohm-m)
App.resistivity (ohm-m)
Phase (degree)
Coherency (Ey-Hx)
Coherency (Ex-Hy)
Skew
Reg.st.(degree)
G-B
Swift
Frequency (Hz)
1E+3
1E+2
1E+1
1E+0
1E-1
1E-2
1E-3
1E+5
1E+4

Station 7

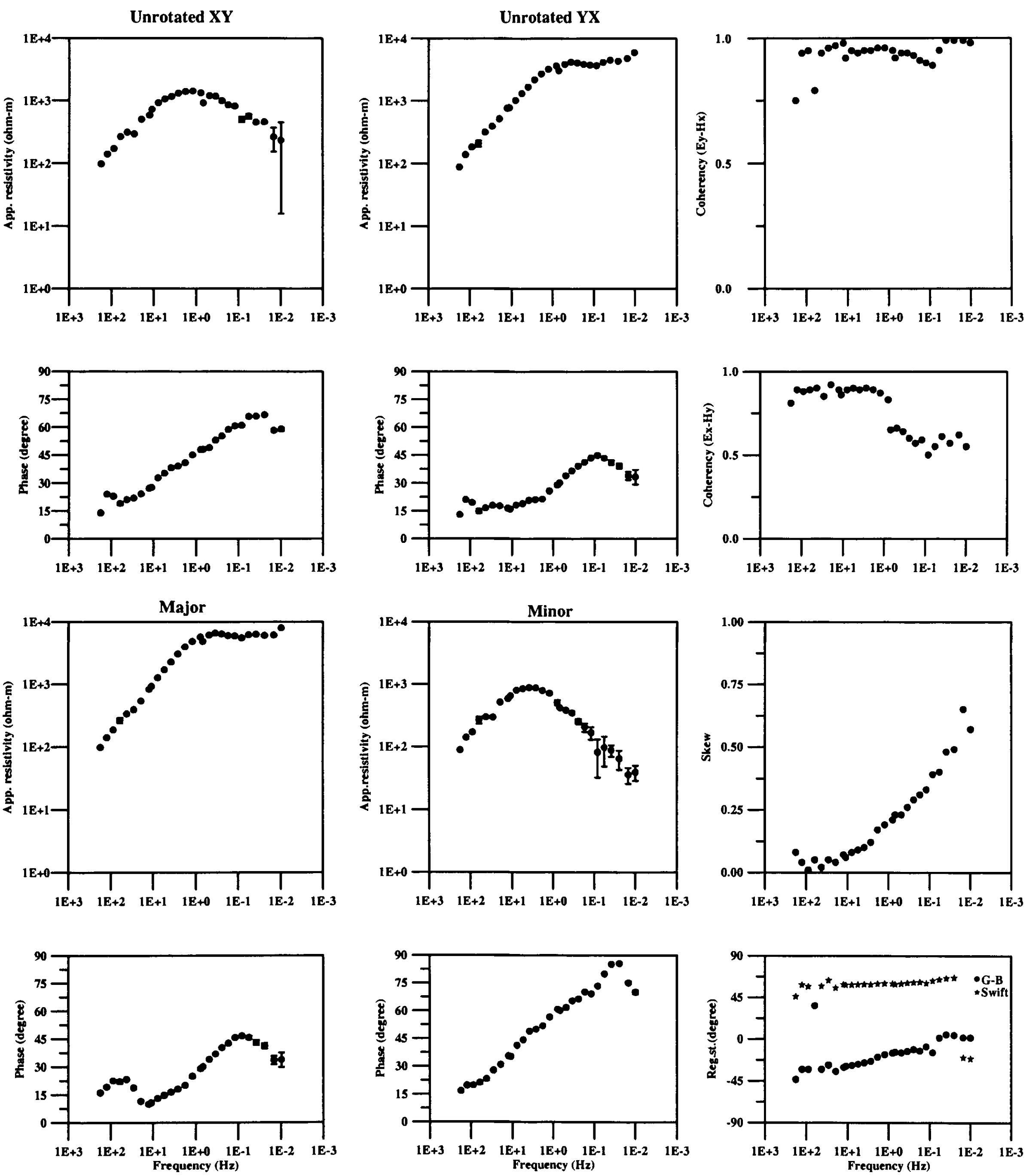

Unrotated XY
Unrotated YX
Major
Minor
App. resistivity (ohm-m)
App.resistivity (ohm-m)
Phase (degree)
Coherency (Ey-Hx)
Coherency (Ex-Hy)
Skew
Reg.st.(degree)
•G-B
*Swift
Frequency (Hz)

Station 8

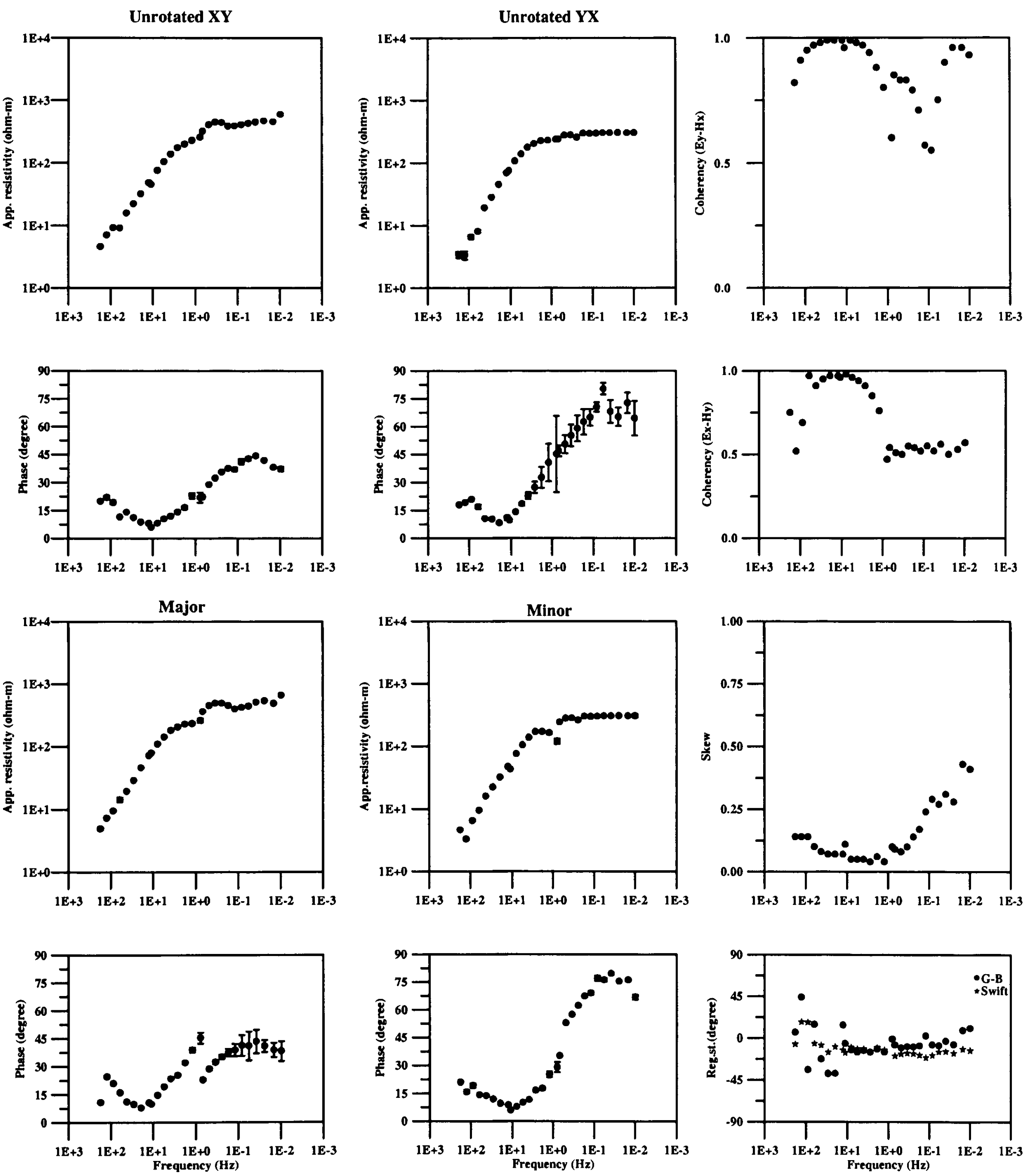

Unrotated XY
Unrotated YX
Major
Minor
App. resistivity (ohm-m)
App.resistivity (ohm-m)
Phase (degree)
Coherency (Ey-Hx)
Coherency (Ex-Hy)
Skew
Reg.st.(degree)
•G-B
*Swift
Frequency (Hz)
1E+3 1E+2 1E+1 1E+0 1E-1 1E-2 1E-3
1E+0 1E+1 1E+2 1E+3 1E+4
0 15 30 45 60 75 90
0.0 0.5 1.0
0.00 0.25 0.50 0.75 1.00
-90 -45 0 45 90

Station 9

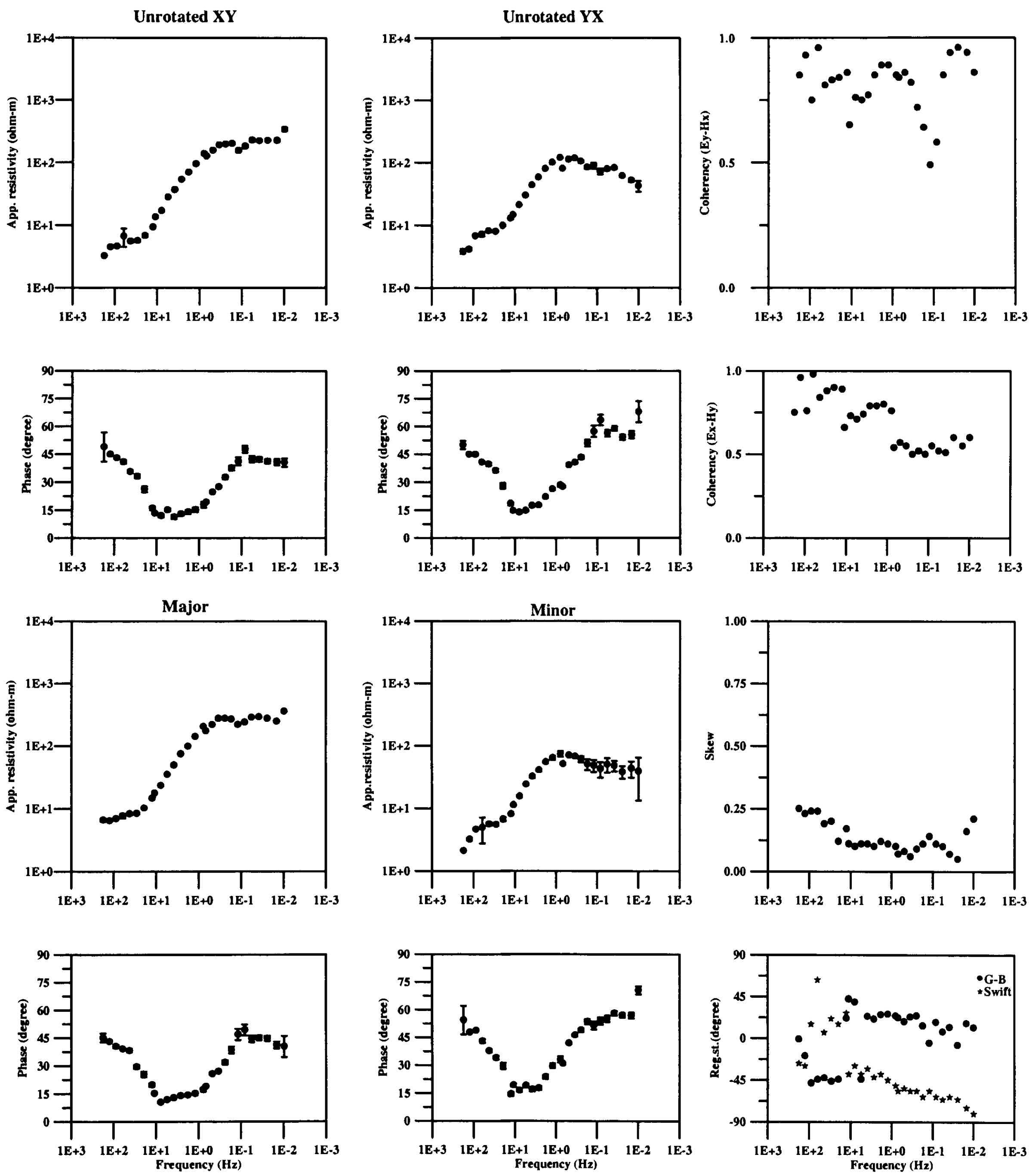
Unrotated XY
Unrotated YX
Major
Minor
App. resistivity (ohm-m)
App.resistivity (ohm-m)
Phase (degree)
Coherency (Ey-Hx)
Coherency (Ex-Hy)
Skew
Reg.st.(degree)
•G-B
*Swift
Frequency (Hz)
1E+4
1E+3
1E+2
1E+1
1E+0
90
75
60
45
30
15
0
1.0
0.5
0.0
1.00
0.75
0.50
0.25
0.00
-45
-90
1E+3 1E+2 1E+1 1E+0 1E-1 1E-2 1E-3

Station 10

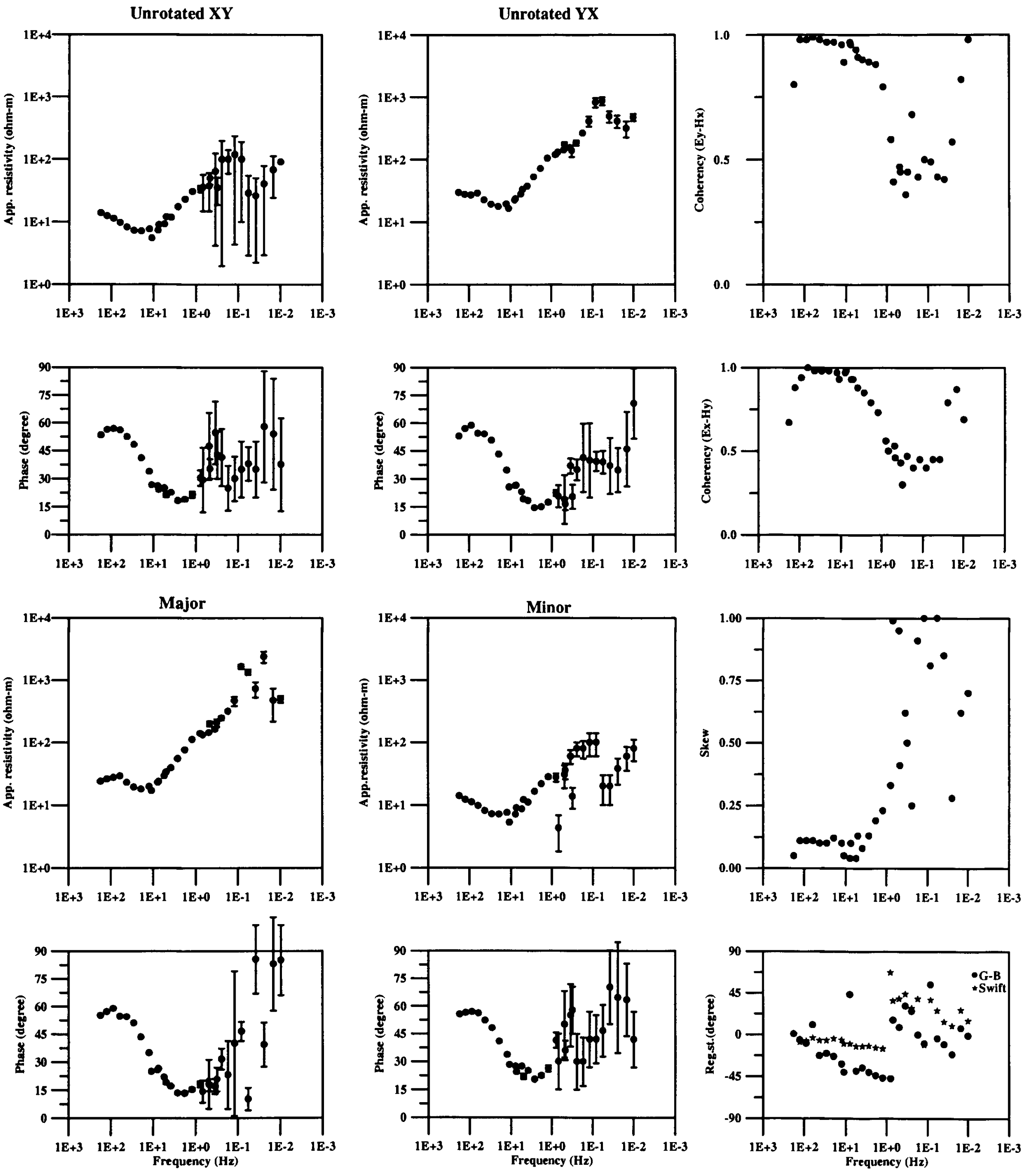
Unrotated XY
Unrotated YX
Major
Minor
App. resistivity (ohm-m)
App.resistivity (ohm-m)
Phase (degree)
Coherency (Ey-Hx)
Coherency (Ex-Hy)
Skew
Reg.st.(degree)
•G-B
*Swift
Frequency (Hz)
1E+3 1E+2 1E+1 1E+0 1E-1 1E-2 1E-3
1E+0 1E+1 1E+2 1E+3 1E+4
0 15 30 45 60 75 90
-90 -45 0 45 90
0.0 0.5 1.0
0.00 0.25 0.50 0.75 1.00

Station 11

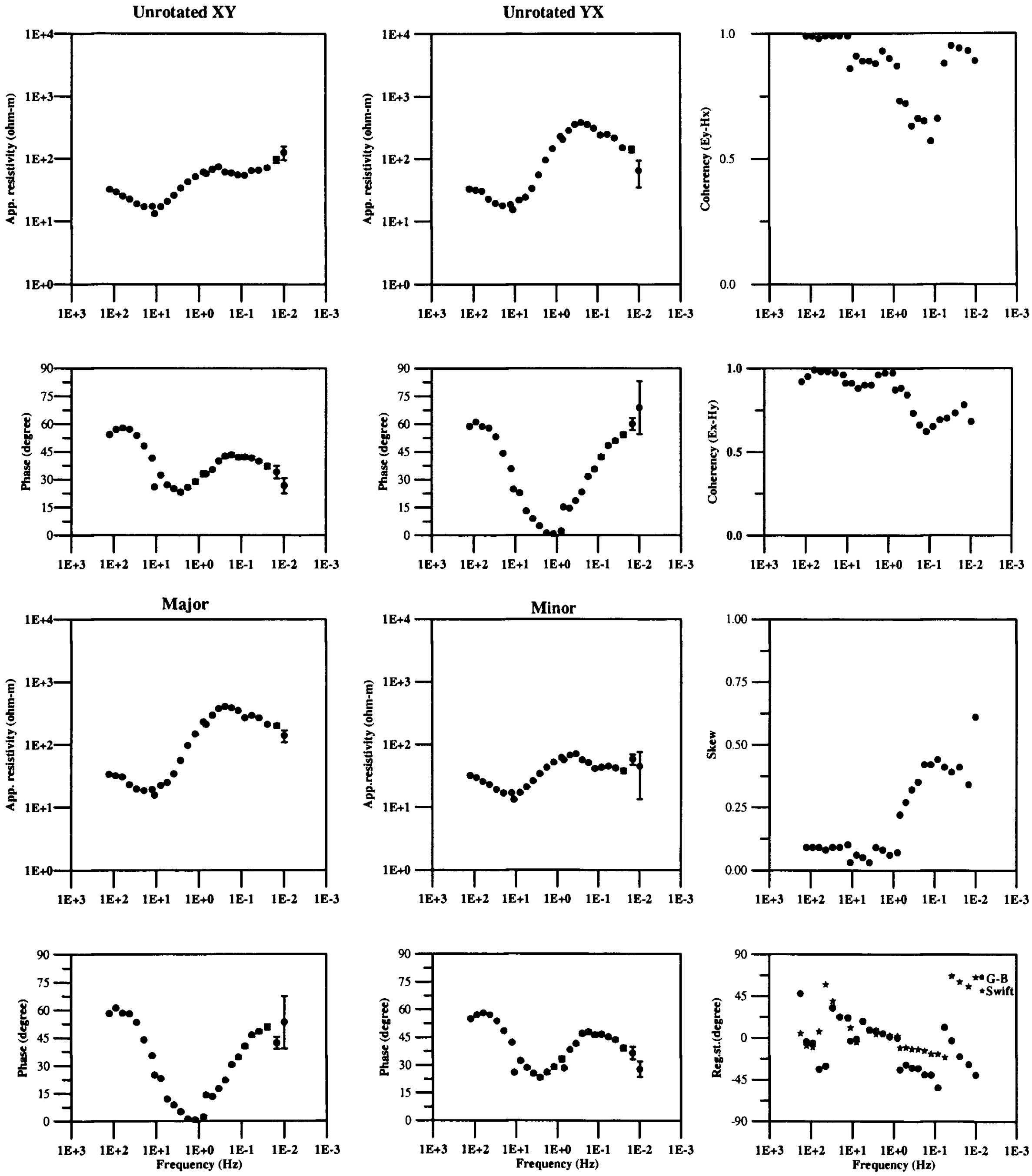
Unrotated XY
Unrotated YX
Major
Minor
App. resistivity (ohm-m)
Phase (degree)
Coherency (Ey-Hx)
Coherency (Ex-Hy)
Skew
Reg.st.(degree)
G-B
Swift
Frequency (Hz)

Station 12

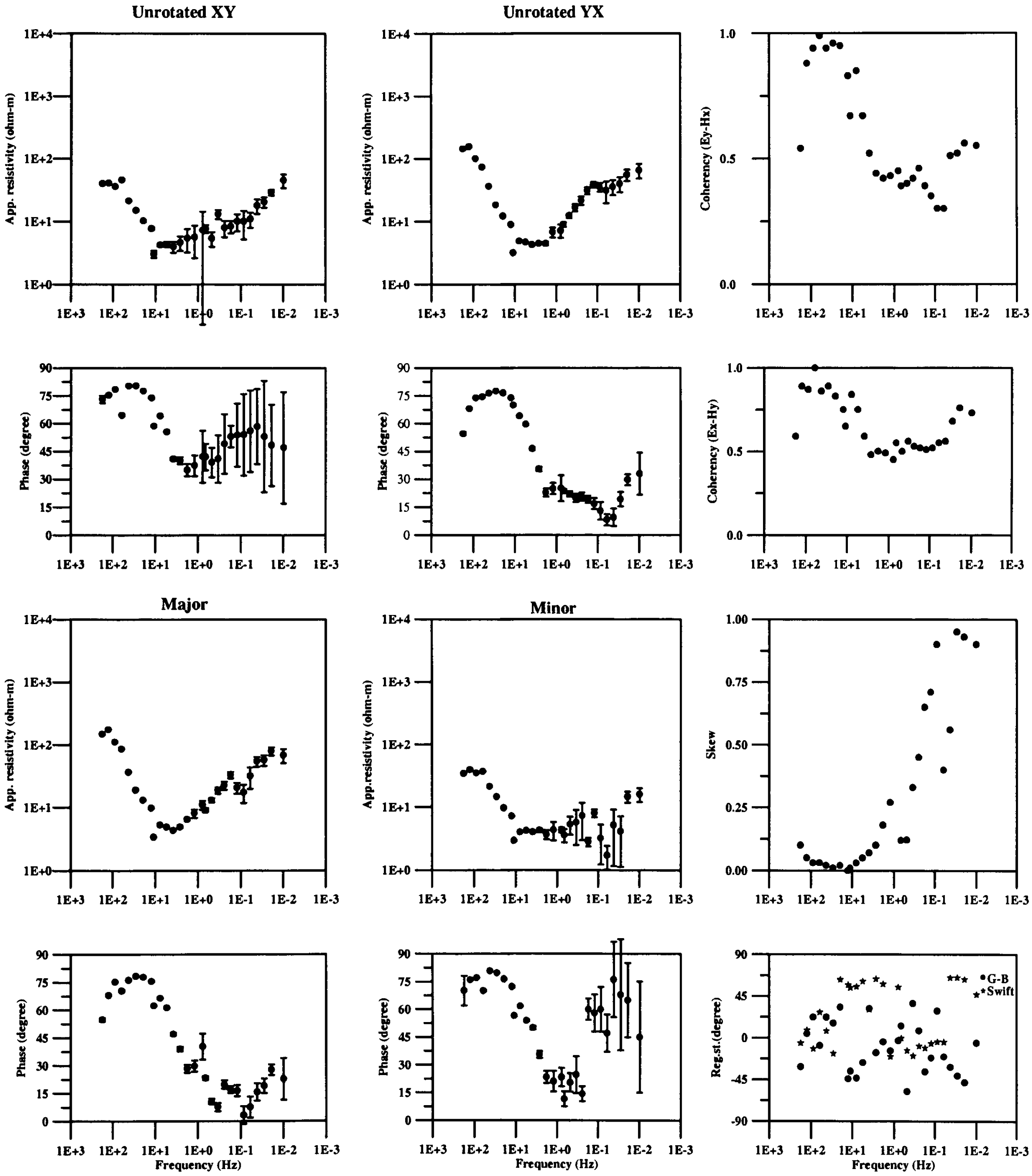

Unrotated XY
Unrotated YX
Major
Minor
App. resistivity (ohm-m)
App.resistivity (ohm-m)
Phase (degree)
Coherency (Ey-Hx)
Coherency (Ex-Hy)
Skew
Reg.st.(degree)
G-B
Swift
Frequency (Hz)
1E+4
1E+3
1E+2
1E+1
1E+0
1E-1
1E-2
1E-3
90
75
60
45
30
15
0
-45
-90
1.0
0.5
0.0
1.00
0.75
0.50
0.25
0.00

Station 13

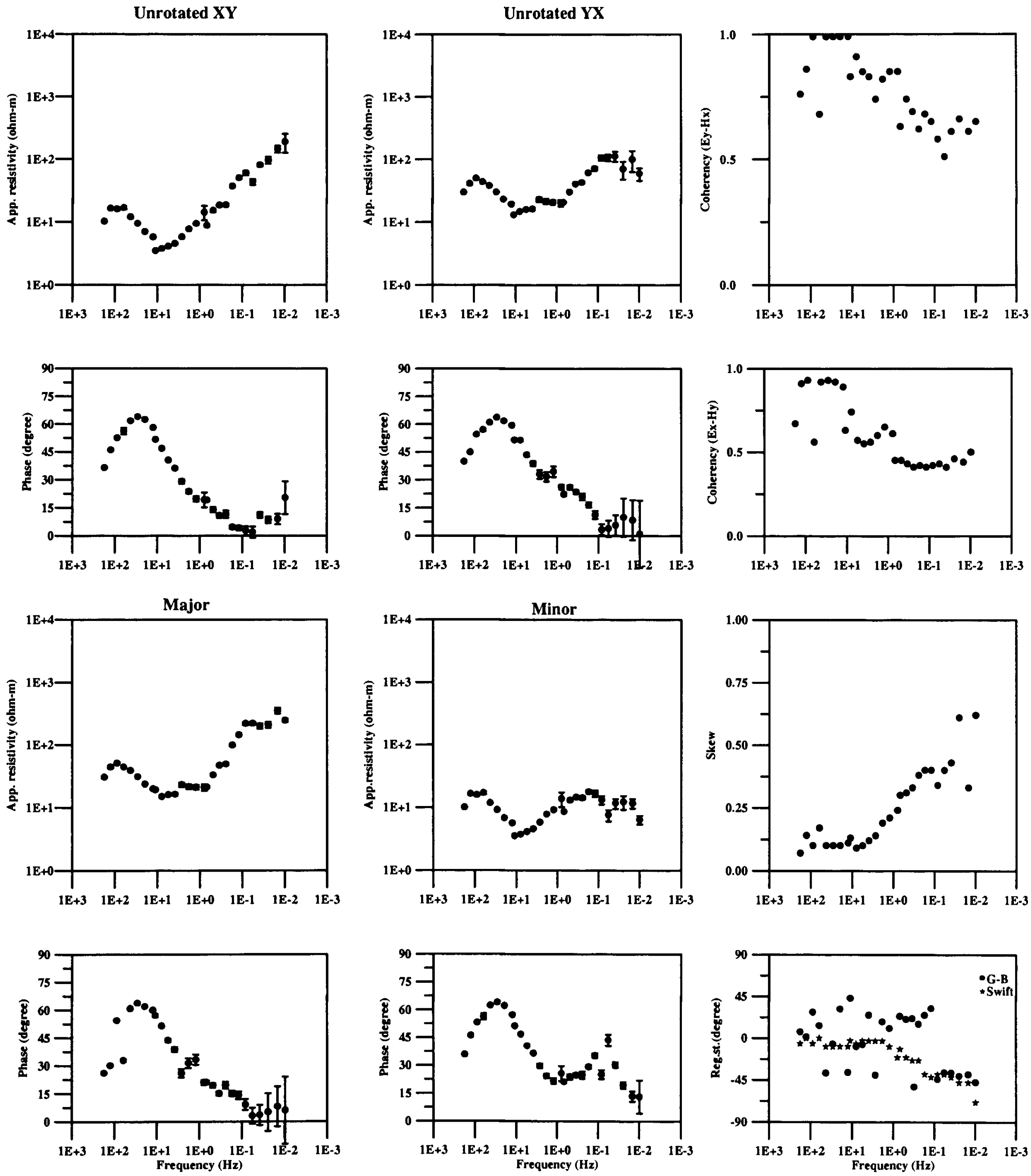
Unrotated XY
Unrotated YX
Major
Minor
App. resistivity (ohm-m)
App.resistivity (ohm-m)
Phase (degree)
Coherency (Ey-Hx)
Coherency (Ex-Hy)
Skew
Reg.st.(degree)
•G-B
*Swift
Frequency (Hz)

Station 14

Appendix A.2

1-D Results of joint inversion of TEM and MT data for the two polarization modes at some selected sites for PN profile, Parnaiba basin, Brazil. (a) represents TEM (square symbol) and MT-TM mode data (cross symbol). (b) displays TEM data and MT-TE mode data. TEM single loop data were used for static shift correction of TM mode and TEM central loop data were adapted for TE mode (Meju, 1996). However, single loop data were noisy at most of sites. Consequently, TEM central loop data were used instead for those soundings.

a)

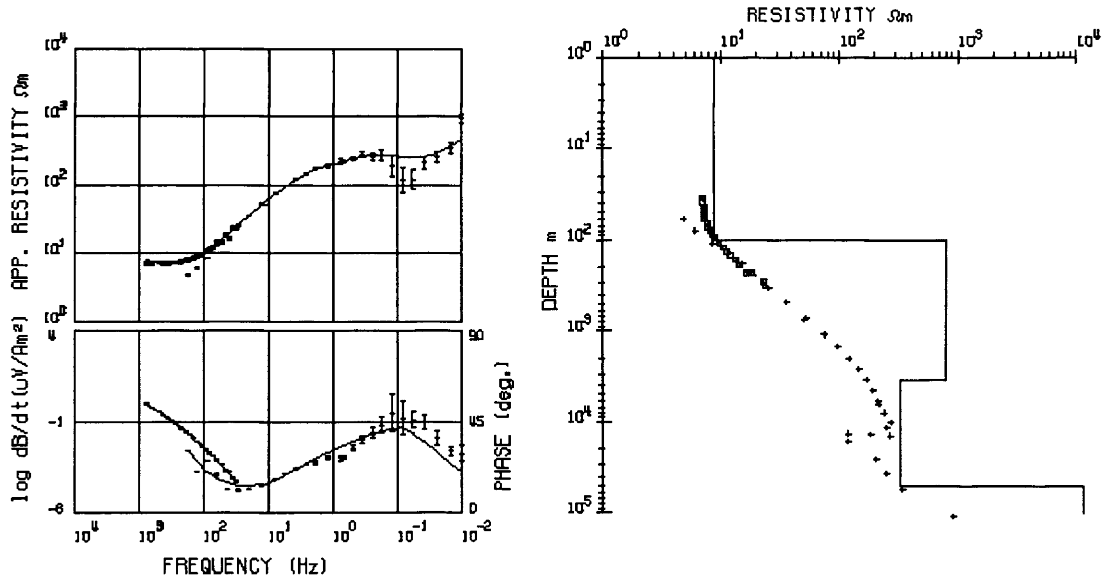

b)

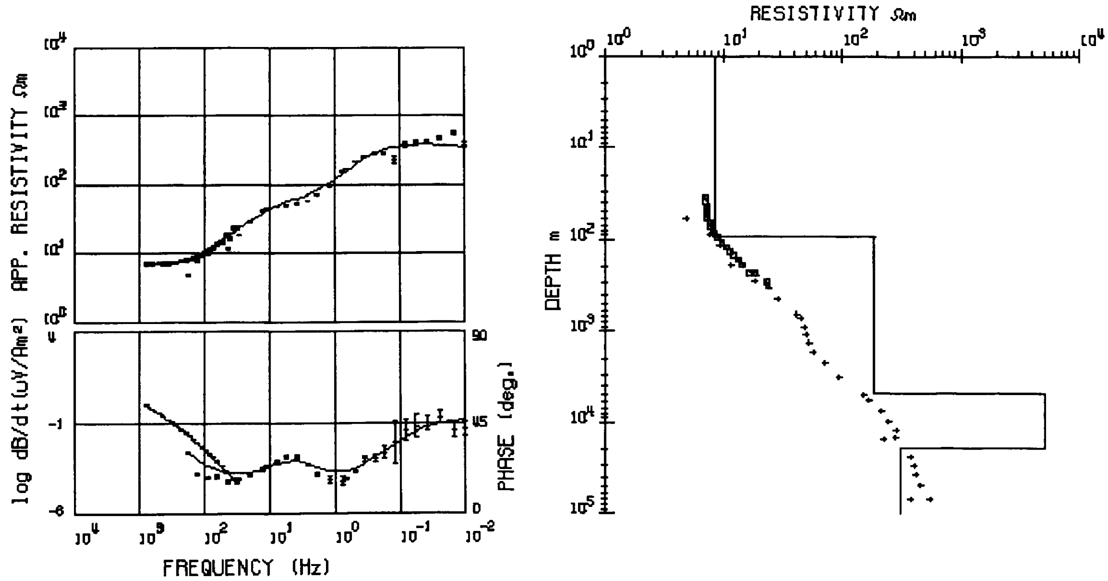

Station 2

a)

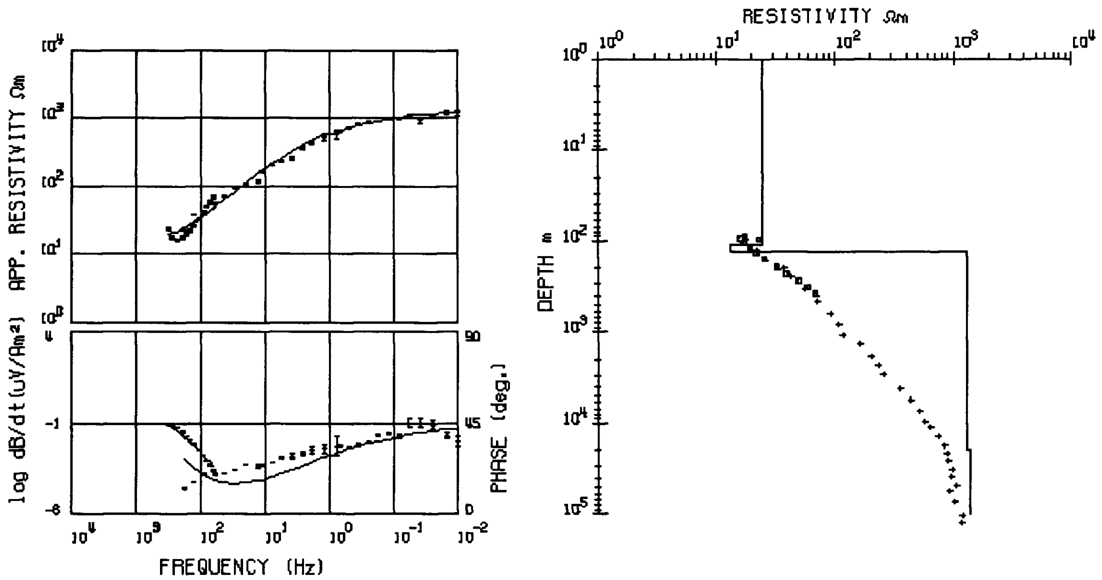
APP. RESISTIVITY Ωm
log dB/dt (uV/Am²)
PHASE (deg.)
FREQUENCY (Hz)
RESISTIVITY Ωm
DEPTH m

b)

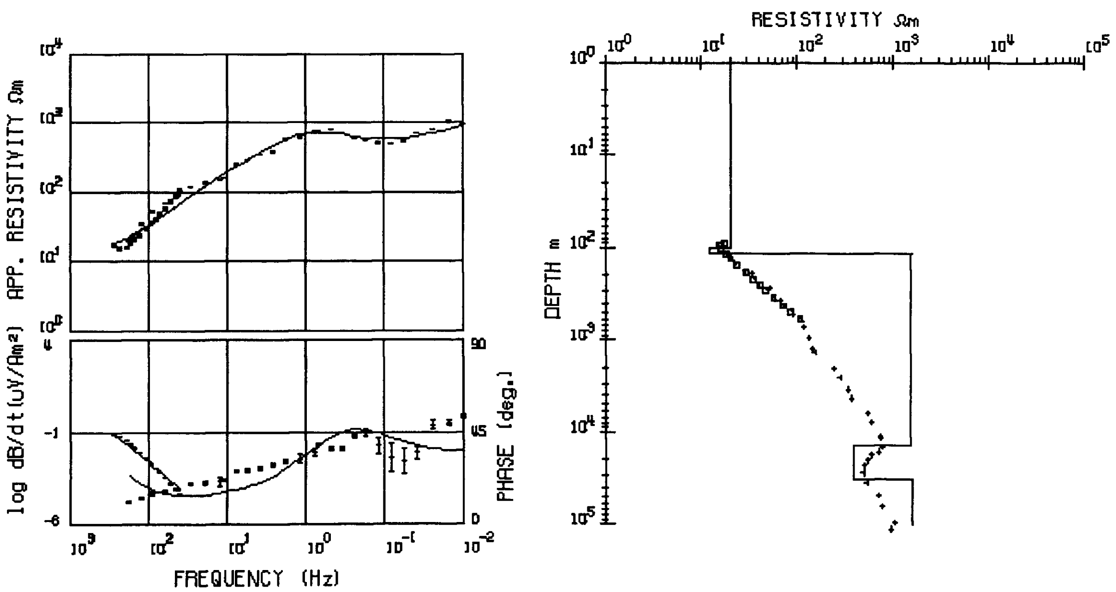
APP. RESISTIVITY Ωm
log dB/dt (uV/Am²)
PHASE (deg.)
FREQUENCY (Hz)
RESISTIVITY Ωm
DEPTH m

Station 4

a)

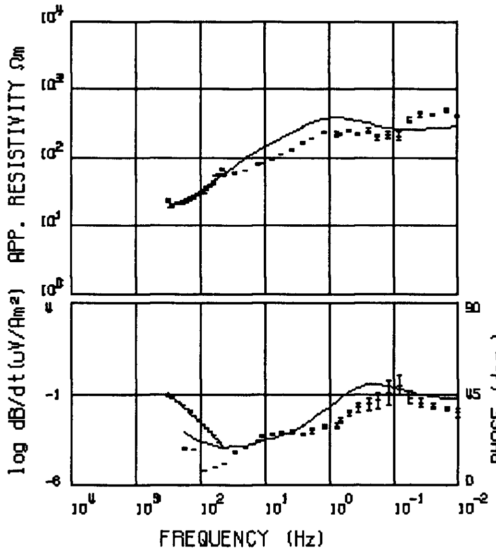
APP. RESISTIVITY Ωm
log dB/dt (uV/Am²)
PHASE (deg.)
FREQUENCY (Hz)

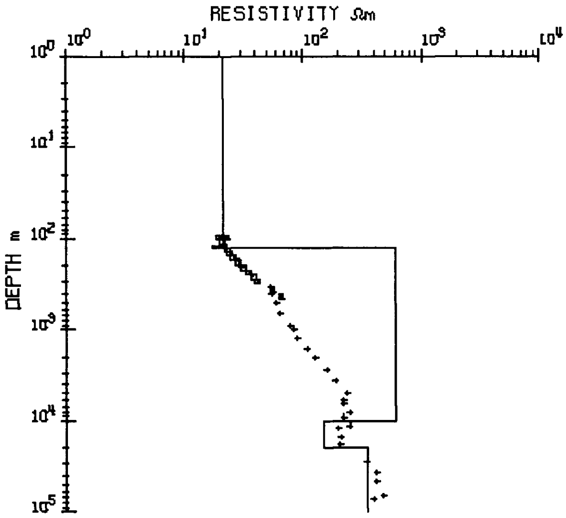
RESISTIVITY Ωm
DEPTH m

b)

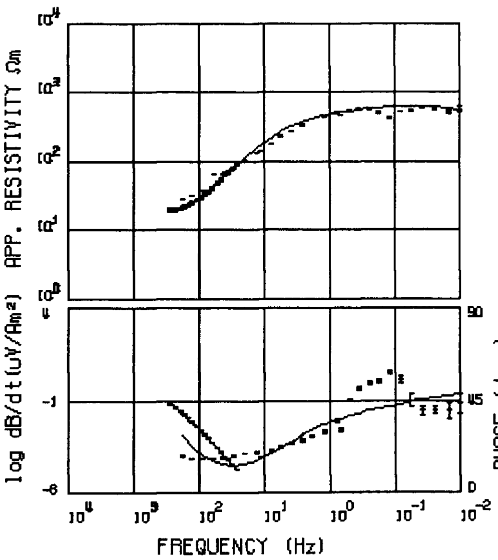
APP. RESISTIVITY Ωm
log dB/dt (uV/Am²)
PHASE (deg.)
FREQUENCY (Hz)

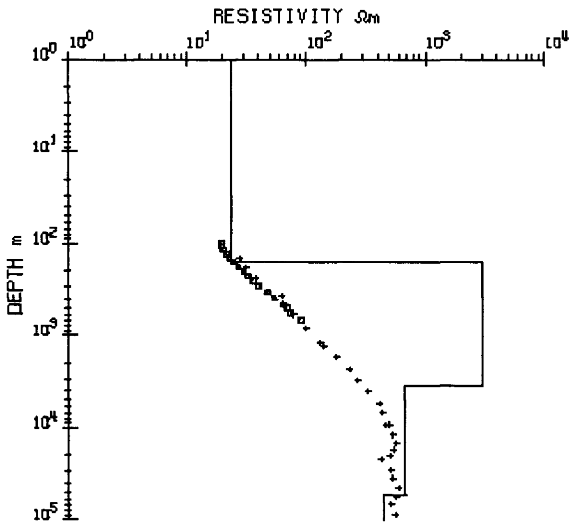
RESISTIVITY Ωm
DEPTH m

Station 5

a)

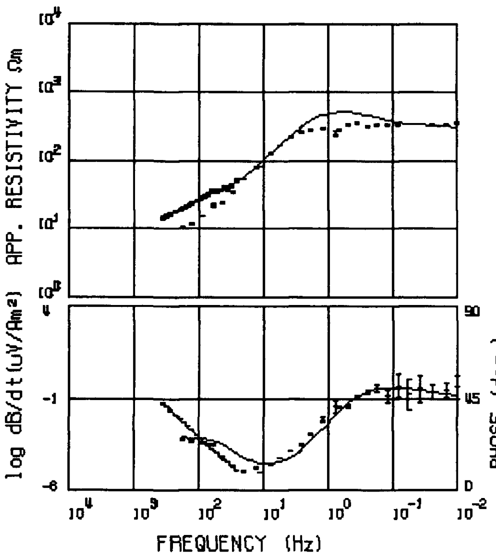
APP. RESISTIVITY Ωm
log dB/dt(uV/Am²)
PHASE (deg.)
FREQUENCY (Hz)

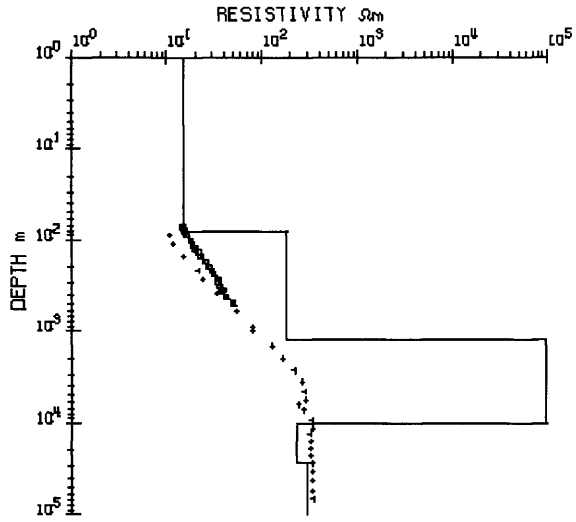
RESISTIVITY Ωm
DEPTH m

b)

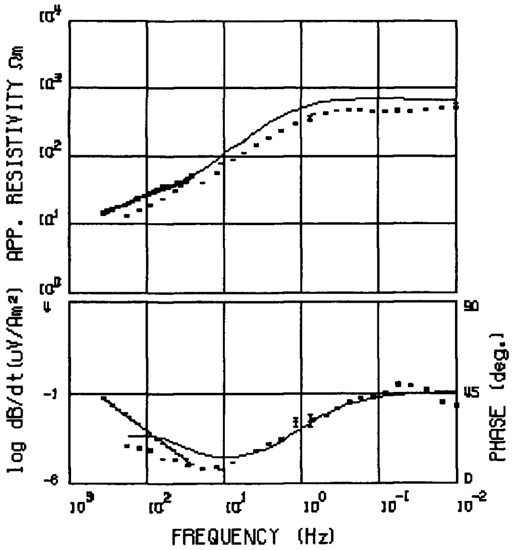
APP. RESISTIVITY Ωm
log dB/dt(uV/Am²)
PHASE (deg.)
FREQUENCY (Hz)

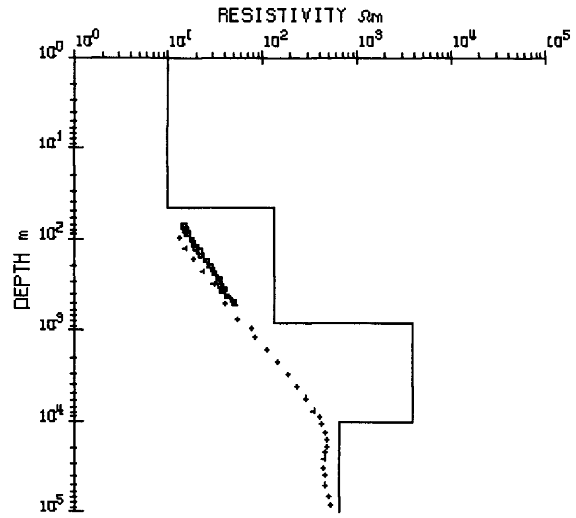
RESISTIVITY Ωm
DEPTH m

Station 9

a)

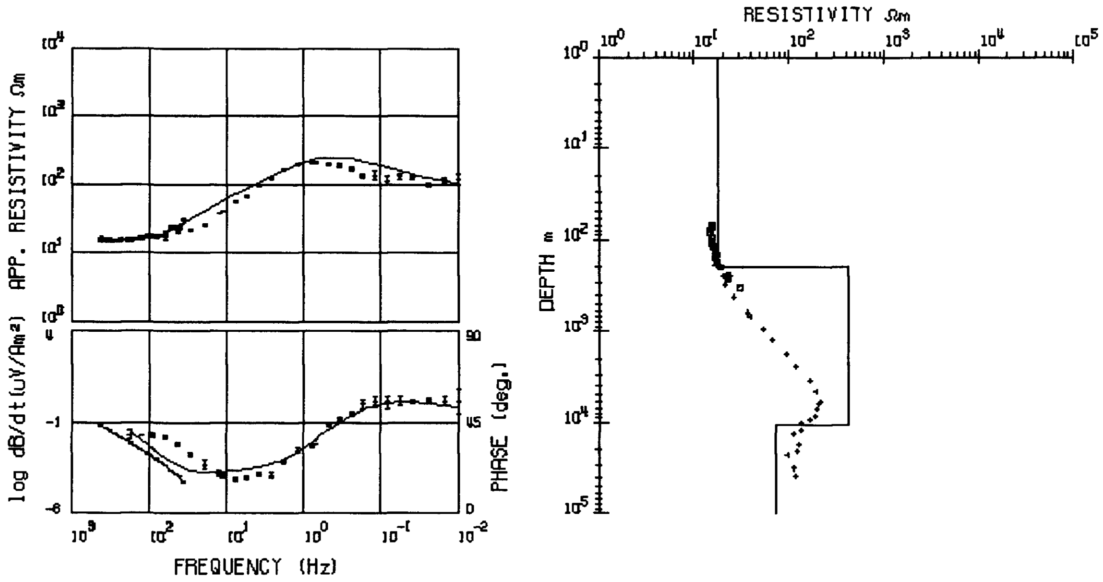

b)

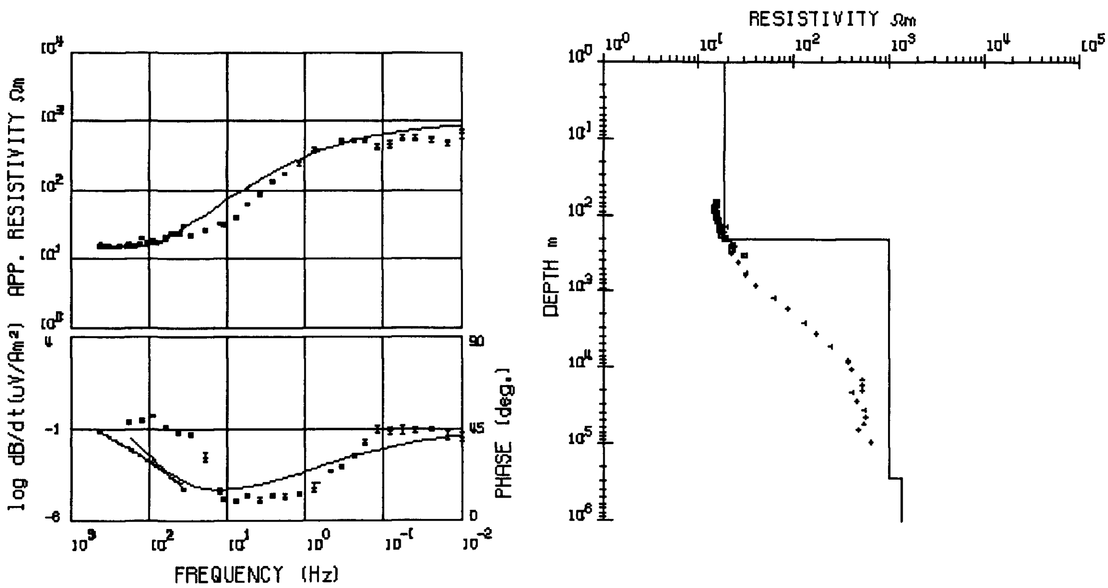

Station 10

a)

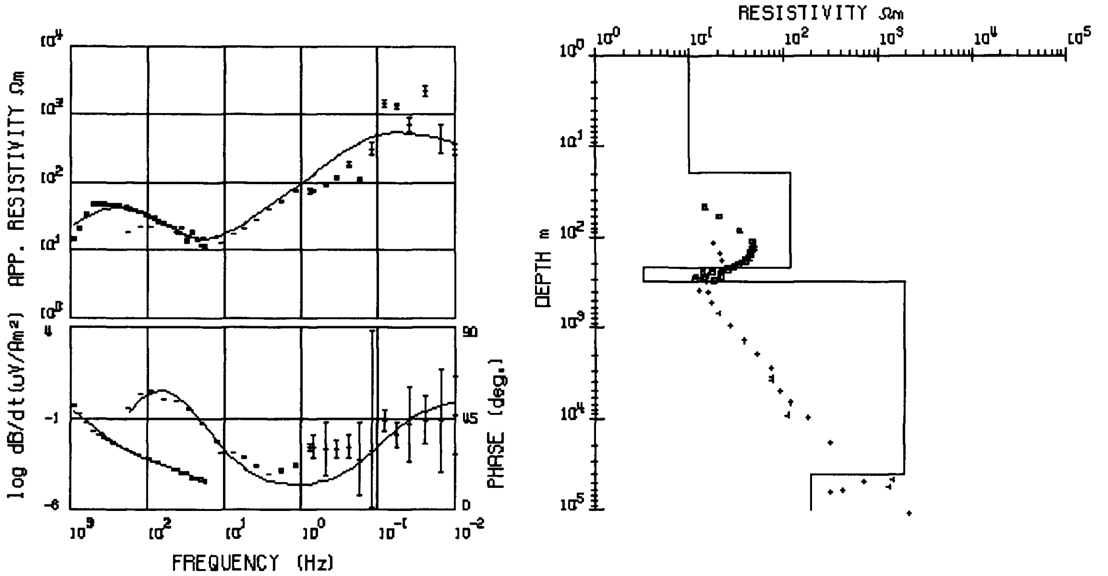

b)

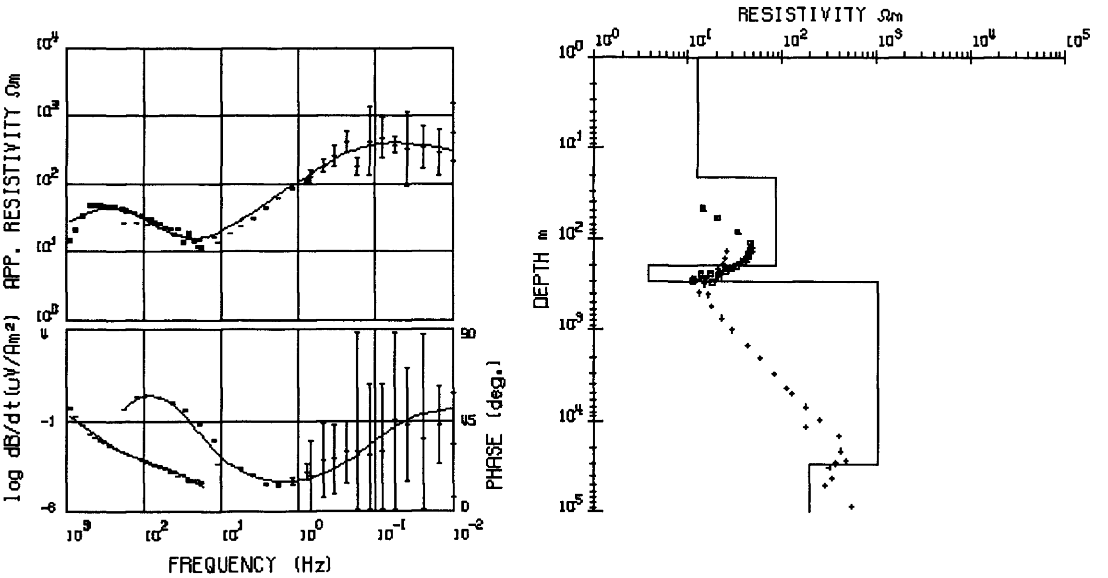

Station 11

a)

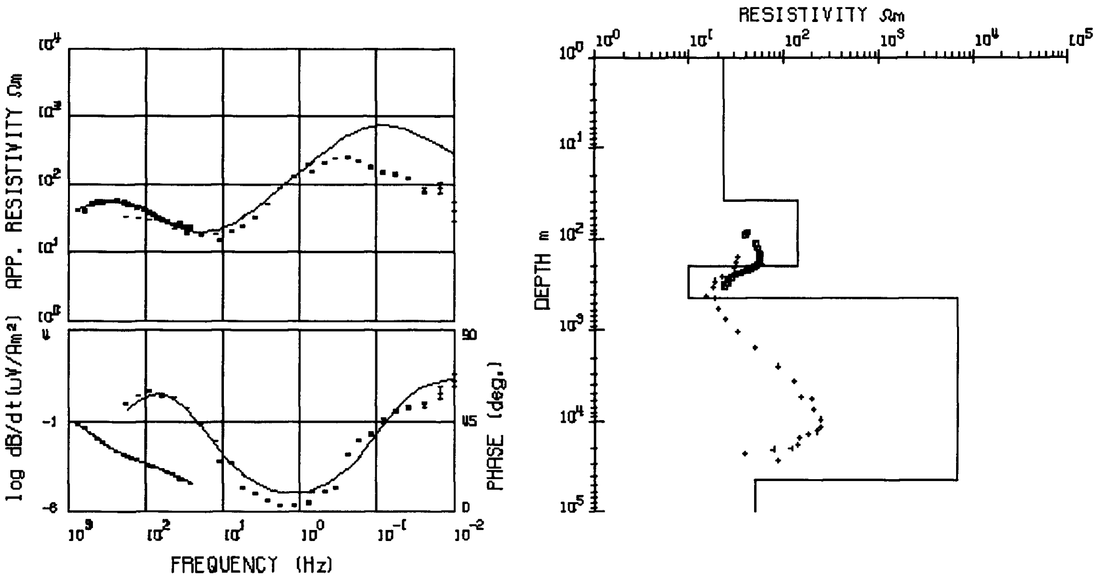

b)

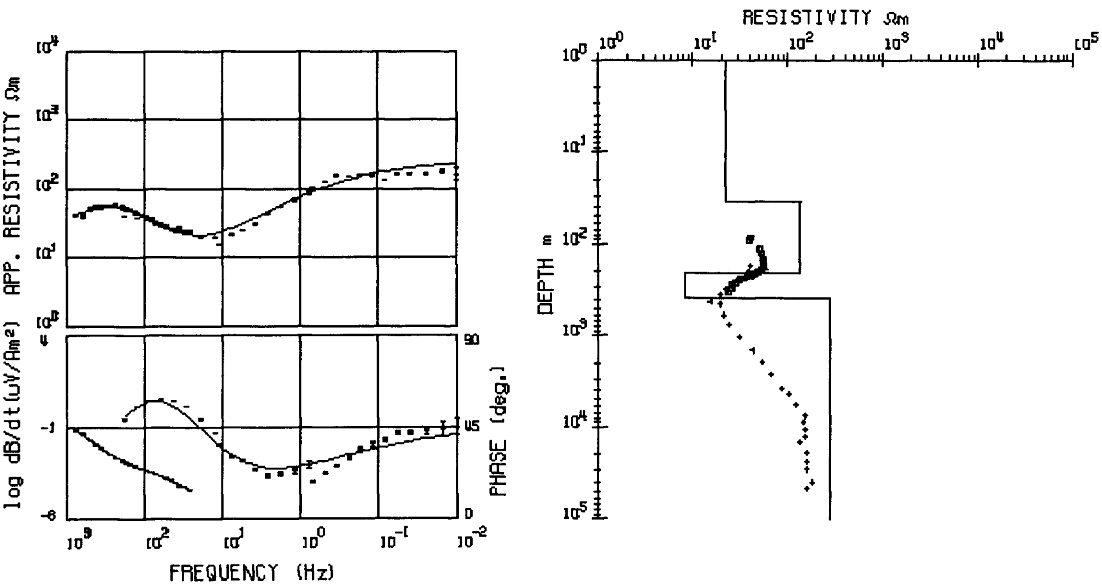

Station 12

Appendix B

Appendix B.1

The MT data obtained for MH profile in Parnaiba basin, Brazil (Figure 5.4). For each site, the data shown are: the apparent resistivity and phase curves of the off diagonal elements of the unrotated impedance tensor, the major and minor apparent resistivity and phase, the regional azimuth (Swift and Groom-Bailey methods) measured positive clockwise from magnetic north), skew, and coherency. The error bars are one standard deviation.

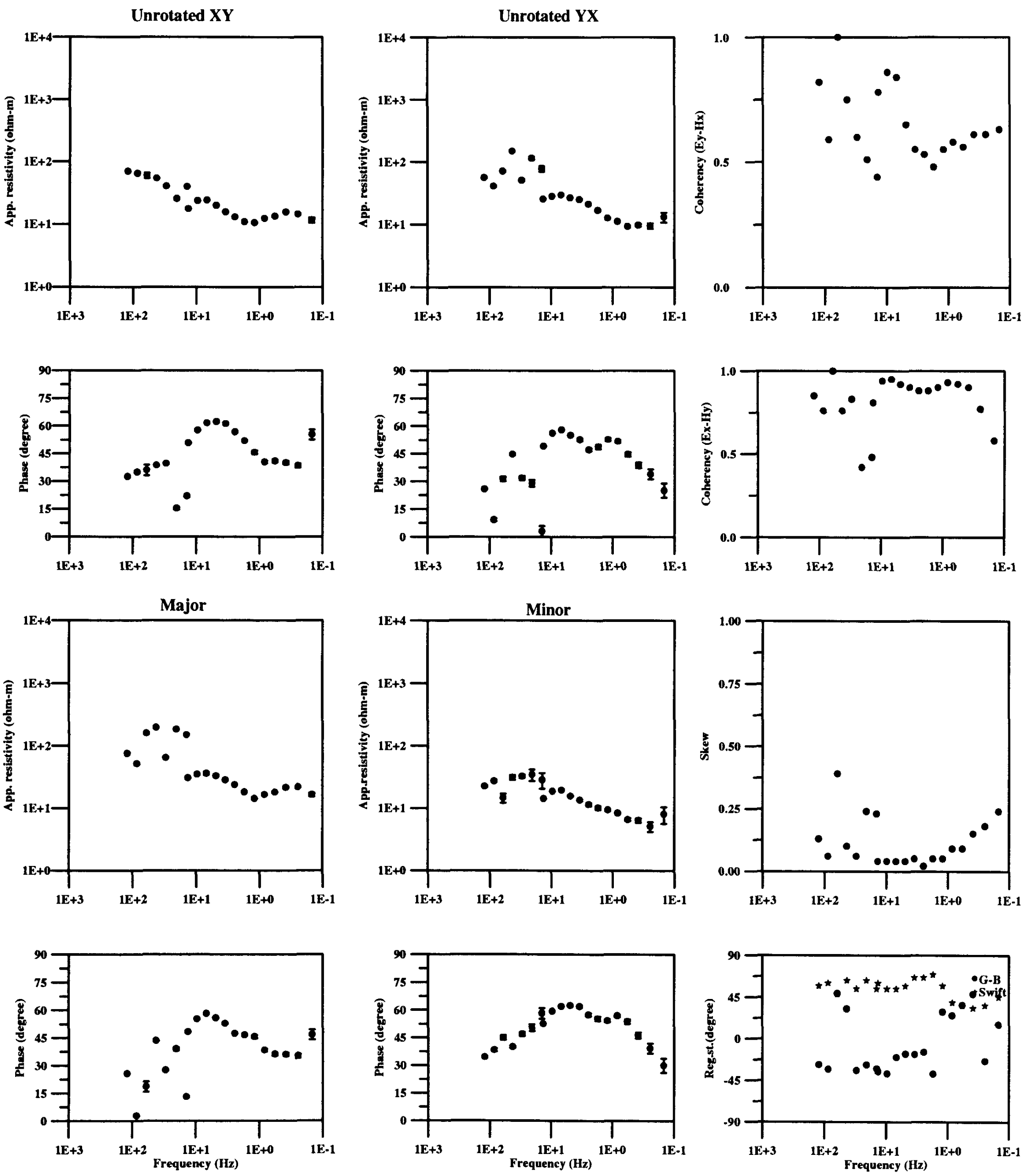

MH2

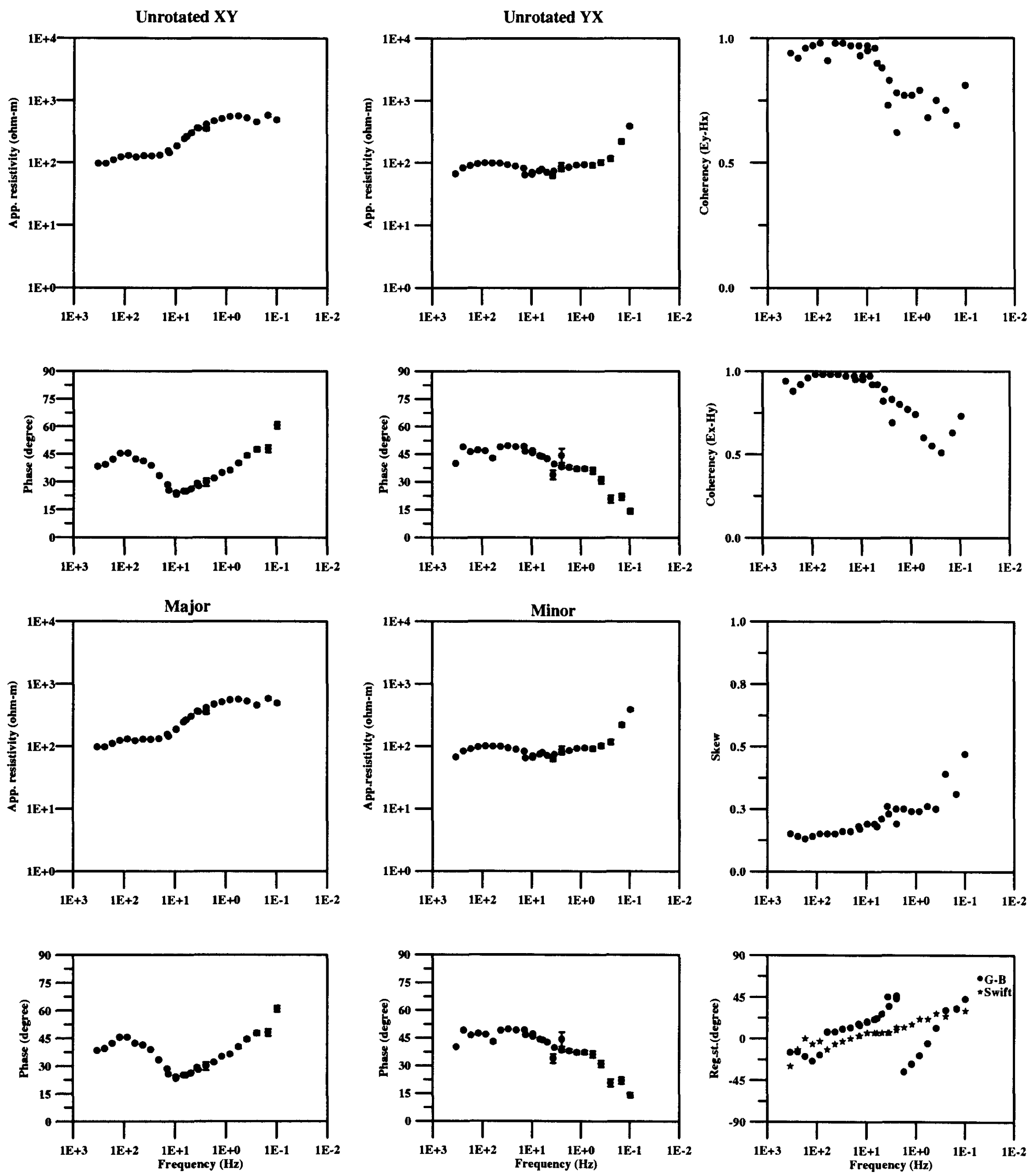
Unrotated XY
Unrotated YX
Major
Minor
App. resistivity (ohm-m)
App.resistivity (ohm-m)
Phase (degree)
Coherency (Ey-Hx)
Coherency (Ex-Hy)
Skew
Reg.st.(degree)
Frequency (Hz)
G-B
Swift

MH3

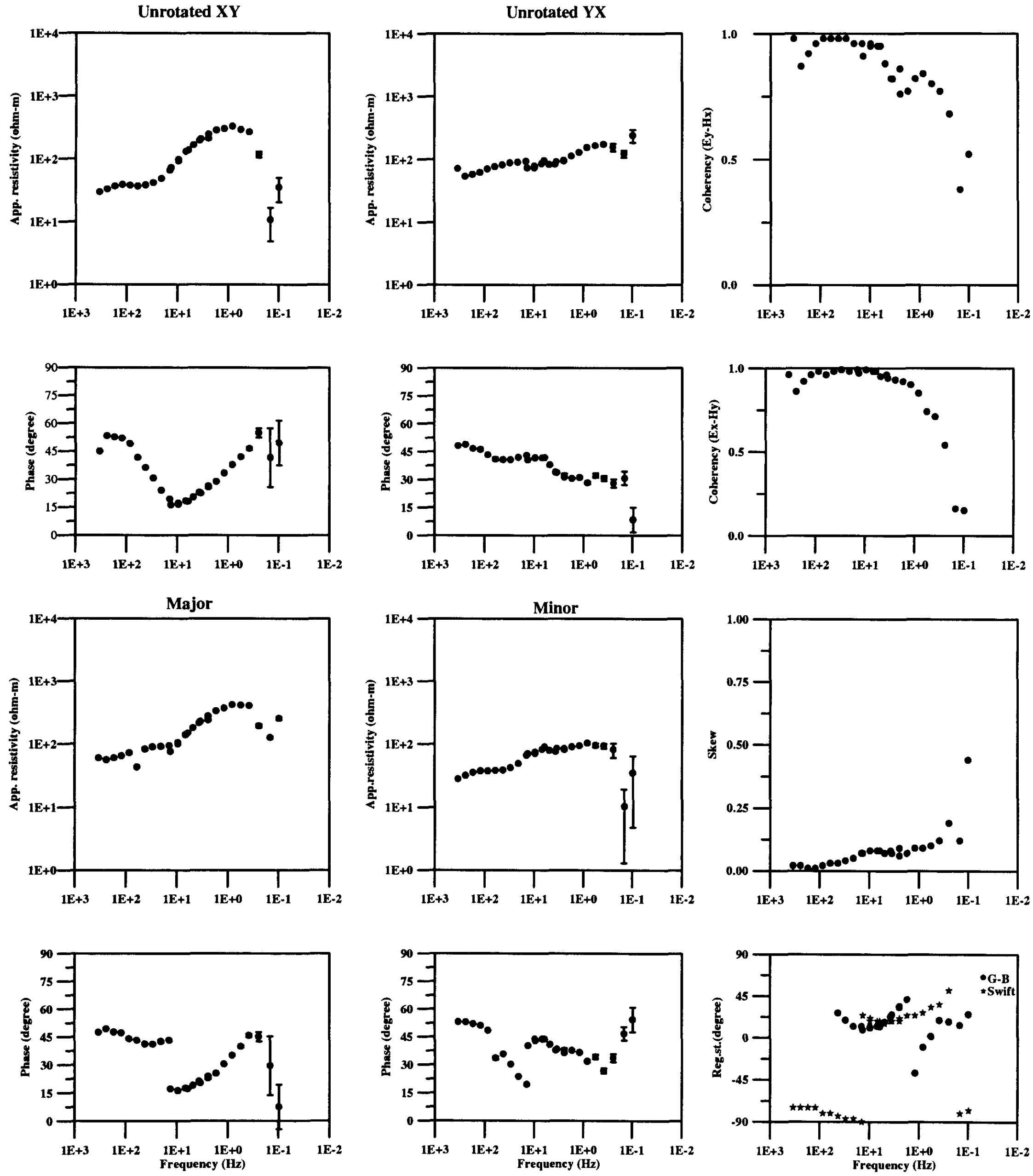
Unrotated XY
Unrotated YX
Major
Minor
App. resistivity (ohm-m)
App.resistivity (ohm-m)
Phase (degree)
Coherency (Ey-Hx)
Coherency (Ex-Hy)
Skew
Reg.st.(degree)
•G-B
*Swift
Frequency (Hz)

MH4

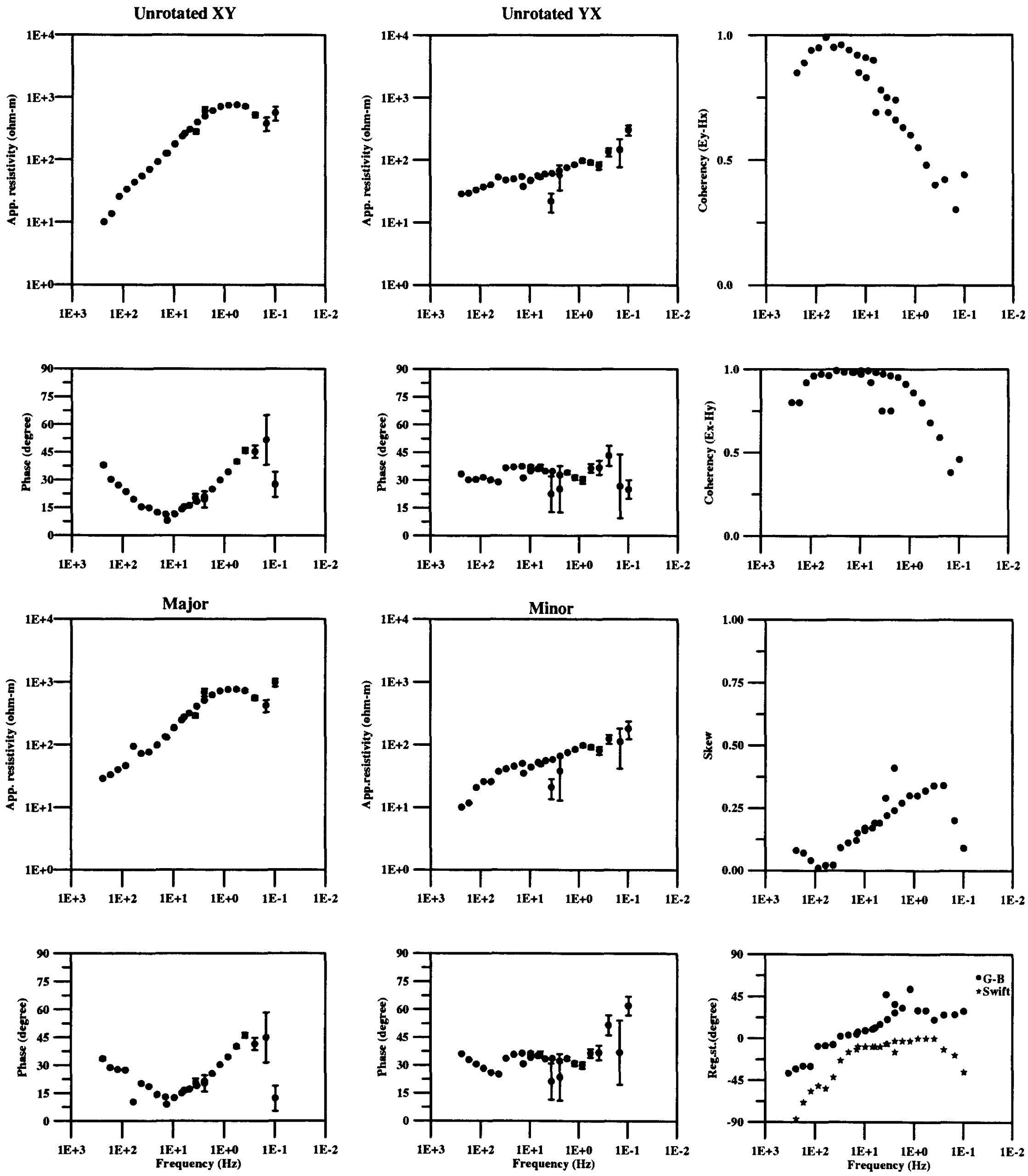

Unrotated XY
Unrotated YX
Major
Minor
App. resistivity (ohm-m)
App.resistivity (ohm-m)
Coherency (Ey-Hx)
Coherency (Ex-Hy)
Phase (degree)
Skew
Reg.st.(degree)
•G-B
*Swift
Frequency (Hz)
1E+3
1E+2
1E+1
1E+0
1E-1
1E-2
1E+4

MH5

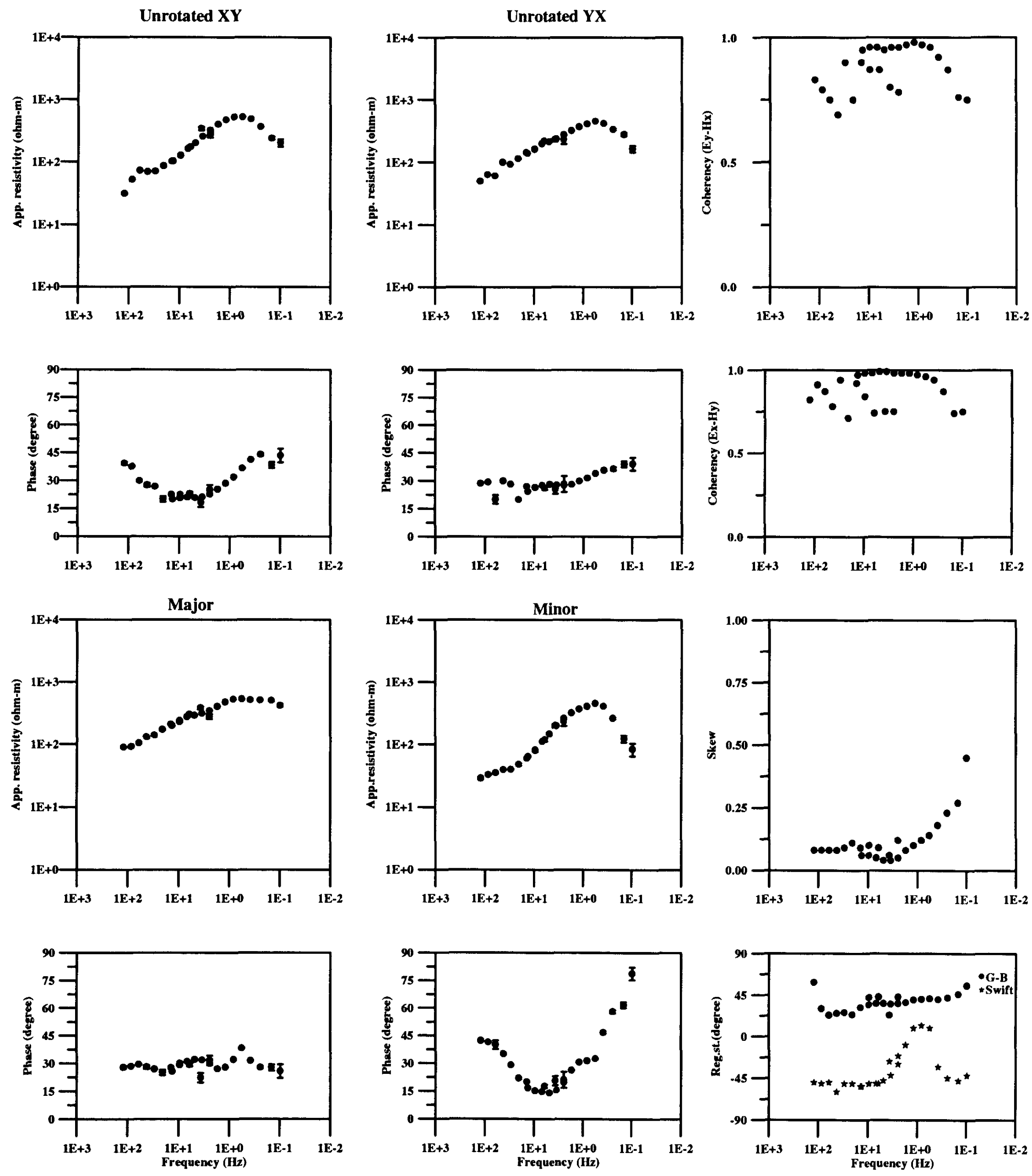
Unrotated XY
Unrotated YX
Major
Minor
App. resistivity (ohm-m)
App.resistivity (ohm-m)
Phase (degree)
Coherency (Ey-Hx)
Coherency (Ex-Hy)
Skew
Reg.st.(degree)
G-B
Swift
Frequency (Hz)
1E+3
1E+2
1E+1
1E+0
1E-1
1E-2
1E+4
1.0
0.5
0.0
1.00
0.75
0.50
0.25
0.00
90
75
60
45
30
15
0
-45
-90

MH6

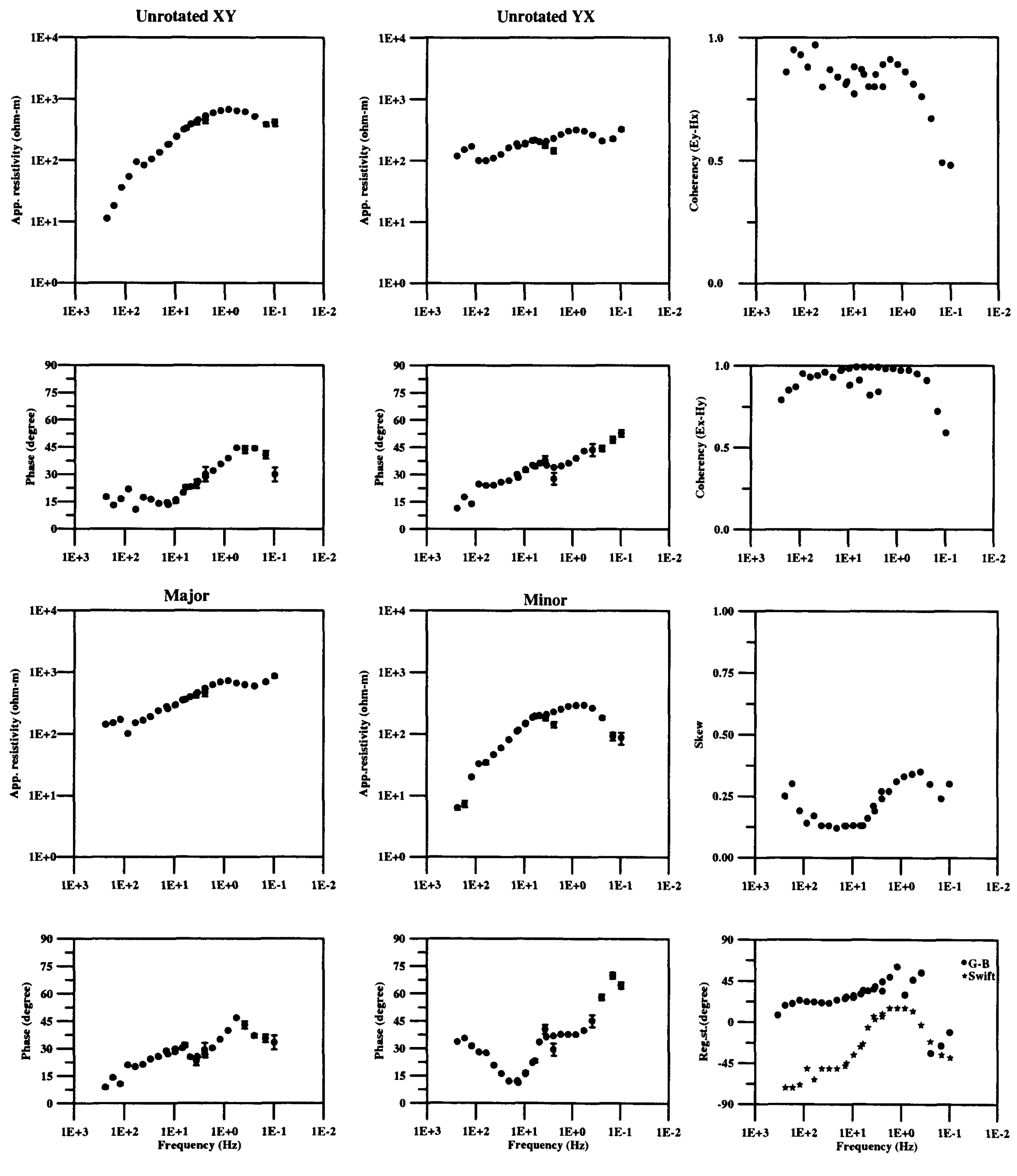
Unrotated XY
Unrotated YX
App. resistivity (ohm-m)
Coherency (Ey-Hx)
Phase (degree)
Coherency (Ex-Hy)
Major
Minor
App.resistivity (ohm-m)
Skew
Reg.st.(degree)
•G-B
*Swift
Frequency (Hz)

MH8

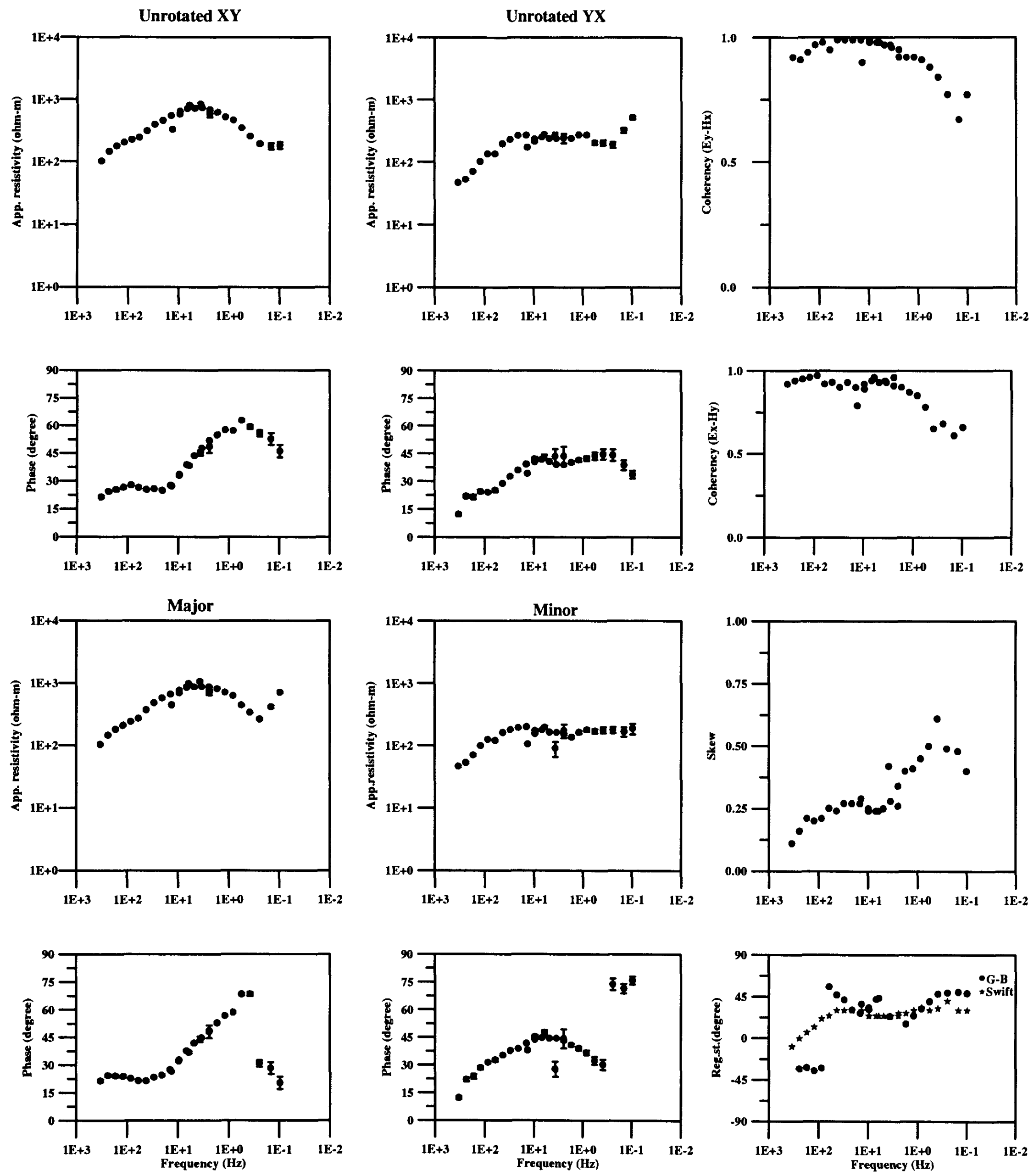
Unrotated XY
Unrotated YX
App. resistivity (ohm-m)
Phase (degree)
Coherency (Ey-Hx)
Coherency (Ex-Hy)
Major
Minor
App.resistivity (ohm-m)
Skew
Reg.st.(degree)
G-B
Swift
Frequency (Hz)

MH9

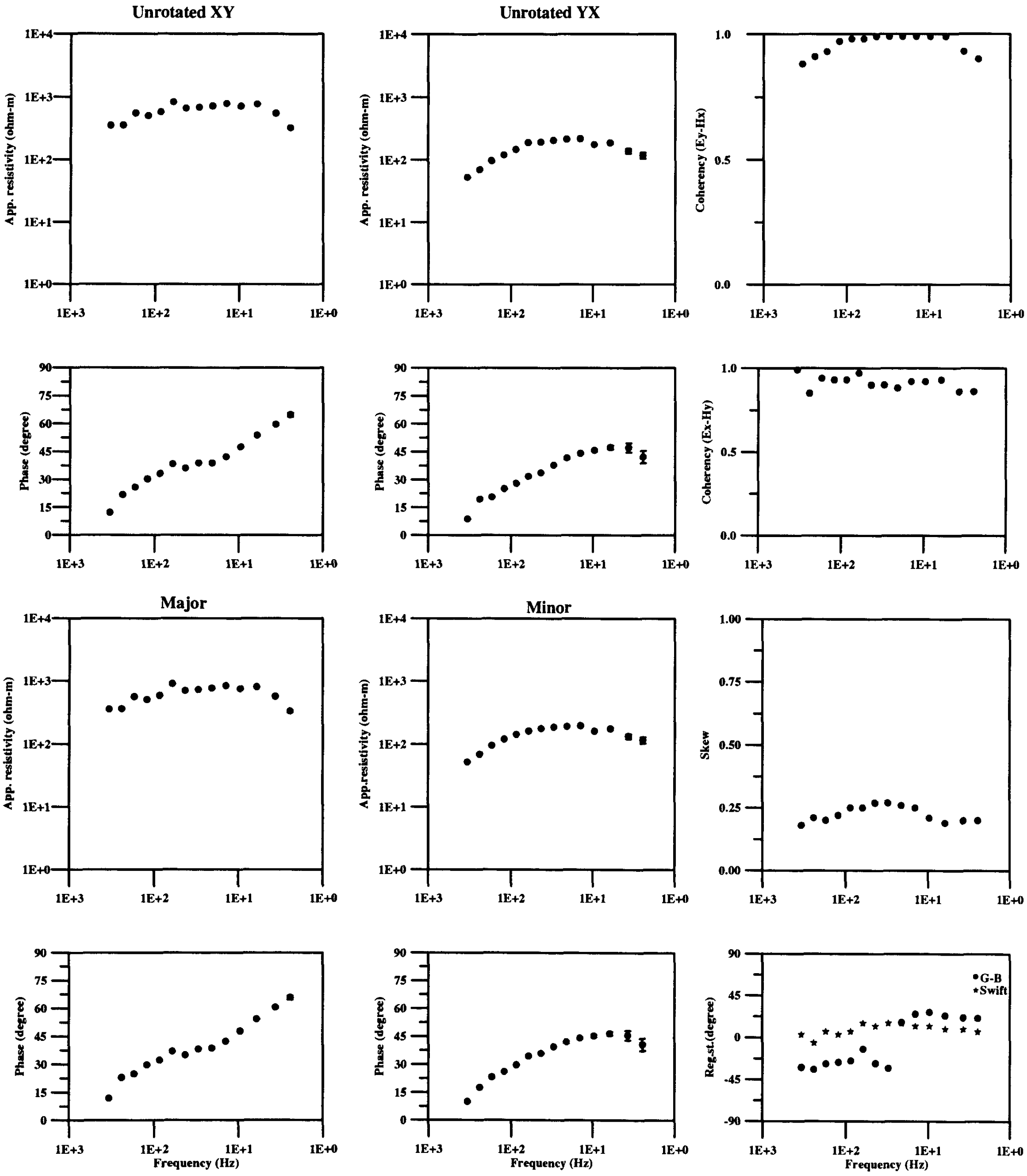
Unrotated XY
Unrotated YX
Major
Minor
App. resistivity (ohm-m)
App.resistivity (ohm-m)
Coherency (Ey-Hx)
Coherency (Ex-Hy)
Phase (degree)
Skew
Reg.st.(degree)
•G-B
*Swift
1E+4
1E+3
1E+2
1E+1
1E+0
Frequency (Hz)

MH10

Appendix B.2

1-D Results of joint inversion of TEM and MT data for the two polarization modes at some selected sites for MH profile, Parnaiba basin, Brazil. (a) represents TEM (square symbol) and MT-TM mode data (cross symbol). (b) displays TEM data and MT-TE mode data. TEM single loop data were used for static shift correction of TM mode and TEM central loop data were adapted for TE mode (Meju, 1996). However, when single loop data were noisy, TEM central loop data were used instead for those soundings.

a)

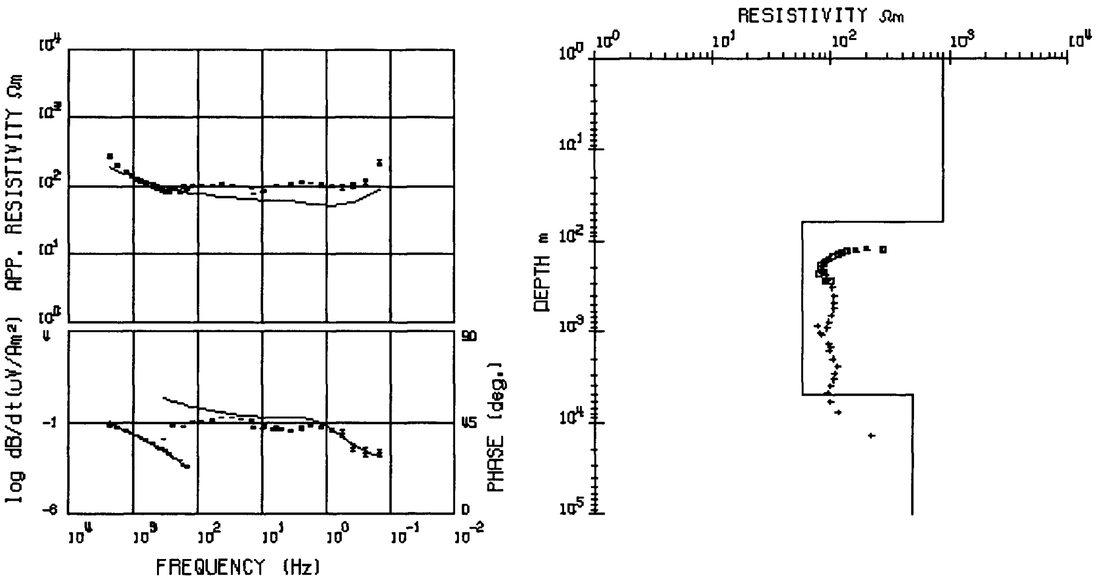

b)

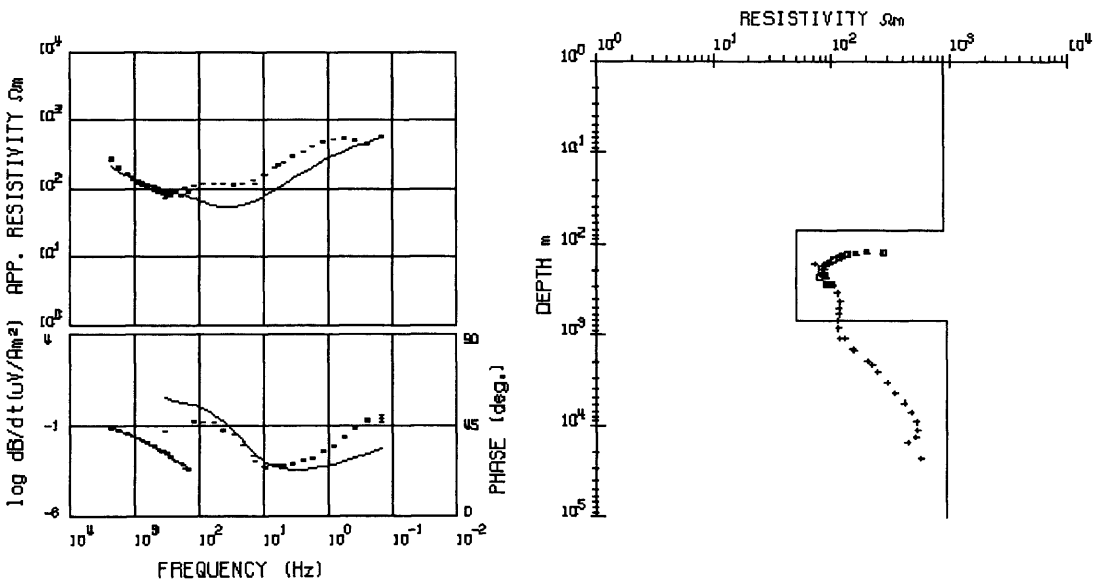

MH3

a)

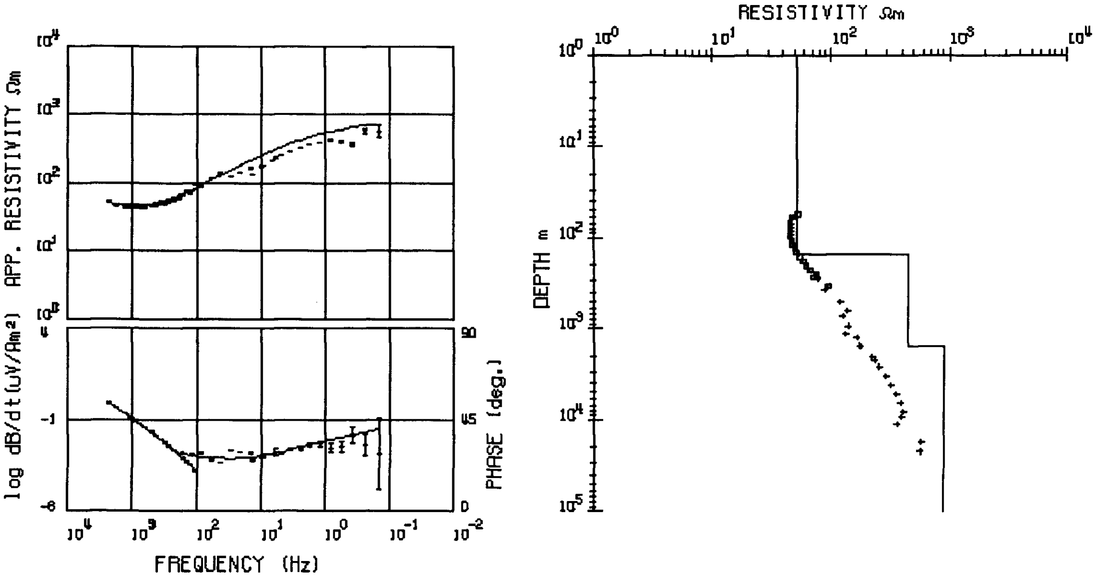
RESISTIVITY Ωm
DEPTH m
APP. RESISTIVITY Ωm
log dB/dt(uV/Am²)
PHASE (deg.)
FREQUENCY (Hz)

b)

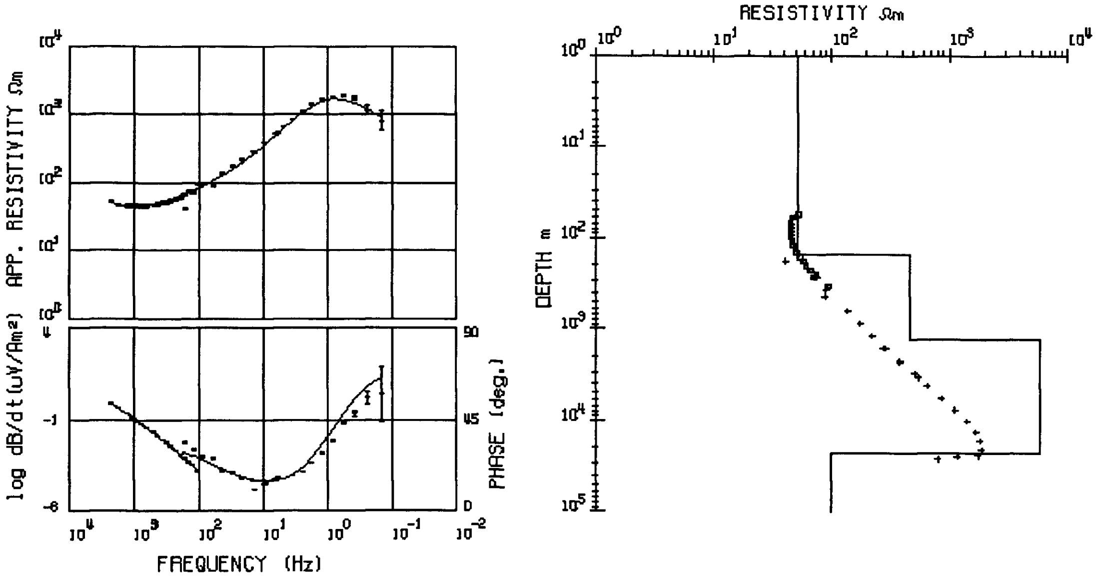
RESISTIVITY Ωm
DEPTH m
APP. RESISTIVITY Ωm
log dB/dt(uV/Am²)
PHASE (deg.)
FREQUENCY (Hz)

MH5

a)

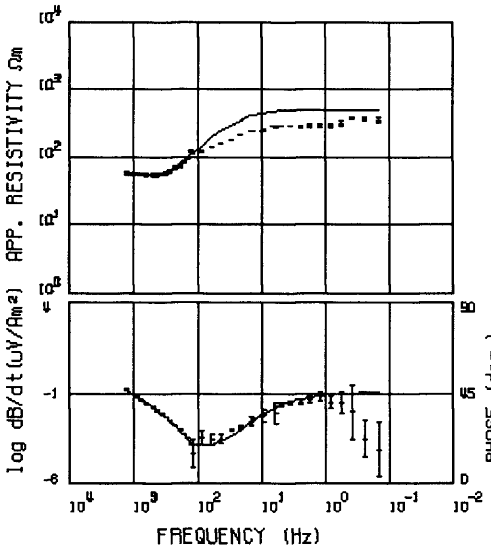
APP. RESISTIVITY Ωm
log dB/dt (uV/Am²)
PHASE (deg.)
FREQUENCY (Hz)

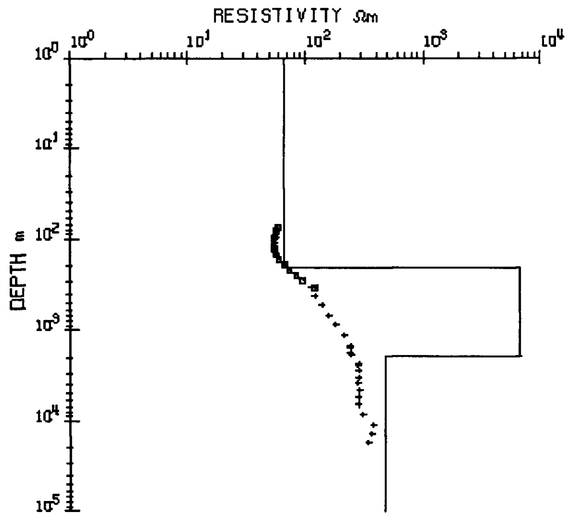
RESISTIVITY Ωm
DEPTH m

b)

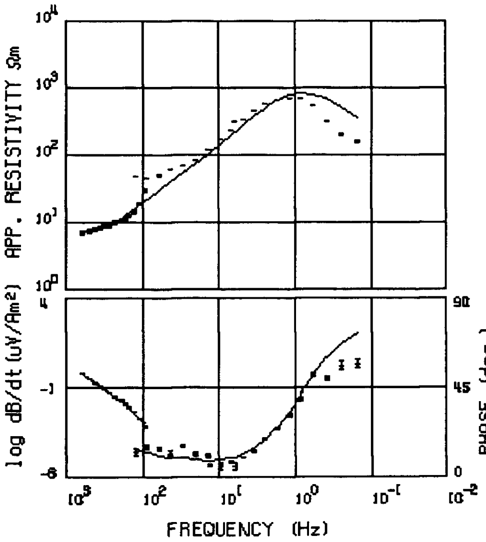
APP. RESISTIVITY Ωm
log dB/dt (uV/Am²)
PHASE (deg.)
FREQUENCY (Hz)

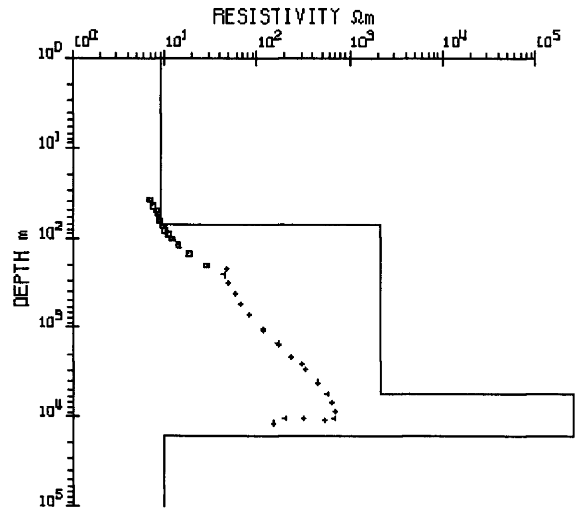
RESISTIVITY Ωm
DEPTH m

MH7

a)

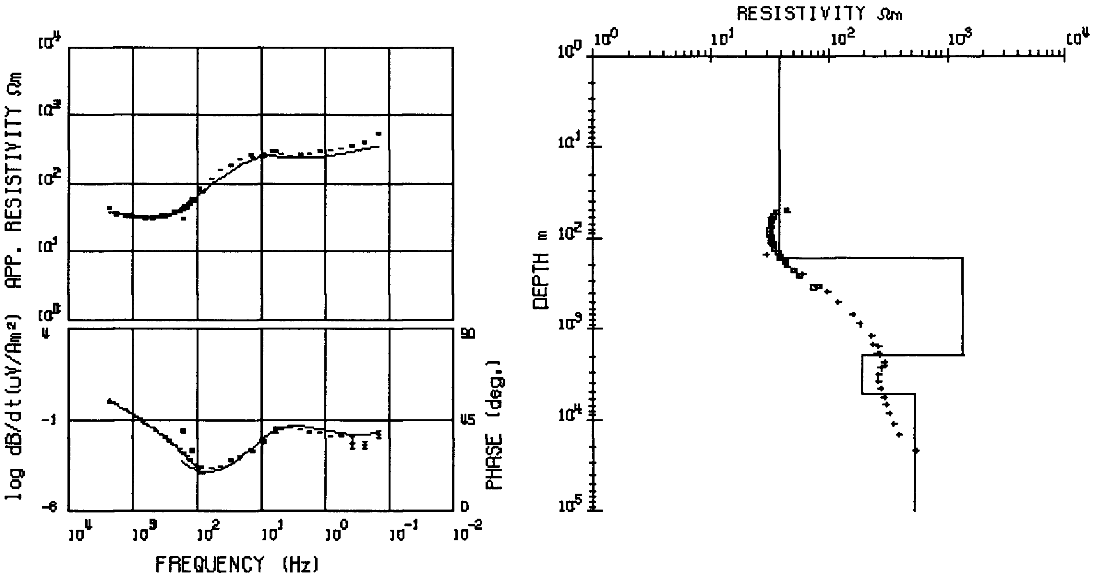
APP. RESISTIVITY Ωm
log dB/dt (uV/Am²)
PHASE (deg.)
FREQUENCY (Hz)
RESISTIVITY Ωm
DEPTH m

b)

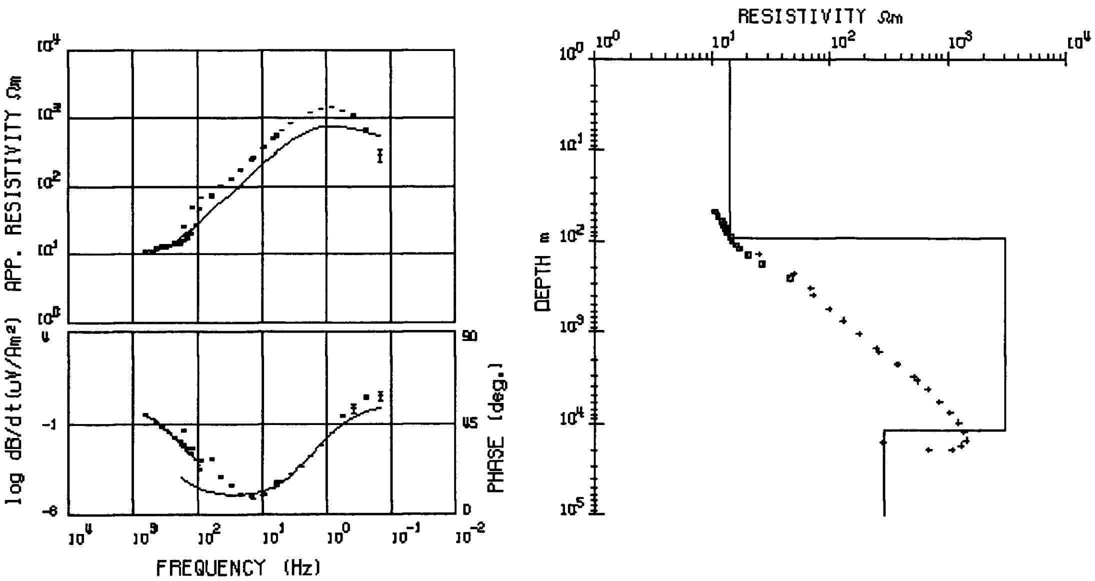
APP. RESISTIVITY Ωm
log dB/dt (uV/Am²)
PHASE (deg.)
FREQUENCY (Hz)
RESISTIVITY Ωm
DEPTH m

MH8

a)

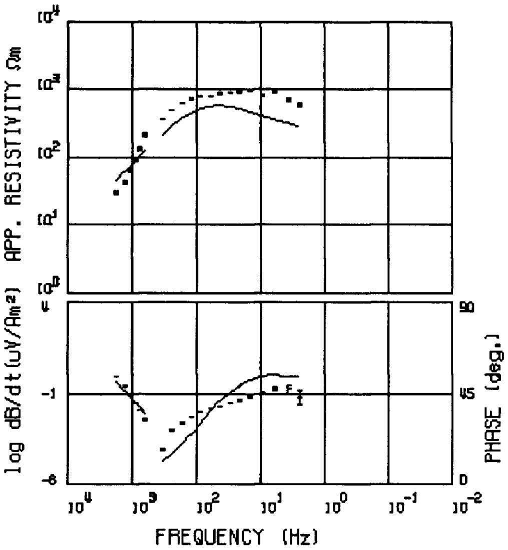
APP. RESISTIVITY Ωm
log dB/dt (uV/Am²)
PHASE (deg.)
FREQUENCY (Hz)

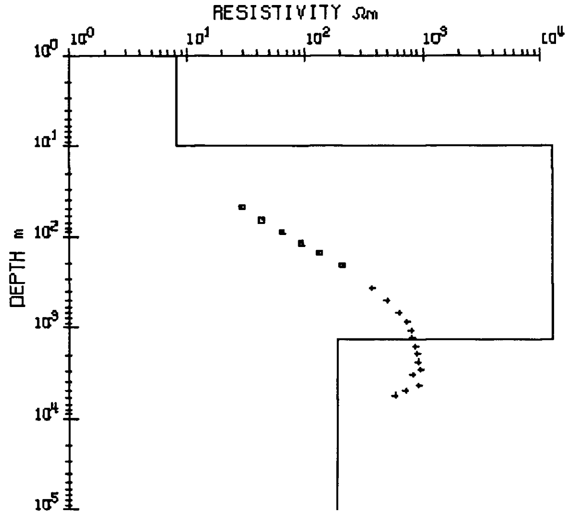
RESISTIVITY Ωm
DEPTH m

b)

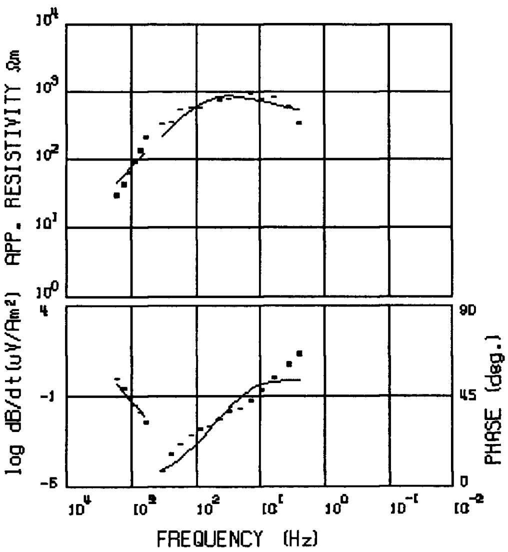
APP. RESISTIVITY Ωm
log dB/dt (uV/Am²)
PHASE (deg.)
FREQUENCY (Hz)

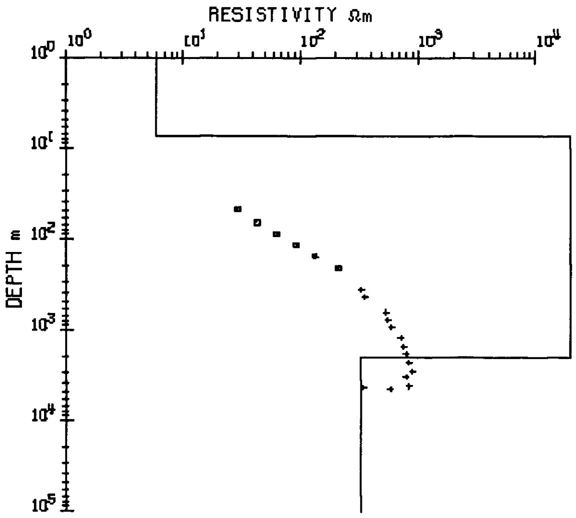
RESISTIVITY Ωm
DEPTH m

MH10

Appendix C

1-D inversion results of DC resistivity and TEM data for Quorn, Leicestershire, UK (Figure 7.2).

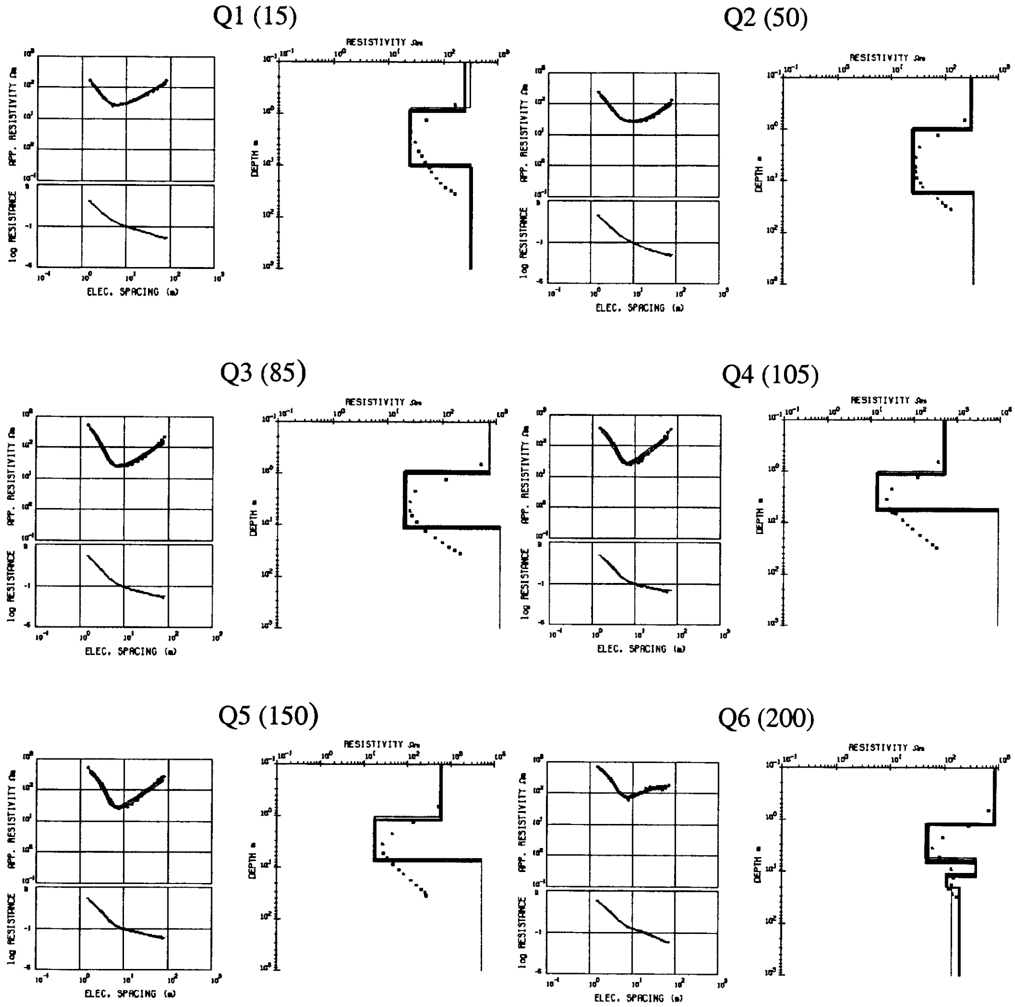

Figures C1: 1-D inversion results of VES resistivity data using most squares inversion scheme along profile 20W (N-S spreading axis).

Q1 (00)

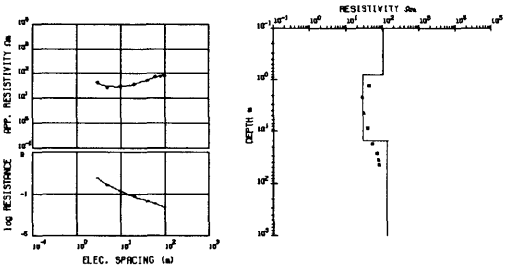

Q2 (20)

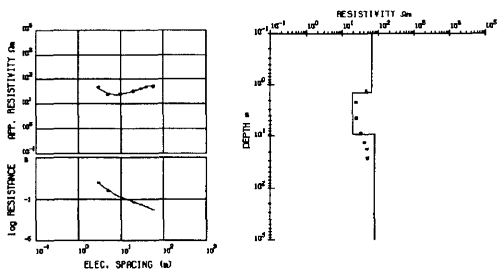

Q3 (40)

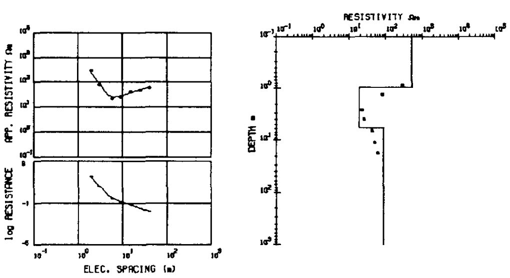

Q4 (80)

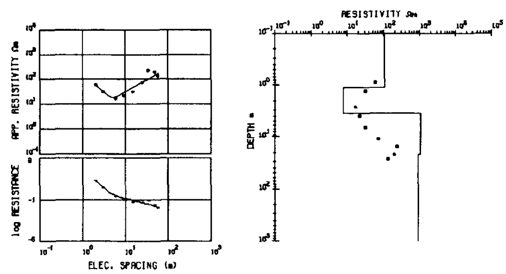

Q5 (120)

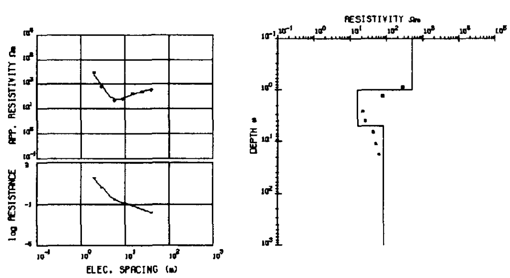

Q6 (160)

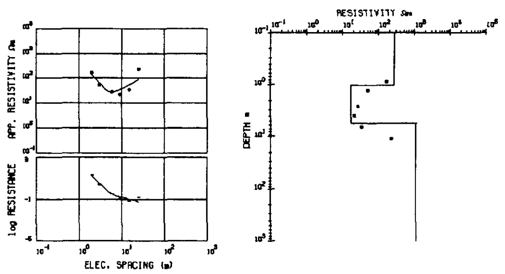

Q7 (220)

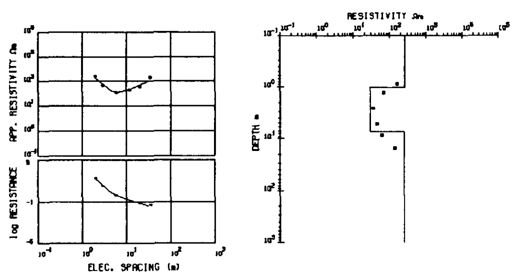

Q8 (265)

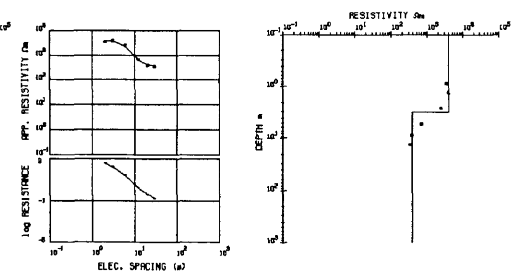

Figures C2: 1-D inversion results of VES resistivity soundings along profile 20W (E-W spreading axis).

Q1 (00)

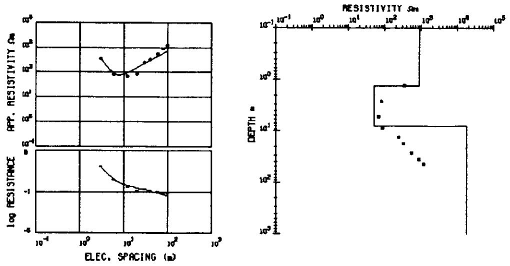

Q2 (20)

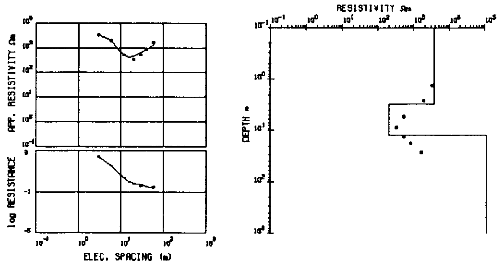

Q3 (40)

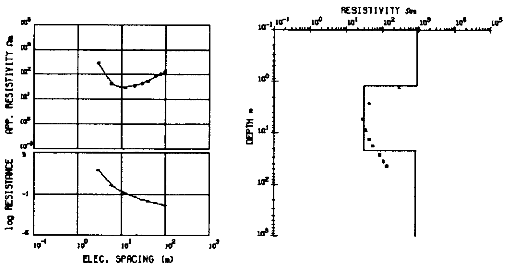

Q4 (80)

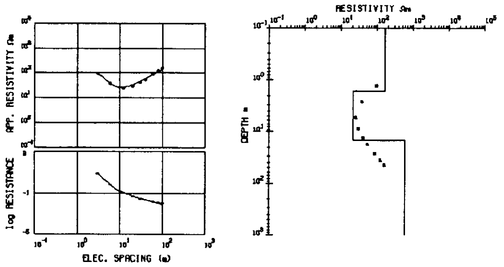

Q5 (125)

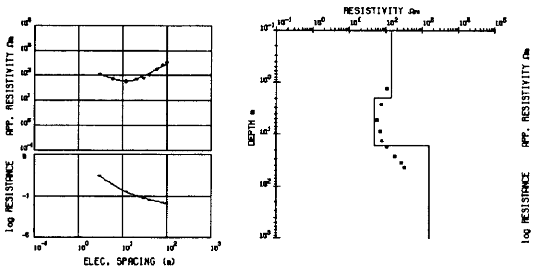

Q6 (165)

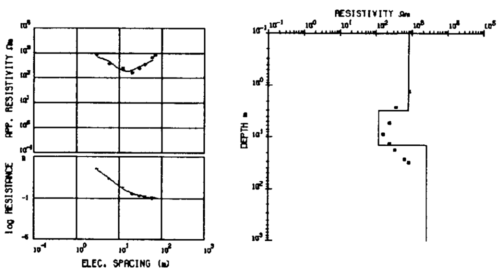

Figures C3: 1-D inversion results of VES resistivity soundings along profile 20E.

Q 1(00)

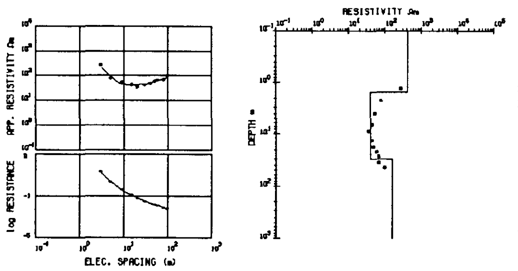

Q2 (20)

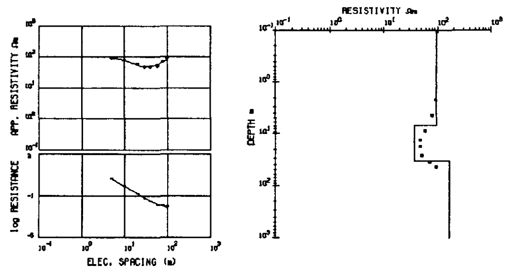

Q3 (40)

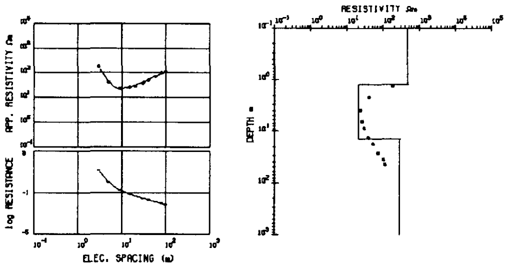

Q4 (60)

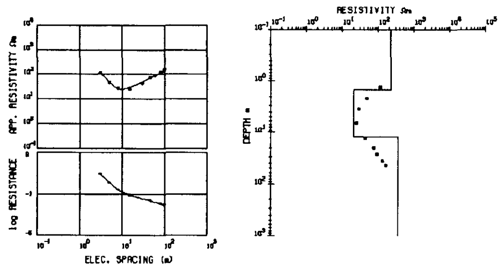

Q5 (80)

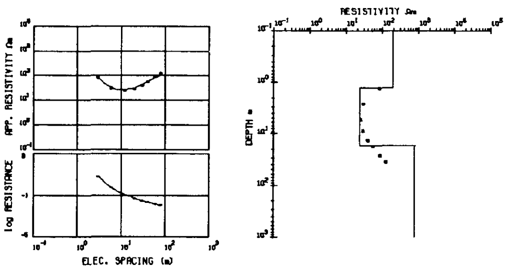

Q6 (100)

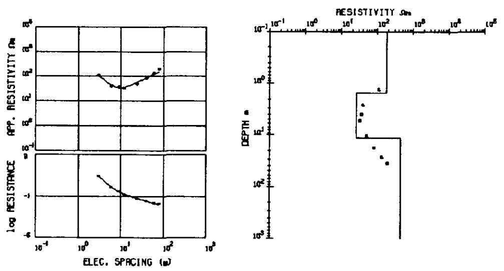

Q7 (120)

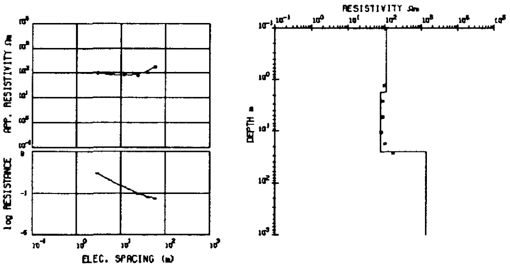

Q8 (160)

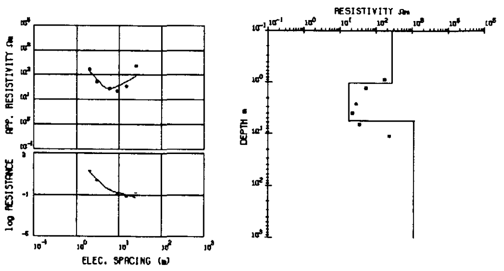

Q9 (220)

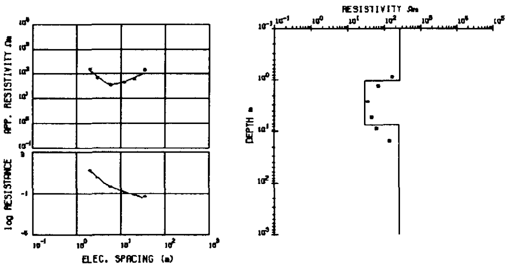

Q10 (265)

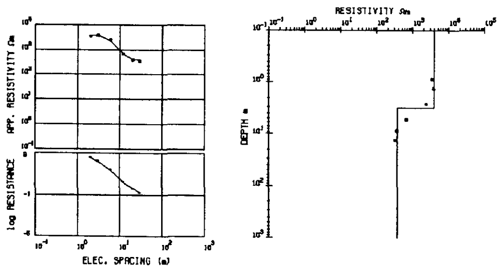

Figures C4: 1-D inversion results of VES resistivity soundings along profile 40E.

Q1 (00)

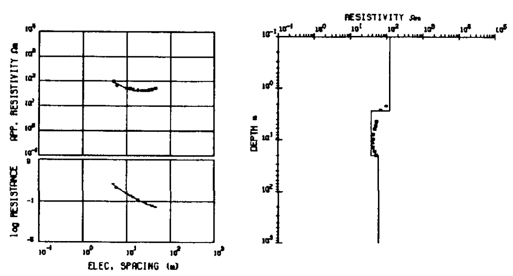

Q2 (20)

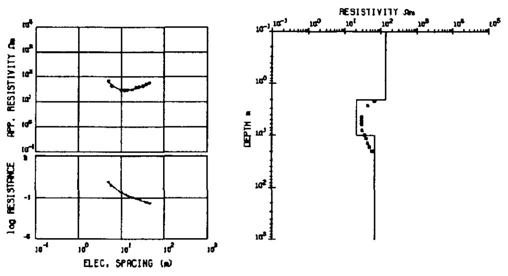

Q3 (40)

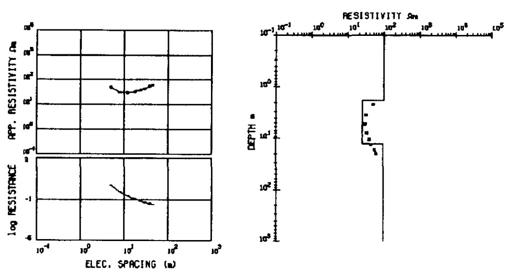

Q 4 (60)

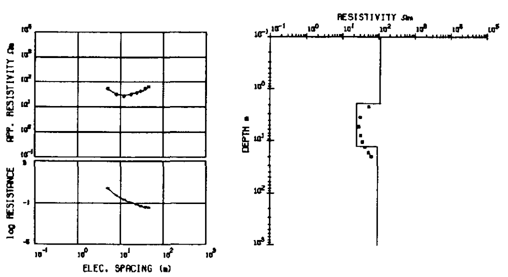

Q5 (80)

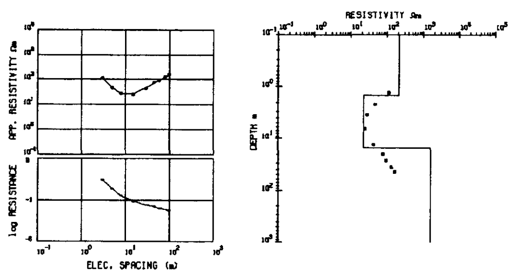

Q6 (100)

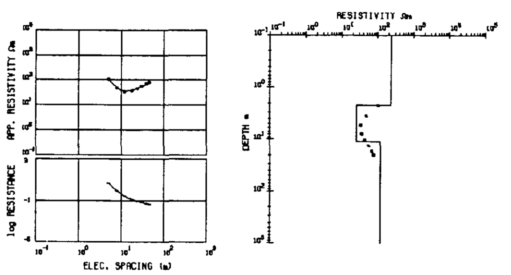

Figures C5: 1-D inversion results of VES resistivity soundings along profile 60E.

Q1 (00)

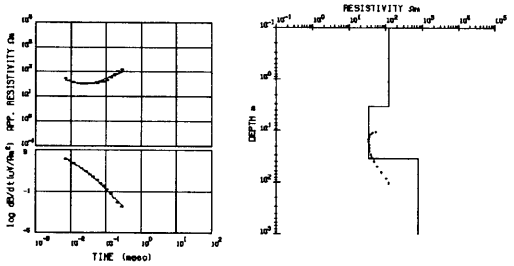

Q2 (20)

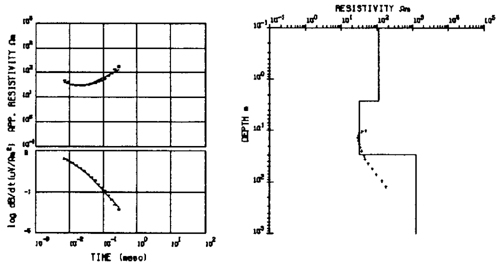

Q3 (40)

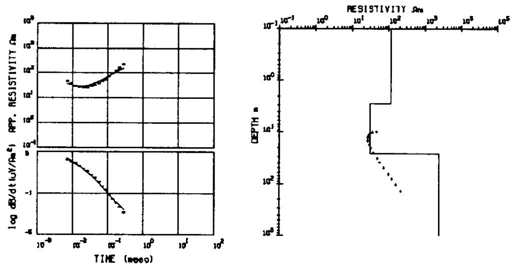

Q4 (60)

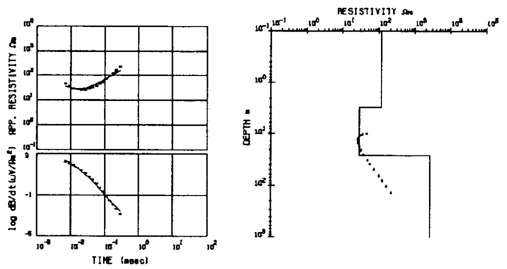

Q5 (80)

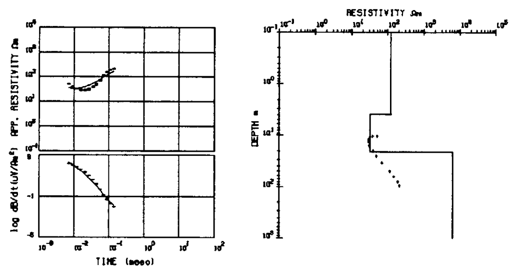

Q6 (100)

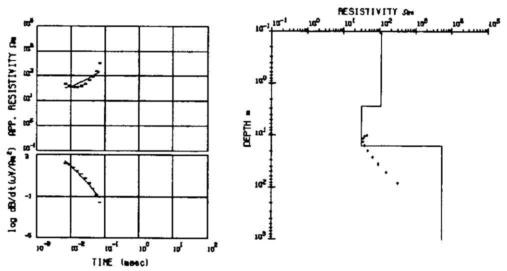

Q7 (120)

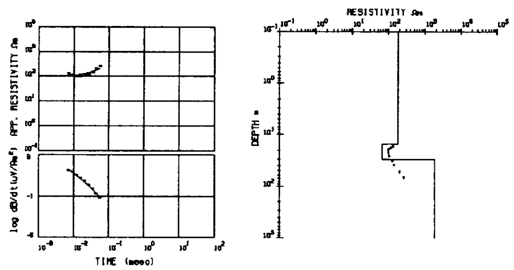

Q8 (140)

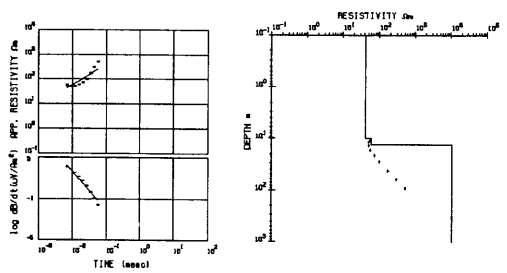

Q9 (160)

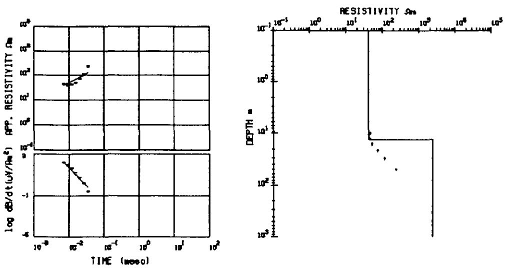

Q10 (180)

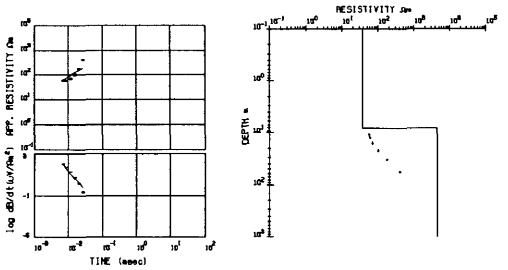

Q11 (200)

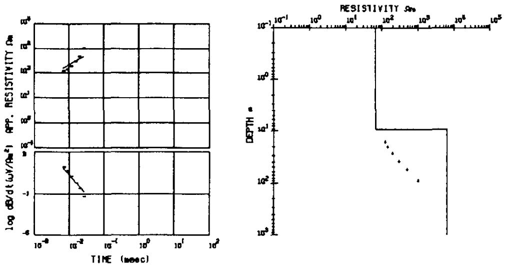

Figures C6: 1-D inversion results from central loop TEM data along profile 20W.

Appendix D

This appendix includes a paper accepted for publication in the journal of Geophysical Prospecting (in press). There is also expanded abstract presented in 7th International Congress of Brazilian Geophysical Society (SBGF), Salvador, which was held in October, 2001.

Geophysical Prospecting #2970 : FINAL revised version

Deep structure of the northeastern margin of Parnaiba basin, Brazil from magnetotelluric imaging

Adel K. Mohamed[1], Maxwell A. Meju[1] and Sergio L. Fontes[2]

[1]Department of Geology, University of Leicester, Leicester LE1 7RH, UK.

[2]Observatorio Nacional-MCT, Rio de Janeiro, Brazil.

Abstract

The magnetotelluric (MT) method has been applied to the determination of the deep resistivity structure of the northeastern margin of Parnaiba basin. Transient electromagnetic (TEM) and MT data were collected in early 1999 along a 95 km long N-S line extending from the coast across the projected subcrop position of a discontinuous fault found to the west of the study area that is believed to be a possible basin-bounding fault. The MT data were processed to yield the TE and TM mode responses and then corrected for static shift using central-loop and single-loop TEM data respectively. Regularised 2-D MT inversion was subsequently undertaken using a structured initial model with the near-surface constrained by TEM inversion results. As a consistency check, we performed another set of 2-D inversions using different smooth initial models. The various optimal 2-D inversion models clearly show the presence of a major basement trough, about 2 km deep, located about 75 km from the coast. We interpret it as possibly marking the main basin margin and suggest that it may have implications for groundwater resource development in the area.

Key words: Magnetotellurics, transient electromagnetics, resistivity inversion, groundwater, structure.

Introduction

The deep structure of the northeastern margin of Parnaiba basin in northeast Brazil (Fig. 1) is poorly understood and structural control on groundwater distribution in the semi-arid margins of the basin is a topical issue at the present time (e.g. Meju *et al.* 1999). The Parnaiba basin is mainly Palaeozoic in age and filled with clastic siliceous sediments of mostly continental origin deposited in five major depositional cycles from the Upper Ordovician to the Cretaceous. The lithological sequence deduced from borehole data in the southeastern and central parts of the basin is described in detail by Góes *et al.* (1993). Three of the megacycles of deposition are represented by the Serra Grande (Silurian), Caninde (Devonian) and Balsas (Permian-Carboniferous-Triassic) Groups. The total sedimentary thickness is about 3400 m near the centre of the basin, with the Serra Grande and Caninde Groups reaching up to 2900 m in thickness and consisting mainly of sandstones with subordinate siltstones and shales (see Meju *et al.* 1999, Fig. 2). The Mesozoic and Cenozoic sediments do not exceed about 600 m in thickness (De Sousa 1996). The Serra Grande and Caninde Groups are exposed only in the southern and eastern parts while the Balsas Group is exposed in the northern part of the oval-shaped basin. The structural and lithological architecture of the basin is highly favourable for the occurrence of several confined aquifers (Meju *et al.* 1999). However, in the semi-arid marginal parts of the basin, the major problem is how to identify areas with thickened aquiferous formations that may be developed for groundwater supply to nearby urban populations.

Recent combined transient electromagnetic (TEM) and magnetotelluric (MT) studies of the southern and eastern margins of the basin identified linear trough-like zones of enhanced conductivity, interpreted as major grabens, close to areas with significant human population (Fontes *et al.* 1997; Ulugergerli 1998; *Meju et al.* 1999). Subsequent follow-up drilling by a Brazilian government agency confirmed this interpretation (see e.g. Fontes *et al.* 1997) and encouraged the regional (Piaui) state government to commission further investigations for urban groundwater supply in the eastern margin of the basin using the TEM-MT method. However, the northern margin of the basin has so far not been investigated for any such occurrences of potentially aquiferous grabens.

The present study therefore focuses on examining the deep structure of the northeastern margin of the basin for possible features of tectonic or hydrogeophysical interest. It may be noted that the exact position of the basin edge is poorly defined on existing geological maps and the basement-sedimentary cover relation is not well known in this part of the basin. A discontinuous fault found in line with basement arches to the west of the present study area (see Fig. 1) may be a possible basin-bounding fault or the site of a potential graben structure. It may contain thick aquiferous materials as is typical of the southern margin of the basin where TEM-MT models have been successfully used to guide deep drilling (ca. 1km) for groundwater for urban supply schemes (Fontes *et al.* 1997).

Geophysical field survey

During March and April 1999, a regional joint TEM and MT survey was carried out across the northeastern segment of the Parnaiba basin. The N-S survey line extends from the Atlantic coast onto the hinterland for 95 km (Fig. 2) and there are 14 observational stations with an average spacing of 7 km. Accessibility is poor in the area of study and the survey line followed the main road across the region but with sites located at significant distances off the road. The horizontal co-ordinates for each station were determined using a portable GPS receiver. It was not possible to find a suitable sounding station in the populated area between our second and third stations, thus creating a gap in our profile as shown in Fig. 2. To facilitate dual-mode static shift correction of MT data (see Meju *et al.* 1999), central-loop and single-loop TEM data were acquired at these sites using 50 or 100 m-sided transmitter loops depending on site geometrical constraints. The Sirotem MK3b equipment was used for the TEM soundings and the recording bandwidth ranged from 14 microseconds to about 30 milliseconds. MT measurements employed the EMI MT-1 equipment. The MT data were measured in the magnetic east-west and north-south directions. The electric dipoles were 50 or 100 m long depending on site constraints. The magnetic field components were recorded using induction coils. The recording bandwidth was 0.01 to 176 Hz. The TEM and MT soundings were centred on the same positions.

MT data analysis and regional strike determination

The MT data have been processed using a robust estimation technique (Egbert and Booker 1986) and the relevant interpretative parameters were computed for the sounding frequency range 176 to 0.01 Hz. In terms of continuity of data points and size of data errors, the data are of good quality at all the stations. Structural dimensionality was investigated for each site using the Groom and Bailey (1989) decomposition (G-B) method and representative examples are given in Figs. 3a and 3b. In Fig. 3a are shown the results for a station located on sedimentary rocks (station 12). In this figure, notice that the data appear to suggest a relatively simple layered earth structure with no dominant G-B azimuth. The results for a site located on outcropping crystalline basement (station 8) are summarized in Fig. 3b. Notice that the data suggest simple subsurface conditions only at frequencies higher than 3 Hz; a complex structure is suggested at lower frequencies. It was noted that the twist and shear parameters from the G-B decomposition are near-zero at frequencies higher than 1 Hz but beyond this point, steadily increase in magnitude with decreasing frequencies. In general, we did not find any significant improvement in the sounding curves at high frequencies using the Groom-Bailey decomposition. At low frequencies (<0.3 Hz), the data show 3-D characteristics (see e.g. Fig. 3b) and may not warrant G-B decomposition (see Bahr 1991).

The regional strike determined using the Groom-Bailey method is shown for selected frequencies in Fig. 4. Notice that the dominant geoelectrical strike is fairly consistent with the main WNW-ESE lithological trend in the field area. The MT data were therefore rotated -30^0 from the measurement direction (i.e. -53^0 from the geographic north since the declination is 23^{0}W) yielding the TE and TM mode data required for 2-D modelling. We note, however, that the MT data show gross 3-D characteristics at frequencies lower than 0.3 Hz and 2-D interpretation or imaging (as appropriate in this case) may be regarded only as a convenient approximation in our quest for the deep subsurface structure in the area of study.

The assumed TE and TM apparent resistivity data set showed evidence of static shift (Berdichevsky and Dmitriev 1976; Jones 1988; Sternberg *et al.* 1988) when compared with the TEM data. Following Meju *et al.* (1999, Fig. 6), the TM mode MT curves were corrected using the single-loop TEM data while the TE mode apparent resistivity curves were corrected using central-loop data for all the stations. Representative examples of the MT and TEM data are shown in Fig. 5. Note that the TEM apparent resistivities were determined using an iterative non-linear scheme after adjustment for transmitter turn-off effects (Raiche 1984).

The ratios of vertical to horizontal magnetic fields or the so-called induction arrows (Parkinson 1959) may be used to infer the presence of linear zones of anomalous current concentrations in the subsurface in our study area. The recorded vertical component magnetic field data are of good quality. The real parts of the induction arrows at two frequencies (8 and 0.025 Hz) selected to sample different depths are superimposed on the known geological features in the area for comparison in Fig. 6. Note the difference in magnitude and azimuth of the induction arrows for both frequencies suggestive of lateral and vertical variations in resistivity structure. However, some other interesting deductions can be made from this figure and other computed data. At low frequencies the so-called coast effect appears to influence the measurements at the first four stations from the coastline. Interestingly, at the high frequencies (>1 Hz) that are important for hydrogeophysical investigations in this area, only the induction arrows for the two northernmost sites point toward the coast. At high frequencies, the induction arrows at stations 9, 11, 12, 13 and 14 point towards the northeast (see Fig. 6) suggesting the presence of a linear NW-SE trending conductive zone at this locality; this may be indicative of the presence of a concealed fault-zone or may be the effect of the linear outcrop of the marine Pimenteiras formation which is known to be conductive (see Meju *et al.* 1999, Fig. 2). This response pattern does not persist at low frequencies and this may suggest that the causative body does not extend to great depths or that the structure sensed laterally at low frequencies now contribute to the vertical field response. Elsewhere, the induction arrows are of very small magnitudes and do not show any preferred orientation.

Two-dimensional MT imaging and interpretation

For 2-D imaging, we have projected our rotated MT data onto a profile perpendicular to the adopted strike (i.e., trending N37°E) so that the distances between the stations are different from those shown on the actual site location map (Fig. 2). Only the apparent resistivity and phase data will be considered here as in conventional practice. (We note that the vertical magnetic field information may furnish additional constraint in detailed 2D interpretation but is not necessary in our adopted data imaging approach). A conjugate gradient non-linear inversion program (Mackie 1996; Mackie *et al.* 1988,1997) has been adopted for the 2-D imaging of our MT data. Simultaneous inversion of TE and TM mode data was done using several initial models with the design of the 2-D calculation mesh optimized for the top 30 km of the subsurface. On the ocean-side, the 2-D grid made use of the available bathymetric data and incorporated a surface conductive slab of 2.5 Ω m representing the seawater layer (cf. Arora *et al.* 1999). Initial trial inversions were done to determine the best regularization parameters (in terms of model smoothness and data fit) for this particular data set; once found, it was held fixed ($\tau = 5$) in the subsequent inversion studies reported below. As a simple way of addressing the problem of non-uniqueness, two sets of initial models were adopted in the inversion studies, viz: (1) structured initial models derived from joint 1-D inversion (Meju 1996) of central-loop TEM and TE mode MT data, and (2) featureless (half-space) models. Only those features common to the optimal reconstructed models are deemed worthy of geological interpretation. The target rms misfit was set to 0.5 in all cases and over 50 iterations were generally required.

Sample result of 2-D inversion with a structured initial model is presented in Fig. 7 (only the top 5 km is shown for convenience). The fit between the calculated model responses and the observed data is shown in Fig. 8 and is satisfactory especially at high frequencies of interest in our hydrogeological work. At low frequencies, the fit is not good at some sites (see e.g., the TE mode at station 8) and may be attributed to the 3-D regional structure at depth (cf. Table 1). It would appear that the unweathered crystalline basement in the area of study is generally highly resistive with a minimum value of 200 Ω m and may be traced to the north and south from that part of our model coinciding with the zone of basement outcrop on the geological map (stations 7 and 8). Relatively conductive sedimentary cover rocks appear to increase in thickness away from the zone of basement outcrop as expected from geology; note that stations 1 to 6 are believed to lie in what is conveniently dubbed the Barreirinhas basin by Goes *et al.* (1993). The cover units extending from stations 1 to 6 probably correspond to Quaternary and Tertiary sediments with the uppermost section being very conductive (≤ 10 Ω m) underneath stations 1 to 3 (a feature constrained by TEM data). Southward from station 8, the basement cover units show anomalous thickening starting from station 12 and attaining a maximum thickness of about 2 km underneath station 13. These cover units exhibit some stratification consisting of an uppermost resistive (>150 Ω m) sliver starting near station 12 (and correlating with the zone of outcropping Cabecas sandstone on the geology map), an underlying conductive (<20 Ω m) unit (correlated with the Pimenteiras shale which is draped over by Quaternary sediments at station 11), and a basal unit of moderate resistivity (ca. 20-50 Ω m) that may represent thickened segments of the Serra Grande formations which outcrop at stations 9 and 10 or a combination of the Serra Grande group and pre-Silurian sediments as suggested for deep grabens found elsewhere in the basin (see De Sousa 1996; Ulugergerli 1998; Arora *et al.* 1999; Meju *et al.* 1999).

In the case of inversion with smooth initial models, the responses of the resulting model matched the field data satisfactorily only for half-spaces of resistivity >50 Ω m. The optimal models constructed from initial models of 250, 500, 750 and 1000 Ω m resistivities are very similar as can be seen in Fig. 9. The fit to the data in each case is comparable to that shown in Fig. 8. The main features of these models are very similar to those of the TEM-constrained model (cf. Fig. 7), and the various 2-D models may thus be accepted as plausible images of the subsurface geology. Note the relatively conductive trough-like feature in the top 4 km of the subsurface at stations 12 to 14, and the highly resistive arch-like feature underneath stations 6 to 8. The highly resistive body beneath stations 6 to 8 coincide geographically with the zone of basement outcrop on the geological map (cf. Fig. 2) and the trough-like feature may possibly be related to the basin-bounding fault seen to the west of the survey line on the regional tectonic map (see Fig. 1). If this correlation is correct, then there is a good agreement between these models and geology.

Tectonic and possible hydrogeological implications

From geological considerations, our survey line would be expected to cross a concealed major fault or basement arch. The resistive arch-like feature found between stations 5 to 8 and the conductive feature at depth near stations 12 and 13 are thus interesting candidate for tectonic consideration. We suggest that they may be part of a block-faulted structure marking the main edge of the basin. Based on the studies conducted further south by Góes *et al.* (1993) using data gathered from surface geology, geochemical surveys, exploratory wells and seismic sections, the projected sedimentary cover thickness would be about 1 km just beyond our station 14. The presence of thickened (ca. 2 km) conductive geoelectric units near stations 12 and 13 in our MT models (inferred to be sedimentary cover rocks) is therefore anomalous; it is best explained by the existence of a hitherto undiscovered graben-like structure. The Serra Grande group contains the most important aquifer in Parnaiba basin and this anomalously thickened zone may thus have hydrogeological implications. Note however, that in the available lithostratigraphic sections of the central and southeastern parts of the Parnaiba basin (see De Sousa 1996; Arora *et al.* 1999; Meju *et al.* 1999), crystalline basement rocks are inferred to be directly overlain by the Riachao and Mirador formations of Cambrian-Ordivician age in some areas. These units contain carbonatic facies which have high geothermal conductivity (De Sousa 1996); it is logical to expect that these will be associated with relatively high electrical conductivity. Based on the current 2-D resistivity models, we suggest as a speculative possibility that Cambro-Ordovician sediments could be present in the deep trough-like structure in our study area and may therefore not be restricted to the central and southeastern parts of the basin.

Conclusion

The structure of the Parnaiba basin can be discerned from conductivity imaging of electromagnetic data. This study has shown the capability of electromagnetic methods for mapping the architecture of the sedimentary cover units and the underlying crystalline basement. Importantly, it has revealed the possible presence of a major faulted structure, about 70 km from the coast, which may represent the main northeastern margin of the basin. Although the MT data indicate gross 3-D characteristics at low frequencies, we have only produced a 2-D MT interpretation aimed at giving a generalized picture of the deep structure of the basin margin. We recommend that the graben-like feature detected on this profile should be investigated by drilling since it may contain aquiferous materials as found elsewhere in the basin.

Acknowledgements

One of the authors (AKM) is grateful to the Egyptian government for a postgraduate scholarship award. The authors are grateful to Emin Ulugergerli, C. Germano and E.F. La Terra for technical support especially during the fieldwork campaign in northeast Brazil. We are grateful to the anonymous referees for their constructive comments which helped improve the clarity of the paper.

References

Arora B.R., Padilha A.L., Vitorello I., Trivedi N.B., Fontes S.L., Rigoti A. and Chamalaun F.H. 1999. 2-D geoelectrical model for the Parnaiba Basin conductivity anomaly of northeast Brazil and its tectonic implications,*Tectonophysics*, **302**,57-69.

Bahr K. 1991. Geological noise in magnetotelluric data: a classification of distortion types. *Physics of the Earth and Planetary Interior* **66**, 24-38.

Berdichevsky M.N. and Dmitriev V.I. 1976. Distortion of magnetic and electrical fields by near-surface inhomogeneities. *Acta Geodaet. Geophys. et Montanist. Hung.* **11**, 447-483.

DeSousa M.A 1996. *Regional gravity modelling and geohistory of the Parnaiba Basin (NE Brazil).* Ph.D thesis, University of Newcastle.

Egbert G.D. and Booker J.R. 1986. Robust estimation of geomagnetic transfer functions. *Geophysical Journal of the Royal Astronomical Society* **87**, 173-194.

Fontes S.L., Meju M.A., Lima J.P.R., Carvalho R.M., La-Terra E.F., Germano C.R. and Metelo M. 1997. Geophysical investigation of major structural controls on groundwater distribution, north of Sao Raimundo Nonato, Piaui. *5th Internat. Congr. Brazilian Geophys. Soc.*, Sao Paulo, Expanded Abstract, Vol.2, 766-769.

Góes A.M.O., Travassos W.A.S. and Nunes K.C. 1993. Projeto Parnaiba: Reavaliacão da bacia e perspectivas exploratórias. Internal report, Petrobras/ DEXNOR-DINTER, 97pp.

Groom R.W. and Bailey R.C. 1989. Decomposition of magnetotelluric impedance tensors in the presence of local three-dimensional galvanic distortion. *Journal of Geophysical Research* **94**, 1913-1925.

Jones A.G. 1988. Static shift of magnetotelluric data and its removal in a sedimentary basin environment. *Geophysics* **53**, 967-978.
Mackie R.L. 1996. Two dimensional inversion of magnetotelluric data: Software. Internet site: MTNET "http://nazca.cg.emr.ca/mtnet/mtnet.html".

Mackie R.L, Rieven S. and Rodi W. 1997. Users manual and software documentation for two-dimensional inversion of magnetotelluric data. Earth Resources Lab. Report, Massachusetts Institute of Technology.

Mackie R.L., Bennett B.R. and Madden T.R. 1988. Long period magnetotelluric measurements near the central California coast: a land-locked view of the conductivity structure under the Pacific Ocean. *Geophysical Journal of the Royal Astronomical Society* **95**, 181-194.

Meju M.A. 1996. Joint inversion of TEM and distorted MT soundings: Some effective practical considerations. *Geophysics* **61**, 56-65.

Meju M.A., Fontes S.L., Oliveira M.F.B., Lima J.P.R., Ulugergerli E.U. and Carrasquilla, A.A. 1999. Regional aquifer mapping using combined VES-TEM-AMT/EMAP methods in the semi-arid eastern margin of Parnaiba Basin, Brazil. *Geophysics* **64**, 337-356.

Parkinson W.D. 1959. Directions of rapid geomagnetic fluctuations. *Geophysical Journal of the oyal Astronomical Society* **2**,1-14.

Raiche A.P. 1984. The effect of ramp function turnoff on the TEM response of a layered earth. *Bulletin of the Australian Society of Exploration Geophysicists* **15**, 37-42.

Sternberg B.K., Washburne J.C. and Pellerin, L. 1988. Correction for the static shift in the magnetotellurics using transient electromagnetic soundings. *Geophysics* **53**, 1459-1468.

Ulugergerli E.U. 1998. *Development and application of 2-D magnetotelluric inversion in complex domain.* PhD thesis, University of Leicester.

Ulugergerli E.U. 1998. *Development and application of 2-D magnetotelluric inversion in complex domain.* PhD thesis, University of Leicester.

Figure captions

FIG. 1 (5.1). Simplified structural framework of the basement of Parnaiba basin deduced from qualitative aeromagnetic interpretation (Góes et al., 1993). The location of the present TEM-MT area of study is also shown.

FIG. 2 (5.3). Geological map of the area of study showing the locations of the TEM-MT stations.

FIG. 3. Sample results of Groom-Bailey (G-B) decomposition of MT impedance tensor. Shown are the usual G-B decomposition data for: (a) station 12 located on sediments, and (b) station 8 located on outcropping crystalline basement.

FIG. 4 (5.13). Pictorial representation of the regional geoelectrical strike obtained using the G-B method for selected frequencies. The azimuths are shown by the site-centred dark bars and are superimposed on the geological map of the area for comparison. Note that the strike angles are shown with respect to geographic north and are thus different from the actual G-B values by a constant angle equal to the declination (23^0W).

FIG. 5 (5.15). Sample illustration of dual-mode MT static shift correction using TEM data. The TE and TM mode apparent resistivity curves were respectively corrected using central- and single-loop TEM data. Shown are the TEM (round symbols), raw MT (triangular ornaments) and corrected MT (crosses) data for each site.

FIG. 6 (5.10). Real component Parkinson induction arrows for two frequencies superimposed on the geological map for comparison.

FIG. 7 (6.10). A geoelectric structure derived from 2-D inversion with a structured initial model. Only the top 5 km is shown to stress the shallow features evinced by the inversion.

FIG. 8 (6.11). The fit between the MT observed data and the 2-D model response. The apparent resistivity and phase information are presented for the TE and TM modes at each station starting from the north to the south on the profile.

FIG. 9 (6.8). 2-D inversion models generated using different initial half space models. The initial models were assigned resistivities of (a) 250 Ω m, (b) 500 Ω m, (c) 750 Ω m, and (d) 1000 Ω m.

Table 1 (5.3).

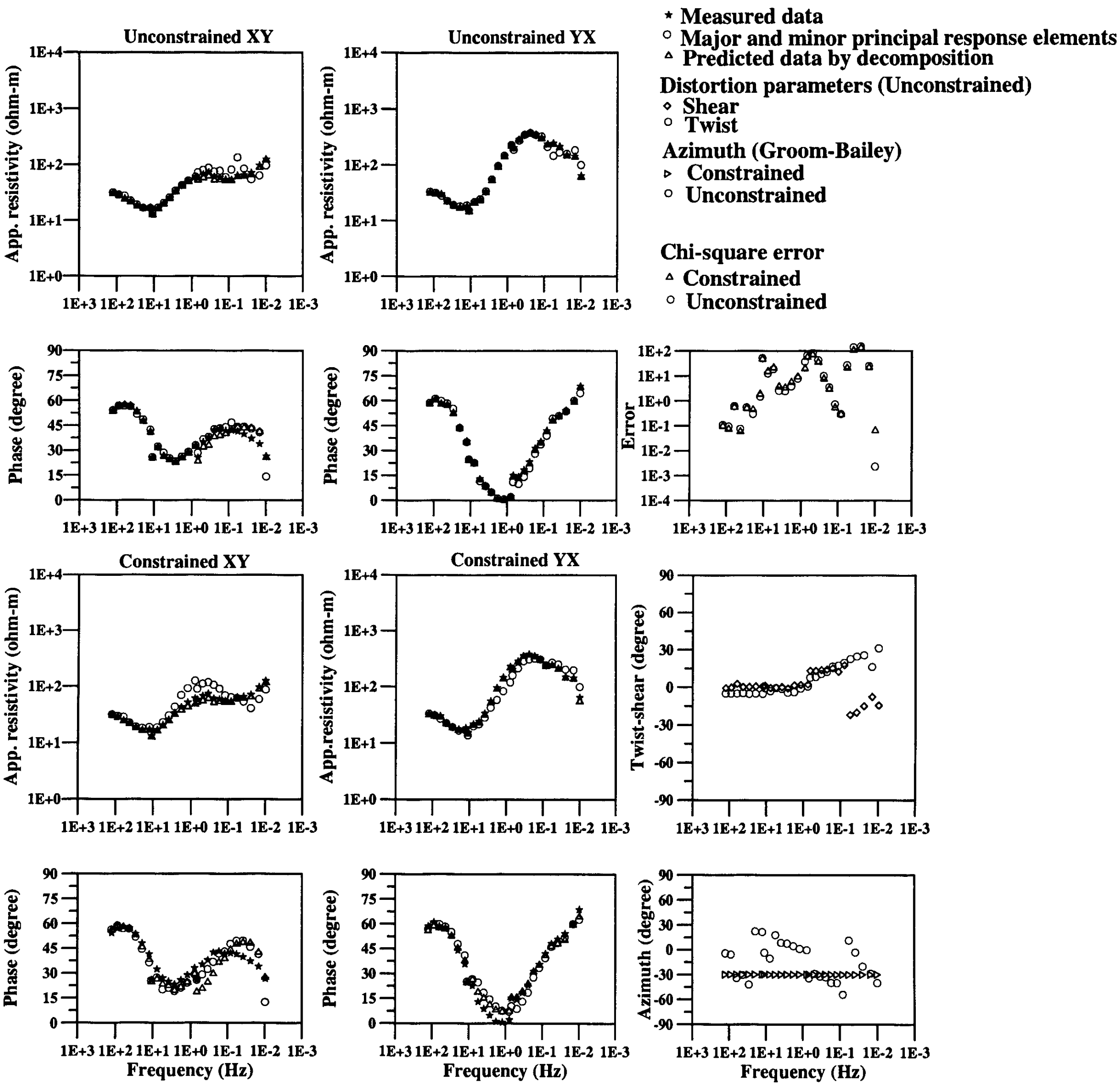

Unconstrained XY
Unconstrained YX
Constrained XY
Constrained YX
App. resistivity (ohm-m)
Phase (degree)
Error
Twist-shear (degree)
Azimuth (degree)
Frequency (Hz)
1E+3 1E+2 1E+1 1E+0 1E-1 1E-2 1E-3
* Measured data
○ Major and minor principal response elements
△ Predicted data by decomposition
Distortion parameters (Unconstrained)
◇ Shear
○ Twist
Azimuth (Groom-Bailey)
▷ Constrained
○ Unconstrained
Chi-square error
△ Constrained
○ Unconstrained

Fig. 3a

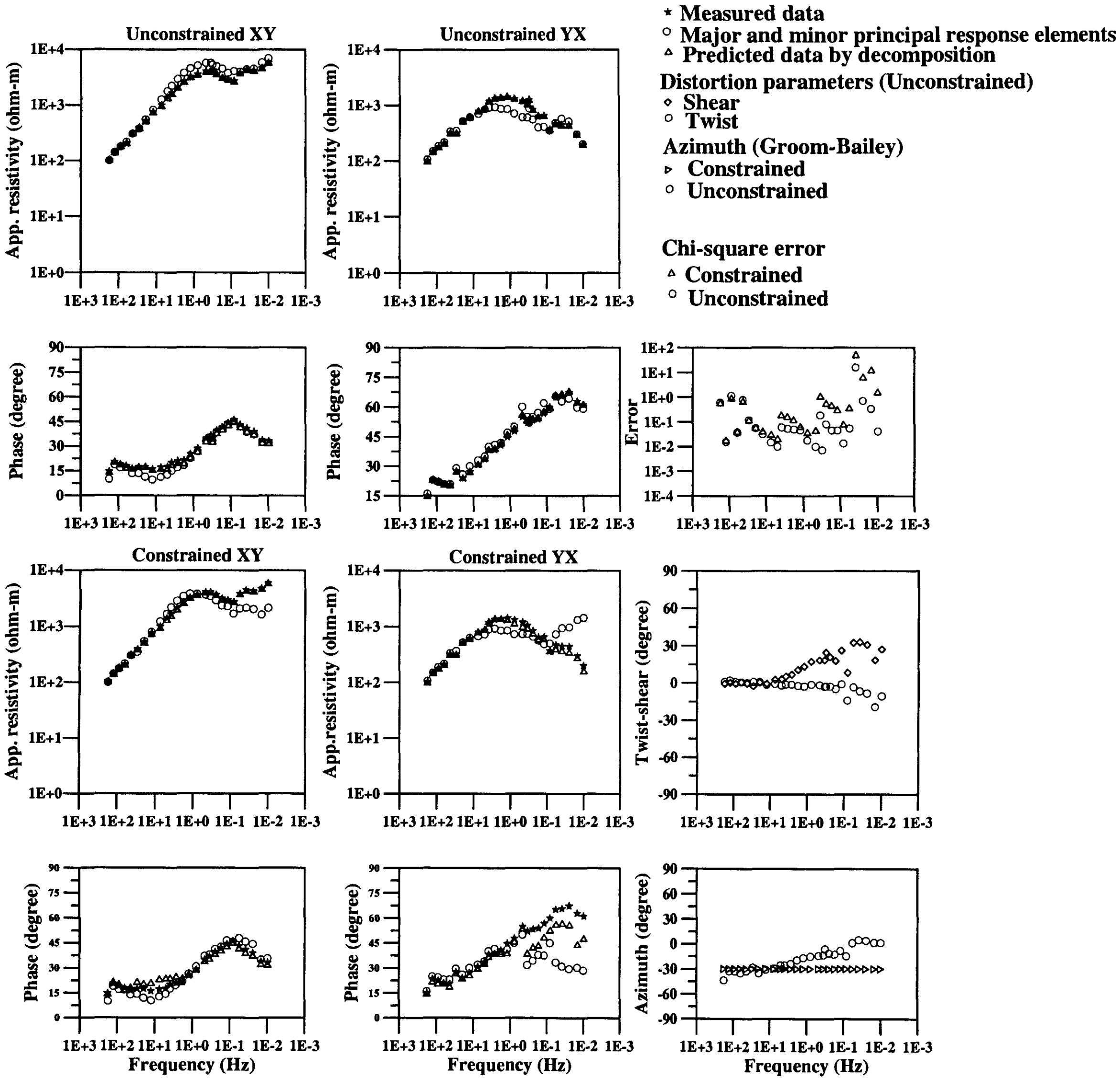
Measured data
Major and minor principal response elements
Predicted data by decomposition
Distortion parameters (Unconstrained)
Shear
Twist
Azimuth (Groom-Bailey)
Constrained
Unconstrained
Chi-square error
Constrained
Unconstrained
Unconstrained XY
Unconstrained YX
Constrained XY
Constrained YX
App. resistivity (ohm-m)
Phase (degree)
Error
Twist-shear (degree)
Azimuth (degree)
Frequency (Hz)

Fig. 3b

Deep electromagnetic mapping of the Serra Grande aquifer for optimum groundwater development on the eastern margin of Parnaiba basin, Piaui state, Brazil.

A. K. Mohamed[+], P. M. Abreu[++], M. A. Meju[+], S. L. Fontes[++], E. F. La Terra[++] and C. R. Germano[++]
[+]Department of Geology, University of Leicester, Leicester LE1 7RH, UK.
[++]Observatorio Nacional-MCT, Rio de Janeiro, Brazil.

Abstract

A combined TEM-AMT survey was recently carried out along three east-west transects at the eastern margin of Parnaíba basin for hydrogeological purposes. The MT data have been processed using conventional tensorial analysis technique and corrected for static shift using dual-mode TEM data. Two-dimensional regularised inversion of the TE and TM MT data revealed distinct geoelectric patterns for the three profiles. The contact between the sedimentary and crystalline basement rocks was clearly imaged in all the profiles. Graben-like structures are present in all cases and are best developed about 20-30 km away from the basin margin in the Monsenhor Hipólito and Itainópolis transects. The graben structures are considered to be the best places for drilling for groundwater in this region. The 2-D resistivity model for the Monsenhor Hipólito profile also appears to define the position of a major fault herein interpreted as the Picos fault, which may have implications for groundwater development in the area.

Introduction

Previous regional TEM-MT studies in southern parts of Piaui state, within the Parnaiba basin, detected zones of anomalously thickened conductive materials interpreted as possible grabens east of Picos (see Fig. 18, Meju et al., 1999) and north of Sao Raimundo Nonato (see Fontes et al., 1997). One of these anomalous graben structures was recently drilled down to 970m and found to contain a prolific aquifer; it now serves as a major water source for São Raimundo Nonato, 35 km away. Based on these studies, the Piauí state government embarked in 2000 on a programme to map out potential future sources of groundwater for the urban populations near the eastern margin of Parnaiba basin. The area is semi-arid and the rainfall rate is low (<400mm per year). In the case of Monsenhor Hipolito (MH) and environs, it was decided that deep EM tracking of the previously suggested graben near Picos should be undertaken to confirm its existence and along-strike continuity to aid groundwater resource evaluation.

The geology is made up of sequences of sedimentary rocks resting on crystalline basement. The sedimentary rocks outcropping in the study area are shown in Figure 1. The Serra Grande group rests on the Precambrian crystalline basement. This group consists successively of the Jaicos, Ipu and Tiangua formations. The Jaicos formation is the dominant member and the target aquifer in the area. The Serra Grande group is overlain by the Pimenteiras formation, which is the main aquitard. It is overlain in turn by the Cabecas formation outside the area of study.

Data acquisition, processing and interpretation

Joint TEM and AMT soundings were carried out in 2000 in the eastern part of Piaui State The survey consisted of three east-west lines, as shown in Figure 1. Monsenhor Hipólito profile (line 1) is 64 km long with ten stations and average spacing of 6.4 km. Jaicós profile (line 2) is 23 Km long, consisting of nine stations and with an average spacing of 2.5 Km. Itainópolis profile (line 3) is 40 Km long with ten stations spaced about 4 Km apart. Central-loop and single-loop TEM data were acquired at all sites using either 50 or 100 m-sided transmitter loops. The Sirotem MK3b system was used for the TEM soundings. The MT measurements employed the EMI MT-1 field equipment with 100m telluric dipoles.

The MT data have been processed using a robust estimation technique (Egbert and Booker, 1986) and the relevant interpretative parameters were computed for the sounding frequency range 336 to 0.14 Hz. Distortion decomposition and structural dimensionality were determined for the various sites using the Groom & Bailey (1989) technique. The computed azimuths at some selected frequencies suggest that there is a dominant strike for each of these profiles. For the MH profile, it is nearly north-south and is consistent with the main geological trend. Subsequently, the MH data were rotated 30^0 from the measurement direction (the declination is 23^0 west of geographic north) yielding the TE and TM modes along approximately north-south and east-west directions, respectively. The other two profiles were rotated 70° and are in accord with the trend of major faults. The TM and TE mode apparent resistivity curves were respectively corrected for static shift using the single-loop and central-loop TEM data (cf. Meju et al., 1999, Fig. 6).

A conjugate gradient 2-D non-linear inversion program (Mackie et al., 1997) has been applied to the corrected MT (TM and TE) data. The 2D inversion results are described below.

Monsenhor Hipólito Profile

The 2-D model (Figure 2, see Figure 6.12) suggests the presence of strong lateral changes in resistivity in the top 4.5 Km of the subsurface. The basement rock units are generally highly resistive and a value of $\rho \geq 200$ ohm-m appears to be appropriate for them. These units outcrop on the surface east of position 55Km. The relatively conductive zone near the surface at positions 55-59km may thus indicate the presence of highly weathered basement rocks. The basement appears to be of irregular topography and is overlain by thickened sedimentary cover at positions 0-7Km and 14-27Km. The contact between the basement and its sedimentary cover may be traced westward along the profile starting at position 53Km (in agreement with the basement-sediment contact on the geological map shown in Fig.1). The Serra Grande group aquifer (dominantly the Jaicos formation in this study area) outcrops at positions 14-48Km and is well imaged by the resistivity inversion model. This part of the transect is the recharge area. The Pimenteiras formation forms the aquitard west of this recharge zone. There appears to be a shallow resistive sill-like intrusive body at positions 0-7Km in agreement with previous MT models of the area (see Meju et al., 1999).

The 2-D model also shows other interesting geological features. A major fault is suggested near position 5Km and extends vertically into the basement. The fault appears as a highly conductive zone and may represent the margin of a major graben structure. This is in accord with the results from previous studies in the area. The smaller graben suggested at positions 15-25Km agrees with that seen on the Jaicos-Picos line (Ulugergeli, 1998). This particular graben appears to contain thick sedimentary materials, possibly of the Serra Grande Group. We recommend that the possible graben at positions 15-25Km has the optimum potential for drilling for groundwater; the deeper graben-like zone at positions 0-5Km may contain highly saline groundwater.

Jaicós Profile

This short transect would correspond to a segment of MH line (positions 37-60 km). The 2D model (Figure 3) suggests a minor graben at position 6-14Km (positions 8-10Km being the deepest part).

Itainópolis Profile

The 2-D model (Figure 4) show appreciable lateral resistivity changes and a graben structure near the centre of the profile (position 12-19Km), which is certainly the most appropriate area for drilling for groundwater.

Conclusion

Based on the present results, it would appear that the MT method is an effective technique for deep structural and stratigraphic mapping in this region. It has been shown that possible grabens and the contact between the basement and its sedimentary cover can be clearly delineated. The 2D inversion models allowed the selection of the graben-like zones in two of the MT profiles that have the best potential for development for major water supply by deep boreholes. We suggest that the recharge areas for the main aquifer can be mapped and used to control land use pattern in the area of study.

Acknowledgements

This work was supported by Secretaria de Meio Ambiente e Recursos Hídricos do Piauí, PROAGUA project.

References

- Egbert, G.D. and Booker, J.R., 1986, Robust estimation of geomagnetic transfer functions, Geophys. J.R.astr. Soc., 87, 173-194.
-Fontes, S.L., Meju, M.A., Lima, J.P.R., Carvalho, R.M., La-Terra, E.F., Germano, C.R., and Metelo, M., 1997, Geophysical investigation of Major structural controls on groundwater distribution, North of Sao Raimundo Nonato, Piaui. 5th International Congress of the Brazilian Geophys. Soc., Sao Paulo, Expanded Abstract, Vol.2, 766-769.
-Groom, R.W., and Bailey, R.C., 1989, Decomposition of magnetotelluric impedance tensors in the presence of local three-dimensional galvanic distortion, J.Geophys. res., 94, 1913-1925.

- Mackie, R.L., 1997, Two-dimensional inversion of magnetotelluric data, software, internetsite:MTNET:nazca.cg.emr.ca/mtnet/mtnet.htm."
- Meju, M.A., Fontes, S.L., Oliveira, M.F.B., Lima, J.P.R., Ulugergerli, E.U., Carrasquilla, A.A., 1999, Regional aquifer mapping using combined VES-TEM/EMAP methods in the semiarid eastern margin of Parnaiba Basin, Brazil, Geophysics, 64, 337-356.
-Ulugergerli, E.U., 1998, Development and application of 2-D magnetotelluric inversion in complex domain, PhD thesis, University of Leicester, UK.

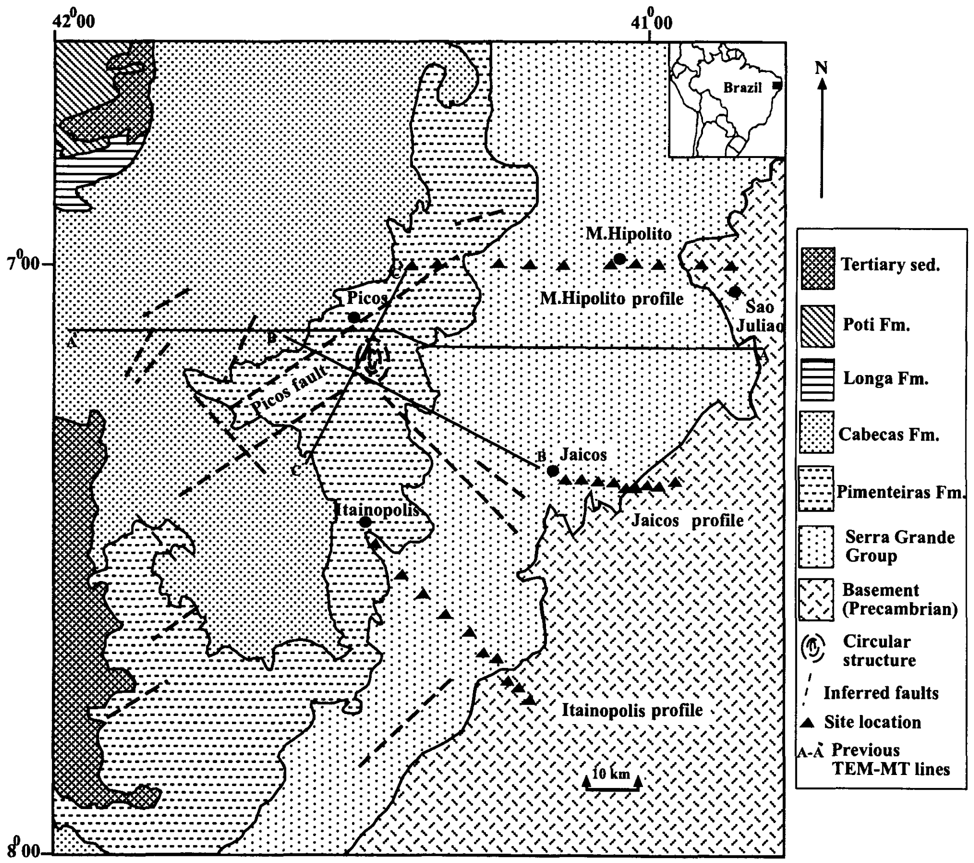

Figure 1. Geological map of the area of study showing the TEM-MT site locations.

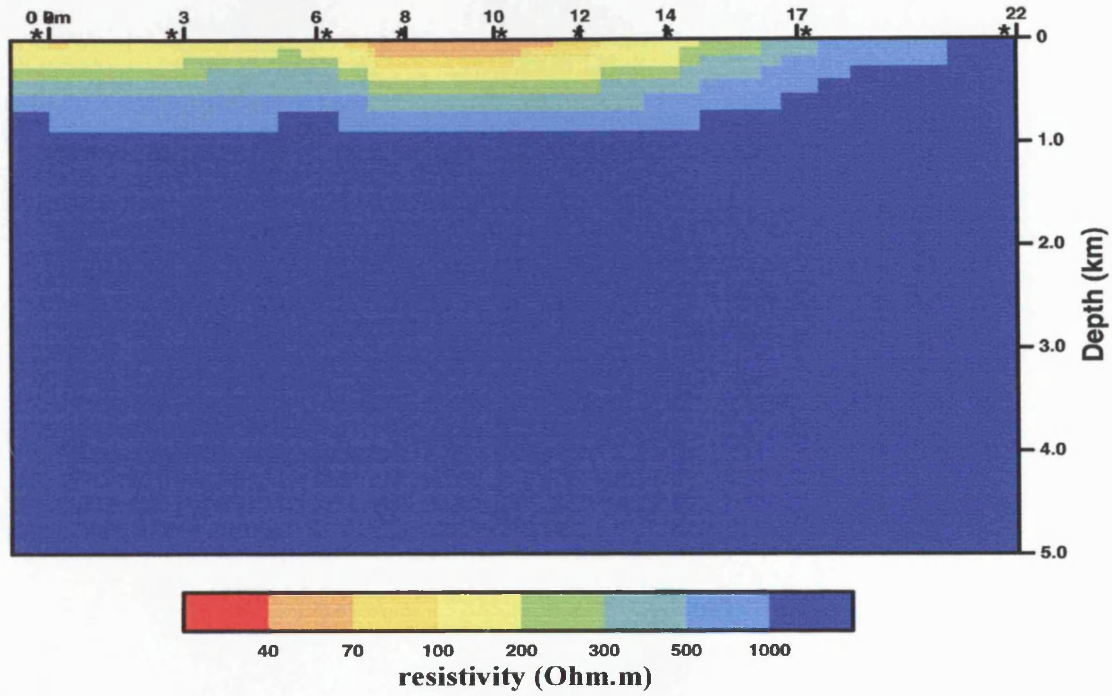

Figure 3. West-east 2D resistivity structure for the Jaicós profile.

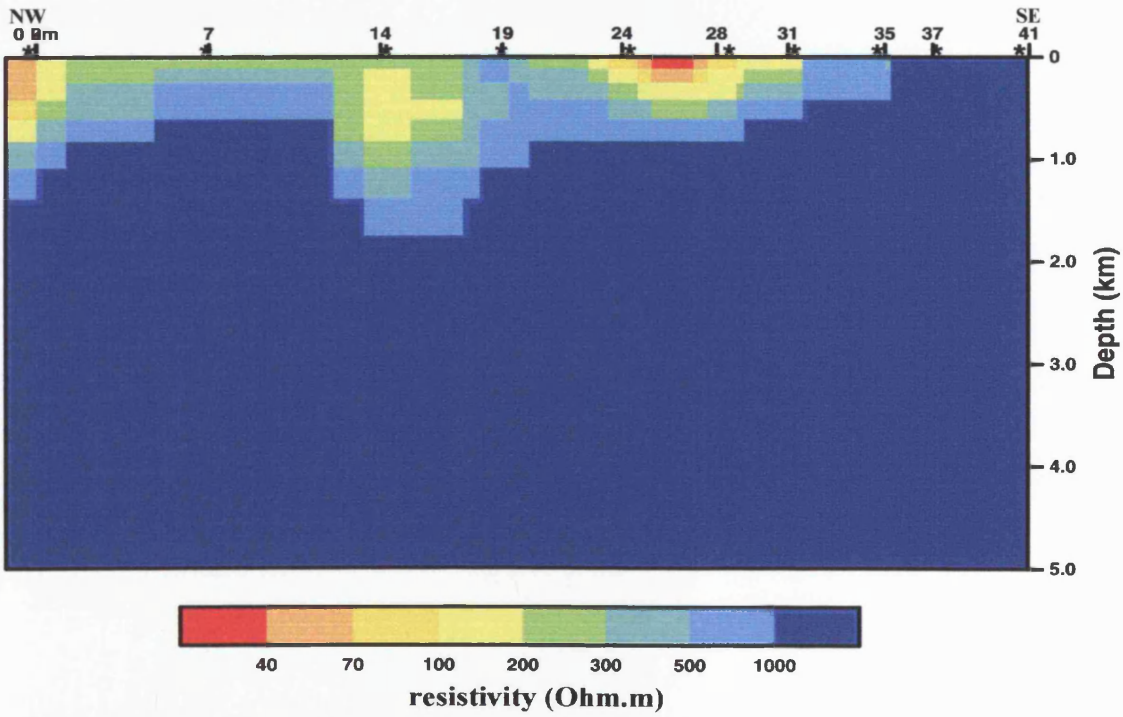

Figure 4. NW-SE 2D resistivity structure for the Itainópolis profile.

Appendix E

The symbols used in this study are given in this appendix.

Symbols used

Symbol	*Definition*
E	Electric field intensity
H	Magnetic field intensity
B	Magnetic induction
I	Electric current
D	Displacement current
J	Current density
ρ^*	Charge density
ε	Electric permittivity
V	Voltage
μ	Magnetic permeability
σ	Electrical conductivity
σ_b	Bulk conductivity
σ_w	Water conductivity
f	Frequency
K	Wave propagation constant
w	Angular frequency
ρ	Resistivity
ρ_a	Apparent resistivity
ρ_{eff}	Effective resistivity
ρ_f	Resistivity of the pore fluid
ρ_b	Bulk resistivity
δ	Skin depth
δ_{eff}	Effective depth
δt	Diffusion depth
z	Depth
h	Thickness
Z	Impedance
Z_{eff}	Effective impedance
φ	Phase
φ_{eff}	Effective phase
ϕ_e	Shear angle
ϕ_t	Twist angle
θ	Rotation angle between the measured direction and strike
θ_0	Rotation angle in the direction of strike
S	Swift skew
$\lfloor A^*B \rfloor$	Cross power
$\lfloor A^*A \rfloor$	Auto power
C	Distortion tensor

R	Rotation matrix
R^T	Transpose of rotation matrix
TDS	Total dissolved solids
g	Site gain
T	Twist
S	Shear
A	Anisotropy
T	Period
A	Matrix
A^T	Transpose of the matrix A
A_o	Layered earth impedance function
β	Lagrange multiplier
W	Weighting matrix
V	Velocity
t	Time
τ	Time constant
a	Radius of the transmitter loop
b	Radius of the receiver loop
P	Laplace transform variable
λ	Integration variable
J_1	Bessel function of order one
N	Number of stacking
Φ	Total porosity
V	Volume
V_V	Volume of voids
V_T	Volume of rock
rms	Root mean square error
TAU	Regularization parameter
TM	Transverse magnetic field
TE	Transverse electric field
m	Model parameter
m_0	A priori model parameter
q_1 & q_2	The quantities required to be minimized in the inverse modelling

References

Ahmed, N., 1993, Application of static correction to seismic refraction data, Quorn Park, Leicestershire, Leicester, Internal report in the University of Leicester.

Andrieux, P., and Wightman, W.E., 1984, The so-called static corrections in magnetotelluric measurements, 54th Ann. Internat. Mtg., Soc. Expl. Geophys, Expanded Abstracts, p. 43-44.

Archie, G.E., 1942, The electrical resistivity log as an aid in determining some reservoir characteristics: Transactions of the American Institute of Mining Engineers, v. 146, p. 54-62.

Aristodemou, E. and Thomas-Betts, A., 2000, DC resistivity and induced polarization investigations at a waste disposal site and its environments: Journal of applied geophysics, v. 44, p. 275-302.

Arora, B.R., Padiha, A.L., Vitorello, L., Trividi, N.B., Fontes, S.L., Rigoti, A., Charmalam, F.H., 1999, Geoelectricl model for the Parnaiba basin conductivity anomaly of the northeast Brazil and tectonic implication: Tectonophysics, v. 302, p. 57-69.

Arora, B.R., Trivedi, N.B., Padilha, A.L., Rigoti, A., Chamalaun, F.H., and Fontes, S.L., 1997, Electrical conductivity distribution in Parnaiba Basin and its tectonic significance, 5th. International Congress of the Brazilian Geophys. Soc., Sao Paulo, Volume 2, p. 755-756.

Asten, M.W., 1987, Full transmitter wave form transient electromagnetic modelling and inversion for sounding over coal measures: Geophysics, v. 52 (3), p. 279-288.

Asten, M.W., and Price, D.G., 1985, Transient sounding by the in/out-loop method, Austral. Soc. Expl. Geophys, Sydney, Abstract, Volume 16, p. 165-168.

Bahr, K., 1988, Interpretation of the magnetotelluric impedance tensor: regional induction and local telluric distortion: J. Geophys., v. 62, p. 119-127.

—, 1991, Geological noise in magnetotelluric data: a classification of distortion types: Phys. Earth Planet. Inter., v. 66, p. 24-38.

Bahr, K., Oslen, N., and Shankland, T.J., 1993, On the combination of magnetotelluric and the geomagnetic depth sounding method for resolving an electrical conductivity increase at 400km depth, Geophys. Res. Lett., v. 20, p. 2937-2940

Bai, D., Meju, M.A., and Liao, Z., 2002, Magnetotelluric images of deep crystal structure of the Rehai geothermal field near Tengchong, Southern China: Geophys. J. Int., v. 148, p. 1-16.

Banks, R.I., Livelybrooks, D., Jones, P., and Longstaff, R., 1996, Causes of high crustal conductivity beneath the Lapetus suture zone in Britain: Geophys. J. Int., v. 124, p. 433-455.

Barker, R.D., 1981, The offset system of electrical resistivity sounding and its use with a multicore cable: Geophysical Prospecting, v. 29, p. 128-143.

—, 1992, A simple algorithm for electrical imaging of the subsurface: First break, v. 10, p. 53-62.

Barker, R.D., White, C.C., Houston, J.F.T., 1992, Borehole siting in an African accelerated drought relief project, *in* Wright, E.P., Burgess, W.G., ed., The hydrogeology of crystalline basement aquifers in Africa, Volume 66, Geological Society of London, London, United Kingdom, p. 183-201.

Barker, R.D., and Moore, J., 1998, The application of time-lapse electrical tomography in ground studies: The leading edge, p. 1454-1458.

Barringer, A.R., 1962, A new approach to exploration- the INPUT airborne-electrical pulse prospecting system: Min. Cong. Jour., v. 48, p. 49-52.

Bartel, L.C., 1991, Results from a controlled-source audio frequency magnetotelluric survey to characterize an aquifer, *in* Ward, S.H., ed., Geotechnical and environmental geophysics, Volume 2, Society of Exploration Geophysicists, p. 219-233.

Beamish, D., and Travassos, J. M., 1992, A study of static shift removal from magnetotelluric data: Journal of Applied Geohysics, v. 29, p. 157-178.

Bellieni, G., Piccirillo, E. M., Cavazzini, G., Petrini, R., Chomin-Chiaramonti, P., Nardy, A.J.R., Civetta, L., Melfi, A.J., and Zantedeschi, P., 1990, Low and high TiO2 Mesozoic tholeitic magmatism of the Maranhhao Basin (NE-Brazil): K/Ar, geochemistry, petrology, isotope characteristics and relationships with Mesozoic low-and high-Tio2 flood basalts of the Parana basin (SE-Brazil): Neues Jahrb. Mineral. Abh, v. 162, p. 1-33.

Berdichevsky, M.N., and Dmitriev, V. I., 1976, Distortion of magnetic and electrical fields by near-surface inhomgeneities: Acta Geod., Geophys. et Montanist Acad. Sci. Hung., v. 11, p. 447-483.

Berdichevsky, M.N., Vanyan, L.L., and Dmitriev, V.I., 1989, Methods used in the USSR to reduce near surface inhomogeneity effects on deep electromagnetic sounding: Phys. Earth Planet. Inter., v. 53, p. 194-206.

Bernard, J., Vachette, C., Valle, P., 1990, Deep groundwater survey with audio-magnetotelluric soundings, Society of Exploration Geophysicists, Sixtieth annual international meeting and exposition, Tulsa, United states, Volume 60, p. 528-531.

Birkelo, B.A., Steeples, D.W., Miller, R.D., and Sophocleous, M. A., 1987, Seismic reflection study of a shallow aquifer during a pumping test: Groundwater, v. 25, p. 703-709.

Bostick, F.X., 1977, A simple almost exact method of MT analysis. Workshop on Electromagnetic methods in Geothermal exploration, U. S, Geol. Surv., Contract No. 14080001-8-359.

Brassington, R., 1988, Field hydrogeology, The geological society of London Handbook series, Open University Press, Milton Kenyes, UK.

Brewitt-Taylor, C.R., and Weaver, J.T., 1976, On the finite difference solution of two-dimensional induction problems: Geophys. J. R. Astr. Soc., v. 47, p. 375-396.

Buck, W.R., and Mutter, J.C., 1987, Convection and density charges due to partial melting: relation to passive margin volcanism, Eos. Tras. AGU, 414 p.

Buselli, G., 1981, The effect of near-surface superparamagnetic material on electromagnetic measurements: Geophysics, v. 47, p. 1315-1324.

Buselli, G., and O'Neill, B., 1977, SIROTEM: A new portable instrument for multichannel TEM measurements: Expl. Geophys., v. 8, p. 82-87.

Buselli, G., Barber, C., Davis, G.B., and Salama, R.B., 1990, Detection of groundwater contamination near waste disposal sites with transient electromagnetic and electrical methods, *in* Ward, S.H., ed., Geotechnical and environmental geophysics, Volume 2, Soc. of Exp. Geophys., p. 27-38.

Cagniard, L., 1953, Basic theory of the magnetotelluric method of geophysical prospecting: Geophysics, v. 18, p. 605-635.

Cantwell, T., 1960, Detection and analysis of low frequency magnetotelluric signals [Ph.D.], M.I.T., Cambridge, Mass., USA.

Carpenter, P.J., Calkin, S.F. and Kaufmann, R. S., 1991, Assessing a fractured landfill cover using electrical resistivity and seismic refraction techniques: Geophysics, v. 56, p. 1896-1904.

Ceron, J., Lombo, C., William, S., 2001, Effective use of non-seismic methods for petroleum exploration: First break, v. 19 (9), p. 523-528.

Christensen, N.B., and Soresen, K.I., 1994, Integrated use of electromagnetic methods for hydrogeological investigations, Proc. EEGS Symposium on applications of Geophysics to Engineering & Environmental Problems, Boston, March, p. 163-176.

Christopherson, K.R., 1991, Application of magnetotellurics to petroleum exploration in Paupa New Guinea: A model for frontier areas: The leading edge, v. 1, p. 21-27.

Constable, S.C., Orange, A. S., and Hoversten, G. M., 1998, Marine magnetotellurics for petroleum exploration Part I: A sea-floor equipment system: Geophysics, v. 63 (3), p. 816-825.

Constable, S.C., Parker, R.L., and Constable, C.G., 1987, Occam's inversion: a practical algorithm for generating smooth models from electromagnetic sounding data: Geophysics, v. 52, p. 289-300.

Cooper, N.J., and Swift, R., 1994, The application of TEM to Cyprus-type massive sulphide exploration in Cyprus: Geophysics, v. 59 (2), p. 202-214.

Crone, J.D., 1977, Ground pulse EM - examples of survey results in the search of massive sulphide. New equipment development: Austral. Soc. Exp. Geophys., v. 8, p. 38-42.

Cunha, F.M.B., 1986, Evolucao paleozoica Da Bacia DO Parnaiba Eseu Arcabouco Tectonico [Msc thesis], Univer sidadfe Federal do Rio de Janeiro.

Cunha, F.M.B., and Góes, A. M. O., 1989, Geologia da parte norte da Bacia do parnaiba, PETROBAAS-SIEX REPORT, No. 130- 07044, 106p.

Davis, S.N., 1969, Porosity and permeability of natural materials, *in* De Wiest, R.J.M., ed., Flow through Porous Media, Academic press, New York, p. 54-89.

Davis, S.N., and De Wiest, R. J. M., 1966, Hydrogeology, John Wiley & Sons, New York, 463 p.

De Sousa, M.A., 1996, Regional gravity modelling and geohistory of the Parnaiba Basin (NE Brazil) [Ph.D. thesis], University of Newcastle (UK).

De Sousa, M.A., Oliveira, M.F.B., 1995, Geophysical evidences of the Transbrasiliano Lineament in the Parnaiba basin: An. Simp. Nac. Estudos Tectonicos, p. 260-263.

Devlin, T., 1984, A broad band electromagnetic induction study of the Travale geothermal Field, Italy [Ph. D. thesis], University of Edinbrugh (UK).

Dolan, W.M., 1970, Geophysical detection of deeply buried sulphide bodies in weathered regions: In Mining and Groundwater Geophysics, Econ. Geol. Report 26, p. 336-344.

Domenico, P.A., and Schwartz, F. W., 1990, Physical and chemical hydrogeology, John Wiley & Sons Inc., New York.

Dyck, A.V., 1991, Drill-hole electromagnetic methods, *in* Nabighian, M.N., ed., Electromagnetic methods in applied geophysics, Volume 2, Soc. of Exp. Geophys., p. 881-923.

Eadie, T., and Staltari, G., 1987, Introduction to downhole electromagnetic methods: Expl. Geophys., v. 18.

Eaton, P.A., and Hohmann, G.W., 1989, An evaluation of Electromagnetic method in the presence of Geologic Noise: Geophysics, v. 8, p. 1106-1126.

Ebraheem, M.W., Bayless, E.R., Krothe, N.C., 1990, A study of acid mine drainage using earth resistivity measurements: Groundwater, v. 28, p. 361-368.

Egbert, G.D, and Booker, J.R., 1992, Very long period magnetotellurics at Tucson observatory: Implications for mantle conductivity, J. Geophys. Res., v. 97 (15), p. 99-115.

Fischer, G., Schnegg, P., Peguiron, M., Le Quang, B. V., 1981, An analytic one-dimensional magnetotelluric scheme: Geophys. J. R. Astr. Soc., v. 67, p. 257-278.

Fitterman, D.V., and Anderson, W.L., 1987, Effect of transmitter-turn-off time on transient soundings: Geoexploration, v. 24, p. 131-146.

Fontes, S.L., Meju, M. A., Lima, J.P.R., Carvalho, R. M., Laterra, E. F., Germano, C. R., and Metelo, M., 1997, Geophysical investigation of major structural controls on groundwater distribution, north of Sao Raimundo Nonato, Piaui State, 5th Internat. Congress, Brazil, Geophysical Society, Expanded abstract, Volume 2, p. 766-769.

Fraser, D.C., 1973, Magnetite ore tonnage estimates from an aerial electromagnetic survey: Geoexploration, v. 11, p. 97-105.

Freeze, R.A., and Cherry, J. A., 1979, Groundwater, Englewood Cliff, N. J., London, Prentice-Hall.

Fuji-ta, K., Ogawa, Y., Yamaguchi, S., and Yaskawa, K., 1997, Magnetotelluric imaging of the SW Japan forearc-a lost paleoland revealed: Phys. Earth Planet Inter., v. 102, p. 231-238.

Fullagar, P.K., 1989, Generation of conductivity depth pseudosection from coincident loop and in-loop TEM data: Expl. Geophys., v. 20, p. 43-45.

Fullagar, P.K., and Reid, J. E., 1992, Conductivity-depth transformations of fixed loop TEM data: Expl. Geophys., v. 23, p. 515-520.

Furlong, K.P., and Fountain, D. M., 1986, Continental crust underplating: Thermal considerations and seismic-petrologic consequences: J. Geophys. Res., v. 91, p. 8285-8294.

Galanopoulos, D., 1989, Magnetotelluric studies in geothermal areas of Greece and Kenya [Ph. D. thesis], University of Edinburgh (UK).

Gendzwill, D. J., Serzu, M. H., and Lodha, G. S., 1994, High-resolution seismic reflection surveys to detect fracture zones at the AECL underground research laboratory: Can. J. Explor. Geophys., v.30, 28-38.

Goes, A.M.O., 1991, Relatorio de viagem a Teresina-Coletanea de dados de alguns pocos perfurados para captacao de aguas subterraneas no Estado do Piaui- Bacia do parnaiba, PETROBAAS-SIEX Report, No. 130-07905.

Goes, A.M.O., Travassos, W. A., and Teixeira, L. B., 1993, Estagio explratorio e perspectivas petroliferas da Bacia do Parnaiba, PETROBAS-DEXNOR-DINTER Report, 97p.

Goldberg, S., and Rotstein, Y., 1982, A simple form of presentation of Magnetotelluric Data using the Bostick Transform: Geophysical Prospecting, v. 30, p. 211-216.

Goldman, M., Arad, A., Kafri, U., Gilad, D., and Melloul, A., 1989, Detection of fresh-water/seawater interface by the time domain electromagnetic (TDEM) method in Israel, Proc. 10th SWIM, Volume 70, p. 329-344.

Goldman, M., Rabinovich, B., Rabinovich, M., Gilad, D., Gev, I., and Schirov, M., 1994a, Application of integrated NMR-TDEM method in groundwater exploration in Israel: Journal of Applied Geophysics, v. 31, p. 27-52.

Goldman, M., Tabarovsky, L., and Rabinovich, M., 1994b, On the influence of 3-D structures in the interpretation of transient electromagnetic sounding data: Geophysics, v. 59, p. 889-901.

Goldstein, N.E., Benson, S. M., and Alumbaugh, D., 1990, Saline Groundwater plume mapping with electromagnetics, *in* Ward, S.H., ed., Geotechnical and environmental geophysics, Volume 2, Soc. Expl. Geophys., p. 17-25.

Gomez-Trevino, E., 1987, Nonlinear integral equations for electromagnetic inverse problems: Geophysics, 52, 1297-1302.

Grant, F.S., and West, G. F., 1965, Interpretation theory in applied geophysics, McGraw-Hill, New York.

Gregori, G.P., and Lanzerotti, L. J., 1980, Geomagnetic depth sounding by induction arrow representation: Rev. Geophys. Space Phys., v. 18, p. 203-210.

Groom, R.W., and Bahr, K., 1992, Corrections for near surface effects: Decomposition of the magnetotelluric resistivities: a tutorial: Survey in Geophysics, v. 13, p. 341-379.

Groom, R.W., and Bailey, R.C., 1989, Decomposition of magnetotelluric impedance tensors in the presence of local three-dimensional galvanic distortion: J. Geophys. Res., v. 94, p. 1913-1925.

—, 1991, Analytic investigations of the effects of the near surface three-dimensional galvanic scatters on MT tensor decompositions: Geophysics, v. 56, p. 496-518.

Hastie, L.M., Cevallos, C., Chant, I. J., 1989, The application of a joint MT CSAMT survey to oil exploration: Exploration Geophysics, v. 20, p. 339-342.

Hatzichristodulu, C., 1998, Application of TEM and DC resistivity techniques in groundwater exploration [Ph.D. thesis], Leicester University (UK).

Hermance, J.F., and Grillot, L.R., 1974, Constraints on temperature below Iceland from magnetotelluric data: Phys. Earth. Plan. Int., v. 8, p. 1-12.

Hobbs, B. A., 1992, Terminology and symbols for use in studies of electromagnetic induction in the earth: Survey in geophysics, v. 13, p. 489-515.

Hobbs, B.A., and Dumitrescu, C. C., 1997, One-dimensional magnetotelluric inversion using an adaptation of Zohdy's resistivity method: Geophysical Prospecting, v. 45, p. 1027-1044.

Hohmann, G.W., 1983, Three-dimensional EM modelling: Surveys in Geophysics, v. 6, p. 27-54.

Honkura, Y., Niblett, E.R., and Kurtz, R.D., 1977, Preliminary study of the use of magnetotelluric fields for earthquake prediction: Acta Geol. Geophys. Montan, v. 12 (1), p. 33-36.

Hoversten, G. M., and Morrison, H. F., 1982, Transient field of a current loop source above a layered earth: Geophysics, v. 47, p. 1068-1077.

Hutton, V.R.S., Dawes, G.J.K., Delvin, T., and Roberts, R., 1984, A broadband tensorial magnetotelluric study in the Travel-Redicondoli geothermal field, EEC report series, Contract NO. EG-A2-031-UK, Final report.

Ingham, M., Whaler, K., and Mcknight, D., 2001, Magnetotelluric sounding of the Hikurangi Margin, New Zealand: Geophys. J. Int., v. 144, p. 343-355.

Ivrine, R.J., and Staltari, G., 1984, Case history illustrating interpretation problems in transient EM surveys: Expl. Geophys., v. 15 (3), p. 155-167.

Jiracek, G.R., 1990, Near surface and topographic distortions in electromagnetic induction: Surveys in Geophysics, v. 11, p. 163-203.

Jiracek, G. R., Haak, V., and Olsen, K. H., 1995, Practical magnetotelluric in a continental rift environment, *in* Olsen, K.H., ed., continental rifts: evolution, tectonics, development in geotectonics, volume 25, p.103-129.

Johansen, H.K., 1977, A man/computer interpretation system for resistivity soundings over a horizontally stratified earth: Geophysical Prospecting, v. 25, p. 667-691.

Jones, A.G., 1983a, The problem of current channelling, a critical review: Geophysical surveys, v. 6, p. 79-122.

—, 1983b, On the equivalence of the "Niblett" and "Bostick" transformations in the magnetotelluric method: J. Geophys., v. 53, p. 72-73.

—, 1988, Static shift of magnetotelluric data and its removal in a sedimentary basin environment: Geophysics, v. 53, p. 967-978.

Jones, F.W., and Price, A. T., 1970, The perturbation of alternating geomagnetic fields by conductivity anomalies: Geophys. J. R. Astr. Soc., v. 20, p. 317-334.

Junge, A., 1996, Characterisation of and correction for cultural noise: Surveys in Geophysics, v. 17 (4), p. 361-391.

Jupp, D.L., and Vozoff, K., 1975, Two-dimensional magnetotelluric inversion: Geophys. J. R. Astr. Soc., v. 50, p. 333-352.

Kagiyama, T., Utada, H., Yamamoto, T., 1999, Magma ascent beneath Unzen Volcano, SW Japan, deduced from the electrical resistivity structure: Journal of Volcanology and Geothermal Research, v. 89, p. 35-42.

Kato, Y., and Kikuchi, T., 1950, On the phase difference of Earth currents induced by changes of the Earth's magnetic field: Geophysics, v. 2, p. 139-145.

Kaufman, A.A., and Keller, G.V., 1983, Frequency and Transient soundings, Methods in Geochemistry and Geophysics, Elsevier Publ. Co., v.16, 685p.

Kaufman, A.A., and Keller, G.V., 1981, The magnetotelluric sounding method, Elsevier, Amsterdam, 559 p.

Keller, G.V., 1988, Rock and mineral properties, *in* Nabighian, M.N., ed., Electromagnetic methods in applied Geophysics, Volume 1, Society of exploration geophysics, p. 13-51.

Keller, G.V., and Frischknecht, F.C., 1966, Electrical methods in geophysical prospecting, Pergamon press, Oxford, 419 p.

Keller, G.V., Pritchard, J.I., Jackson, J.J., and Harthill, N., 1984, Megasource time-domain electromagnetic methods: Geophysics, v. 49 (7), p. 993-1009.

Kelly, W.E., and Mares, S., 1993, Applied geophysics in hydrogeological and engineering practice, Amestrdam-Oxford-New York Elsevier, v. 44, 284 p.

Knight, J.H., and Raiche, A.P., 1982, Transient electromagnetic calculations using the Gaver-Stehfest inverse laplace transform method: Geophysics, v. 47 (1), p. 47-50.

Kruse, S.E., Brudzinsk, M.R., Geib, T. L., 1998, Use of electrical and electromagnetic techniques to map seawater intrusion near the cross-Florida Barge canal: Environmental & Engineering Geosciences, v. IV (3), p. 331-340.

Kurtz, R.D., DeLaurier, J. M., and Gupta, J.C., 1990, The electrical conductivity distribution beneath Vancouver Island: a region of active plate subduction: J. Geophys. Res., v. 95, p. 10929-10946.

Kurtz, R.D., DeLaurier, J.M., and Gupta, J.C., 1986, A magnetotelluric sounding across Vancouver Island detects the subducting Juan de Fuca Plate: Nature, v. 321, p. 596-599.

Lagios, E., Galanopoulos, D., Hobbs, B. A., and Dawes, G.J.K.1998, Two-Dimensional magnetotelluric modelling of the Kos Island geothermal region (Greece), Tectonophysics, v. 287 (1-4), p. 157-172.

Lamantagne, Y.L., 1975, Application of wideband, Time domain EM measurements in mineral exploration [Ph.D. thesis], Univ. of Toronto.

Larsen, J.C., 1977, Removal of the local surface conductivity effects from low frequency mantle response curves: Acta Geod., Geophys. et Montanist. Acad. Sci. Hung., v. 12, p. 183-186.

Lee, T., 1984, The effect of superparamagnetic layer on the transient electromagnetic response of a ground: Geophysical Prospecting, v. 32, p. 480-496.

Lefleur, R.G., 1984, Groundwater as a geomorphic agent, Allen & Unwin Inc. New Jersy.

Legrand, H.E., 1949, Sheet structure, a major factor in the occurrence of ground water in the granites of Georgia: Econ. Geol., v. 44, p. 110-118.

—, 1954, Geology and groundwater in the Statesville area, North Carolina, North Carolina Dept. Conservation development, Div. Mineral Resources. Bull.68.

Leonard-Mayer, P.J., 1984, Development and use of azimuthal resistivity surveys for jointed formations, Nat. Water Well Assn/EPA Conf. Surf. Borehole Geophys. Meth. in Ground Water Invest., Nileson, D. M., and Curl, M., Eds., NWWA, Worthington, Ohio, p. 52-91.

Lilley, F.E.M., and Bennett, D. J., 1972, An array experiments with magnetic variometers near the coasts of south-east Australia: Geophysical J. Roy. astro. Soc., v. 29, p. 49-64.

Linsley, R.K., Kohler, M. A., and Paulhus, L. H., 1988, Hydrology for Engineering, SI Metric edition, McGraw-Hill Book Company, London, 492 p.

Livelybrooks, D., Mareschal, M., Blais, E., and Smith, J.T., 1996, Magnetotelluric delineation of the Trillabelle massive sulphide body in Sudbury, Ontario: Geophysics, v. 61 (4), p. 971-986.

Lowrie, W., and West, G.F., 1965, The effect of conducting overburden on EM prospecting measurements: Geophysics, v. 30, p. 624-632.

Lu, X., 1995, Application of magnetotelluric sounding to hydrocarbon exploration in Tarim Basin, China: Oil Geophysical prospecting (Chinese journal), v. 30 (6), p. 788-796.

Mackie, R.L., 1996, Two dimensional inversion of magnetotelluric data, software, internet site: MTNET "http://nazca.cg.emr.ca/mtnet/mtnet.htm.".

Mackie, R.L., and Madden, T.R., 1993, Conjugate direction relaxation solutions for 3-D magnetotelluric modelling: Geophysics, v. 58, p. 1052-1057.

Mackie, R.L., Bennett, B. R., and Madden, T. R., 1988, Long period magnetotelluric measurements near the central California coast: a land-locked view of the conductivity structure under the Pacific Ocean: Geophys. Journal, v. 95, p. 181-194.

Mackie, R.L., Madden, T.R., and Wannamaker, P. E., 1993, Three-dimensional magnetotelluric modelling using difference equations-Theory and comparisons to integral equation solutions: Geophysics, v. 58, p. 215-226.

Madden, T.R., and Mackie, R.L., 1989, Three-dimensional Magnetotelluric modelling and inversion, Proc. IEEE, Volume 77, p. 318-333.

Madden, T.R., and Thompson, W., 1965, Low frequency electromagnetic oscillations of the earth-ionosphere cavity: Rev. Geophys., v. 3, p. 211-254.

Mahesha, A., and Nagaraja, S.H., 1995, Effect of surface source variation on seawater intrusion in aquifer: Journal of Irrigation and Drainage Engineering-ASCE, v. 121 (1), p. 109-113.

Marini, O.J., 1984, Provincia tocantins, setores central e sudeste, *in* Almeida, F.F.M., Hasui, Y., ed., Pre-Cambriano do Brazil, Editora Edgard Blucher, Sao Paulo, p. 205-264.

Marquardt, D.W., 1970, Generalized inverses, ridge regression, biased linear estimation and nonlinear estimation, Technometrics, v.12, p. 591-612.

Matsushima, N., Oshima, H., Ogwa, 2001, Magma prospecting in Usu Volcano, Hokkaido, Japan, using magnetotelluric soundings: Journal of Volcanology and Geothermal Research, v. 109 (4), p. 263-277.

Mauldin-Mayerle, C., Carlson, N.R., Zong, K., 1998, Environmental applications of high-resolution TEM methods, The 4th Meeting on Environmental and Engineering Geophysics: Barcelona, Spain., p. 14-17.

McCracken, K.G., Oristaglio, M.L., and Hohmann, G. W., 1986, Minimisation of noise in EM exploration systems: Geophysics, v. 51, p. 819-832.

McCracken, K.G., Pik, J.P., and Harris, R. W., 1984, Noise in EM exploration systems: Exploration Geophysics, v. 51, p. 819-832.

McNeill, J.D., 1980a, EM37 Ground TEM System, Tech Note 10, Geonics Ltd, Ontario, Canada.

McNeill, J.D., 1980b, Electrical conductivity of soils and rocks, Technical note TN-5, Geonics Limited.

McNeil, J.D., 1990, Use of electromagnetic methods for groundwater studies, *in* Ward, S. H., ed., Geotechnical and environmental geophysics, Volume 1, Society of Exploration Geophysics, p. 191-218.

Meju, M.A., 1988, The deep electrical structure of the Great Glen Fault, Scotland [Ph.D. thesis], University of Edinburgh.

—, 1992, An effective ridge regression procedure for resistivity data inversion: Computers & Geosciences, v. 18, p. 99-118.

—, 1994, Geophysical data analysis: Understanding inverse problem theory and practice, SEG Course Notes Series, V. 6, 296 p.

—, 1995, Simple effective resistivity- depth transformations for infield or real-time data processing: Computer & Geosciences, v. 21, p. 985-992.

—, 1996, Joint inversion of TEM and distorted MT soundings, Some effective practical considerations: Geophysics, v. 61, p. 56-65.

—, 1998, A simple method of transient electromagnetic data Analysis: Geophysics, v. 63, p. 405-410.

—, 2000, Geoelectrical investigation of old/abandoned, covered landfill sites in urban areas: model development with a genetic diagnosis approach: Journal of Applied Geophysics, v. 44, p. 115-150.

Meju, M.A., and Fontes, S.L., 1993, An investigation of static shifts in MT data from Parnaiba Basin using central-loop TEM data, 3rd Internat. Congr. Brazil, Geophys. Soc., Expanded abstracts, p. 1474- 1479.

Meju, M.A., and Hutton, V.R.S., 1992, Iterative most-squares inversion: application to magnetotelluric data: Geophys. J. Int., v. 108, p. 758-766.

Meju, M.A., Fenning, P.J., Hawkins, T.R.W., 2000, Evaluation of small- loop transient electromagnetic soundings to locate the Sherwood sandstone aquifer and confining formations at well sites in the vale of York, England: J. Applied Geophysics, v. 44, p. 217-236.

Meju, M.A., Fonts, S.L., Oliver, M.F.B., Lima, J.P.R., Ulugergerli, E.U., and Carrasquilla, A.A., 1999, Regional aquifer mapping using combined VES-TEM/EMAP methods in the Semiarid eastern margin of Parnaiba Basin, Brazil: Geophysics, v. 64, p. 1-20.

Meju, M.A., Fontes, S.L., Ulugergerli, E.U., La Terra, E.F., Germano, C.R. and Carvalho, R.M., 2001, A joint TEM- HLEM geophysical approach to borehole sitting in deeply weathered granitic terrain: Groundwater, v. 39 (4), p. 1-10.

Miele, M.J., Jansen, J., Davila Arizpe, J., Magallans, M.A., 2000, A regional groundwater evaluation using magnetotelluric soundings for Monclova, Mexico, Proceeding of the symposium on the application of geophysics to engineering and environmental problems, Environmental and Engineering Geophysical Society, Wheat Ridge, CO, United States, p. 699-708.

Mills, T., Hoekstra, P., Blohm, M., and Evans, L., 1988, Time domain electromagnetic sounding for mapping sea-water intrusion in Monterey County, California: Groundwater, v. 26 (6), p. 771-782.

Montgomery, G.E., 1987, Geophysical activity in 1986: The leading edge, v. 6 (6), p. 25-49.

Morat, P., 1974, Technical processes for the offshore collection of magnetic and telluric data: Phys. Earth Plan Int., v. 8, p. 202-206.

Nabighian, M.N., 1979, Quasi- static response of a conductive-half space: An Approximation Representation: Geophysics, v. 44 (10), p. 1700- 1705.

Nabighian, M.N., and Macanae, J.C., 1991, Time Domain electromagnetic prospecting methods, *in* Nabighian, M.N., ed., Electromagnetic methods in applied Geophysics, Volume 2, Society of exploration geophysics, p. 427-514.

Nekut, A.G., 1987, Direct inversion of time-domain electromagnetic data: Geophysics, v. 52, p. 1431-1435.

Newman, G.A., Anderson, W. L., and Hohmann, G. W., 1987, Interpretation of transient electromagnetic soundings over three-dimensional structures for the central loop configuration: Geophys. J. R. Astr. Soc., v. 89, p. 889-914.

Niblett, E.R., and Sayn-Wittgensetein, 1960, Variation of electrical conductivity with depth by the magnetotelluric method: Geophysics, v. 25, p. 998-1008.

Nobes, D.C., 1994, Using non-invasive, non-destructive geophysical methods to map and to monitor the source and extent of contamination, Proceedings of the Symposium of the Geotechnical Aspects of waste management, IPENZ Proceedings of Technical Groups, The New Zealand Geomechanics Society, Volume 2, p. 89-98.

—, 1996, Troubled waters: Environmental applications of electrical and electromagnetic methods: Surveys in Geophysics, v. 17, p. 393-454.

Num, K.R., Barker, R.D., and Bamford, D., 1983, In-situ seismic and electrical measurements of fracture anisotropy in the Lincolnshire chalk.: Quart. J.Eng. Geol., v. 16, p. 187-195.

Nunes, K.C., 1993, Interpretacao integrada da Bacia do Parnaiba com enfase nos dados aeromagneticos, 3rd internat. Congr., Brazil, Geophys. Soc., Expanded Abstracts, 152-157.

Oldenburg, D.W., 1990, Inversion of electromagnetic data: An overview of new techniques: Surveys in Geophysics, v. 11, p. 231-270.

Oliveira, M.F.B., and Fontes, S.L., 1991, Magnetotelurica na Bacia do Parnaiba: primeiros resultados, An. II Cong. Int. Soc. Bras. Geofis, Salvador, Volume 1, p. 294-299.

Palacky, G.J., 1987, Resistivity characteristics of geological targets, *in* Nabighian, M.N., ed., Electromagnetic methods in applied geophysics, Volume 1, Society of Exploration Geophysics, p. 53-129.

Palacky, G.J., Ritsema, I.J., and De Jong, S.J., 1981, Electromagnetic prospecting for Groundwater in Precambrian Terrains in the Republic of Upper Volta: Geophysical Prospecting, v. 29, p. 932-955.

Park, S.K., Orange, A.S., and Madden, T.R., 1983, Effects of three-dimensional structures on magnetotelluric sounding curves: Geophysics, v. 48, p. 1402-1405.

Parker, L.R., 1984, The inverse problem of resistivity sounding, Geophysics, v. 49, p. 2143-2158.

Parkinson, W.D., 1959, Direction of rapid geomagnetic fluctuations: Geophysical Journal, v. 2, p. 1-14.

—, 1983, Introduction to Geomagmatism, Scottish Academic Press, Edinburgh, 433 p.

Parr, R.S., 1991, Development of magnetotelluric processing and modelling procedures; application to northern England [Ph. D. thesis], University of Edinburgh, UK.

Patra, H.P., 1967, A note on the possibility of saline water invasion around the Jaldha coast, West Bengal (India): Geoexploration, v. 5 (2), p. 95-101.

Patra, H.P., and Mallick, K., 1980, Geosounding principles, 2. Time varying geoelectric soundings, Elseveir.

Patrick, F.W., and Bostick, F. X., 1969, Magnetotelluric modelling techniques, Elec. Geophys. Res. Lab., University of Texas, Tech. Report, 59.

Pedersen, L.B., Bastani, M., Dynesius, L., Oskool, B., 2001, Ground water exploration using high resolution RMT and CSTMT methods, EAGE 63rd Conference& Technical exhibition, Amsterdam, The Netherlands.

Pedersen, L.B., Qian, W., Dynesius, L., and Zhang, P., 1994, An airborne tensor VLF system: From concept to realization: Geophysical Prospecting, v. 42, p. 863-883.

Pellerin, L., and Hohmann, G.W., 1990, Transient electromagnetic inversion: a remedy for MT static shift: Geophysics, v. 55, p. 1242-1250.

Pererira, A.J., and Hamza, V.M., 1991, Fluxo geotermico na Bacia do Parnaiba, International Congress Brazilian Geophysical Society, Salvador, Volume 2, p. 177-182.

Perez-Flores, M.A., 1995, 2-D fast inversion of DC resistivity and MT data and of CSEM measurements at low induction numbers [Ph.D. thesis], CICESE.

Perez-Flores, M.A., Mendez-Delgado, S., and Gomez-Trevino, E., 2001, Imaging low frequency and dc electromagnetic fields using a simple linear approximation: Geophysics, v. 66 (4), p. 1067-1081.

Petieau, G., and Dupis, A., 1980, Noise temperature coefficient and long time stability of electrodes for telluric observations: Geophysical Prospecting, v. 28, p. 792-804.

Petri, S., and Fulfaro, V. J., 1983, Geologia de Brasil, Editora Universida de Sao Paulo, 558p.

Price, M., 1985, Introduction to Groundwater, British Geological survey, London.

Raiche, A.P., 1984, The effect of ramp function turn-off on TEM response of a layered Ground: Expl. Geophys., v. 15, p. 37-41.

Ranganayki, R.P., 1984, An interpretative analysis of magnetotelluric data: Geophysics, v. 49, p. 1730-1748.

Reddy, I.K., and Rankin, D., 1973, Magnetotelluric response of a two-dimensional sloping contact by the finite element method: Pure Appl. Geophys., v. 105, p. 847-857.

Rikitake, T., 1950, Electromagnetic induction within the earth and its relation to the electrical state of the earth's interior: Bull. Earthq. Res. Inst., Tokyo University, v. 28, p. 45-98.

Risk, G.F., Caldwell, T.G., Bibby, H.M., 1999, Use of magnetotelluric signals from 50 Hz power lines for resistivity mapping of geothermal fields in New Zealand: Geophysical Prospecting, v. 47, p. 1091-1104.

Rokityanski, I.I., 1982, Geoelctromagnetic investigation of the earth's crust and mantle, Springer-Verlag, Berlin.

Sandberg, S.k., 1993, Examples of resolution improvement in geoelectrical soundings applied to groundwater investigations: Geophysical Prospecting, v.41, p. 207-227

Sasaki, Y., 1981, Automatic interpretation of resistivity sounding data over two-dimensional structure: Geophysical Exploration of Japan (Butsuri Tanko), v. 34, p. 341-350.

—, 1992, Resolution of resistivity tomography inferred from numerical simulation: Geophysical Prospecting, v. 40, p. 453-463.

Sauck, W., A., and Zabik, S.M., 1992, Azimuthal resistivity techniques and the directional variations of hydraulic conductivity in glacial sediments., Symposium on the application of geophysics to engineering and environmental problems, Soc. Eng. Min. Expl. Geophys., p. 197-222.

Savin, C., Ritz, M., Join, J., Bachelery, P., 2001, Hydrothermal system mapped by CSAMT on Karthala Volcano, Grande Comore Island, Indian Ocean: Journal of Applied Geophysics, v. 48 (3), p. 143-152.

Schopper, J., 1982, Electrical conductivity of rocks containing electrolytes: Physical Properties of Rocks, v. 1b, p. 276-291.

Seol, S.J., Kim, J.H., Song, Yoonho, and Chung, S. H., 2001, Finding the strike direction of fractures using GPR: Geophysical Prospecting, v. 49, p. 300-308.

Sharma, P.V., 1997, Environmental and Engineering geophysics, Cambridge University press, 475 p.

Shtivelman, V., and Goldman, M., 2000, Integration of shallow reflection seismic and time domain electromagnetic for detailed study of the coastal aquifer in the Nitzaim area of Israel: Journal of Applied Geophysics, v. 44, p. 197-215.

Smith, R.S., and West, G.F., 1988, An explanation of abnormal TEM response: Coincident-loop negatives and loop effect: Expl. Geophys., v. 19, p. 435- 446.

—, 1989, coincident loop transient electromagnetic response: Geophysics, v. 53, p. 677-690.

Smith, R.S., Edwards, R.N., and Buselli, G., 1994, An automatic technique for presentation of coincident- loop, impulse -response, transient electromagnetic data: Geophysics, v. 59, p. 872-888.

Smith, R.S., Walker, P.W., Polzer, B.D., and West, G.F., 1988, The time-domain response of polarizable bodies: An approximate convolution algorithm: Geophysical Prospecting, v. 36, p. 772-786.

Sorensen, K.I., Efferso, F., and Christensen, A.J., 1995, Pulled array transient electromagnetic method PA-TEM, SAGEEP, extended abstracts, p. 899-903.

Spies, B.R., 1980, A field occurrence of sign reversals with the transient electromagnetic methods: Geophysics, v. 54, p. 872-888.

Spies, P.R., and Parker, P.D., 1984, Limitations of large loop transient electro-magnetic surveys in conductive terrains: Geophysics, v. 49, p. 902-912.

Spies, R.P., 1989, Depth of investigation in electromagnetic sounding methods: Geophysics, v. 54 (7), p. 872-888.

Stanley, W.D., Saad, A.R., and Ohofugi, W., 1985, Regional magnetotelluric surveys in hydrocarbon exploration, Parnaiba Basin, Brazil: Amer. Assoc. Petrol. Geol., v. 69 (3), p. 346-360.

Sternberg, B.K., Washburne, J.C., and Pellerin, L., 1988, Correction of static shift in MT using TEM soundings: Geophysics, v. 53, p. 1459-1468.

Sternberg, B.K., Poluton, M. M., and Thomas, S.J., 1990, Geophysical investigations in support of the Arizna SSC project, *in* Ward, S.H., ed., Geotechnical and environmental geophysics, Volume 3, Society of Exploration Geophysicists, p. 211-227.

Stewart, M.T., and Gay, M.C., 1986, Evaluation of transient electromagnetic soundings for deep detection of conductive fluids: Groundwater, v. 24 (3), p. 351-356.

Strack, K.M., Lebrocq, K., Moss, D.C., Vozoff, K.G, Wolfgram, P.A., 1989, Case histories of LOTEM surveys in hydrocarbon prospective areas: First break, v. 7, p. 467-478.

Strangway, D.W., 1983, Audio frequency magnetotelluric (AMT) sounding in developments in Geophysical exploration methods, Applied science, London, New York, Volume 5.

Strangway, D.W., Swift, C.M., and Holmer, R.C., 1973, The applications of audio-frequency magnetotellurics (AMT) to mineral exploration: Geophysics, v. 38 (6), p. 1159-1175.

Street, J.G., and Engel, R., 1990, Geophysical surveys of dry land salinity, *in* Ward, S.H., ed., Geotechnical and environmental geophysics, Volume 2, Society of Exploration Geophysicists, p. 187-199.

Swift, C.M., 1967, A magnetotelluric investigation of electrical conductivity anomaly in the South-western United States [Ph.D.], M.I.T., *in* Vozoff, K., ed., 1986, Magnetotelluric Methods, SEG, p. 156-166.

Swift, R., 1990, Transient electromagnetic soundings in complex geological environments [Ph. D. thesis], Leicester University (UK).

Taylor, R.W., and Fleming, A.H., 1988, Characterizing jointed systems by azimuthal resistivity surveys: Groundwater, v. 26, p. 464-474.

Tezkan, B., Goldman, M., Greinwald, S., Hordt, A., Muller, I., Neubauer, F.M., Zacher, G., 1996, A joint application of radio magnetotellurics and transient electromagnetic to the investigation of a waste deposit in Cologne (Germany): Journal of Applied Geophysics, v. 34, p. 199-212.

Theis, C.V., 1935, The relation between the lowering of the Piezometric surface and the rate and the duration of discharge of a well using groundwater: Trans. Amer. Geophys. Union, v. 2, p. 519-524.

Tikhonov, A.N., 1950, Determination of the electrical characteristics of the deep strata of the Earth's crust: Dokl. Akad. Nauk, v. 73, p. 295-297.

—, 1963, Regularization of ill-posed problems: Doklady Akad, Nauk, USSR, v. 153, p. 1-6.

Tikhonov, A.N., and Berdichevesky, M.N., 1966, Experience in the use of magnetotelluric methods to study the geologic structure of sedimentary basins: Bull. Izv. Acad. Sci. USSR, Geophysics Ser., v. 2, p. 93-97.

Ting, S., C., and Hohmann, G.W., 1981, Integral equation modelling of three-dimensional magnetotelluric response: Geophysics, v. 46, p. 182-197.

Todd, B.J., and Dallimore, S.R., 1998, Electromagnetic and geological transect across Permafrost terrain, Mackenzie River delta, Canada: Geophysics, v. 63, p. 1914-1924.

Todd, D.K., 1959, Groundwater Hydrology, John W. & Sons Inc., Berkeley.

Tolman, C.F., 1937, Groundwater, McGraw-Hill, New York, 593 p.

Uchida, T, and Murakami, Y., 1990, Development of a fortran code for two-dimensional Schlumberger inversion, open file report: Geological survey of Japan, No. 150.

Ulugergerli, E.U., 1998, Development and application of 2D magnetotelluric inversion in the complex domain [Ph.D. thesis], University of Leicester (UK).

Unsworth, M.J., LU, X., Watts, M.D., 2000, CSAMT exploration at Sellafield; characterization of a potential radioactive waste disposal site: Geophysics, v. 65 (4), p. 1070- 1079.

Velikin, A.B., and Buggakov, Y.I., 1967, Transient method of electrical prospecting (one loop version): Seminar on geophysical methods of prospecting for ore minerals, U. N. O., Moscow.

Vidotti, R.M., 1997, Lithospheric structure beneath the Parana and Panaiba basins, Brazil [Ph.D. thesis], Leeds University (UK).

Vozoff, K., 1972, The MT methods in exploration of sedimentary basin: Geophysics, v. 37, p. 98-141.

—, 1991, The magnetotelluric method, *in* Nabighian, M.N., ed., Electromagnetic methods in applied geophysics, Volume 2, p. 641-711.

Vozoff, K., and Jupp, D.L.B., 1975, Joint inversion of geophysical data: Geophys. J. R. Astr. Soc., v. 42, p. 977-991.

Walker, G.G., and Kawasaki, K., 1988, Observation of double sign reversals in transient electromagnetic central induction soundings: Geoexploration, v. 25, p. 245-254.

Wannamaker, P.E., 1997, Tensor CSAMT survey over the sulphur springs thermal areas, Valles Caldera, New Mexico, U. S. A., Part I: Implications for structure of the western Caldera: Geophysics, v. 62 (2), p. 451-465.

Wannamaker, P.E., Booker, J.R., Jones, A.G., Chave, A.D., Filloux, J.H., Waff, H.S., and Law, L.K., 1989, Resistivity cross section through the Juan de Fuca subduction system and its tectonic implications: J. Geophys. Res., v. 94, p. 14127-14144.

Wannamaker, P.E., Hohmann, G.W., and Sanfilipo, W.A., 1984a, Electromagnetic modelling of three-dimensional bodies in layered earth using integral equations: Geophysics, v. 49, p. 60-74.

Wannamaker, P.E., Hohmann, G.W., and Ward, S. H., 1984b, Magnetotelluric responses of three dimensional bodies in layered Earths: Geophysics, v. 49, p. 1517-1533.

Wannamaker, P.E., Stodt, J.A. and Rijo, L., 1985, PW2D-Finite element program for solution of two-dimensional Earth resistivity structure, User Documentation, Univ. of Utah Res. Inst. Rep. ESL-158.

Wannamaker, P.E., Stodt, J.A., and Rijo, L., 1986, Two-dimensional topographic responses in magnetotellurics modelled using finite elements: Geophysics, v. 51, p. 2131-2144.

—, 1987, A stable finite-element solution for two-dimensional magnetotelluric modelling: Geophys. J. R. Astr. Soc., v. 88, p. 277-296.

Ward, R.C., and Robinson, M., 1990, Principle of Hydrology, McGraw-Hill Book Company, London.

Ward, S.H., Hohmann, G.W., 1998, Electromagnetic theory for geophysical applications, *in* Nabighian, M.N., ed., Electromagnetic methods in applied Geophysics, Volume 1, Society of exploration geophysics, p. 131-311.

Ward, S.H., Peebles, W.J., and Ryu, J., 1973, Analysis of geomagnetic data, methods in computational physics, Geophysics academic press, New York.

Watson, K.A., and Barker, R.D., 1999, Differentiating anisotropy and lateral effects using azimuthal resistivity offset Wenner soundings: Geophysics, v. 64 (3), p. 739-745.

Weaver, J.T., 1970, The general theory of EM induction in a conducting half-space: Geophys. J. Roy. Astr. Soc., v. 22, p. 82-100.

Weidelt, P., 1983, The harmonic and transient electromagnetic response of a thin dike: Geophysics, v. 48, p. 934-952.

West, G.F., Macnae, J.C., and Lamontagne, Y., 1984, A time-domain electromagnetic system measuring the step response of the ground: Geophysics, v. 49, p. 1010-1026.

Wiese, H., 1962, Die Streichrichtung der Untergrundstrukten des electrschen Widerstandes, erschlossen aus geomagnetischen: PAGEOPH, v. 52, p. 83-103.

Worthington, P.F., 1993, The uses and abuses of Archie equations: 1. The formation factor-porosity relationship: Journal of applied geophysics, v. 30, p. 215-228.

Wright, E.P., 1992, The hydrogeology of crystalline basement aquifer in Africa: Geological society (special publication), v. 66, p. 1-27.

Yang, C.H., Tong, L.T., and Hung, C.F., 1999, Combined application of DC and TEM to seawater intrusion mapping: Geophysics, v. 64 (2), p. 417-425.

Yungul, S. H., 1961, Magnetotelluric sounding three layers interpretation curves: Geophysics, v.26 (4), p. 465-473

Yungul, S. H., 1996, Electrical methods in geophysical exploration of deep sedimentary Basin, Publ., Champan and Hall, London., 208 p.

Yungul, S. H., 1982, Geoelectricity in McGraw-Hill Encyclopaedia of Science and technology, 5/e, p.171-175.

Zhdanov, M.S., and Keller, G. V., 1994, The geoelectrical methods in geophysical exploration, Elsevier science, 837 p.